Springer Series in Chemical Physics 125

Kaoru Yamanouchi
Alina A. Manshina
Vladimir A. Makarov *Editors*

Progress in Photon Science

Emerging New Directions

Springer

Springer Series in Chemical Physics

Volume 125

The Springer Series in Chemical Physics consists of research monographs in basic and applied chemical physics and related analytical methods. The volumes of this series are written by leading researchers of their fields and communicate in a comprehensive way both the basics and cutting-edge new developments. This series aims to serve all research scientists, engineers and graduate students who seek up-to-date reference books.

More information about this series at http://www.springer.com/series/676

Kaoru Yamanouchi · Alina A. Manshina ·
Vladimir A. Makarov
Editors

Progress in Photon Science

Emerging New Directions

Springer

Editors
Kaoru Yamanouchi
Department of Chemistry
The University of Tokyo
Tokyo, Japan

Alina A. Manshina
Institute of Chemistry
Saint Petersburg State University
Saint Petersburg, Russia

Vladimir A. Makarov
Faculty of Physics
Lomonosov Moscow State University
Moscow, Russia

ISSN 0172-6218 ISSN 2364-9003 (electronic)
Springer Series in Chemical Physics
ISBN 978-3-030-77645-9 ISBN 978-3-030-77646-6 (eBook)
https://doi.org/10.1007/978-3-030-77646-6

This Springer imprint is published by the registered company Springer Nature Switzerland AG
The registered company address is: Gewerbestrasse 11, 6330 Cham, Switzerland

Preface

In October 2014, School of Science, The University of Tokyo (UTokyo), jointly with the Department of Civil Engineering, School of Engineering, established the Students and Researchers Exchange Program in Sciences (STEPS) with Lomonosov Moscow State University (MSU) and Saint Petersburg State University (SPbU) with financial support from the Re-Inventing Japan Project, which was renamed later and is now called Inter-University Exchange Project, of the Ministry of Education, Culture, Sports, Science and Technology. Since then, we have been working to promote the STEPS program not only by exchanging students and researchers but also by holding scientific symposia and gatherings.

With support from the STEPS program, we held the 1st STEPS Symposium on Photon Science on March 21 and 22, 2015, in the auditorium of the Chemistry Main Building on the Hongo Campus of the University of Tokyo, and the contents of the 28 lectures given at the symposium were compiled as a form of a book entitled "Progress in Photon Science—Basics and Applications," which was published in 2017 as the 115th volume of Springer Series in Chemical Physics. In order to keep the momentum we gained through the fruitful discussion we had during the 1st symposium, followed by a number of international research cooperation among the attendees, we decided to keep holding STEPS Symposium on Photon Science in cooperation with the research groups involved in the STEPS program.

The 2nd STEPS Symposium on Photon Science was held during March 14–16, 2016, in Hotel New Peterhof, Saint Petersburg, Russia, and invited talks were given by 33 researchers from MSU, SPbU, and UTokyo. The third of this symposium series was held on March 11 and 12, 2018, in Korston Hotel Moscow, Moscow, Russia, and 36 researchers gave invited talks from the three institutes. The contents of lectures in these two symposia were compiled into a second volume of "Progress in Photon Science" series, "Progress in Photon Science—Recent Advances," which was published from Springer in January 2019.

The fourth and the final STEPS Symposium was held at The University of Tokyo during March 20–22, 2019. The lectures were given by the following 34 researchers from MSU, SPbU, and UTokyo: Mikhail Federov, Kirill Griogriev, Olga Kosareva, Konstantin Kouzakov, Vladimir Makarov, Vyacheslav Morozov, Alexander Shkurinov, Svyatoslav Shlenov, and Andrey Stolyarov from MSU;

Alexander Andreev, Alexander Konev, Alexei Kononov, Natalia Kopteva, Alina Manshina, Andrey Mereschchenko, Artem Rybkin, Alexander Shikin, Sergey Tunik, and Oleg Vyvenko from SPbU; and Toshiaki Ando, Keisuke Goda, Takashi Hiroi, Norikatsu Mio, Eiichi Nakamura, Hiroshi Nishihara, Yutaka Ohira, Shin-ichi Ohkoshi, Jun Okabayashi, Tatsuya Tsukuda, Kana Yamada, Hideaki Yoshimura, Junji Yumoto, Qiqi Zhang, and Youyuan Zhang from UTokyo.

All of the lectures were very exciting and informative, and we thought it appropriate to record the topics at the forefront of photon science addressed in the lectures into a third volume of the series, which was entitled, "Progress in Photon Science—Emerging New Directions." We extended an invitation to the researchers who gave a presentation at the 4th symposium to write a review-style chapter for the third volume. Thanks to their enthusiastic responses, we were able to compile as many as 10 peer-reviewed chapters. Each chapter of this book begins with an introductory part, in which a clear and concise overview of the topic and its significance are given, and moves onto a description of the authors' most recent research results.

The chapters of this volume cover a diverse range of the research field of photon science, and the topics may be grouped into six categories: light propagation and plasma physics (Chaps. 1 and 2); molecules interacting with intense laser fields (Chap. 3); photochemistry and novel materials (Chaps. 4 and 5); photobiology (Chap. 6); photons and applications (Chap. 7); and optical responses of solid and nanostructures (Chaps. 8–10). We hope this volume will convey the excitement of a variety of activities in photon science to the readers and stimulate interdisciplinary interactions among researchers, thus paving the way to explorations of new frontiers in photon science. We also hope this book, together with the first two volumes, will be regarded as a valued record of the STEPS program, which ended in March 2019.

We would like to take this opportunity to thank all of the authors who kindly contributed to "Progress in Photon Science—Emerging New Directions," by describing their most recent work at the frontiers of photon science. We also thank the reviewers who have read the submitted manuscripts carefully.

One of the co-editors (KY) thanks Ms. Mihoshi Abe, a secretary to his research group, for her help with the preparation of this book.

Finally, we would like to thank Ms. Takako Jono at the STEPS Office of School of Science, University of Tokyo, for helping us prepare for the 4th STEPS Symposium on Photon Science, and Dr. Zachary Evenson at Springer for his kind support for our third volume of "Progress in Photon Science" in the Springer Series in Chemical Physics.

The 4th STEPS Symposium on Photon Science in Tokyo (2019)

Tokyo, Japan — Kaoru Yamanouchi
Saint Petersburg, Russia — Alina A. Manshina
Moscow, Russia — Vladimir A. Makarov

Contents

Contributors

A. Andreev SPbSU, Saint Petersburg, Russia;
MBI, Berlin, Germany;
ELI-ALPS, Szeged, Hungary

Vladimir G. Arakcheev Faculty of Physics, M.V. Lomonosov Moscow State University, Moscow, Russia

Alexei N. Bekin Faculty of Physics, M.V. Lomonosov Moscow State University, Moscow, Russia

A. A. Dergachev Faculty of Physics and International Laser Center, M.V. Lomonosov Moscow State University, Moscow, Russia

V. A. Diukov Physics Faculty, Moscow State University, Moscow, Russia

K. S. Grigoriev Physics Faculty, Moscow State University, Moscow, Russia

V. P. Kandidov Faculty of Physics and International Laser Center, M.V. Lomonosov Moscow State University, Moscow, Russia

Ilya Kolesnikov Saint Petersburg State University, Saint Petersburg, Russia

Alexander S. Konev Institute of Chemistry, Saint Petersburg State University, Saint Petersburg, Russia

Chen Lan ELI-ALPS, Szeged, Hungary

Zs. Lecz ELI-ALPS, Szeged, Hungary

Erik Lötstedt Department of Chemistry, School of Science, The University of Tokyo, Bunkyo-ku, Tokyo, Japan

Daniil A. Lukyanov Institute of Chemistry, Saint Petersburg State University, Saint Petersburg, Russia

V. A. Makarov Physics Faculty, Moscow State University, Moscow, Russia;
International Laser Center, Moscow State University, Moscow, Russia

Alina Manshina Saint Petersburg State University, Saint Petersburg, Russia

Shigemi Mizukami WPI-Advanced Institute for Materials Research, Tohoku University, Sendai, Japan;
Center for Spintronics Research Network (CSRN), Tohoku University and Center for Science and Innovation in Spintronics (CSIS), Tohoku University, Sendai, Japan

Vyacheslav B. Morozov Faculty of Physics, M.V. Lomonosov Moscow State University, Moscow, Russia

Koji Nakabayashi Department of Chemistry, School of Science, The University of Tokyo, Tokyo, Japan

Shin-ichi Ohkoshi Department of Chemistry, School of Science, The University of Tokyo, Tokyo, Japan

Jun Okabayashi Research Center for Spectrochemistry, The University of Tokyo, Tokyo, Japan

Takeaki Ozawa Department of Chemistry, School of Science, The University of Tokyo, Tokyo, Japan

I. A. Perezhogin Technological Institute for Superhard and Novel Carbon Materials, Troitsk, Russia;
International Laser Center, Moscow State University, Moscow, Russia

S. A. Shlenov Faculty of Physics and International Laser Center, M.V. Lomonosov Moscow State University, Moscow, Russia

F. I. Soyfer Faculty of Physics and International Laser Center, M.V. Lomonosov Moscow State University, Moscow, Russia

Olaf Stefanczyk Department of Chemistry, School of Science, The University of Tokyo, Tokyo, Japan

Kazuya Z. Suzuki WPI-Advanced Institute for Materials Research, Tohoku University, Sendai, Japan;
Center for Spintronics Research Network (CSRN), Tohoku University and Center for Science and Innovation in Spintronics (CSIS), Tohoku University, Sendai, Japan

E. V. Vasilyev Faculty of Physics and International Laser Center, M.V. Lomonosov Moscow State University, Moscow, Russia

Kaoru Yamanouchi Department of Chemistry, School of Science, The University of Tokyo, Bunkyo-ku, Tokyo, Japan

Hideaki Yoshimura Department of Chemistry, School of Science, The University of Tokyo, Tokyo, Japan

Youyuan Zhang Department of Chemistry, School of Science, The University of Tokyo, Bunkyo-ku, Tokyo, Japan

Chapter 1
Self-action of Femtosecond Optical Vortex in a Medium with Kerr Nonlinearity

S. A. Shlenov, E. V. Vasilyev, V. P. Kandidov, A. A. Dergachev, and F. I. Soyfer

Abstract We numerically study the dynamics of the formation of optical vortex from collimated Gaussian beam behind a spiral phase plate, and assess the characteristic scale of azimuthal instability developing in a Kerr medium. The near zero values of intensity on axes arise shortly after the plate but the ring profile is formed at the distance of approximately half of the diffraction length. The break-up of the vortex into several hot spots in the Kerr medium is more rapid for the large-scale noise. The transformation of the vortex spatial spectrum is analyzed along with changes in its phase profile. The interference of the self-focusing mode and the radiation extending to the periphery leads to the formation of rings in the beam spectrum.

1.1 Introduction

The interest in the propagation of laser radiation in media with Kerr nonlinearity is largely due to the actual problems of femtosecond filamentation, during which extended high-intensity light filaments are formed [1]. The basis for the nucleation of filaments is the self-focusing of radiation in a medium with cubic nonlinearity [2, 3], which, together with other competing mechanisms, in particular, aberrational defocusing in self-induced plasma, ensures the maintenance of a high fluence in a bulk transparent medium at distances substantially longer than the diffraction (Rayleigh) length. Spatial effects are accompanied by a strong broadening of the frequency spectrum of the pulse. In media with anomalous group velocity dispersion due to

S. A. Shlenov · E. V. Vasilyev (✉) · V. P. Kandidov · A. A. Dergachev · F. I. Soyfer
Faculty of Physics and International Laser Center, M.V. Lomonosov Moscow State University, Leninskie Gori 1, Moscow 119991, Russia
e-mail: vasilev.evgeniy@physics.msu.ru

S. A. Shlenov
e-mail: shlenov@physics.msu.ru

V. P. Kandidov
e-mail: kandidov@physics.msu.ru

A. A. Dergachev
e-mail: aa.dergachev@physics.msu.ru

K. Yamanouchi et al. (eds.), *Progress in Photon Science*, Springer Series in Chemical Physics 125, https://doi.org/10.1007/978-3-030-77646-6_1

simultaneous spatial self-focusing and temporary self-compression of the pulse, the formation of wave packets with a high localization of the light field, the so-called "light bullets", is possible [4]. The phenomenon of filamentation can be considered as the basis of new laser technologies and applications related to the transmission of light energy with high fluence over long distances, the creation of remote white light sources, and the use of induced plasma channels of filaments [5].

The physical picture of femtosecond filamentation and the accompanying supercontinuum generation are well studied for the Gaussian and Bessel-Gaussian beams. However, more and more studies have recently appeared on the filamentation of beams of a more complex profile [6], including ring beams with a spiral phase dislocation on the axis—optical vortices [7], which can be described by the expression for the complex field amplitude using Lagger polynomials

$$E_{mn}(r, \varphi, z = 0) = E_0 \left(\frac{r}{r_0} \right)^m L_n^m \left(\frac{4r^2}{r_0^2} \right) \exp\left\{ -\frac{r^2}{2r_0^2} + im\varphi \right\}, \qquad (1.1)$$

where m is the topological charge, φ is the azimuthal angle, L_n^m—generalized n-order Laguerre polynomial, r_0 is the characteristic spatial scale. In the simplest case $L_0^m = 1$ the beam at $m > 0$ has the form of a ring, the inner and outer diameters of which depend on r_0 and m. Note that the absence of a topological charge ($m = 0$) transforms the formula (1.1) into an expression for a Gaussian beam of radius r_0. Vortex beams (1.1) have an orbital angular momentum and a helical phase front [7, 8], which prevents the "penetration" of the light field on the optical axis, where the zero-intensity point is located.

Optical vortex generation can be performed in various ways. It can be formed as a result of the interference of laser beams with an initially regular wavefront as they pass through randomly inhomogeneous media, optic fibers or specially made holograms [9]. In addition, the generation of vortex fields is possible directly in laser resonators [10]. It is relevant to obtain femtosecond vortices as ring beams with a phase dislocation in a wide frequency range typical for ultrashort pulses. In particular, dispersion-free schemes using uniaxial crystals and polarizing filters are proposed [11]. In principle, it is possible to use relatively simple spiral phase plates, passing through which collimated Gaussian beam acquires an annular intensity distribution with a phase dislocation on the axis [12].

The propagation of optical vortices in a linear medium has much in common with the diffraction of Gaussian beams. In [13], the behavior of the outer and inner radii of an optical vortex's ring-like profile as it propagated was analyzed, and a comparison was made with an experiment using a He-Ne laser. It was shown that the maximum intensity value at the diffraction length $z_d = kr_0^2$ both in the Gaussian and in vortex beams decreases by 2 times, and the width of the spatial profile increases by $\sqrt{2}$ times.

The study of self-focusing of optical vortices in a medium with cubic nonlinearity in the quasi-optical approximation was first performed in [14]. The critical power at which the self-similar solution corresponds to the collapse of the beam into an infinitely narrow ring was found. It was shown numerically and analytically that the critical power of an optical vortex increases with increasing topological charge m. The dependence of the critical power for self-focusing of the vortex beam $P_V^{(m)}$ on the topological charge m in units of the critical power of the Gaussian beam P_G is presented in [15]. For example, for $m = 1$ the critical power of optical vortex is $P_V^{(1)} = 4P_G$. Experimental confirmation of the increase in critical power with increasing m was obtained in [16] on the example of the optical vortices propagation in air.

It was shown in [17] that the collapse of a self-similar ring intensity distribution during self-focusing of an optical vortex can stop without additional competing mechanisms—only due to diffraction, which occurs during self-focusing of slit beams, corresponding to radial sections of vortex. One of the scenarios for further self-focusing of optical vortices is the formation of a thin high-intensity ring, which decreases in radius as it propagates.

In an experiment, the modulation instability in a cubic medium breaks the azimuthal symmetry of the beam, and it breaks up into individual hot spots—regions of filament formation. It was experimentally and numerically demonstrated that the presence of 10% amplitude-phase noise leads to the decay of a femtosecond vortex into several hot spots located along a circle, and the number of spots increases with increasing topological charge and pulse power [18]. In [19] it is shown that in a medium with the cubic-quintic nonlinearity optical vortices with a small topological charge are linearly stable, provided that they are very broad. In other words, we can get stable spinning spatio-temporal solitons as a result of the competition between focusing and defocusing nonlinearities [20]. Another opportunity to observe a stable propagation of the spatially localized single- and double-charge optical vortices in a self-focusing nonlinear medium is to use partially incoherent light [21].

It is significant for pulsed radiation that the azimuthal instability does not occur at the pulse front, where the instantaneous power is relatively small, and the optical vortex retains its axisymmetric shape in the intensity distribution [22]. Nevertheless, even when the intensity is high enough, so that the peak power exceeds the critical power of self-focusing, the breakup into hot spots occurs after the nonlinear focus [23] if the noise in the femtosecond vortex beam is small enough. This feature allows us to use the axisymmetric approximation for modeling the propagation of optical vortices at the initial stages of self-action. In [24], the decay of vortices with various topological charges under conditions of instantaneous and inertial plasma nonlinearity was studied. It is found that vortices with a topological charge $m = 1$ are more stable while propagating than vortices with a large topological charge. It was also found that the frequency of pulse refocusing increases with a topological charge of the beam.

Along with the spatiotemporal characteristics, the generation of the supercontinuum due to the self-action of optical vortices, particularly in calcium fluoride, has been studied. The vortex nature of the beam in the near and far zones are shown, and

the distribution of the spectral components of the radiation is obtained depending on the position of the beam waist relative to the input face of the crystal [25]. It was shown in [23] that, due to the high gradient of the intensity near the axis, the angular spectrum of the vortex beam is wider than that of the Gaussian beam with the same excess of the peak power over the critical value.

The propagation of femtosecond optical vortices under filamentation in a medium with anomalous group velocity dispersion was studied in the axisymmetric approximation in [26, 27]. It is shown that in the case of self-action of ring beams with a phase dislocation with a topological charge $m = 1$ in fused silica at a central wavelength $\lambda_0 = 1800$ nm, a sequence of annular light bullets with a duration of about 10 fs and a radius of at least 10 μm is formed. In this case, the radiation has a multifocus structure with the sharpest last focus, where global maxima of the intensity and plasma concentration on the propagation path are reached. Quantitative estimates of the transformation of the spectral energy of the pulse from the central region to the Stokes and anti-Stokes parts of the spectrum are obtained.

At the beginning of this paper, we numerically study the dynamics of the formation of optical vortices from Gaussian beam behind a spiral phase plate in order to evaluate the characteristic conversion distances and the possibility of using the same spiral phase plate to obtain optical vortices at adjacent wavelengths. Then we assess the characteristic scale of azimuthal instability development of the optical vortex in a medium with cubic nonlinearity, and, finally, analyze the features of transformation of its wave front and angular spectrum.

1.2 Vortex Formation from a Gaussian Beam in a Scheme with a Spiral Phase Plate

The most common laser beams used in experimental studies have Gaussian intensity profile (Fig. 1.1a) and plane or parabolic phase. To obtain an optical vortex we need to introduce the phase singularity into the phase profile (Fig. 1.1b), which can be done with the use of specific phase plates. Free propagation of the originally Gaussian beam with spiral phase, as we will show later, leads to a formation of an optical vortex having a ring-like intensity distribution (Fig. 1.1c).

To estimate lengths of propagation needed for the formation of the vortex, we used a 3D model of laser beam propagation:

$$2ik\frac{\partial A(x,y,z)}{\partial z} = \left[\frac{\partial^2}{\partial x^2} + \frac{\partial^2}{\partial y^2}\right]A(x,y,z) \tag{1.2}$$

The initial conditions for the slowly varying complex envelope $A(x, y, z = 0)$ were the following:

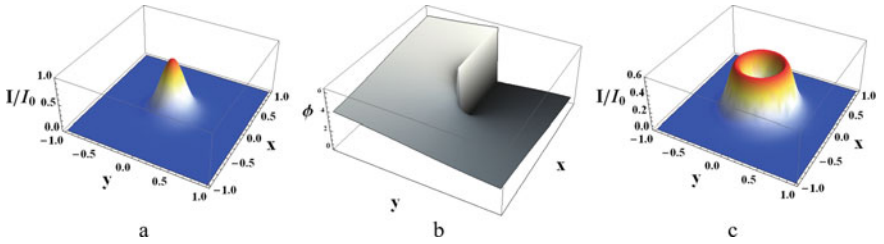

Fig. 1.1 Intensity distribution in the cross-section of the original Gaussian beam (**a**), the phase singularity in the beam after passing through the phase plate (**b**), intensity distribution in the cross-section of the optical vortex (**c**)

$$A(x, y, z = 0) = A_0 \exp\left\{-\frac{r^2}{2r_0^2}\right\} \exp\left\{im\varphi(x, y)\right\}, \tag{1.3}$$

where $r = \sqrt{x^2 + y^2}$, $\tan\varphi = y/x$. The topological charge of the vortex phase is $m = 1$ throughout the study. The beam radius is $r_0 = 1$ mm.

The simulation of the vortex propagation has several difficulties due to the phase singularity on the axis $x = y = 0$. In the formed vortex, the intensity of the laser field in the point of phase singularity is zero, but in our model, it is not zero right after the phase plate. The intensity near the axis rapidly declines and it reaches near zero values shortly after the plate. This is because of the destructive interference of the field at which the phase varies by 2π along the path enclosing the singularity. The ring-like intensity distribution is formed and is accompanied with the energy exchange between the central and peripheral parts of the beam which takes the form of ring-like waves from the central part to the peripheral, propagating at high angles to the optical axis. In numerical simulation, a finite computational grid is used so that these waves reaching the edges of the grid—reflect from them, return to the central part and interfere with the beam, producing numerical artifacts.

To overcome the problem of the indeterminate phase on the axis, phase jump is located between grid nodes (Fig. 1.2).

To overcome the interference with the reflected waves we extend the computational area in the cross-sectional dimensions so that there is some buffer areas around the beam for the ring waves to propagate farther from the beam. The typical grid has the size of 8192×8192 in the cross-section and the step along the propagation axis z is about 10^{-4} of the diffraction length $z_d = kr_0^2$, which allows us to correctly reproduce the initial stages of the beam evolution.

We compared the process of the vortex formation from the Gaussian beam after it passes through the phase plate and the propagation of the true vortex (see 1.1) with the same power. Their intensity profiles $I(r, \varphi = 0, z)$ are shown in Fig. 1.3. Shortly after the plate (Fig. 1.3a), the intensity profile of the beam is close to the original Gaussian form and far from the needed ring form of the vortex. At the distance $z = 0.01 z_d$ (Fig. 1.3b), the beam intensity in the area near the axis is close to zero and the peak intensity is higher than the original Gaussian beam due to the

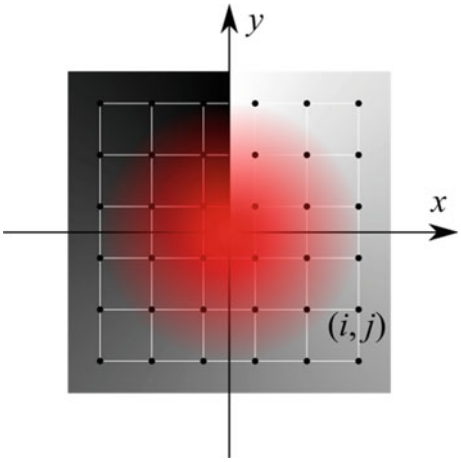

Fig. 1.2 The scheme of the Cartesian grid (black dots) used for numerical simulation of vortex formation behind the phase plate. The grayscale gradient represents the phase obtained after passing the plate. The initial Gaussian beam is shown in red. The picture does not show the scale of the used grid and beam size. The typical size of the grid was about several thousands of points along each cross-sectional coordinate

oscillations in the profile. The size of the low intensity area near the axis is also much smaller than for the vortex. At the distance $z = 0.5z_d$ (Fig. 1.3c), the beam in the simulation is very close to the vortex.

The radii of the optical vortex and the collimated Gaussian beam have the same dependence on the propagation distance in a linear medium:

$$r_v(z) = r_0\sqrt{1 + (z/z_d)^2}. \tag{1.4}$$

The radius of the beam in the simulation was defined as the distance from the beam axis and the position of the intensity global maximum. The obtained dependency of the beam radius on the propagation distance is shown in Fig. 1.4.

The analysis shows that the size of the ring and its profile reaches the expecting value at the distances of about $0.5z_d$. This value was taken as an estimate of the vortex formation distance.

We consider the use of spiral phase plate designed for the wavelength of 1800 nm to obtain an optical vortex in femtosecond pulses at this central wavelength. The wide spectrum of the femtosecond pulse means that the plate will be actually used for wavelengths different from those it was designed for. It leads to different phase shifts for different wavelengths in the spectrum. If the spectrum of the femtosecond pulse has a half-width of about 80 nm, a part of the femtosecond pulse whose wavelength is longer than the central wavelength by about 4.5% will also propagate through the same phase plate.

We conducted a series of numerical simulations using the phase plate designed for 1800 nm, producing a vortex with topological charge $m = 1$ at this wavelength. We used beams whose wavelengths are longer and shorter than 1800 nm. We found that there is up to 25% difference in the wavelength of the beam and of the plate when a clearly seen ring with a phase singularity is formed. Beams whose wavelengths are

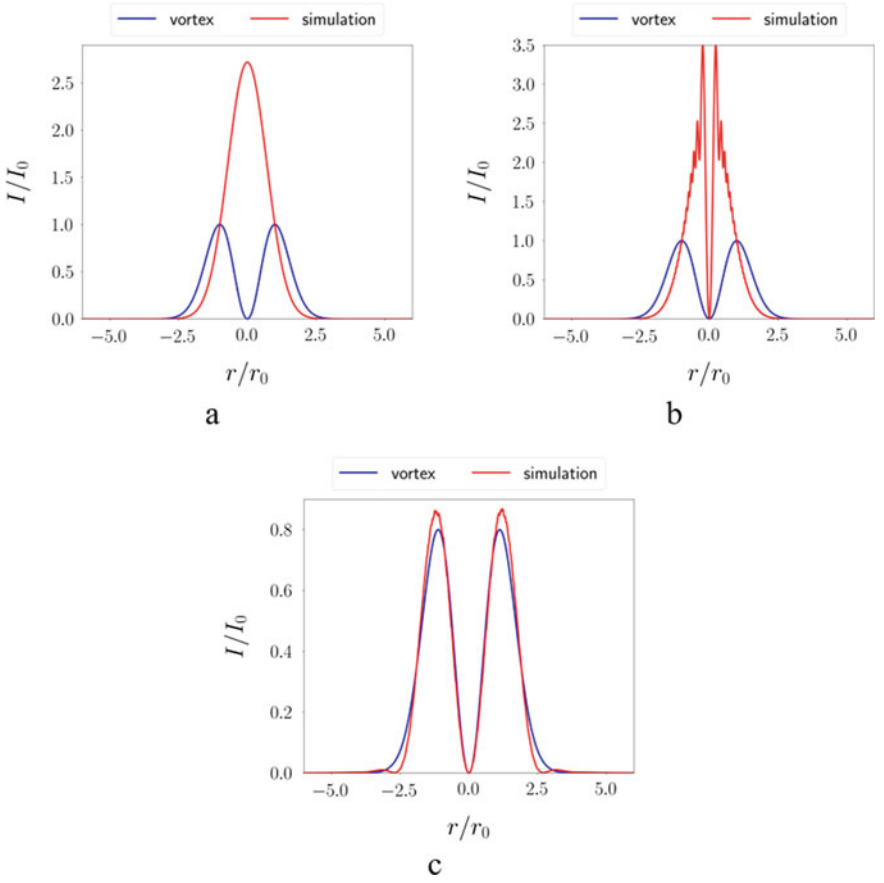

Fig. 1.3 Intensity profiles of the Gaussian beam after the spiral phase plate (red curves) and optical vortex (blue curves) at the distances $z/z_d = 0.00001$ (**a**), 0.01 (**b**), 0.5 (**c**); z_d is the diffraction length of the beam, I_0 is the vortex peak intensity at $z = 0$

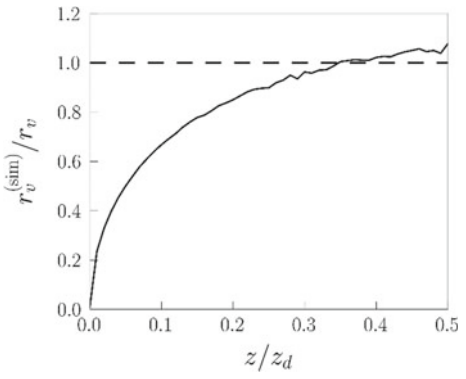

Fig. 1.4 The dependency of the beam radius obtained in simulation $r_v^{(sim)}$ and normalized by the radius of the vortex beam (1.5) $r_v(z)$ on the propagation distance z after the phase plate normalized by the diffraction length z_d. The dashed horizontal line stays for the radius of the optical vortex

longer than 2250 nm do not form a ring. Therefore, we hope that in the experiment the same spiral phase plate can be used to form a femtosecond optical vortex up to the central wavelength of 2100 nm.

1.3 Spatial Stability of the Optical Vortex in the Kerr Medium

The seed for the break-up of the vortex beam in Kerr medium is either a non-ideal beam profile or fluctuations of refractive index. We studied the process of the break-up for the laser beam of the form:

$$A^{(m)}(x, y, z = 0) = A_0\left(\frac{r}{r_0}\right)^m \exp\left\{-\frac{r^2}{2r_0^2}\right\} \exp\left\{im\varphi(x, y)\right\}, \tag{1.5}$$

where $\tan\varphi = y/x$. The central wavelength was 1800 nm, the beam radius $r_0 = 92$ μm, topological charge $m = 1$. The peak intensity is $I_{max}(z = 0) = 1/e \times (cn_0A_0^2)/8\pi$, the beam power is $P = (cn_0A_0^2)/8\pi \times \pi r_0^2$, which is 5 times higher than the critical power of self-focusing for the vortex. In LiF crystal, for instance, the peak power would be 704 MW. For the 67 fs laser pulse, it corresponds to the total energy of 50 μJ.

The propagation equation for the complex envelope $A^{(m)}(x, y, z)$ (1.5) in the Kerr medium takes the form:

$$2ik\frac{\partial A(x, y, z)}{\partial z} = \left[\frac{\partial^2}{\partial x^2} + \frac{\partial^2}{\partial y^2} + \frac{2k^2}{n_0}n_2 I(x, y)\right]A(x, y, z) \tag{1.6}$$

This model is valid for the first stage of the pulse propagation, self-focusing, until the increasing intensity leads to the ionization of the medium. The intensity distributions in the cross-section of the beam at different propagation distances z obtained in the simulation illustrate the beam evolution in the nonlinear propagation process (Fig. 1.5). In the first stage the ring of the vortex exhibits self-contraction, i.e. its thickness decreases while the radius of the ring remains practically unchanged. The self-focusing in this stage does not lead to the beam collapse with the infinite increase in intensity even in the absence of defocusing factors like self-induced plasma or high-order nonlinearities. This is due to the fact that the energy concentrates only in one dimension (radial) so that it is similar to the self-focusing of the beam passed through a thin slit where the collapse is stopped by diffraction [17]. Therefore, the first nonlinear focus in the multi-focusing structure of the vortex filamentation can be achieved in the ionization-free regime [27].

At the distance $z = 0.8$ cm (Fig. 1.5c), a ring whose intensity is smaller than the main ring starts appearing in the peripheral part of the beam, being detached from the main ring, and the radius increases as the distance z increases.. After that, the radius of the main ring decreases and the new nonlinear focus is formed. The profile of the

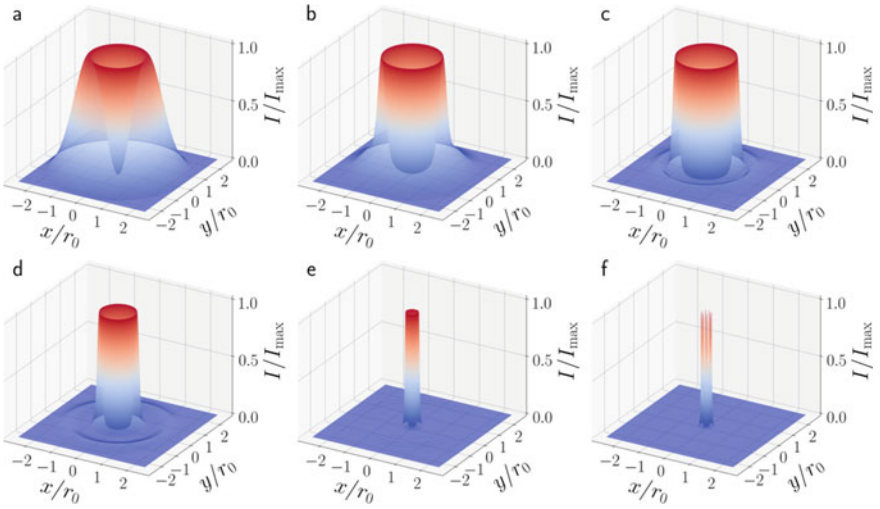

Fig. 1.5 Intensity distributions in the cross-section of the vortex at different distances z in the nonlinear medium: **a** 0 cm, **b** 0.6 cm, **c** 0.82 cm, **d** 1.36 cm, **e** 1.56 cm, **f** 1.58 cm. The intensity is normalized by its maximum at the given distance. The size of the shown region is 0.5 mm × 0.5 mm, total size of the grid is 1 mm × 1 mm

beam remains axially symmetric until $z = 1.58$ cm (Fig. 1.5f), where modulation instability leads to the break-up of the ring into several hot spots clearly separated in the azimuthal direction. Indeed, in the numerical simulation, the grid size is not fine enough even when we adopt ideal initial beam conditions with a uniform medium, that is, if the beam intensity becomes significantly large, a self-focusing proceeds, leading to a smaller cross-section of the beam than the grid size.

In the experimental conditions, the initial beam has spatial non-uniformities. Therefore the next series of calculations introduced some multiplicative noise $\xi(x, y)$ in the initial conditions. The noise was Gaussian. We used two values of its correlation radius r_c that differed by an order, which we hereafter call the large-scale ($r_c = 25$ μm) noise and the small-scale noise ($r_c = 2.5$ μm) (Fig. 1.6).

The total field amplitude had the form

$$A_{noise}(x, y, z = 0) = A^{(m)}(1 + \sigma\xi(x, y)), \tag{1.7}$$

where $A^{(m)}$ is defined by (1.5). The parameter σ was used to vary noise relative amplitude. Large-scale fluctuations near the intensity maximum in the ring contain the power of about $0.5P_{cr}$ for the Gaussian beam.

The discrepancy between maximum and minimum intensity at the same radius may be initially small but increases while propagating in nonlinear medium. To estimate the break-up quantitatively we introduced the decay coefficient $k_{decay}(z)$ as follows. We define the distance between the position of the intensity maximum and the beam axis as the ring radius $r_{ring}(z)$. We find the intensity minimum $I_{r,min}$ and

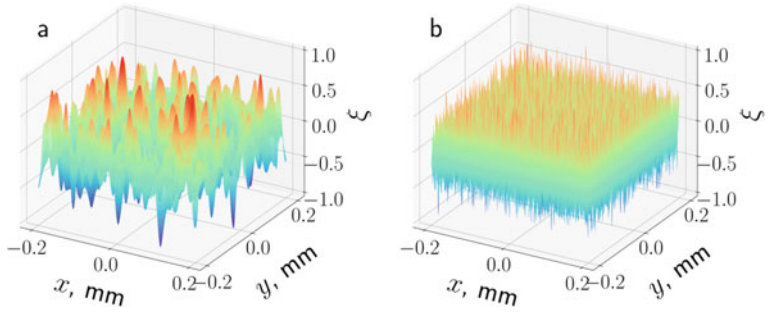

Fig. 1.6 The random noise distribution ξ in the initial conditions (1.7) with large-scale (**a**) and small-scale (**b**) noise

maximum $I_{r,max}$ over the circle centered on the beam axis with the radius $r_{ring}(z)$. The decay coefficient is defined as the relative difference between minimum and maximum intensity on the circle:

$$k_{decay}(z) = (I_{r,max} - I_{r,min})/I_{r,max} \tag{1.8}$$

For the ideal ring with constant intensity, the decay coefficient equals 0, for completely broken azimuthal symmetry it tends to be 1.

Figure 1.7 shows the dependence of the decay coefficient on the propagation distance. As it may be predicted, the increase in the noise ratio leads to the increase in modulation instability and earlier break-up, which holds both for the large- and small-scale noise. The value of the decay coefficient remains small until the propagation distance reaches about 0.1, beyond which it grows rapidly, leading to the abrupt break-up. The lesser the noise, the farther the beam propagates without break-up, and the more abrupt is the decay. In all the cases, the break-up occurred earlier than that in the noiseless beam. Therefore we proved that numerical instability and the grid noise in our simulations added little in comparison with the explicit noise in the initial conditions.

To estimate the distance to the visible break-up, we used the value z_{decay} at which $k_{decay} = 0.5$ (Fig. 1.8). The optical vortex brakes-up faster in the case of large-scale noise, because diffraction effectively smooths small-scale phase fluctuations.

1.4 Spatial Spectra of Annular Beams

We begin the analysis of angular spectra features of the optical vortices by considering the cross-section of the ring beam, which we set for simplicity as the sum of two Gaussian beams of width w located at distances ξ to the right and to the left of the point $x = 0$ (the axis of the ring beam):

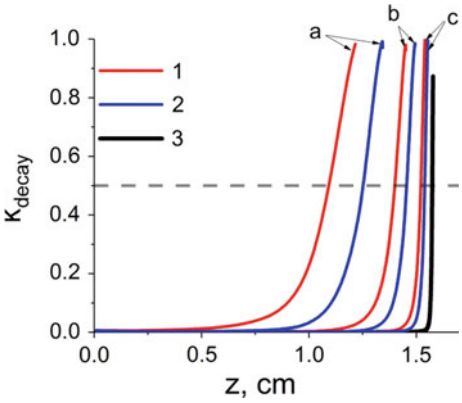

Fig. 1.7 The dependency of the decay coefficient k_{decay} from propagation distance z for large-scale noise (1), small-scale noise (2) and noiseless ($\sigma = 0$) vortex (3). Parameter $\sigma = 10^{-3}$ (**a**), 10^{-5} (**b**), 10^{-7} (**c**). The dashed line marks the threshold value which was used to determine the beam break-up distance

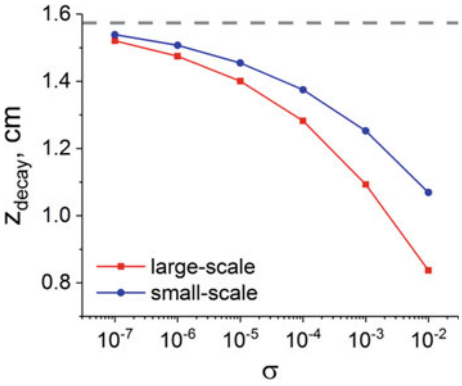

Fig. 1.8 The dependency of the break-up distance z_{decay} from the noise magnitude determined by σ for large-scale (red) and small-scaled (blue) noise. The dashed line marks the break-up distance for noiseless vortex (due to grid noise)

$$A(x) = A_0\left[\exp\left\{-\frac{(x-\xi)^2}{2w^2}\right\} + \exp\left\{-\frac{(x+\xi)^2}{2w^2}\right\}\right]. \tag{1.9}$$

We will assume that $\xi > w$. The spatial spectrum $S(k_x)$ of such a beam can be easily obtained analytically:

$$S(k_x) = 4w^2 \cos^2 k_x\xi \exp\left\{-(k_x w)^2\right\} \tag{1.10}$$

It has many local maxima ("spikes", in the two-dimensional case, rings) at spatial frequencies $k_x = n\pi/\xi, n = 0, \pm 1, \pm 2$. The distance between them is π/ξ, and their amplitude is modulated by a Gaussian envelope with characteristic width $1/w$. With an increase in the radius ξ, the width of each "spike" in the spectral space decreases, and their number within the envelope increases at a constant value of w. For clarity, Fig. 1.9 shows the beam profile and its spectrum for various values of ξ (a) and w (b).

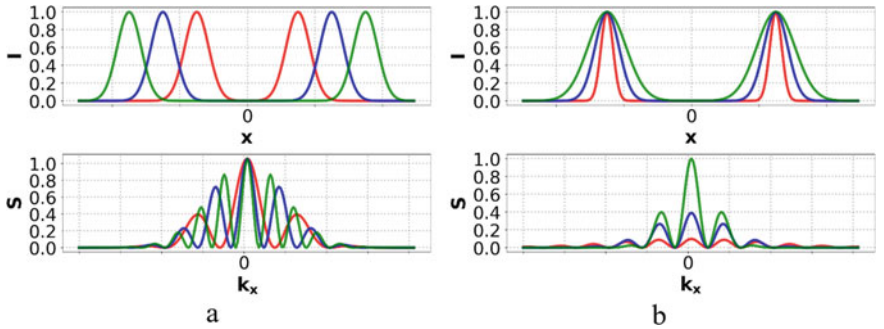

Fig. 1.9 The intensity distribution I of the diametrical cut of a three-dimensional ring beam (on the top) and the normalized spectral intensity S (at the bottom) for different beam radius ξ and ring width w

The behavior of the angular spectrum can be understood in terms of interference from two point sources, which are local maxima of the initial field distribution at distances ξ from the axis. The characteristic width of the interference fringes is inversely proportional to the distance between them. Therefore, the angular distance between the maxima decreases with increasing ξ.The smaller width w of the partial beams gives a wider spatial spectrum, that is the envelope width of local maxima in the spectrum grows and the spectral energy is redistributed to the region of high spatial frequencies. The relative magnitude of the central (global) maximum in the spectrum decreases.

In fact, the spatial distribution of intensity in the beam and its spectral components are visually similar to the radio pulse and its spectrum. Now the high-frequency packing and the envelope take place in the spectral space, and in ordinary coordinate space we have two maxima displaced with respect to zero, the width of which is determined by the width of envelope in the spectrum.

Similar conclusions are valid for a two-dimensional ring beam, but in this case one-dimensional local maxima will turn to rings. An important difference is that in the two-dimensional case one can also consider ring beams with a phase singularity on the axis, which leads to the disappearance of zero spatial harmonic in the spectrum. Instead, two maxima of smaller amplitude appear at spatial frequencies approximately corresponding to the first minimum in the spectrum for a beam without phase singularity. To illustrate the idea, consider a two-dimensional annular beam:

$$A_R(r) = A_0 \exp\left\{-\frac{(r-\xi)^2}{2w^2}\right\}, \tag{1.11}$$

where ξ is the radius of the ring, and w is its characteristic thickness. Adding a helical phase to (1.11) converts a collimated ring beam into an optical vortex, keeping the beam power unchanged:

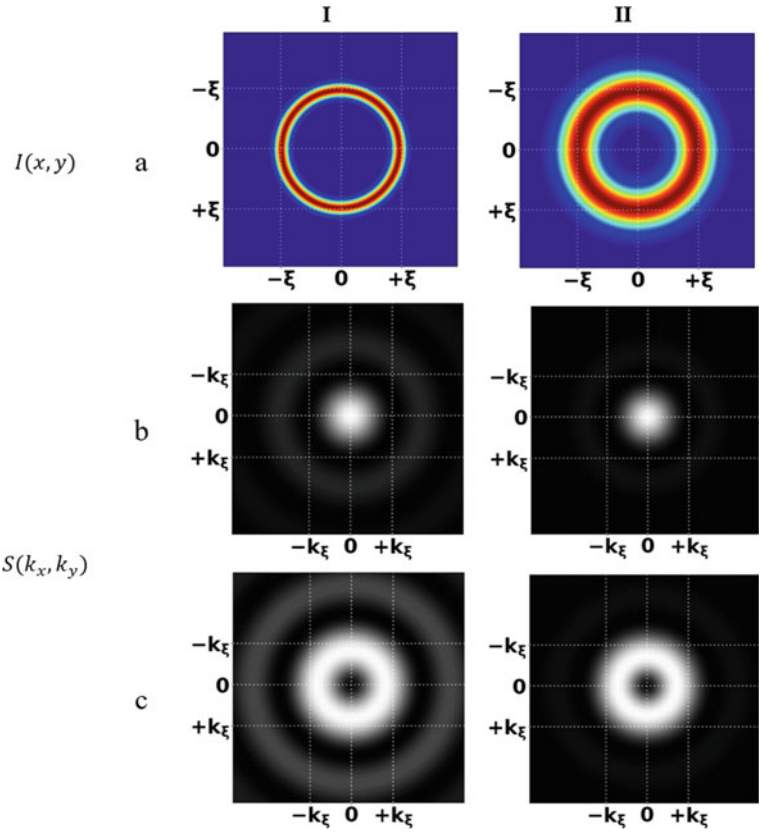

Fig. 1.10 Spatial distributions of the intensity $I(x, y)$ (**a**) and the spatial spectrum $S(k_x, k_y)$ for an annular beam without phase singularity (**b**) and for an optical vortex with a topological charge $m = 1$ (**c**) for a narrower ($w/\xi = 0.1$) (I) and wider ($w/\xi = 0.3$) (II) ring

$$A_V(r) = A_R \exp\left\{im\varphi(x, y)\right\}, \tag{1.12}$$

Figure 1.10 shows the intensity distributions $I(x, y)$ in the beam cross-section and its spatial spectra $S(k_x, k_y)$ for $w/\xi = 0.1$ (I) and 0.3 (II), where $\xi = 100$ μm. The spatial spectrum of the annular beam without phase singularity has a Bessel-like structure with a maximum at zero frequency and additional rings, the relative amplitude of which increases with decreasing width of the annular distribution of the beam intensity. At a relative ring width $w/\xi = 0.3$ (Fig. 1.10b, II), the spatial spectrum is almost unimodal—the second ring in it is very weak. In the case of a narrower ring with $w/\xi = 0.1$ μm, two additional rings with relatively low spectral intensity are clearly visible in the spectrum (Fig. 1.10b, I).

At the center of the spatial spectrum of the vortex there is always a minimum (Fig. 1.10c). It can be explained on the basis of the idea that at a distance ξ from

the optical axis there are many out-of-phase point sources of radiation. In particular, for an optical vortex with a topological charge $m = 1$, the out-of-phase sources are at the other end of the diameter. For a vortex beam with a relative ring thickness $w/\xi = 0.3\ \mu$m, the spatial spectrum has mainly one pronounced ring. As in the case of a ring beam without a phase singularity, a decrease in the parameter w leads to an increase in the relative spectral intensity in the secondary rings.

1.5 The Self-focusing Effect on the Wavefront and Spatial Spectrum of an Optical Vortex

The wavefront of the optical vortex (1.5) is a spiral isosurface $z = m/k\varphi(x, y)$, several steps of which are shown in Fig. 1.11a. Note that for $m = 0$, expression (1.5) describes a collimated Gaussian beam.

Intensity $I(x, y)$ and phase $\varphi(x, y)$ distributions in beam cross section of the optical vortex with $m = 1$ propagating in a linear medium are presented in Fig. 1.12 at various distances z. Hereinafter, the phase $\varphi(x, y)$ of the complex field $A = \Re[A] + i\Im[A]$ in the plane $z = const$ is calculated in the range of $-\pi$ to $+\pi$ as atan2$(\Im[A], \Re[A])$. Because of the beam diffraction, boundary at which the phase jump occurs turns from a straight line into a curve spinning clockwise (Fig. 1.12b–d). A similar picture was observed the interferograms obtained after the diffraction of the Gaussian beam transmitted through a vortex plate [12].

Self-focusing of the optical vortex (1.5) can be described by a nonlinear wave equation (1.6). Consider an optical vortex with a topological charge $m = 1$ and a

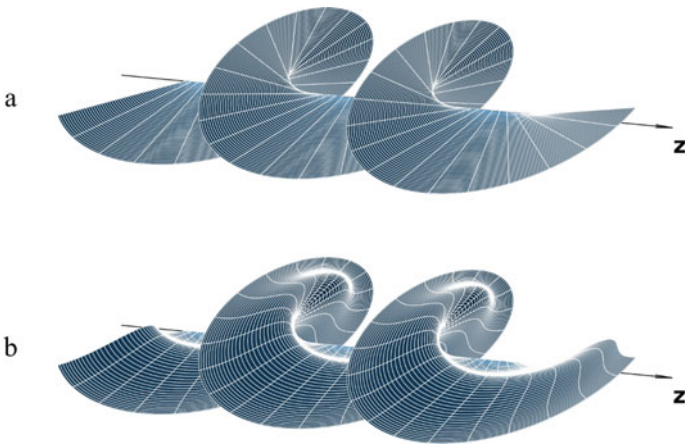

Fig. 1.11 The wavefront (phase isosurface) of the vortex beam at the beginning of the medium (**a**) and after self-focusing at a distance $z = 0.07z_d$ (qualitative picture, obtained in the approximation of a thin nonlinear lens) (**b**)

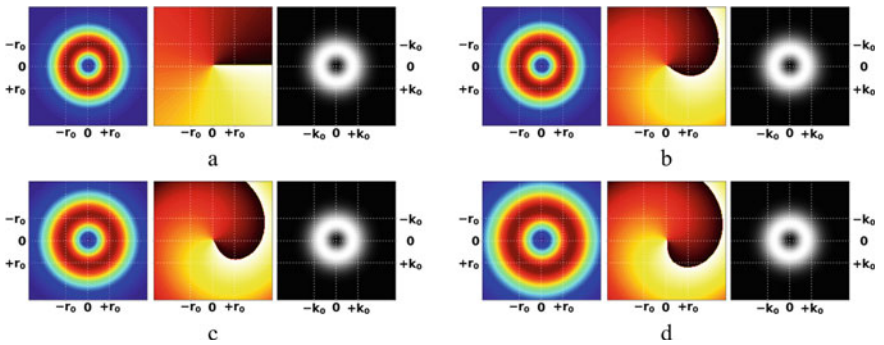

Fig. 1.12 Intensity (left), phase (center) and spectrum (right) distributions during optical vortex diffraction with a topological charge $m = 1$ at the beginning of the medium (**a**) and distances $z = 0.33$ (**b**), 0.66 (**c**) and 1.0 z_d (**d**) along the propagation direction $z_d = kr_0^2$

spatial parameter $r_0 = 100$ μm at a wavelength of $\lambda = 1800$ nm propagating in lithium fluoride. The excess of power over the critical value is chosen to be equal to $P/P_V^{(1)} = 5$, which corresponds to a nonlinear focus at a distance $z = 0.5z_d$ in the case of a Gaussian beam.

Figure 1.13 shows the intensity and phase spatial distribution of the beam, as well as its spatial spectra at different distances along the direction of the beam propagation. At the beginning of the medium (Fig. 1.13a), the intensity distribution has the form of a relatively wide ring with an e^{-2} width $w = 185$ μm, the phase across the beam has one jump by 2π, and one ring appears in the spatial (angular) spectrum. The self-action of an optical vortex begins with an increase in the peak intensity in the ring and a decrease in its width (Fig. 1.13b). Due to nonlinearity, the addition to the phase is larger in the high-intensity annular region; therefore, a phase jump of 2π does not occur along the radius across the beam. The boundary of the phase jump turns from a straight line into a curved one. The spiral surface of the wavefront in this case becomes convex (Fig. 1.11b), which corresponds to the stage of reducing the thickness of the ring intensity distribution. The twisting of the phase jump line at the periphery of the beam cross-section is associated with diffraction (Fig. 1.12).

Further propagation of the optical vortex twists counterclockwise the phase jump line in the beam cross section even more (Fig. 1.13c). Similar changes in the phase jump under self-focusing of the optical vortex were observed in [21]. Note that the direction of twisting is determined by the sign of the topological charge, i.e. in the case $m = -1$, the corresponding twist would be clockwise. In the spatial spectrum a small plateau forms on the outer side of the ring.

At a distance $z \sim 0.20z_d$ (Fig. 1.13d), the width of the ring in the intensity distribution achieves its minimum value, while the peak intensity reaches a local maximum (first nonlinear focus). At this distance, a decrease in the radius of the ring becomes noticeable, and the self-focusing mode of the optical vortex changes. A decrease in the width of the annular distribution while maintaining an almost constant average radius is replaced by a decrease in the radius when power is contracted to the axial

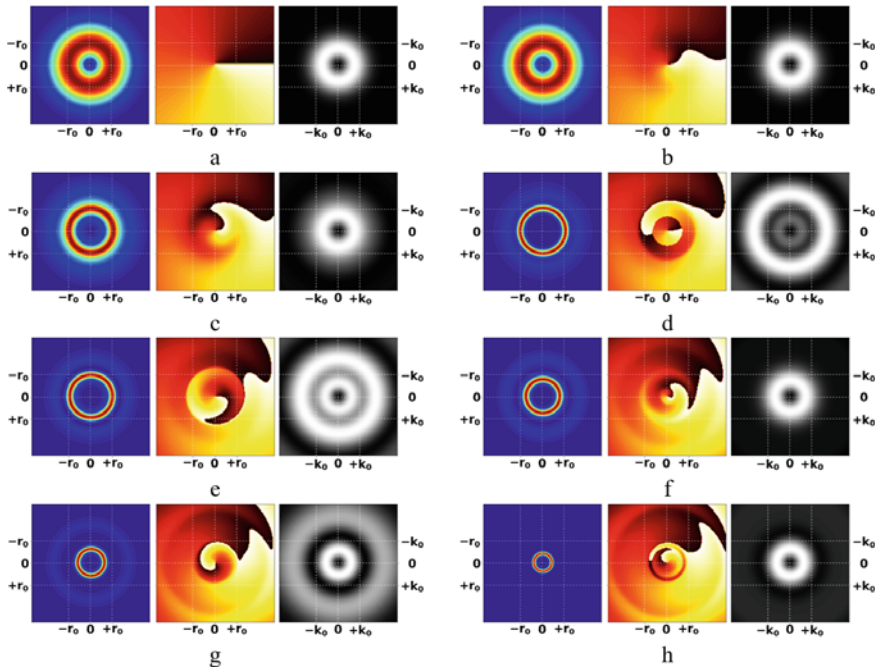

Fig. 1.13 The spatial distribution of the intensity $I(x, y)$ (left) and the phase $\theta(x, y)$ (center), and the spatial spectrum $S(k_x, k_y)$ (right) upon self-focusing of an optical vortex with a topological charge $m = 1$ at distances $z/z_d = 0.0$ (**a**), 0.07 (**b**), 0.14 (**c**), 0.20 (**d**), 0.25 (**e**), 0.31 (**f**), 0.36 (**g**), 0.43 (**h**) in nonlinear medium

region. In this case, aberrations appear on the beam profile—a new less intense ring appears, which, as the vortex propagates, shifts to the periphery of the beam, and the peak intensity of the main ring decreases.

Simultaneously, in the transverse distribution of the phase of the beam, three circular regions with distinct boundaries are formed, nested within each other along the aperture. In the inner circle, the phase behavior is similar to that of an optical vortex at the beginning of the medium (Fig. 1.13a). In the outer rings, the line of the phase jump is not straight but curved due to self-action, and resembles a spiral.

Hypothetically, these three regions can be related to the phase distributions of three different vortices of a limited aperture, nested in such a way that the vortex of a larger aperture is a continuation of the vortex of a smaller aperture. The phase of each of these spiral vortices is shifted by π relative to the closest vortex.

In the spatial spectrum of the optical vortex, the spectral intensity of the aberration rings increases. Moreover, the brightest ring with the highest spectral intensity is no longer the ring with the smallest radius. In the process of vortex propagation, the resulting spectrum is a superposition of partial spectra from each of the rings in the field distribution. An interference field from each of the rings is subject to a phase shift due to the formation of the embedded vortex structure in the phase. The vortex phase

leads to the absence of a central maximum in the spatial spectrum and the formation of a radiation cone around the optical axis. In Fig. 1.13d, the central low-intensity ring in the spectrum is generated by an external relatively wide, but low-intensity ring in the field distribution. The next high-intensity spectral ring is mainly the result of the high-intensity self-focusing mode formation, and the subsequent low-intensity rings in the spectrum are the result of the partial spectra addition from both rings in the field distribution.

We can explain the features of the formation of rings in the spectrum and their mutual intensity using a synthetic example. Let us consider a simple case of two out-of-phase embedded vortices with a topological charge $m = 1$ (Fig. 1.14). We set the field in the form of two ring beams of different radius ξ_{in} and ξ_{out} and a phase that experiences a jump at some distance from the axis of the beams:

$$A(r) = \begin{cases} A_{in} \exp\left\{-\frac{(r-\xi_{in})^2}{2w_{in}^2}\right\} \exp\left\{i \ \text{atan2}(x, y)\right\} & , \quad r \le \xi_{bound} \\ A_{out} \exp\left\{-\frac{(r-\xi_{out})^2}{2w_{out}^2}\right\} \exp\left\{i \ \text{atan2}(x, y) + \pi/m\right\} & , \quad r > \xi_{bound}, \end{cases} \tag{1.13}$$

where the values A_{in} (A_{out}), w_{in} (w_{out}) describe the amplitude and width of the inner and outer rings, respectively. This field distribution can be named as two nested vortices. Let the circle boundary of the phase shift be at a distance from the axis equal to $\xi_{bound} = 0.5(\xi_{in} + \xi_{out})$. The radii and widths of the rings are chosen so that they are far enough from each other and do not overlap: $\xi_{in} = 100$ μm, $w_{in} = 10$ μm, $\xi_{out} = 300$ μm, $w_{out} = 50$ μm. The initial field distribution (1.13) assumes that the radiation from the inner ring has one vortex phase, and the outer ring has the other, shifted by π.

The spatial spectrum of the field (1.13) also has two pronounced rings. The inner spectral ring corresponds to smaller angles of divergence of radiation, i.e. to the larger ring in the intensity distribution, and vice versa. The spectral intensity of the outer ring in the spectrum depends on the field amplitude in the inner ring. The ratio of amplitudes at fixed radii and widths of the rings determines their spectral intensities. With $A_{in} = 5A_{out}$, the intensity of the rings in the spectrum coincides (Fig. 1.14b). Deviation from the indicated ratio up (Fig. 1.14a) or down (Fig. 1.14c) results in the outer or inner ring having a higher spectral intensity. In Fig. 1.13d, the transverse field distribution formed during the self-focusing of the vortex is similar to distribution (1.13). However, in this phase there are three ring regions with clear boundaries. Each of these regions generates its spectral ring, the most intense of which corresponds to the middle spiral vortex, since the field with the largest amplitude is contained within its aperture.

It should be noted that the width of the central minimum in spatial spectrum increases with increasing topological charge. The nature of the pattern of maxima and minima depends on the parameters of the vortex. The angular distance between the maxima of the neighboring rings in the spectrum increases with the radius of the vortex ring. The wider the spectrum, the smaller the width of the ring in the beam. Since the optical vortex propagation is associated with the appearance of two modes:

one that is self-focusing and the other that spreads to the periphery, the resulting spectrum is the superposition of the ring systems that each mode generates.

Ongoing self-focusing of the optical vortex leads to a change in the twisting structure of the phase distribution. The internal and middle spiral vortices become in-phase and merge into one at a distance $z \sim 0.25 z_d$ (Fig. 1.13e). Moreover, the corresponding rings in the spatial spectrum become similar in amplitude and practically merge. The radius of the self-focusing mode continues to decrease, and the intensity becomes larger. The distance to the outer low-intensity ring increases. The internal spiral vortex becomes in phase with the external spectral vortex, i.e. the

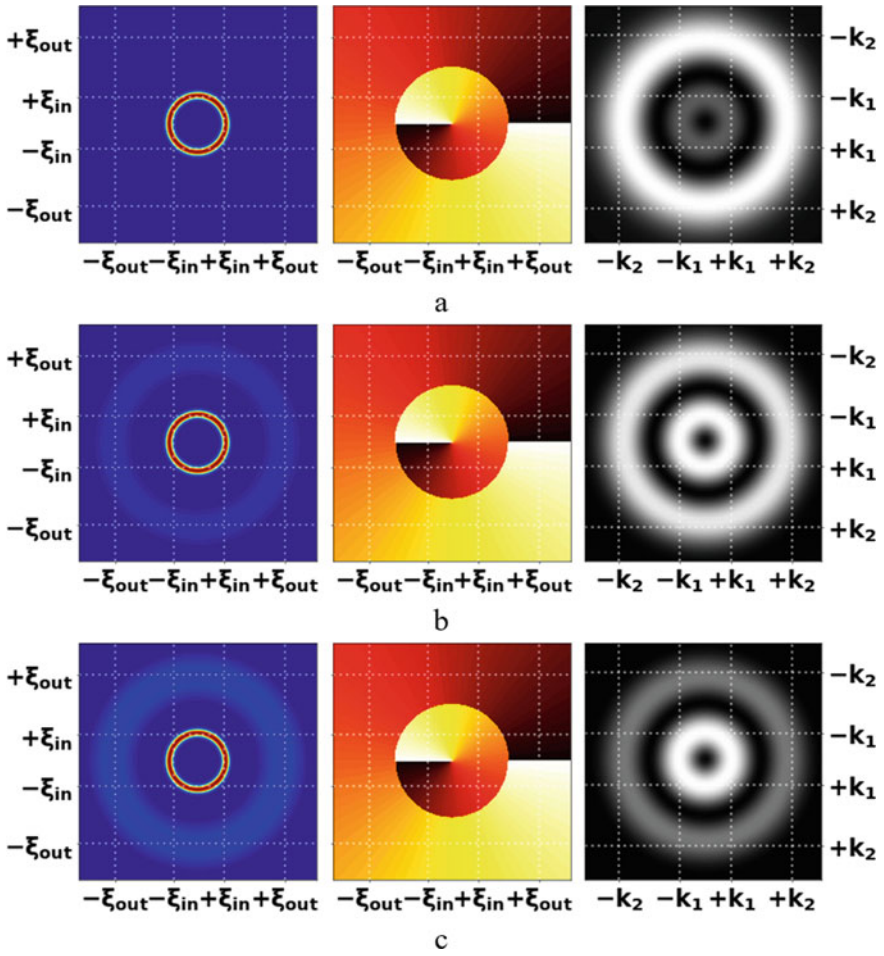

Fig. 1.14 The spatial distribution of the intensity $I(x, y)$ (left), phase $\varphi(x, y)$ (in the center) and the spectrum $S(k_x, k_y)$ (right) of the optical vortex defined by formula (1.13) with the ratio of the coefficients field amplitudes of the inner and outer rings $A_{in}/A_{out} = 10$ (**a**), 5 (**b**) and 2.5 (**c**)

spatial phase distribution becomes similar to the initial spectral vortex, only with a strongly curved line of the phase jump (Fig. 1.13f). The spatial spectrum of radiation is also similar to those of the initial vortex, i.e. it has a pronounced single ring. At a distance $z \sim 0.36 z_d$ (Fig. 1.13g), the distribution of the intensity and that of the phase become very similar to the synthetic example considered above (Fig. 1.14b), i.e. two distinctly spaced rings with different intensities and two embedded spiral vortices give rise to two spatial spectral rings with approximately the same brightness. Further propagation of the optical vortex (Fig. 1.13h) is accompanied by a decrease in the radius of the central ring and the periodic appearance of nested spiral vortices in the phase distribution.

1.6 Conclusion

We studied the process of the vortex formation after the spiral phase plate. We found that the near zero values of the intensity on the axes arise shortly after the plate but the ring profile is formed much further at the distance of approximately half of the diffraction length. A better idea would be to produce the vortex in the waist of the focused beam. The spectral width of the femtosecond pulse is not an obstacle for the vortex formation. We showed that we could separate the effects of noise in the initial conditions and the grid noise for typical sizes of the computational grid. The break-up of the vortex into several hot spots in the Kerr medium due to modulation instability is more rapid for the large-scale (in the conditions of the simulation) noise. The revealed features of transformation of the phase profile of the optical vortex and its spatial spectrum in a Kerr medium can be used in the analysis of spectral broadening in the filamentation mode.

Self-focusing of the optical vortex was analyzed in detail. It is shown that in the process of nonlinear propagation of a vortex beam, embedded spiral vortices appear in the phase distribution. The constructive interference of the self-focusing mode and the ring extending to the periphery leads to the formation of rings in the beam spatial spectrum.

Acknowledgements This research was supported by the Russian Foundation for Basic Research, grant 18-02-00624, and was carried out using the equipment of the shared research facilities of HPC computing resources at Lomonosov Moscow State University.

References

1. V.P. Kandidov, S.A. Shlenov, O.G. Kosareva, Filamentation of high-power femtosecond laser radiation. Quantum Electron. **39**(3), 205–228 (2009)
2. G.A. Askaryan, The effect of the field gradient of an intense electromagnetic beam on electrons and atoms. JETP **42**, 1567 (1962)

3. R.Y. Chiao, E. Garmire, C.H. Townes, Self-trapping of optical beams. Phys. Rev. Lett. **13**, 479 (1964)
4. L. Berge, S. Skupin, Few-cycle light bullets created by femtosecond filaments. Phys. Rev. Lett. **100** (2008)
5. J. Kasparian, J.-P. Wolf, Physics and applications of atmospheric nonlinear optics and filamentation. Opt. Express **16**(1), 466 (2008)
6. P. Polynkin, M. Kolesik, J. Moloney, Opt. Express **17**(2), 575–584 (2009)
7. V.V. Kotlyar, A.A. Kovalev, *Accelerated and Vortex Laser Beams* (FIZMATLIT, Moscow, 2018), p. 256
8. L. Allen et al., Orbital angular momentum of light and transformation of Laguerre Gaussian laser modes. Phys. Rev. A **45**(11), 8185–8189 (1992)
9. Z.S. Sacks, D. Rozas, G.A. Swartzlander, Holographic formation of optical-vortex filaments. J. Opt. Soc. Am. B **15**(8), 2226–2234 (1998)
10. L.E. Grin, P.V. Korolenko, N.N. Fedotov, On the generation of laser beams with a helical wavefront structure. Opt. Spectrosc. **73**(5), 1007–1010 (1992)
11. V.G. Shvedov, C. Hnatovsky, W. Krolikowski, A.V. Rode, Efficient beam converter for the generation of high-power femtosecond vortices. Opt. Lett. **35**(15), 2660–2662 (2010)
12. V.V. Kotlyar, A.A. Kovalev, R.V. Skidanov, S.N. Khonina, O.Yu. Moiseev, V.A. Soifer, Simple optical vortices formed by a spiral phase plate. J. Opt. Technol. **74**, 686–693 (2007)
13. S.G. Reddy, C. Permangatt, S. Prabhakar, A. Anwar, J. Banerji, R.P. Singh, Divergence of optical vortex beams. Appl. Opt. **54**, 6690–6693 (2015)
14. V.I. Kruglov, Yu.A. Logvin, V.M. Volkov, The theory of spiral laser beams in nonlinear media. J. Mod. Opt. 2277–2291 (1992)
15. L.T. Vuong, T.D. Grow, A. Ishaaya, A.L. Gaeta, G.W. Hooft, E.R. Eliel, G. Fibich, Phys. Rev. Lett. **96** (2006)
16. P. Polynkin, C. Ament, J.V. Moloney, Phys. Rev. Lett. **111** (2013)
17. E.V. Vasiliev, V.P. Kandidov, V.O. Kompanets, S.V. Chekalin, S.A. Shlenov, Formation of annular light bullets in a femtosecond vortex beam. Bull. Russ. Acad. Sci. Phys. **83**(12), 1443–1449 (2019)
18. A. Vincotte, L. Berge, Femtosecond optical vortices in air. Phys. Rev. Lett. **95** (2005)
19. I. Towersa, A.V. Buryaka, R.A. Sammuta, B.A. Malomedb, L.-C. Crasovanc, D. Mihalachec, Phys. Lett. A **288**, 292–298 (2001)
20. D. Mihalache, D. Mazilu, L.-C. Crasovan, I. Towers, A.V. Buryak, B.A. Malomed, L. Torner, J.P. Torres, F. Lederer, Stable spinning optical solitons in three dimensions. Phys. Rev. Lett. **88** (2002)
21. C.-C. Jeng, M.F. Shih, K. Motzek et al., Phys. Rev. Lett. (2004)
22. G. Maleshkov et al., Proc. SPIE (2009)
23. R.A. Vlasov, V.M. Volkov, D.Yu. Dedkov, Spectrum superbroadening in self-focusing of pulsed vortex beams in air. Quantum Electron. **43**(2), 157–161 (2013)
24. O. Khasanov, T. Smirnova, O. Fedotova, G. Rusetsky, O. Romanov, High-intensive femtosecond singular pulses in Kerr dielectrics. Appl. Opt. **51**, 198–207 (2012)
25. D.N. Neshev et al., Supercontinuum generation with optical vortices. Opt. Express **18**(17), 18368–18373 (2010)
26. E.V. Vasilyev, S.A. Shlenov, V.P. Kandidov, Annular light bullets of a femtosecond optical vortex in a medium with anomalous group velocity dispersion. Laser Phys. Lett. **15**, 115402–115407 (2018)
27. E.V. Vasilyev, S.A. Shlenov, V.P. Kandidov, The Multifocus structure of radiation upon femtosecond filamentation of an optical vortex in a medium with an anomalous group velocity dispersion. Opt. Spectrosc. **126**(1), 24–31 (2019)

Chapter 2
Diagnostic of Peak Laser Intensity by Electron and Positron Production from Laser Plasma

A. Andreev, Chen Lan, and Zs. Lecz

Abstract It is known that in the small quantum parameter regime the Breit-Wheeler electron-positron pair creation cross section is extremely sensitive on the photon energy and on the background field. We present the dependence of positron yield on laser intensity in shaped laser under/over dense (gas/foil) plasma interactions with the help of analytical modeling and PIC simulations. This allows for establishing in situ laser intensity diagnostic by measuring the positron yield in experiments where multi PW lasers are used.

2.1 Introduction

Despite of the great success in the development of multi PW laser systems, [1] the development of diagnostics used to determine its ultra-high peak has been left to be explored. A relatively simple method is needed to find the peak intensity of a laser pulse during the experiment at full energy level near the laser focal spot. Usually, the peak intensity in the focal volume is determined from the characteristics such as pulse duration and focal spot size separately measured at significantly lowered pulse energy. Therefore, the estimated peak intensity can be largely different from the correct value. The low accuracy of this method makes it difficult to compare experimental results achieved at different laser facilities [2]. For example, recompression errors, that are specific for the CPA technique can lead to significant errors in determination of the pulse duration in the focal region. Thus, the development of alternative methods for the estimation of focused intensity directly in the experimental chamber is of great importance for investigations in super strong laser field science. A variety of different indirect techniques to diagnose the peak intensity was already proposed in [3–10]. One of the techniques involves laser irradiation of a low-density noble gas

A. Andreev (✉)
SPbSU, Saint Petersburg, Russia

MBI, Berlin, Germany

A. Andreev · C. Lan · Zs. Lecz
ELI-ALPS, Szeged, Hungary

K. Yamanouchi et al. (eds.), *Progress in Photon Science*, Springer Series in Chemical Physics 125, https://doi.org/10.1007/978-3-030-77646-6_2

target and the registration of multiple-stage ionization of the gas [3, 4], and another concerns analysis of the accelerated electrons and back Thomson/Compton scattering [5, 6]. Most of these methods work in relatively narrow ranges of laser intensity and require external beams of nearly mono-energetic electrons or ions of prepared in a well-defined ionization state. This, strongly narrows the possibilities of using such diagnostic techniques because of the required specifications of corresponding additional particle source. Therefore, it has been awaited to find other methods of to determine the laser peak intensity in a focal volume. In this paper, we analyze some more simple and inexpensive variants of such diagnostics based on electron and positron production from laser plasma.

2.2 Diagnostics of Peak Laser Intensity Based on the Measurement of Parameters of Electrons Emitted from Laser Focal Region

The method developed in [7–10] is based on the measurement of energy spectrum of electrons, directly accelerated by a laser pulse from rarefied gas or an ultra-thin foil in the beam waist. This allows one to omit impact from additional spurious plasma effects and directly connects laser pulse parameters with electron angular-spectral distributions. Direct electron acceleration by a focused laser pulse was studied theoretically in numerous publications (see for example [11]]) and experimentally observed just in a few studies [12, 13]. In the publication [7], we study an approach, proposed recently [9]. This method is based on the measurement of energies of electrons, accelerated in the focal volume that carry residual energy comparable with the oscillation energy in the intense laser field. The electrons are created via the ionization process of a low-density gas target (their concentration is low enough to make the effects stemming from both the Coulomb interactions between the charged particles and the collisions between them negligible, as well as acceleration by plasma wake fields). Dynamics and energy distribution of electrons expelled from the interaction area are determined by the laser pulse parameters. Consequently, measurement of the particle energy distribution can serve as an instrument of diagnosing the laser pulse parameters in the focal spot, in particular the maximum intensity. It was shown that for a certain period of time the electron remains trapped by the laser pulse and moves with it along the pulse propagation axis. This approach (see Fig. 2.1) does not require any additional target or a particle beam and can be used on an everyday basis for a fast control of the laser system.

In the research [7], we realized this method by diagnosing the peak intensity based on the detection of the angular distribution of electrons accelerated in near-vacuum directly by the field of tightly focused relativistic laser pulse. Using the analytical test particle method and 2D PIC simulations, the spatial and energy distributions of scattered electrons from the focal volume have been studied with different sets of laser pulse parameters. The results of numerical calculations and analytical expressions

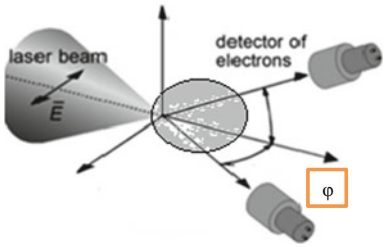

Fig. 2.1 Simulation and experimental setup [7]

are presented in Fig. 2.2, where we considered propagation of a Gaussian-shaped laser pulse with intensity $I \geq 10^{19}$ W/cm^2 in the Ar plasma of ion density $n_i = 10^{14}$ cm^{-3} along the Y-axis. The dependence of the average charge of Ar atoms on the laser intensity was taken from the ADK model. The pulse duration (t_L) is $t_L = 40$ fs and the beam diameter (d_L) is $d_L = 10$ μm. The size of the simulation box was 100 × 100 μm^2 and the grid size was 40 nm. The time step was 0.1 fs and 20 particles per cell were taken.

The particles were emitted with high residual momentum mostly in a relatively narrow range of the angles from the beam axis. With the growth of the peak intensity, this direction of electron emission moves toward this axis. At the same time in the considered range of peak intensities (below 5×10^{19} Wcm^{-2}, not shown in Fig. 2.2), the electron spatio-energetic characteristics are found to be weakly dependent on the laser transverse energy distribution. This allows for monitoring the peak intensity of the laser radiation by measuring the angular spectra of high energy electrons. The experimental measurements [7] of the angular distribution of electrons being exposed to the focused high power femtosecond laser radiation with a low density helium gas were found to be in good agreement with the calculation results. We have

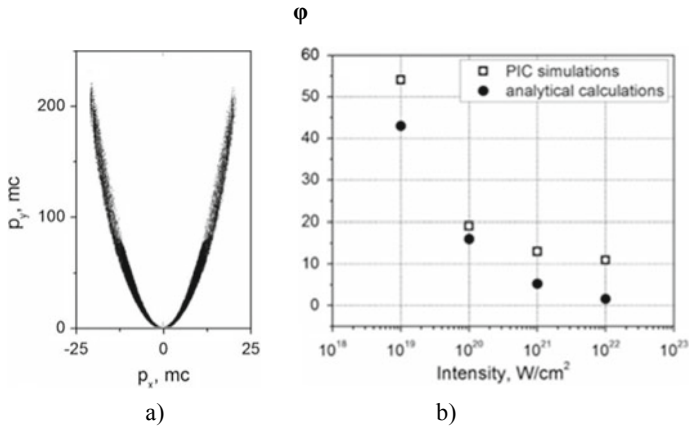

Fig. 2.2 **a** The momenta distribution of electrons propagating out of the focal volume at laser intensity 10^{20} W/cm^2; **b** The position of the maximum of angular electron density distribution (open squares—simulation results) and angle φ of single electron propagation in a plane wave (closed circles—analytical results) [7]

demonstrated that, with the use of our technique, the peak intensity may be estimated and controlled in each laser shot.

2.3 Diagnostic of Peak Laser Intensity by Pair Production in Low Density Plasma

The method considered above is based on the measurement of energy spectrum of electrons, directly accelerated by a laser pulse from rarefied gas or an ultra-thin foil in the beam waist. This allows one to directly connect laser pulse parameters to electron angular spectral distributions. At ultrahigh intensity ($> 10^{22}$ W/cm^2), this technique cannot have a high accuracy mainly because of the radiation reaction, or photon recoil effect. Moreover, secondary electrons are also produced via pair creation, which can change the angular distribution of detected electrons. In this paragraph, we consider another straightforward diagnostic of the laser intensity based on the detection of the number and angular distribution of positrons generated from low density plasma, which is created from residual gas in experimental target chamber. A moderate intensity laser pre-pulse can produce such plasma. In such medium, the electrons (shown by red) are directly accelerated in a laser caustic by the field of a focused ultra-intense laser pulse, which is reflected at some point of a focusing parabolic mirror M.

The dominant process responsible for pair creation in our conditions is the multi-photon Breit-Wheeler process, which has a very sharp intensity threshold slightly above $I = 10^{22}$ W/cm^2. Below this threshold no pairs are created, but, above the threshold, the number of pairs increases extremely fast with laser intensity. The highly sensitive dependence of the positron detection efficiency on the laser intensity makes the precise diagnostic possible. In [14], we proposed a process to diagnose the laser intensity by measuring the positron yield. The process consists of two steps. First, the electrons (red dot in Fig. 2.3) with relatively low energy are accelerated by the axial electric field generated from the reflected part (violet lines) of the incident shaped laser pulse (blue lines) by dented mirror M, which is approximated by two crossing pulses [8] with a small angle of propagation (see Fig. 2.3). In the second step, the accelerated electrons then collide with the rest of the laser pulse in order

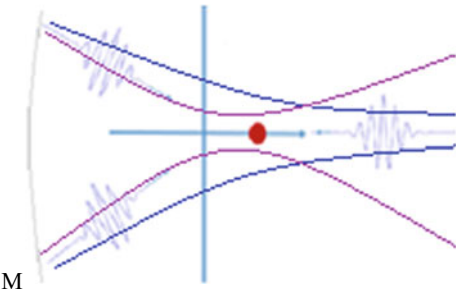

Fig. 2.3 Schematic diagram of setup

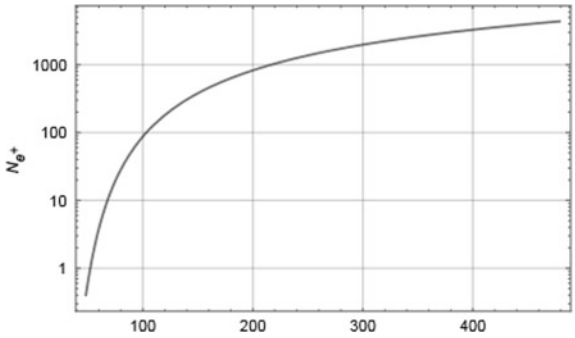

Fig. 2.4 The dependence of positron-number with $a \in [48,480]$ in the LCFA, where laser pulse duration is 10 fs, $\Delta\phi = 23.56$ and $N_{e-} = 100$

to produce electron-positron pairs. The laser intensities at each step satisfy a certain relation, which is appropriate and can be prepared by shaping a laser with optical apparatus. The electrons are supposed to be located on the horizontal axis with small initial energy. Thus, the acceleration can be realized by a tightly focused laser beam.

To demonstrate this process, it is enough to consider only sinusoidal fields [15]. The electron energy can be written as: $\varepsilon_{max} = mc^2(1 + 8a^2)$, where a is the dimensionless magnitude of the vector potential. In our case, $a = eE/m\omega c \gg 1$, which is also known as local constant field approximation (LCFA), see e.g. [16]. Here E and ω are strength and frequency of laser field, $a = 6\sqrt{I_0}[10^{20}\ \mathrm{W/cm^2}]\lambda_0[\mu\mathrm{m}]$. In LCFA all fields can be regarded as a constant crossed field, thus if all parameters are the same, the shapes of the field would not affect the differential rate too much. The corresponding probability P_2 for constant crossed field can be represented via the approximate formula of the differential rate $J_{\gamma e}$ (see for example [16, 17]): $P_2 \approx 0.5 \times (a\Delta\phi)^2 \times (3\alpha^2/16\chi_e) \times ln(1 + \chi_e/12) \times \exp(-16/3\chi_e) \times (1 + 0.56\chi_e + 0.13{\chi_e}^2)^{1/6}$, where fine-structure constant in the used units $\alpha = e^2$, $\chi_e = a \times 10^{-4} \times [-6.1 + 2.45a + 6.17\sqrt{}(1 + 0.16a^2 - 0.79a)]$ and $\Delta\phi$ are the formation phase length, see [17]. The differential rate $J_{\gamma e}$ is valid in the range $\chi_e \in (1, \infty)$. Thus, the positron numbers in one pulse can be estimated by $N_{e+} = P_2 N_{e-}$, where N_{e-} is the initial number of electrons, see Fig. 2.4.

Here the probability of pair production is carried out in LCFA, i.e. the background field is regarded as constant crossed field. However, as several authors reported, see e.g. [18–20], the production rate may be enhanced due to the finite extent of a laser field. Therefore, the finite size effect of the diagnostics of intensity should be taken into account in order to increase the accuracy of this method. These represent the program for future research.

2.4 Diagnostic of Peak Laser Intensity by Pair Production from Thin Foil Target

In the paper [21], we propose another simpler diagnostic of the laser intensity based on the detection of the number and angular distribution of positrons generated from

thin foil, which is a usual target in recent experiments. A moderate intensity laser pulse, or a prepulse, can produce the desired density distribution at the surface of a flat foil target. In such medium, the electrons are directly accelerated by the field of focused ultra-intense laser pulse, which at some point is reflected in the overdense region of the expanded plasma. In contrast with the previous schemes, in our method a single laser pulse is sufficient to generate pairs instead of two counter propagating pulses.

Figure 2.5 shows that in our numerical experiment, the high power laser pulse (shown by red) is focused on the surface of a thin foil target. The generated positrons are well separated from all other secondary radiations and are detectable at angle θ with respect to the laser axis. The dominant process responsible for the pair creation in our conditions is also the Breit-Wheeler process, which has a sharp intensity threshold. Below this threshold no pairs are created but, above the threshold, the number of pairs increases extremely fast with laser intensity. We used the 2D EPOCH simulation code to demonstrate the dependence of positron number on the laser intensity [22]. The P-polarized laser pulse has Gaussian temporal (longitudinal) and transversal profiles with 30 fs (FWHM) duration and 3 μm focal spot diameter. The incident angle was 30° and $n_0 = 350n_{cr}$ is used for the maximum plasma density. The preplasma has an exponential density profile with a scale length of $L_n = 0.5$ μm and the total preplasma length of $L_p = 2$ μm. The thickness of the uniform plasma (unperturbed target) was 1 μm. The simulation box was 16 μm long and 16 μm wide which is resolved by 4000 × 4000 grid cells. In each cell, 20 macro-particles of electrons and ions were initially loaded. The target material was gold and 30^+ charge state is used. The length of the preplasma is important not only for seeding the pair creation but also for determining the acceleration path of electrons. In this particular case, the electrons are accelerated via the direct laser acceleration mechanism [20], which provides electron energies high enough to emit gamma photons with several hundred MeV energy. The propagation of low energy (< 75 meV) photons are not included in the simulation, because they do not contribute to the pair creation, but their

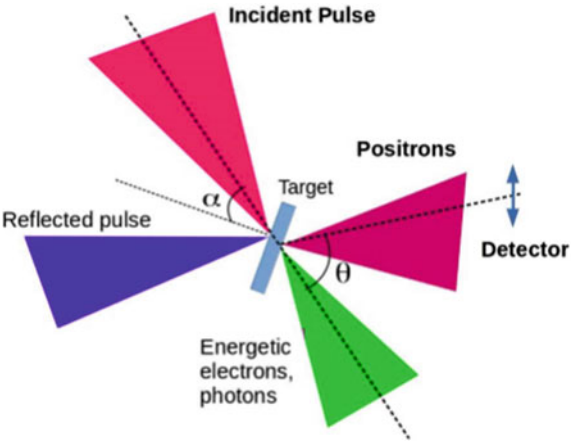

Fig. 2.5 Basic setup of our simulations and of possible experiments [21]

recoil on the emitting electrons is always calculated in the code for consistency. The photons are generated inside the preplasma when the fast electrons collide with the reflected pulse. During the pulse reflection, the positive amplitude of the laser field is responsible for the pair creation. The electron-positron pairs are generated during less than a quarter laser period, and the pairs will be separated by the positive electric field. The positrons acquire a significant transversal momentum and are deflected with a wide angular spread in a direction almost perpendicular to the original direction of the incident pulse. The large angular spread can be attributed to the large energy spread of photons which are emitted according to the quantum synchrotron function. The laser electric field deflects lower energy positrons because they are less relativistic and their initial momentum is smaller. After the pulse is fully reflected, we count the number of positrons in the simulation domain. The results are presented in Fig. 2.6, where for analytical calculations, different electron cut-off energies (γ_{max}) are considered.

In Fig. 2.6, the number of positrons calculated from our analytical model (see [21]) are shown by blue squares (joined by straight lines) integrated for all γ up to $\gamma_{max} = 5a$, by green up to $\gamma_{max} = 4a$ and by red up to $\gamma_{max} = 6a$. The large round marks show the simulation results. The positron number can be determined with high accuracy by a standard experimental technique. Because of this sensitive dependence of the positron detection efficiency, the very precise diagnostic becomes possible. At lower intensities, pairs can be generated via the Bethe-Heitler process, which involves the collision of bremsstrahlung photons with highly charged high-Z ions using much thicker targets ($\sim$ 100 μm or more) [23]. In this case, the positron number increases very slowly with laser intensity, therefore the precision cannot be high enough for diagnostics.

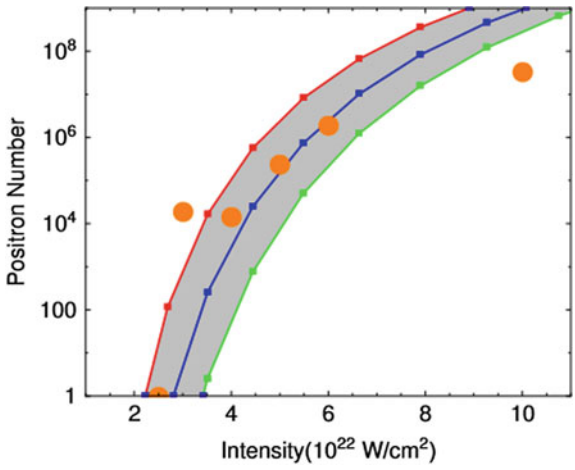

Fig. 2.6 The dependence of total number of positrons on laser intensity [21]

2.5 Conclusion

In this paper, we present some possible methods to determine laser peak intensity in the focal volume, based on electron acceleration or positron production from laser plasma interactions. In the case of high power lasers well below the PW level, the measurement of electron energy spectra is relevant, while near or above this level the positron count can be used to estimate the peak intensity. It was shown that, by using the production of positrons from different targets irradiated by high intensity laser pulses, one can determine the laser intensity in the range above 10^{22} W/cm^2 till 10^{25} W/cm^2, and the peak intensity can be determined with the accuracy up to ~ 1%.

References

1. G.A. Mourou, T. Tajima, Science **331**, 41 (2011)
2. G.A. Mourou, N.J. Fisch, V.M. Malkin, Z. Toroker, E.A. Khazanov, A.M. Sergeev, T. Tajima, B. Le Garrec, Opt. Commun. **285**, 720 (2012)
3. A. Link et al., Rev. Sci. Instrum. **77**, 10E723 (2006); M.F. Ciappina, S.V. Popruzhenko, S.V. Bulanov, T. Ditmire, G. Korn, S. Weber, Phys. Rev. A **99**, 043405 (2019)
4. C. Smeenk, J. Salvail, L. Arissian L.P. Corkum et al., Opt. Express **19**, 9336 (2011); M.F. Ciappina, S.V. Popruzhenko, Laser Phys. Lett. **17**, 025301 (2020)
5. J. Gao, J Appl. Phys. Lett. **88**, 091105 (2006); O. Har-Shemesh, A. Di Piazza, Opt. Lett. **37**, 1352 (2012)
6. W. Yan et al., Nat. Photon. **11**, 514 (2017)
7. M. Kalshnikov, A. Andreev, K. Ivanov et al., Laser Part. Beams **33**, 361 (2015)
8. O. Vais, S. Bochkarev, S. Ter-Avetisyan, V. Bychenkov, Quantum Electron. **47**, 38 (2017); K.I. Popov et al., Phys. Plasmas **16**, 053106 (2009)
9. A. Galkin, M. Kalashnikov, V. Korobkin et al., Phys. Plasmas **17**, 053105 (2010)
10. K.A. Ivanov, I.N. Tsymbalov, O.E. Vais, S.G. Bochkarev, R.V. Volkov, V.Y. Bychenkov, A.B. Savel'ev, Plasma Phys. Controlled Fusion **60**, 105011 (2018)
11. Y. Li, Y. Gu, Z. Zhu et al., Phys. Plasmas **18**, 53104 (2011)
12. C. Varin et al., Appl. Sci. **3**, 70 (2013)
13. M. Thévenet, K. Leblanc, S. Kahaly et al., Nat. Phys. **12**, 355 (2016)
14. A. Andreev et al., *International Conference on Ultrafast Optical Science*, LPI RAS, Moscow, Sept 2019; C. Lan et al., *ELI ALPS SciDay Meeting Szeged*, 12 Oct 2018
15. Y.I. Salamin, C.H. Keitel, Phys. Rev. Lett. **88**, 095005 (2002)
16. V.N. Baier, V.M. Katkov, V.M. Strakhovenko, Higher-order effects in external field: pair production by a particle. Technical Report (Novosibirsk State University, USSR 1971); A.I. Nikishov, V.I. Ritus, Quantum processes in the field of a plane electromagnetic wave and in a constant field. I. Sov. Phys. JETP **19**, 529–541 (1964)
17. B. King, H. Ruhl, Phys. Rev. D **88**, 013005 (2013)
18. T. Heinzl, A. Ilderton, M. Marklund, Phys. Lett. B **692**, 250–256 (2010)
19. A. Titov, H. Takabe, B. Kämpfer, A. Hosaka, Phys. Rev. Lett. **108**, 240406 (2012)
20. C. Lan, Y. Wang, H. Geng, A. Andreev, Eur. Phys. J. C **79**, 917 (2019)
21. Zs. Lecz, A. Andreev, Laser Phys. Lett. **17**, 056101 (2020)
22. Z. Lecz, A. Andreev, PP&CF **61**, 045005 (2019)
23. H. Chen, S.C. Wilks, J.D. Bonlie, E.P. Liang, J. Myatt, D.F. Price, D.D. Meyerhofer, P. Beiersdorfer, Phys. Rev. Lett. **102**, 105001 (2009)

Chapter 3
Theoretical Model for Simulation of Rotational Excitation in Air-Lasing

Youyuan Zhang, Erik Lötstedt, and Kaoru Yamanouchi

Abstract The role of the rotational coherence in the air lasing at 391 nm, corresponding to the coherent $B^2\Sigma_u^+(v' = 0) - X^2\Sigma_g^+(v'' = 0)$ emission of N_2^+ exposed suddenly to an ultrashort intense near-IR laser field, is investigated theoretically by referring to the recent experimental and theoretical studies on the air lasing that elucidated the mechanism of the population inversion between the $B^2\Sigma_u^+$ and $X^2\Sigma_g^+$ states in terms of the sudden turn-on of the interaction of N_2^+ with the laser field combined with the post-ionization coupling among the $X^2\Sigma_g^+$, $A^2\Pi_u$, and $B^2\Sigma_u^+$ states of N_2^+.

3.1 Introduction

When molecules are exposed to an ultrashort intense laser pulse, a variety of characteristic phenomena can be induced such as high-order harmonic generation [1], above-threshold ionization and dissociation [2], rotational excitation and molecular alignment [3]. Recent studies showed that another type of phenomenon called filamentation can be induced by an ultrashort intense laser pulse. When an intense laser pulse propagates in a gaseous medium, a thin plasma column called a filament is generated [4] and a white light continuum is created [5–8]. Therefore, by shooting intense laser pulses into the sky, we can create a white light source at a distant point in the sky, which can be an ideal light source for remote sensing and standoff spectroscopy [9].

Y. Zhang (✉) · E. Lötstedt · K. Yamanouchi
Department of Chemistry, School of Science, The University of Tokyo,
7-3-1 Hongo, Bunkyo-ku, Tokyo 113-0033, Japan
e-mail: youyuan.zhang@chem.s.u-tokyo.ac.jp

E. Lötstedt
e-mail: lotstedt@chem.s.u-tokyo.ac.jp

K. Yamanouchi
e-mail: kaoru@chem.s.u-tokyo.ac.jp

K. Yamanouchi et al. (eds.), *Progress in Photon Science*, Springer Series in Chemical Physics 125, https://doi.org/10.1007/978-3-030-77646-6_3

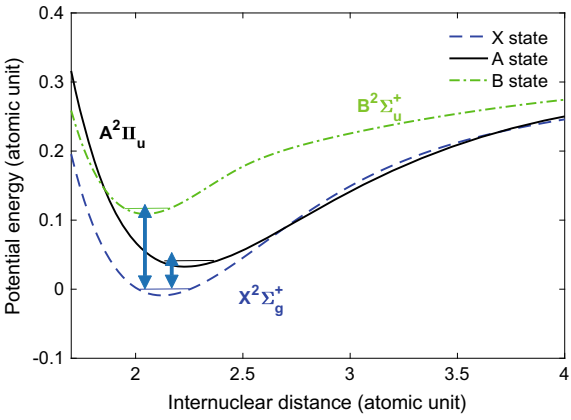

Fig. 3.1 Potential energy curves of electronic $X^2\Sigma_g^+$, $A^2\Pi_u$, and $B^2\Sigma_u^+$ states of N_2^+ . The transitions between electronic states are shown in deep-blue double arrows

It has been known that unidirectional coherent emission is generated from a laser-induced filament in air at specific wavelengths, showing that the populations are inverted in oxygen atoms [5, 10], nitrogen atoms [10], neutral nitrogen molecules (N_2) [11–14] and nitrogen molecular ions (N_2^+) [15–18]. Among them, the emission at 391 nm from N_2^+ [15, 19] assigned to the $B^2\Sigma_u^+(v' = 0) - X^2\Sigma_g^+(v'' = 0)$ transition created in a femtosecond near-IR (800 nm) attracted much attention in view of the mechanism of the population inversion between the $B^2\Sigma_u^+$ state and the $X^2\Sigma_g^+$ state. Through a series of our recent experimental and theoretical studies [19–23], it was revealed that the sudden creation of N_2^+ in an intense laser field plays a primary role in creating the population efficiently in the vibrational ground state of the second electronically excited $B^2\Sigma_u^+$ state, leading to the population inversion, and the successive population pumping from the vibrational ground state of the electronic ground $X^2\Sigma_g^+$ state to the first electronically excited $A^2\Pi_u$ state, through which the population in $X^2\Sigma_g^+(v'' = 0)$ is decreased, enhances further the population inversion (see Fig. 3.1).

In the course of the creation of the inverted population between the $B^2\Sigma_u^+$ state and the $X^2\Sigma_g^+$ state, the rotational motion of N_2^+ is also excited, and the rotational coherence has been studied by pump-probe measurements [16] and time-resolved spectroscopy [24]. It was also shown that the rotational excitation also contributes to the creation of the population inversion between the $B^2\Sigma_u^+$ state and the $X^2\Sigma_g^+$ state [25–28]. The rotational excitation in N_2^+ in the population inversion process was also investigated in recent experimental studies by pump-probe measurements [22, 29, 30].

The theoretical treatment of the rotational excitation of molecules in an intense laser field, leading to molecular alignment and orientation, has been well established [31–34]. However, to the best of our knowledge, no report had been made on a complete theoretical model by which we can simulate time-dependent population transfer processes among the rovibronic levels of N_2^+ by including the rotational degrees of freedom explicitly before our recent studies [23, 35]. In this chapter, we

will show how the rotational degrees of freedom of N_2^+ play a role in the creation of the population inversion between $B^2\Sigma_u^+(v = 0) - X^2\Sigma_g^+(v'' = 0)$ based on our recent theoretical model.

3.2 Theoretical Model

3.2.1 Rotational Excitation

The dynamics of N_2^+ can be obtained by solving the time-dependent Schrödinger equation,

$$i\hbar\frac{\partial}{\partial t}\Psi(r,t) = H(t)\Psi(r,t), \tag{3.1}$$

where $\hbar$ is Planck's constant divided by 2π, and H is the Hamiltonian operator.

To simulate the rotational motion induced by intense near IR laser field, we treat N_2^+ as a rigid rotor. The equations shown in this section closely follow the derivations in [36, 37]. When a diatomic molecule is placed in a three-dimensional space without an external field, the static Schrödinger equation becomes

$$-\frac{\hbar^2}{2\mu}\nabla^2\Psi(\mathbf{r}) = E\Psi(\mathbf{r}), \tag{3.2}$$

where $\nabla^2 = \frac{\partial^2}{\partial x^2} + \frac{\partial^2}{\partial y^2} + \frac{\partial^2}{\partial z^2}$. In the polar coordinate system composed of the radial coordinate r, the polar angle θ, and the azimuthal angle φ, the x, y and z coordinates in the space-fixed Cartesian coordinate system can be written as

$$\begin{cases} x = r\sin\theta\cos\varphi \\ y = r\sin\theta\sin\varphi \\ z = r\cos\theta \end{cases} \tag{3.3}$$

When a diatomic molecule is treated as a rigid rotor in which the internuclear distance r is fixed, the Laplacian can be represented as

$$\nabla^2 = \frac{\Lambda}{r^2} = \left(\frac{1}{\sin\theta}\frac{\partial}{\partial\theta}\left(\sin\theta\frac{\partial}{\partial\theta}\right) + \frac{1}{\sin^2\theta}\frac{\partial^2}{\partial\varphi^2}\right)\frac{1}{r^2}. \tag{3.4}$$

As the rotational basis functions, the spherical harmonics, $Y_m^J(\theta,\varphi)$, are most commonly used, where $J(= 0, 1, 2, ...)$ is the angular momentum quantum number and $m = -J, -(J-1), ..., J$ is the projection of the angular momentum onto the z-axis of the space-fixed coordinate system.

In the case of N_2 in the gas phase at temperature T, the population in the rotational level having the rotational angular momentum quantum number J can be represented as

$$P_J \sim g_J(2J+1)e^{-\frac{-E_J}{k_B T}}, \tag{3.5}$$

where E_J, represented as $E_J = BJ(J+1)$ using the rotational constant B, is the rotational eigenenergy, k_B is the Boltzmann constant, T is the temperature, and g_J is the nuclear spin statistical weight given by

$$g_J = \begin{cases} 2, & \text{for even } J \\ 1, & \text{for odd } J \end{cases} \tag{3.6}$$

The time-dependent Schrödinger equation for rotating N_2 interacting with a laser field can be expressed as

$$i\hbar\frac{\partial}{\partial t}\Psi(\theta,\varphi,t) = H(t)\Psi(\theta,\varphi,t), \tag{3.7}$$

where $H(t)$ includes the field-induced angle-dependent potential energy $U(\theta,t) = -\delta\overrightarrow{\mu}\cdot\overrightarrow{\mathcal{E}}$, the change of which is

$$dU = -\delta\overrightarrow{\mu}\cdot d\overrightarrow{\mathcal{E}} = -\delta\mu_{//}d\mathcal{E}_{//} - \delta\mu_{\perp}d\mathcal{E}_{\perp} = -\alpha_{//}\mathcal{E}_{//}d\mathcal{E}_{//} - \alpha_{\perp}\mathcal{E}_{\perp}d\mathcal{E}_{\perp}, \tag{3.8}$$

where // and $\perp$ represent respectively the parallel and perpendicular directions with respect to the z-axis of the molecular axis, $\delta\overrightarrow{\mu}$ is the induced dipole moment, α is the polarizability, and $\overrightarrow{\mathcal{E}}$ is the laser electric field. The angle-dependent $U(\theta,t)$ can be obtained as

$$U(\theta,t) = -\frac{1}{2}\alpha_{\perp}\mathcal{E}^2 - \frac{1}{2}\Delta\alpha\mathcal{E}^2\cos^2\theta, \tag{3.9}$$

where $\Delta\alpha = \alpha_{//} - \alpha_{\perp}$. The first term in (3.9), which takes a constant value regardless of the orientation angle θ, can be dropped because it does not influence the rotational motion driven by the external laser light field. Therefore the time-dependent Schrödinger equation becomes

$$i\frac{\partial}{\partial t}\Psi(\theta,\varphi,t) = [B\mathbf{J}^2 - U(t)\cos^2\theta]\Psi(\theta,\varphi,t), \tag{3.10}$$

where $-U(t)\cos^2\theta = -\frac{1}{2}\Delta\alpha\mathcal{E}^2\cos^2\theta$ is the second term of (3.9) representing the angular-dependent potential energy.

When the oscillation of the laser electric field represented as $\mathcal{E}(t) = \mathcal{E}_0 f(t)\sin(\omega t)$ is sufficiently fast compared with the molecular rotation, the time-dependent potential energy can be averaged over one optical cycle as

$$U(\theta,t) = -\frac{\omega}{2\pi}\int_0^{\frac{2\pi}{\omega}} \frac{1}{2}\Delta\alpha\mathcal{E}_0^2 f^2(t)\sin^2(\omega t')\cos^2(\theta)\mathrm{d}t' \\ = -\frac{1}{4}\Delta\alpha\mathcal{E}_0^2 f^2(t)\cos^2\theta = \frac{1}{2}U_0(t)\cos^2(\theta). \tag{3.11}$$

Thus, in the numerical time propagation, only the time-dependence of the envelope function needs to be considered, which reduces the necessary time steps, and consequently, reduces the calculation time.

3.2.2 *Electronic, Vibrational and Rotational Excitation*

The theoretical model shown below is that presented in [23]. When N_2^+ is generated in the laser pulse, the rovibrational levels in the three electronic states, $X^2\Sigma_g^+$, $A^2\Pi_u$, and $B^2\Sigma_u^+$, are involved in the post-ionization interaction induced by the laser field. The time-dependent dynamics is described by 3.1, and the general solution can be expressed as

$$\Psi(\mathbf{r},t) = \sum_{\alpha=X,A_+,A_-,B}\sum_{v=0}^{V_{\max}}\sum_{K=0}^{K_{\max}}\sum_{m=-K}^{K} c_{\alpha vKm}(t)\psi_{\alpha vKm}(\mathbf{r}), \tag{3.12}$$

where $\mathbf{r}$ is the internuclear separation vector with $\mathbf{r} = |\mathbf{r}|$ being the N-N internuclear distance, K is the total angular momentum excluding the spin angular momentum, m is the projection of the total angular momentum onto the z-axis, $P_{\alpha vKm} = |c_{\alpha vKm}(t)|^2$ represents the probability of finding the system in the rotational state, labeled with K and m, in the vth vibrational state in the electronic state α, and α denotes one of the four lowest-energy electronic states; the electronic ground $X^2\Sigma_g^+$ state, the doubly degenerate $A^2\Pi_u$ state, which is composed of the A_+ and A_- states, and the $B^2\Sigma_u^+$ state.

In the simulation, the maximum vibrational quantum number and maximum rotational quantum number included on each electronic state are set to be $V_{\max}$ and $K_{\max}$, respectively, for all the four electronic states. The complete molecular basis wave functions, $\psi_{\alpha vKm}(\mathbf{r})$, of N_2^+, are prepared first under the field free conditions using the finite difference method with the potential curves of the $X^2\Sigma_g^+$, $A^2\Pi_u$ and $B^2\Sigma_u^+$ states given in [38, 39]. The field-free basis set is obtained as the eigenfunctions of Hamiltonian H_0 under the field free conditions, that is, as the solution of the Schrödinger equation,

$$H_0\psi_{\alpha vKm}(r) = \varepsilon_{\alpha vKm}\psi_{\alpha vKm}(r), \tag{3.13}$$

where

$$H_0 = -\frac{\hbar^2}{2\mu}\frac{\partial^2}{\partial r^2} + V_\alpha(r) + \frac{K(K+1)-k^2}{2\mu r^2}, \tag{3.14}$$

and k is the projection of the electronic orbital angular momentum onto the N-N molecular axis. In the calculation using the finite difference method, the space is divided into a finite number of equally spaced nodes, separated by Δr, so that $\psi_{\alpha v K m}(r)$ is represented as a vector having the elements at all the points in the space as

$$\psi_{\alpha v K m}(r) = \begin{pmatrix} \psi_{\alpha v K m}(r_1) \\ \psi_{\alpha v K m}(r_2) \\ \vdots \\ \psi_{\alpha v K m}(r_{max}) \end{pmatrix}, \tag{3.15}$$

where $r_l = l \cdot \Delta r$ and r takes the value in the range of $(0, r_{\max})$ covering the entire internuclear distance region where the interatomic potentials are defined.

The second derivative of the kinetic energy part in H_0 is estimated from the first derivatives, that is, the first-order forward derivative at $r = r_l$

$$\frac{\partial}{\partial r}\psi_{\alpha v K m}|_{r=r_l \text{forward}} = \frac{\psi_{\alpha v K m}(r_{l+1}) - \psi_{\alpha v K m}(r_l)}{\Delta r}, \tag{3.16}$$

and the backward first-order derivative at $r = r_l$:

$$\frac{\partial}{\partial r}\psi_{\alpha v K m}|_{r=r_l \text{backward}} = \frac{\psi_{\alpha v K m}(r_l) - \psi_{\alpha v K m}(r_{l-1})}{\Delta r}, \tag{3.17}$$

so that the second derivative is represented using a difference operator by

$$\begin{aligned} \frac{\partial^2}{\partial r^2}\psi_{\alpha v K m}(r)|_{r=r_l} &= \frac{1}{\Delta r}\left(\frac{\partial}{\partial r}\psi_{\alpha v K m}|_{r=r_l \text{forward}} - \frac{\partial}{\partial r}\psi_{\alpha v K m}|_{r=r_l \text{backward}}\right) \\ &= \frac{\psi_{\alpha v K m}(r_{l+1}) - 2\psi_{\alpha v K m}(r_l) + \psi_{\alpha v K m}(r_{l-1})}{\Delta r^2} \end{aligned}. \tag{3.18}$$

By substituting (3.15) into (3.13) and using (3.18), we can express the Hamiltonian as

$$H_{il} = \begin{cases} -\frac{1}{2\mu}\frac{-2}{\Delta r^2} + V(r_i) + \frac{K(K+1)-k^2}{2\mu r_i^2} & \text{when } i = l, \\ -\frac{1}{2\mu}\frac{1}{\Delta r^2} & \text{when } i - l = \pm 1, \\ 0 & \text{when } i \neq l \text{ and } i - l \neq \pm 1. \end{cases} \tag{3.19}$$

As the solutions of the Schrödinger equation with the Hamiltonian above, we derive the eigenvalues, $\{\varepsilon_{\alpha v K m}\}$, corresponding to the rovibrational energies in the respective electronic states, and the eigen vectors, $\{\psi_{\alpha v K m}(r)\}$, corresponding to the wave function of the K-th rotational level in the v vibrational state.

In order to describe the symmetry of the $A^2\Pi_u$ state, we label the corresponding rotational basis wave function in the different electronic state as $|K, m\rangle^{\alpha}$, defined as

$$|K, m\rangle^{\alpha} = \begin{cases} |K, m, 0\rangle & \text{when } \alpha = \text{X, B}, \\ (|K, m, 1\rangle + |K, m, -1\rangle)/\sqrt{2} & \text{when } \alpha = \text{A}_+, \\ (|K, m, 1\rangle - |K, m, -1\rangle)/\sqrt{2} & \text{when } \alpha = \text{A}_-, \end{cases} \tag{3.20}$$

where the rotational basis wave function $|K, m, k\rangle$ defined as [40]

$$\begin{aligned} |K, m, k\rangle = & \frac{1}{\sqrt{2}}\sqrt{(K+m)!(K-m)!(K+k)!(K-k)!(2K+1)} \\ & \times \sum_{\sigma}(-1)^{\sigma}\frac{[\cos(\theta/2)]^{2K+k-m-2\sigma}[-\sin(\theta/2)]^{m-k+2\sigma}}{\sigma!(K-m-\sigma)!(m-k+\sigma)!(K+k-\sigma)!}e^{im\varphi}. \end{aligned} \tag{3.21}$$

Note that the rotational basis functions, $|K, m, k\rangle$, of the $X^2\Sigma_g^+$ and $B^2\Sigma_u^+$ states having $k = 0$ are the standard spherical harmonics while the rotational wave functions $|K, m, +1\rangle$ and $|K, m, -1\rangle$ of the degenerate $A^2\Pi_u$ state having $k = \pm 1$ are not symmetric with respect to the transformation $\theta \to \pi - \theta$. By the subtraction and addition, the two symmetric basis sets, $|K, m\rangle^{A_+}$ and $|K, m\rangle^{A_-}$ of the $A^2\Pi_u$ state are constructed as given by (3.20).

3.2.3 Rovibronic Dynamics in Time-Dependent Schrödinger Equation

By substituting (3.12) into (3.1), and multiplying with $\psi^*_{\beta v' K' m'}(r)$ from left and integrating over $\mathbf{r}$, we obtain

$$i\hbar\frac{d}{dt}c_{\beta v' K' m'}(t) = \sum_{\alpha=\text{X},\text{A}_+,\text{A}_-,\text{B}}\sum_{v=0}^{N}\sum_{K=0}^{K_{\max}}\sum_{m=-K}^{K} c_{\alpha v K m}(t)H_{\beta v' K' m' \alpha v K m}(t), \tag{3.22}$$

where

$$H_{\beta v' K' m' \alpha v K m}(t) = \int_0^{\infty}\int_0^{\pi}\int_0^{2\pi}\psi^*_{\beta v' K' m'}(\mathbf{r})H(t)\psi_{\alpha v K m}(\mathbf{r})\mathrm{d}r\sin\theta\mathrm{d}\theta\mathrm{d}\phi. \tag{3.23}$$

Under an intense laser pulse, the total Hamiltonian H of the system interacting with the laser field becomes

$$H(t) = -\frac{\hbar^2}{2\mu}\nabla^2 + V + H_1(t) = H_0 + H_1(t), \tag{3.24}$$

where μ is the reduced mass of N_2^+, V is the interatomic potential energy, and H_1 stands for the interaction with the laser field. Therefore, $H_{\beta v' K' m' \alpha v K m}(t)$ becomes

$$H_{\beta v' K' m' \alpha v K m}(t) = (H_0)_{\beta v' K' m' \alpha v K m} + (H_1)_{\beta v' K' m' \alpha v K m}(t), \tag{3.25}$$

where

$$\begin{aligned}(H_0)_{\beta v' K' m' \alpha v K m} &= \left\langle \psi_{\beta v' K' m'} \right| H_0 \left| \psi_{\alpha v K m} \right\rangle \\ &= \varepsilon_{\alpha v K m} \delta_{\alpha\beta} \delta_{v' v} \delta_{K' K} \delta_{m' m},\end{aligned} \tag{3.26}$$

and

$$\begin{aligned}(H_1)_{\beta v' \alpha v}(t) &= \left\langle \psi_{\beta v' K' m'} \right| H_1(t) \left| \psi_{\alpha v K m} \right\rangle \\ &= \left\langle \psi_{\beta v' K' m'} \right| D_{\alpha\beta} F_\theta^{\alpha\beta} \left| \psi_{\alpha v K m} \right\rangle \mathcal{E}(t),\end{aligned} \tag{3.27}$$

representing the coupling between rotational states via the transition dipole moment $D_{\alpha\beta}$. In (3.27), $\mathcal{E}(t)$ stands for the laser field strength at time t, defined as

$$\mathcal{E}(t) = \mathcal{E}_0 f(t) \cos(\omega t), \tag{3.28}$$

where $f(t)$ is an envelope function, ω is the frequency of the laser pulse, and $F_\theta^{\alpha\beta}$ is the angle factor representing the polar angle-dependent coupling among the $X^2\Sigma_g^+$, $A^2\Pi_u$ and $B^2\Sigma_u^+$ states, defined as

$$F_\theta^{\alpha\beta} = \cos(\theta)(\delta_{B\alpha}\delta_{X\beta} + \delta_{X\alpha}\delta_{B\beta}) + \frac{\sin(\theta)}{\sqrt{2}}(\delta_{A_\pm\alpha}\delta_{X\beta} + \delta_{X\alpha}\delta_{A_\pm\beta}). \tag{3.29}$$

Because the laser field is linearly polarized, $F_\theta^{\alpha\beta}$ does not depend on the azimuth angle φ, which means that the quantum number m is conserved during the interaction with the laser field. The rotational transition probability is given by

$$|p^{K,m}_{X\beta(\Delta K_\beta)}|^2 = |{}^X\langle K, m | F_\theta^{X\beta} | K + \Delta K_\beta, m \rangle^\beta|^2, \tag{3.30}$$

where $\Delta K_B = \pm 1$ is taken for $\beta = B$, and $\Delta K_{A_\pm} = \pm 1, 0$ for $\beta = A_\pm$.

For given K and m,

$$p^{K,m}_{XB(\Delta K_B)} = \begin{cases} \left(\frac{(K-m+1)(K+m+1)}{(2K+1)(2K+3)}\right)^{\frac{1}{2}} & \text{when } \Delta K_B = 1, \\ \left(\frac{(K-m)(K+m)}{(2K+1)(2K-1)}\right)^{\frac{1}{2}} & \text{when } \Delta K_B = -1. \end{cases} \tag{3.31}$$

$$
\begin{aligned}
p^{K,m}_{\mathrm{XA}_\pm(\Delta K_{\mathrm{A}_\pm})} &= K!\sqrt{(K+m)!(K-m)!(K+\Delta K_{\mathrm{A}_\pm}+m)!(K+\Delta K_{\mathrm{A}_\pm}-m)!} \\
&\times\sqrt{(K+\Delta K_{\mathrm{A}_\pm}+1)!(K+\Delta K_{\mathrm{A}_\pm}-1)!(2K+1)(2(K+\Delta K_{\mathrm{A}_\pm})+1)} \\
&\times\sum_{\sigma=0}^{K-m}\left\{\frac{(-1)^\sigma}{\sigma!(K-m-\sigma)!(m+\sigma)!(K-\sigma)!(2+2K+\Delta K_{\mathrm{A}_\pm})!}\right. \\
&\times\Big[\sum_{\sigma'}(-1)^{\sigma'-1}\frac{(1-m+2K+\Delta K_{\mathrm{A}_\pm}-\sigma-\sigma')!(m+\sigma+\sigma')!}{\sigma'!(K+\Delta K_{\mathrm{A}_\pm}-m-\sigma')!(m-1+\sigma')!(K+\Delta K_{\mathrm{A}_\pm}+1-\sigma')!} \\
&\left.+(-1)^{\Delta K_{\mathrm{A}_\pm}}\sum_{\sigma'_s}(-1)^{\sigma'_s+1}\frac{(2K-m+\Delta K_{\mathrm{A}_\pm}-\sigma-\sigma'_s)!(1+m+\sigma+\sigma'_s)!}{\sigma'_s!(K+\Delta K_{\mathrm{A}_\pm}-m-\sigma'_s)!(m+1+\sigma'_s)!(K+\Delta K_{\mathrm{A}_\pm}-1-\sigma'_s)!}\Big]\right\},
\end{aligned}
\tag{3.32}
$$

where σ' starts from the larger of 0 and $(1-m)$ and ends at $(K+\Delta K_{\mathrm{A}_\pm}-m)$, and σ'_s starts from 0 and ends at the smaller of $(K+\Delta K_{\mathrm{A}_\pm}-m)$ and $(K+\Delta K_{\mathrm{A}_\pm}-1)$.

The envelope function is defined as

$$
f(t) = e^{-t^2/2\sigma_0^2}, \tag{3.33}
$$

where σ_0 is chosen according to the intensity half-width of the laser pulse.

3.3 Rovibronic Excitation in N_2^+

When N_2 is ionized in an intense laser field at the field intensity of 2×10^{14} W cm^{-2}, the relative probability of N_2^+ to be prepared in the electronic ground $X^2\Sigma_g^+$ state by the tunneling ionization of N_2 can be estimated by molecular Ammosov-Delone-Krainov (MO-ADK) theory to be 90% [41], which is much larger than the probability to be prepared in the $A^2\Pi_u$ state (5%) and the $B^2\Sigma_u^+$ state (5%). In addition, the Franck-Condon factor of exciting the vibrational ground state of N_2 to the vibrational ground $X^2\Sigma_g^+$ state of N_2^+ is 0.9. Therefore we can assume that N_2^+ is prepared only in the vibrational ground state of the $X^2\Sigma_g^+$ state at $t=0$, hereafter referred to as $X(v=0)$. Because N_2^+ generated in the ground $X^2\Sigma_g^+$ is suddenly exposed to an intense laser field, a sudden turn-on pulse with an envelope function defined in (3.33) for $t\geq0$ is applied in simulating the time-dependent dynamics in the rovibronic transitions in N_2^+ starting from the $X(v=0)$ state.

In calculating the interaction with the sudden turn-on pulse, the lowest four vibrational levels are included ($V_{\max}=3$ in (3.12)) in all the three electronic states, and the temporal variation of the populations in the respective rotational levels are obtained at a sufficiently small time step of 0.024 fs. Note that the transition dipole moment between $X^2\Sigma_g^+$ and $A^2\Pi_u$ is perpendicular to the N-N molecular axis, while that between $X^2\Sigma_g^+$ and $B^2\Sigma_u^+$ is parallel to the molecular axis, and the numerical values of these two transition dipole moments are taken from [38, 39]. The initial population is assumed to be represented by the Boltzmann distribution at $T=300$ K, and $K_{\max}$ in (3.5) and (3.12) is set to be 40.

As the initial state is taken at $t=0$, we adopt the respective rotational levels and solve the time-dependent Schrödinger equation so that the populations in the rotational levels $|\alpha v K' m\rangle$ at time t are obtained from the time-propagation.

The final populations in the rotational levels after the laser pulse vanishes are evaluated according to the initial populations in the respective rotational levels at $T = 300$ K as

$$p_{\alpha v K'}(t) = \frac{1}{\zeta} \sum_{K=0}^{K_{\max}} \sum_{m=-K}^{K} |c^{\mathrm{X}0Km}_{\alpha v K' m'}(t)|^2 g_K e^{-\frac{-B_{\mathrm{X}0}K(K+1)}{k_B T}}, \tag{3.34}$$

where $c^{\mathrm{X}0Km}_{\alpha v K' m'}(t)$ are the time-dependent coefficients obtained from the solution of (3.22) using the initial conditions $c^{\mathrm{X}0Km}_{\alpha v K' m'}(t=0) = \delta_{\mathrm{X}\alpha}\delta_{0v}\delta_{KK'}\delta_{mm'}$, $B_{\alpha v}$ is the rotational constant, k_B is the Boltzmann constant, g_K the nuclear spin statistical weight, which takes the values of $g_K = 2$ for even K and $g_K = 1$ for odd K, and ζ is the normalization factor given by

$$\zeta = \sum_{K=0}^{K_{\max}} g_K (2K+1) e^{-\frac{-B_{\alpha v}K(K+1)}{k_B T}}. \tag{3.35}$$

The final population after the interaction with the laser pulse is denoted by $P_{\alpha v K}$,

$$P_{\alpha v K} = \lim_{t \to \infty} p_{\alpha v K}(t). \tag{3.36}$$

First, we consider the rotational excitation induced by the half pulse until just before the ionization occurs. Such rotational excitation in N_2 induced until just before the ionization can be calculated numerically by solving the (3.10). We assume that the rotational wavepacket is expressed as

$$\Phi(\theta, \varphi, t) = \frac{e^{im\varphi}}{\sqrt{2\pi}} \sum_{K=0}^{K_{\max}} C_{Km}(t) |K, m\rangle^{\mathrm{N}_2}, \tag{3.37}$$

where $|K, m\rangle^{\mathrm{N}_2}$ is the normalized associated Legendre functions. $\Delta\alpha = 0.71$ Å^3 [42] and the rotational constant of $B = 1.9895$ cm^{-1} [43] are adopted.

The calculations start with the respective rotational states of N_2 from $t = -50$ fs until $t = 0$, and the resulting coherent rotational state of the rigid rotor, calculated as shown in Sect. 3.2.1, is taken as the initial state for the simulation of N_2^+, which then interacts with the sudden turn-on pulse at $t = 0$.

We also perform the numerical simulation by neglecting the rotational excitation within the neutral N_2 manifold during the first half pulse until just before the ionization and confirm that the final population distribution of N_2^+ is very close to that we obtained above by taking into account the rotational excitation in N_2. As shown in Fig. 3.2, for example, at peak laser field intensity of 4×10^{14} W cm^{-2}, the differences in the populations in the respective rotational levels are found to be only less than 0.20% and the population differences in the respective vibrational levels obtained by the summation over the K and m quantum numbers are all less than 0.26%.

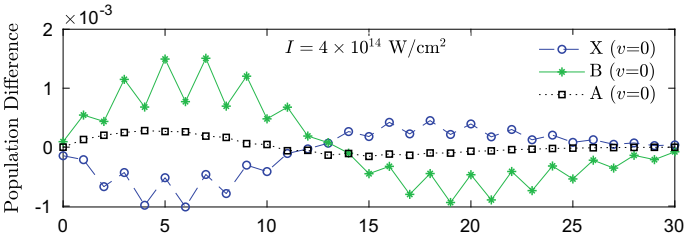

Fig. 3.2 The difference in the final population distributions obtained when the rotational excitation of neutral N_2 in an intense 800 nm laser field during the period of the earlier half of the Gaussian envelope between $t = -50$ fs and $t = 0$ fs and those obtained when no rotational pre-excitation of neutral N_2 is considered. The field intensities at $t = 0$ are set to be 4×10^{14} W cm^{-2}. In the calculation, it is assumed that N_2^+ is prepared in the $X^2\Sigma_g^+(v = 0)$ state at $t = 0$. For the A state, the sum of the populations in the A_+ and A_- states is shown. The label "$\alpha(v = n)$" stands for the nth vibrational state of the α state

When the resultant rotational distributions at 4×10^{14} W cm^{-2} are fitted by the Boltzmann distribution, the rotational temperatures for the rotational level distribution in the $X^2\Sigma_g^+$, $A^2\Pi_u$, and $B^2\Sigma_u^+$ states are obtained to be 424 K, 295 K and 505 K, respectively. On the other hand, when the rotational pre-excitation in the neutral N_2 is not considered, the resultant rotational temperatures for the $X^2\Sigma_g^+$, $A^2\Pi_u$, and $B^2\Sigma_u^+$ states are obtained to be 401 K, 302 K, and 573 K, respectively, which are close to the temperatures obtained with the rotational pre-excitation in the N_2 manifold. Therefore, it can be said that the variation in the rotational level distributions after N_2^+ interacts with the sudden turn-on laser pulse can be calculated without considering the rotational pre-excitation in N_2.

We calculate the final population distributions in the rotational levels in the $X^2\Sigma_g^+$, $A^2\Pi_u$, and $B^2\Sigma_u^+$ states at different laser field intensities by assuming that N_2^+ starts interacting with the sudden turn-on pulse by neglecting rotational pre-excitation of neutral N_2. According to the rovibronic selection rules, the population inversion achieved between $B^2\Sigma_u^+(v = 0)$ and $X^2\Sigma_g^+(v = 0)$ can lead to the emission composed of the P-branch and R-branch transitions. The population difference for the P-branch transitions is given by

$$\Delta P_{\mathrm{P}} = P_{B,v=0,K} - P_{X,v=0,K+1}, \tag{3.38}$$

and that for the R-branch transitions is given by

$$\Delta P_{\mathrm{R}} = P_{B,v=0,K+1} - P_{X,v=0,K}. \tag{3.39}$$

As shown in Fig. 3.3a, at the laser field intensity of 2×10^{14} W cm^{-2}, the population inversion is not achieved between the $B^2\Sigma_u^+(v = 0)$ state and the $X^2\Sigma_g^+(v = 0)$ state. However, in Fig. 3.3c, at the laser field intensity of 6×10^{14} W cm^{-2}, the population inversion is achieved in the entire range of the rotational quantum numbers,

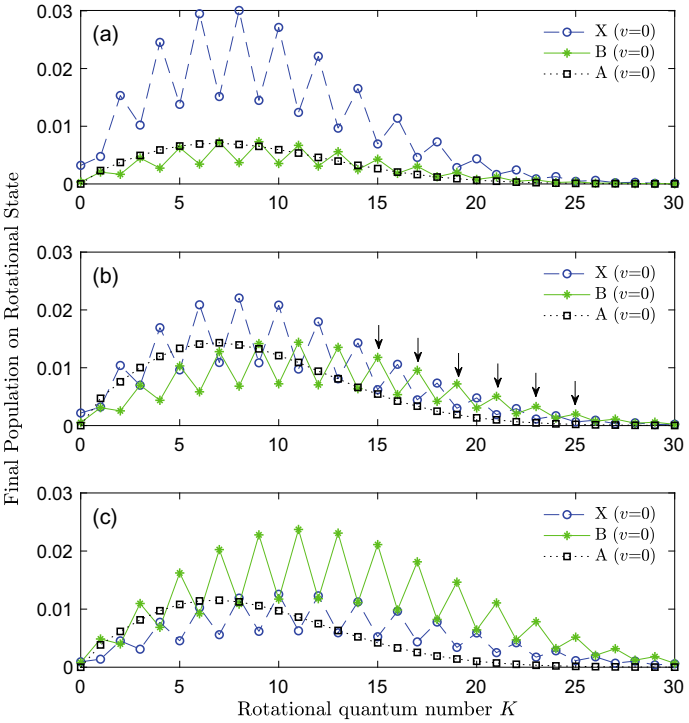

Fig. 3.3 Final population distribution in the rotational levels of N_2^+ obtained after the interaction with an intense 800 nm laser pulse. The field intensities are set to be **a** 2×10^{14} W cm^{-2}, **b** 4×10^{14} W cm^{-2} and **c** 6×10^{14} W cm^{-2}. In the calculation, it is assumed that N_2^+ is prepared in the $X^2\Sigma_g^+(v = 0)$ state at $t = 0$. For the A state, the sum of the populations in the A_+ and A_- states is shown. The short downward arrows in (**b**) indicate the rotational levels in the $B^2\Sigma_u^+$ state from which the lasing emission occurs via the P-branch transitions to the $X(v = 0)$ state. The label "$\alpha(v = n)$" stands for the nth vibrational state of the α state

and consequently, the total population inversion is achieved between the $B(v = 0)$ state and the $X(v = 0)$ state, which is consistent with the previous experimental results [27], in which both P-branch and R-branch emission lines are observed at the laser field intensity of 6×10^{14} W cm^{-2}. The zig-zag pattern reflects the nuclear spin statistical weights of N_2^+ appearing in (3.34).

What draws our attention is that, at the intermediate laser field intensity of 4×10^{14} W cm^{-2} shown in Fig. 3.3b, the population inversion is achieved in the rotationally highly excited levels as shown in Fig. 3.3b. Indeed, the P-branch emission from $B(v = 0)$ becomes possible when $K' \geq 15$ and the R-branch emission from $B(v = 0)$ becomes possible when $K' \geq 21$. This situation can be realized in experiment, if the light field intensity is chosen appropriately in the intermediate intensity range and the $B(v = 0)$–$X(v = 0)$ emission spectrum is recorded with sufficiently high resolution so that P branch and R branch emission transitions are resolved.

Another interesting aspect found in Fig. 3.3 is that the rotational population distribution of the $B(v = 0)$ state exhibits the peak at around $K' = 10$, corresponding to the rotational temperature of 573 K, and the rotational population distribution of the $X(v = 0)$ state exhibits a peak at $K' = 8$, corresponding to the rotational temperature of 401 K and that of the $A(v = 0)$ state exhibits a peak at $K' = 7$, which corresponds to the rotational temperature of 302 K. This discrepancy in the effective rotational temperature in the $B(v = 0)$ state and that in the $X(v = 0)$ state can be ascribed to the difference in the rotational selection rules of the $B^2\Sigma_u^+$–$X^2\Sigma_g^+$ transitions and those of the $A^2\Pi_u$–$X^2\Sigma_g^+$ transitions as explained below.

As shown in (3.31), the $B^2\Sigma_u^+$–$X^2\Sigma_g^+$ rovibronic transition probability $|p^{K,m}_{\mathrm{XB}(\Delta K_B=\pm1)}|^2$ is the squared modulus of ${}^B\langle K \pm 1, m|\cos\theta|K, m\rangle^X$ and the $A^2\Pi_u$–$X^2\Sigma_g^+$ rovibronic transition probability $|p^{K,m}_{\mathrm{XA}(\Delta K_A=0,\pm1)}|^2$ is the squared modulus of ${}^A\langle K \text{ or } K\pm 1, m|\frac{\sin(\theta)}{\sqrt{2}}|K, m\rangle^X$ according to the rotational transition selection rules of $\Delta K_B = K' - K'' = \pm1$ for the $B^2\Sigma_u^+$–$X^2\Sigma_g^+$ transition and $\Delta K_A = K' - K'' = 0, \pm1$ for the $A^2\Pi_u$–$X^2\Sigma_g^+$ transition. By considering the symmetries of the rotational basis represented by the spherical harmonics in the $X^2\Sigma_g^+$ and $B^2\Sigma_u^+$ states, we find $|p^{K,m}_{\mathrm{XB}(\Delta K_B=1)}|^2 \sim |p^{K,m}_{\mathrm{XB}(\Delta K_B=-1)}|^2$. This means that the population in the K level in the $X^2\Sigma_g^+$ state can be transferred to the higher and lower rotational levels in the $B^2\Sigma_u^+$ state with almost equal probabilities and that transitions to the rotational states with large K in the $B^2\Sigma_u^+$ state can be populated by a sequence of transitions $X(K) \to B(K+1) \to X(K+2) \to B(K+3)\ldots$ On the other hand, for the $A^2\Pi_u$–$X^2\Sigma_g^+$ transition, the probabilities of the Q-branch transitions are much larger than those of the R ($\Delta K_A = 1$) and P ($\Delta K_A = -1$) transitions and the probability of the R-branch transition is always larger than that of the P-branch transition, that is, $|p^{K,m}_{\mathrm{XA}(\Delta K_A=0)}|^2 \gg |p^{K,m}_{\mathrm{XA}(\Delta K_A=1)}|^2 > |p^{K,m}_{\mathrm{XA}(\Delta K_A=-1)}|^2$, which means that the $A^2\Pi_u$–$X^2\Sigma_g^+$ transition starting from a certain rotational level K preferentially stays in the original or neighboring rotational levels, resulting in the suppression of the population transfer to the higher K levels.

Because the $X^2\Sigma_g^+$ state is coupled with both of the $B^2\Sigma_u^+$ and $A^2\Pi_u$ states, the rotational population distribution in the $X^2\Sigma_g^+$ state is influenced not only by the $B^2\Sigma_u^+ - X^2\Sigma_g^+$ rovibronic transitions, having a tendency to promote the population transfer to the higher rotational levels, but also by the $A^2\Pi_u - X^2\Sigma_g^+$ rovibronic transitions, having a tendency to suppress the population transfer to higher-lying rotational levels, the extent of the rotational excitation in the $X^2\Sigma_g^+$ state is smaller than that of the $B^2\Sigma_u^+$ state and larger than that of the $A^2\Pi_u$ state. These differences in the extent of the rotational excitation in the $X^2\Sigma_g^+$, $A^2\Pi_u$, and $B^2\Sigma_u^+$ states can make the population inversion appear only among the highly excited rotational levels of the $B^2\Sigma_u^+(v = 0)$ and $X^2\Sigma_g^+(v = 0)$ in the specific range of the laser field intensity, resulting in the emission at 391 nm of N_2^+ without achieving population inversion between the $B^2\Sigma_u^+(v = 0)$ and $X^2\Sigma_g^+(v = 0)$ states.

3.4 Summary

We show that the air-lasing emission at 391 nm originating from the population inversion between $B^2\Sigma_u^+(v=0)$ and $X^2\Sigma_g^+(v=0)$ states of N_2^+ induced by a near-IR intense laser pulse can be understood theoretically based on the sudden turn-on excitation model with the population pumping by the $A^2\Pi_u - X^2\Sigma_g^+$ transition [19–23] and that the theoretical model in which the rotational degrees of freedom of N_2^+ is explicitly included interpreted well how rotationally inverted populations can be created in a specific range of the laser field intensity. The theoretical simulation reproduced well recent experimental findings, showing that the air-lasing phenomenon at 391 nm can be fully accounted for by our numerical simulator in which the rotational and vibrational degrees of freedom are explicitly included in the optical couplings in the three low-lying electronic states, $X^2\Sigma_g^+$, $A^2\Pi_u$, and $B^2\Sigma_u^+$, of N_2^+ .

Acknowledgements This research was supported by JSPS KAKENHI grants no. JP15K17805, no. JP24245003, no. JP15H05696, and no. 20H00371.

References

1. R. Velotta, N. Hay, M.B. Mason, M. Castillejo, J.P. Marangos, High-order harmonic generation in aligned molecules. Phys. Rev. Lett. **87** (2001)
2. A. Giusti-Suzor, X. He, O. Atabek, F.H. Mies, Above-threshold dissociation of H_2^+ in intense laser fields. Phys. Rev. Lett. **64**, 515 (1990)
3. H. Sakai, C.P. Safvan, J.J. Larsen, K.M. Hilligso/e, K. Hald, H. Stapelfeldt, Controlling the alignment of neutral molecules by a strong laser field. J. Chem. Phys. **110**, 10235 (1999)
4. Q. Luo, W. Liu, S. Chin, Lasing action in air induced by ultra-fast laser filamentation. Appl. Phys. B **76**, 337 (2003)
5. A. Dogariu, J.B. Michael, M.O. Scully, R.B. Miles, High-gain backward lasing in air. Science **331**, 442 (2011)
6. P.R. Hemmer, R.B. Miles, P. Polynkin, T. Siebert, A.V. Sokolov, P. Sprangle, M.O. Scully, Standoff spectroscopy via remote generation of a backward-propagating laser beam. Proc. Natl. Acad. Sci. USA **108**(3130), 21297033 (2011)
7. S. Mitryukovskiy, Y. Liu, P. Ding, A. Houard, A. Mysyrowicz, Backward stimulated radiation from filaments in nitrogen gas and air pumped by circularly polarized 800 nm femtosecond laser pulses. Opt. Express **22**, 12750 (2014)
8. G. Point, Y. Liu, Y. Brelet, S. Mitryukovskiy, P. Ding, A. Houard, A. Mysyrowicz, Lasing of ambient air with microjoule pulse energy pumped by a multi-terawatt infrared femtosecond laser. Opt. Lett. **39**, 1725 (2014)
9. V. Kocharovsky, S. Cameron, K. Lehmann, R. Lucht, R. Miles, Y. Rostovtsev, W. Warren, G.R. Welch, M.O. Scully, Gain-swept superradiance applied to the stand-off detection of trace impurities in the atmosphere. Proc. Natl. Acad. Sci. **102**, 7806 (2005)
10. A. Laurain, M. Scheller, P. Polynkin, Low-threshold bidirectional air lasing. Phys. Rev. Lett. **113** (2014)
11. P. Ding, S. Mitryukovskiy, A. Houard, E. Oliva, A. Couairon, A. Mysyrowicz, Y. Liu, Backward Lasing of Air plasma pumped by Circularly polarized femtosecond pulses for the saKe of remote sensing (BLACK). Opt. Express **22**, 29964 (2014)

12. J. Yao, H. Xie, B. Zeng, W. Chu, G. Li, J. Ni, H. Zhang, C. Jing, C. Zhang, H. Xu, Y. Cheng, Z. Xu, Gain dynamics of a free-space nitrogen laser pumped by circularly polarized femtosecond laser pulses. Opt. Express **22**, 19005 (2014)
13. P. Ding, E. Oliva, A. Houard, A. Mysyrowicz, Y. Liu, Lasing dynamics of neutral nitrogen molecules in femtosecond filaments. Phys. Rev. A **94** (2016)
14. D. Kartashov, S. Ališauskas, A. Baltuška, A. Schmitt-Sody, W. Roach, P. Polynkin, Remotely pumped stimulated emission at 337 nm in atmospheric nitrogen. Phys. Rev. A **88** (2013)
15. J. Yao, B. Zeng, H. Xu, G. Li, W. Chu, J. Ni, H. Zhang, S.L. Chin, Y. Cheng, Z. Xu, High-brightness switchable multiwavelength remote laser in air. Phys. Rev. A **84** (2011)
16. H. Zhang, C. Jing, J. Yao, G. Li, B. Zeng, W. Chu, J. Ni, X. Hongqiang, H. Xu, S. Leang Chin, K. Yamanouchi, H. Sun, Z. Xu, Rotational coherence encoded in an "air-laser" spectrum of nitrogen molecular ions in an intense laser field. Phys. Rev. X **3** (2013)
17. Y. Liu, Y. Brelet, G. Point, A. Houard, A. Mysyrowicz, Self-seeded lasing in ionized air pumped by 800 nm femtosecond laser pulses. Opt. Express **21**, 22791 (2013)
18. T.-J. Wang, J. Ju, J.-F. Daigle, S. Yuan, R. Li, S.L. Chin, Self-seeded forward lasing action from a femtosecond Ti:sapphire laser filament in air. Laser Phys. Lett. **10** (2013)
19. H. Xu, E. Lötstedt, A. Iwasaki, K. Yamanouchi, Sub-10-fs population inversion in $N_2{}^+$ in air lasing through multiple state coupling. Nat. Commun. **6**, 8347 (2015)
20. H. Xu, E. Lötstedt, T. Ando, A. Iwasaki, K. Yamanouchi, Alignment-dependent population inversion in N_2^+ in intense few-cycle laser fields. Phys. Rev. A **96** (2017)
21. Y. Zhang, E. Lötstedt, K. Yamanouchi, Mechanism of population inversion in laser-driven N_2^+. J. Phys. B At. Mol. Opt. Phys. **52** (2019)
22. T. Ando, E. Lötstedt, A. Iwasaki, H. Li, Y. Fu, S. Wang, H. Xu, K. Yamanouchi, Rotational, vibrational, and electronic modulations in N_2^+ lasing at 391 nm: evidence of coherent $B^2\Sigma_u^+ - X^2\Sigma_g^+ - A^2\Pi_u$ coupling. Phys. Rev. Lett. **123** (2019)
23. Y. Zhang, E. Lötstedt, K. Yamanouchi, Rotationally induced population inversion between the $B^2\Sigma_u^+$ and $X^2\Sigma_g^+$ states of N_2^+ exposed to an intense laser pulse. Phys. Rev. A **101** (2020)
24. B. Zeng, W. Chu, G. Li, J. Yao, H. Zhang, J. Ni, C. Jing, H. Xie, Y. Cheng, Real-time observation of dynamics in rotational molecular wave packets by use of air-laser spectroscopy. Phys. Rev. A **89** (2014)
25. H. Xie, B. Zeng, G. Li, W. Chu, H. Zhang, C. Jing, J. Yao, J. Ni, Z. Wang, Z. Li, Y. Cheng, Coupling of N_2^+ rotational states in an air laser from tunnel-ionized nitrogen molecules. Phys. Rev. A **90** (2014)
26. M. Lei, C. Wu, A. Zhang, Q. Gong, H. Jiang, Population inversion in the rotational levels of the superradiant N_2^+ pumped by femtosecond laser pulses. Opt. Express **25**, 4535 (2017)
27. A. Azarm, P. Corkum, P. Polynkin, Optical gain in rotationally excited nitrogen molecular ions. Phys. Rev. A **96** (2017)
28. W. Zheng, Z. Miao, L. Zhang, Y. Wang, C. Dai, A. Zhang, H. Jiang, Q. Gong, C. Wu, Enhanced coherent emission from ionized nitrogen molecules by femtosecond laser pulses. J. Phys. Chem. Lett. **6598** (2019)
29. H. Xie, H. Lei, G. Li, Q. Zhang, X. Wang, J. Zhao, Z. Chen, J. Yao, Y. Cheng, Z. Zhao, Role of rotational coherence in femtosecond-pulse-driven nitrogen ion lasing. Phys. Rev. Res. **2** (2020)
30. M. Richter, M. Lytova, F. Morales, S. Haessler, O. Smirnova, M. Spanner, M. Ivanov, Rotational quantum beat lasing without inversion. Optica **7**, 586 (2020)
31. S. Tamar, Rotational excitation and molecular alignment in intense laser fields. J. Chem. Phys. **103**, 7887 (1995)
32. L. Matsuoka, E. Segawa, Localization in rotational excitation of diatomic molecules induced by a train of optical pulses. Interdiscip. Inf. Sci. **23**, 51 (2017)
33. A. Maan, A. Tyagi, V. Prasad, Rotational excitation of diatomic molecule: time dependent study. Acta Phys. Pol. A **133**, 1266 (2018)
34. T. Szidarovszky, M. Jono, K. Yamanouchi, LIMAO: cross-platform software for simulating laser-induced alignment and orientation dynamics of linear-, symmetric- and asymmetric tops. Comput. Phys. Commun. **228**, 219 (2018)

35. H. Li, M. Hou, H. Zang, Y. Fu, E. Lötstedt, T. Ando, A. Iwasaki, K. Yamanouchi, H. Xu, Significant enhancement of N_2^+ lasing by polarization-modulated ultrashort laser pulses. Phys. Rev. Lett. **122** (2019)
36. P.W. Dooley, I.V. Litvinyuk, K.F. Lee, D.M. Rayner, M. Spanner, D.M. Villeneuve, P.B. Corkum, Direct imaging of rotational wave-packet dynamics of diatomic molecules. Phys. Rev. A **68** (2003)
37. B. Friedrich, D. Herschbach, Alignment and trapping of molecules in intense laser fields. Phys. Rev. Lett. **74**, 4623 (1995)
38. S.R. Langhoff, C.W. Bauschlicher, H. Partridge, Theoretical study of the $N_2{}^+$ Meinel system. J. Chem. Phys. **87**, 4716 (1987)
39. S.R. Langhoff, C.W. Bauschlicher Jr., Theoretical study of the first and second negative systems of $N_2{}^+$. J. Chem. Phys. **88**, 329 (1988)
40. J.M. Brown, A. Carrington, *Rotational Spectroscopy of Diatomic Molecules, Cambridge Molecular Science* (Cambridge University Press, Cambridge, 2003)
41. S.-F. Zhao, C. Jin, A.-T. Le, T.F. Jiang, C.D. Lin, Determination of structure parameters in strong-field tunneling ionization theory of molecules. Phys. Rev. A **81** (2010)
42. P.J. Bruna, F. Grein, The $A^2\Pi_u$ state of N_2^+: electric properties, fine and hyperfine coupling constants, and magnetic moments (g-factors). A theoretical study. J. Mol. Spectrosc. **250**, 75 (2008)
43. A. Lofthus, P.H. Krupenie, The spectrum of molecular nitrogen. J. Phys. Chem. Ref. Data **6**, 113 (1977)

Chapter 4
Photocatalysts for Reduction of Molecular Oxygen to Hydrogen Peroxide

Daniil A. Lukyanov and Alexander S. Konev

Abstract A brief overview of compounds and materials exhibiting photocatalytic activity in reduction of molecular oxygen to hydrogen peroxide is given with focus on comparison of the performance of reported photocatalysts. The photocatalysts are treated in two major classes: the inorganic semiconductors, which include various metal oxides and chalcogenides, and carbon-based photocatalysts, which cover a wide range of carbon-based compounds from small organic molecules to graphene materials. The review is preceded by brief description of analytical techniques available for quantification of hydrogen peroxide formation.

4.1 Introduction

The oxygen reduction reaction (ORR) may result in the formation of two stable oxygen species. Formal two-electron reduction affords hydrogen peroxide, while the four-electron process produces water. The product of the two-electron reduction, H_2O_2, represents a low-hazardous energy-rich compound, which can serve either as energy storage material [1] or as a "green" and strong oxidant, widely used in chemical industries. Hydrogen peroxide is mostly produced via the anthraquinone process of indirect oxygen hydrogenation developed by BASF [2]. In this process, 2-ethylanthraquinone is subjected to palladium-catalyzed hydrogenation to form the corresponding hydroquinone, which then selectively reduces oxygen to hydrogen peroxide. The anthraquinone process, in addition to hazardous reagents and expensive catalyst, consumes a large amount of energy for the hydrogenation reaction. An appealing new approach to H_2O_2 production exploits the solar energy in a photocatalytic oxygen reduction.

For the first time, the photochemical formation of hydrogen peroxide upon exposure to light of ZnO particles in the presence of oxidizable material was published

D. A. Lukyanov (✉) · A. S. Konev
Institute of Chemistry, Saint Petersburg State University, Saint Petersburg 199034, Russia

A. S. Konev
e-mail: a.konev@spbu.ru

K. Yamanouchi et al. (eds.), *Progress in Photon Science*, Springer Series in Chemical Physics 125, https://doi.org/10.1007/978-3-030-77646-6_4

by Baur and Neuweiler in 1927 [3]. Later, the photocatalytic formation of hydrogen peroxide was observed on various heterogeneous and homogeneous photocatalysts.

In the middle of the previous century, natural photocatalytic systems for two-electron ORR were discovered. In 1951, Alan Mehler showed that molecular oxygen is reduced in chloroplasts to hydrogen peroxide under the action of sunlight [4]. The reaction proceeded in two steps—the one-electron reduction of molecular oxygen to superoxide anion by ferridoxine followed by its disproportionation to oxygen and hydrogen peroxide under the action of superoxide dismutase.

In the recent decades, major advances have been achieved in the development of photocatalysts for ORR. A great effort was made on the way to improve the photocatalytic performance of the metal oxide semiconductors. A number of the next generation semiconductor catalysts based on 2D and 3D nanomaterials was developed, including graphene derivatives, graphene-like carbon nitride, etc. Molecular photocatalysts for ORR were found amongst organic and metal-organic molecules. Several reviews were devoted to the fundamentals and performance of organic [5, 6], inorganic [7, 8] and nanostructured [9] ORR photocatalysts. In the present overview, we aim to cover and compare these types of photocatalysts.

4.1.1 Oxygen Reduction Reactions

The main redox reactions involving molecular oxygen and related particles are shown in Latimer diagram (Fig. 4.1).

Standard electrode potential of the two-electron process of interest (4.1) is 0.695 V. The photocatalytic ORR may employ water as an electron donor in a so-called non-sacrificial process, or consume any additional reductant as a sacrificial electron donor. Depending on the nature of the sacrificial donor, reaction may be either exothermic or endothermic. The non-sacrificial ORR reaction, described by 4.6, is endothermic with ΔG of ca. 100 kJ per mole H_2O_2, thus requiring an external energy source (light with $\lambda < 1100$ nm or external bias), but most of the sacrificial donors shift the ORR to the exothermic region.

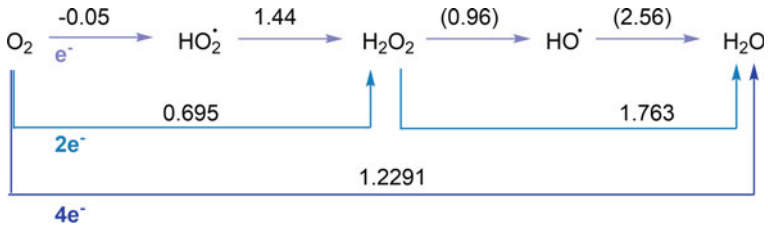

Fig. 4.1 Latimer diagram of oxygen. Standard redox potentials are reported in V versus SHE. The number of digits reflects the accuracy of measurements. Estimated values are given in parentheses. Data taken from [10]

$$O_2 + 2H^+ \xrightarrow{2e} H_2O_2 \tag{4.1}$$

$$O_2 \xrightarrow{e} O_2^{\cdot -} \tag{4.2}$$

$$2O_2^{\cdot -} + 2H^+ \rightarrow H_2O_2 + O_2 \tag{4.3}$$

$$H_2O_2 + H^+ \xrightarrow{e} HO^{\cdot} + H_2O \tag{4.4}$$

$$2OH^{\cdot} \rightarrow H_2O_2 \tag{4.5}$$

$$O_2 + 2H_2O \rightarrow 2H_2O_2 \tag{4.6}$$

However, the kinetics of the direct ORR is sluggish for both two-electron and four-electron processes, even strong reducing agents are often unable to reduce oxygen molecule without a catalyst. Photocatalysis facilitates this reaction, generally via one of two processes that potentially lead to the formation of hydrogen peroxide. The first process is the one-electron reduction of oxygen to the superoxide anion (4.2) with standard potential of − 0.046 V. The superoxide anion can spontaneously or catalytically dismutate in the presence of protons (4.3). The second process, occurring mainly on the surface of a heterogeneous catalyst, is the reduction of the hydrogen peroxide to afford hydroxyl radical (4.4) with a potential of 0.96 V. Hydroxyl radical may then recombine according to (4.5). In addition, catalyst-specific reduction pathways are known, mostly for molecular catalysts.

In practice, the two-electron ORR is accompanied by decomposition of the target product, hydrogen peroxide. It was shown that at room temperature, hydrogen peroxide decomposes quickly enough to affect the results of the photocatalytic synthesis, but when the temperature drops below + 14 °C the decomposition rate in the absence of impurities catalyzing the reaction becomes negligible [11]. In addition, the photocatalyst itself may catalyze the decomposition of H_2O_2, either as a dark process or under illumination. As a result, a plateau of H_2O_2 concentration corresponding to quasi-stationary concentration, $[H_2O_2]_{QS}$, is often observed when the decomposition rate of the hydrogen peroxide reaches its formation rate. Another problem, is the degradation of the ORR photocatalysts over the time of operation, which results in decreasing of the H_2O_2 concentration after it reaches the maximum.

4.1.2 Evaluation of Photocatalysts

Based on the aggregate state, ORR photocatalysts may be divided into solid state and molecular catalysts. Solid state photocatalysts are continuous solids with two-band electronic structure typical of semiconductors. Photoexcitation from the valence band

promotes an electron to the conduction band, where the electron may traverse to an oxygen adsorbed on the surface and reduces the oxygen molecule. Abstraction of an electron from a reductant to the valence band of the photocatalyst completes the photocatalytic cycle. Molecular photocatalysts are single molecules with discrete levels of electronic energy. The catalytic cycle in this case includes photoexcitation of the catalyst, abstraction of an electron from the photoexcited catalyst molecule by oxygen and reduction of the oxidized catalyst by a sacrificial electron donor. The mechanism of catalytic action is thus similar in both cases. However, the difference in the aggregate state leads to a difference in possible operation modes of the photocatalytic process: the solid state photocatalysts inevitably lead to a heterogenous reaction mode, while molecular photocatalysts can operate in a homogenous mode.

The photocatalytic performance of a catalyst in two-electron ORR is estimated using different indicators, depending on the catalyst type. Turnover number (TON) and turnover frequency (TOF) are used for molecular photocatalysts, while for solid state catalysts H_2O_2 production per 1 g of catalyst and H_2O_2 production per 1 g of catalyst in 1 s might be used instead of TON and TOF respectively. In case of a sacrificial ORR, the conversion of the sacrificial donor, the yield of H_2O_2, and selectivity are also used to characterize the photocatalytic process. Due to the possible decomposition of H_2O_2, the maximal achievable concentration of H_2O_2 is a good indicator for comparison of different photocatalytic systems. Wavelength specific quantum yields for the ORR photocatalysts or more practical solar light utilization efficiencies are measured to determine the light utilization performance of the catalyst. The coulombic efficiency, two- versus four-electron ORR selectivity, and external bias value should also be determined for photoelectrocatalysts.

To determine the H_2O_2 content in the reaction mixture, a large variety of analytical methods are employed. Iodometric titration [12], which was employed in early studies, is quite time-consuming and is rarely used now due to the low selectivity and low sensitivity. More useful are photometric methods such as iodide photometric [13], cobalt peroxide [14] and peroxotitanyl assays [15]. Iodide and cobalt peroxide assays employ photometry using ultraviolet light at the wavelength below 300 nm, which is absorbed by many sacrificial donor additives and organic solvents, interfering thus with the results of analysis. In a titanyl assay, an absorption at 400 nm is measured, which is more suitable for complex systems. Besides, formation of peroxy compounds of metals is not influenced by other oxidants like dissolved oxygen, which makes it a more selective method.

The most selective and sensitive photometric determination of hydrogen peroxide is achieved with horse radish peroxidase assay [16]. The use of peroxidase enzyme secures the selectivity of H_2O_2 determination in the presence of any oxidants, and the working wavelength is determined by the peroxidase substrate, which may be chosen from the large variety of commercial compounds. However, the possible interferences from sacrificial donors should be studied in each case. Chemiluminescent luminol-peroxidase assays for hydrogen peroxide delivers even higher sensitivity, providing the quantitative determination with detection limit below 100 nM [17].

Many electrochemical sensors for the hydrogen peroxide determination are developed, including the enzymatic electrodes [18]. The chromatographic determination

of H_2O_2 may be performed directly using HPLC with an ion exchange column [19] or by analyzing the products of the derivatization [20]. Direct GC determination of hydrogen peroxide is impossible due to thermal decomposition, but the headspace determination of the oxygen released by its catalytic decomposition is possible [21].

Mechanistic studies of the photocatalytic ORR may be performed by different techniques. For model studies, organic dyes are widely used as sacrificial electron donors, since their concentration may be easily monitored photometrically. However, the dye degradation assays do not provide direct information on the oxygen reduction, so the kinetic curves for hydrogen peroxide formation and/or oxygen uptake should be obtained for more detailed investigation. In case of photoelectrocatalysis, the reaction current may also be used.

The two-electron ORR is often accompanied with an intermediate formation of reactive oxygen species (ROS), including superoxide radicals, hydroxyl radical and singlet oxygen. The detection of radical ROS's may be done using EPR technique or radical scavengers. In case of solid state catalysts, the surface bound radical particles may be determined by FTIR and/or Raman spectroscopy. Singlet oxygen, which also may be produced during photocatalysis, exhibits chemiluminescence at 1270 nm, which allows its facile fluorimetric determination [22].

4.2 Photocatalysis on Inorganic Semiconductors

Metal oxides were historically the first photocatalysts of the two-electron ORR discovered following the observation of light-induced degradation of organic matter in the presence of zinc and titanium white pigments. The photocatalytic activity of these pigments in ORR is due to a good match of their conducting band edge and the oxygen redox potentials (Fig. 4.2). Following this discovery, the photocatalytic activities of other transition metal oxides and related compounds were studied.

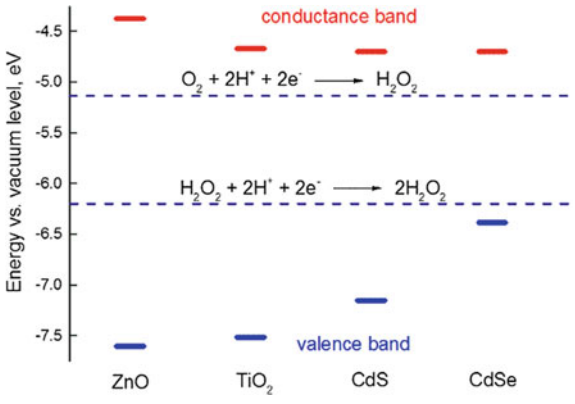

Fig. 4.2 Valence band and conductance band levels of ZnO, TiO_2, CdS and CdSe (data taken from [23]) and half reactions associated with ORR

4.2.1 Zinc Oxide

Zinc oxide is an *n*-type semiconductor with a band-gap of 3.37 eV [24], which effectively absorbs light up to 385 nm [25] (Fig. 4.3) and has a surface with high capacity of sorption of molecular oxygen [26]. The concentration of hydrogen peroxide achieved by photoreduction of molecular oxygen with pristine ZnO was shown to reach a plateau, with position determined by the form of the photocatalyst [27, 28], the nature and concentration of the oxidizable substance [29–34] and temperature. The highest level of H_2O_2 production comprising 0.06 mM or 9 μmol of H_2O_2 production per gram of pristine ZnO was observed in the absence of a sacrificial donor [35].

The mechanism of oxygen photoreduction by pristine ZnO was supposed to include the following steps: one-electron reduction of water at ZnO surface (4.7), addition of the resulting hydrogen radical to oxygen molecule (4.8), dismutation of the resulting superoxide to hydrogen peroxide and molecular oxygen (4.3), one-electron oxidation of the hydroxide anion at the surface of the photocatalyst to form a hydroxyl radical (4.9), and recombination of two hydroxyl radicals to form hydrogen peroxide (4.5) [11].

$$H_2O \xrightarrow{e} H^{\cdot} + OH^{-} \tag{4.7}$$

$$H^{\cdot} + O_2 \rightarrow HO_2^{\cdot} \tag{4.8}$$

$$OH^{-} \xrightarrow{h} OH^{\cdot} \tag{4.9}$$

$$ZnO + O_2 + 2H_2O \rightarrow H_2O_2 + Zn(OH)(OOH) \tag{4.10}$$

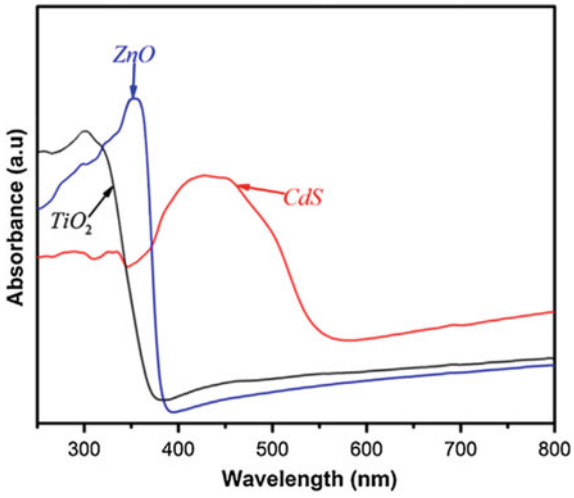

Fig. 4.3 Absorbance spectra of ZnO, TiO_2 and CdS. Image adapted from [36], Copyright 2015, with permission from Elsevier

The maximum quantum yield of the reaction, implying the formation of hydrogen peroxide in step (4.3) is 0.5. Hydroxyl recombination (4.5) which could give a quantum yield of up to 1, makes only a minor contribution to the formation of hydrogen peroxide, the majority of the peroxide particles remain bound to the surface in the form of zinc peroxyhydroxide, and eventually the material balance of the reaction is described by 4.10, which is confirmed by partial photodissolution of zinc oxide observed in the reaction [37]. Moreover, the adsorption of hydroxyl radicals passivates the catalyst surface and inhibits the formation of hydrogen peroxide.

Later studies using isotopically labeled oxygen, water, and zinc oxide [38], combined with the reaction kinetics studies [26, 39, 40] confirmed the one-electron oxygen reduction (4.3) to be the key step in the photocatalysis. An additional contribution to the formation of hydrogen peroxide is made by an electron transfer from the photocatalyst to hydrogen superoxide (4.11) [28], while additional ways of hydrogen peroxide decomposition are given by (4.12) and (4.13).

$$HO_2^{\cdot} + H^+ \xrightarrow{e} H_2O_2 \tag{4.11}$$

$$H_2O_2 + O_2^{\cdot -} \rightarrow OH^{\cdot} + OH^- + O_2 \tag{4.12}$$

$$H_2O_2 \xrightarrow{e} OH^{\cdot} + OH^- \tag{4.13}$$

The hydrogen peroxide formation obeys pseudo-zero order kinetics under continuous aeration, since it occurs under tremendous excess of the reactants (water, hydroxide ions and dissolved oxygen). The reactions consuming hydrogen peroxide have at least the first order kinetics in hydrogen peroxide. This creates the quasi-stationary conditions for the concentration of hydrogen peroxide, with the plateau concentration, $[H_2O_2]_{QS}$, depending only on the initial parameters of the system. In accord with this, addition of a surplus amount of H_2O_2 over $[H_2O_2]_{QS}$ leads to the restoration of a quasi-stationary value in the course of a photocatalytic reaction [11].

Sacrificial photocatalytic two-electron ORR on ZnO was reported for a wide set of reductants including formamide, acetamide, acetanilide and other amides [11], phenols [26, 29, 41], aliphatic alcohols [33, 35, 42, 43] and carboxylic acid salts [30, 38–40, 44]. The maximum H_2O_2 concentration achieved with pristine ZnO reaches 60 mM when isopropyl alcohol was used as a sacrificial donor [35].

In terms of the reaction mechanism, two principal schemes can be proposed for reactions with the addition of an oxidizable substrate. The first scheme implies the oxygen reduction (4.3) as anodic process and the oxidation of the sacrificial electron donor as cathodic process. Further transformations are individual for each substrate and can proceed both on the surface of the photocatalyst and in the solution. Most of the organic substrates are subsequently mineralized to CO_2, H_2O and N_2. The second scheme involves the oxidation of the substrate by hydroxyl radicals formed during the reduction of oxygen and the oxidation of water at the surface of the photocatalyst.

4.2.2 Titanium Dioxide

Titanium dioxide is an *i*-type semiconductor with a 3.24 eV band gap, which effectively absorbs light up to 400 nm [45] (Fig. 4.3). The advantages of titanium oxide as a photocatalyst are its high chemical and photochemical stability, as well as low dark catalytic activity with respect to the decomposition of hydrogen peroxide, unlike ZnO [46, 47].

The molecular mechanism of photocatalytic oxygen reduction on pristine TiO_2 is similar to that of ZnO. Molecular oxygen adsorbed on the catalyst surface is reduced at the catalyst surface upon photoexcitation of an electron from the valence band to the conduction band of TiO_2, the resulting superoxide particle then dismutates with the formation of hydrogen peroxide [48, 49]. In the absence of sacrificial donors, the holes in the valence band are quenched by the oxidation of hydroxide anions or water molecules to produce hydroxyl radicals.

The role of the electron donor is not limited to its function as a reductant. Some electron donors reduce the hydroxyl radicals formed in the above process, which prevents the surface passivation of the photocatalyst [48]. Others, known as redox mediators, such as formate ion, dimethylviologen dication or Cu^{2+} ions can facilitate electron transfer from the photocatalyst to the oxygen molecule, moving the process from the catalyst surface to the solution. The redox mediators may serve either as oxidation mediators for sacrificial donors, or as formate ion, as electron donors themselves [50].

Surface modification of TiO_2 is widely used to increase its photocatalytic activity in ORR by facilitating electron transfer, enhancing light absorption, increasing the catalyst stability or by suppressing the catalytic decomposition of hydrogen peroxide.

The success of these modifications requires careful optimization of the photocatalytic system. For example, fluorinated titania shows high $[H_2O_2]_{QS}$ in the presence of formate ions (7 mM), but with benzoate ions $[H_2O_2]_{QS}$ is much lower (0.035 mM) and exceeds that of pristine TiO_2 (0.07 mM) [50, 51]. Formate serves as a redox mediator, transporting an electron from the photocatalyst conduction band to dissolved oxygen, and acts as an effective hole suppressor for the valence band, inhibiting the oxidative photodecomposition of hydrogen peroxide. However, fluoride modification hinders the processes of electron transfer on the semiconductor surface for bulky electron donors, which is the reason for the decrease in performance observed in the case of benzoic acid [50].

The dopation of TiO_2 surface with Zn^{2+} inhibits the sorption of the radical and peroxide species, suppressing the unwanted side-processes [52]. More effective surface protection may be achieved with SnO_2 passivation coating [53].

A problem with the practical application of both TiO_2 and ZnO is their zero absorbance in the visible spectrum range. In case of TiO_2, this problem can be solved by dopation of the catalyst with nitrogen or sulfur atoms, which causes a redshift of ca. 100 nm of the absorbance edge [54]. When irradiated with blue light (λ_{max} 442 nm), both N- and S-doped catalyst exhibited non-sacrificial photocatalytic two-electron ORR activity and provided quasi-stationary peroxide concentration of

60 nM. An alternative way to enhance light absorbance is the surface modification with dyes, such as cobalt carboxylate [55] and phthalocyaninate [56]. The effect caused by the surface modification of titanium dioxide by Cu^{II} ions is more complex [57, 58]. On the one hand, due to the surface band gap narrowing, the material becomes active when irradiated with a wavelength of 450 nm. On the other hand, Cu^{2+} ions are reduced to Cu^{+} and Cu^{0} species, which serve as one- or two-electron redox mediators [58]. Titanium dioxide modified with copper ions is able to generate a quasi-stationary concentration of hydrogen peroxide 2.1 times greater than N-doped titanium dioxide under similar conditions. Surface modification of titanium dioxide by Rh^{III} ions causes a similar effect [59]. However, unlike copper ions, the main mechanism for the synthesis of hydrogen peroxide in this case is the two-electron reduction of oxygen by Rh^{I} particles. In addition, rhodium ions catalyze the oxidation of sacrificial electron donors on the surface of titanium dioxide. Direct two-electron ORR on TiO_2 can also be employed using 2-ethylanthraquinone as an "electron condenser" [60]. The name originates from the role of the anthraquinone compound, which undergoes two one-electron reductions followed by oxidation in a two-electron process. This approach allows hydrogen peroxide concentrations to reach up to 8.7 mM.

Nanoengineering of TiO_2-based photocatalysts leads to significant enhancement of its photocatalytic performance in ORR because the photocatalytic activity depends on the morphology of the photocatalyst particles [37, 45, 61]. Titanium dioxide exists in two modifications, anatase and rutile, with different photocatalytic activities. Anatase has been shown to produce greater quasi-stationary concentrations of hydrogen peroxide than rutile, and the mixed phase is superior in this respect to both modifications of pristine TiO_2 [62].

4.2.3 Other Inorganic Semiconductors

Other semiconductor oxides which demonstrate photocatalytic activity in two-electron ORR include Ga_2O_3, [41] Sb_2O_3 [63] and CuO [64]. Sb_2O_3 works in the UV-range (300 nm) and shows $[H_2O_2]_{QS}$ of 0.3 mM in non-sacrificial and 1 mM in sacrificial modes with glycerol as an electron donor [65]. CuO, due to the low band gap, absorbs light up to 660 nm, and exhibits a visible-light driven photocatalytic ORR. Unfortunately, due to the high catalytic activity of CuO for the decomposition of hydrogen peroxide, the achievable quasi-stationary concentration of H_2O_2 is relatively small [64]. The photocatalytic potential of Cu(II) is disclosed in combination with WO_3 as inert light harvesting matrix. When WO_3 is grafted with Cu^{2+} ions, which enable two-electron reduction of O_2, a high rate of H_2O_2 formation in the presence of acetaldehyde are observed upon illumination with 470 nm light. Low concentration of Cu^{2+} ions secures a negligible rate of H_2O_2 decomposition on WO_3/Cu^{2+} photocatalyst [57, 58].

In addition to metal oxides, a number of metal chalcogenides show photocatalytic activity in O_2 to H_2O_2 reduction. These compounds have often more narrow band

gap as compared to ZnO or TiO_2 and can operate in visual spectral range (e.g., see comparison of absorbance spectra for ZnO, TiO_2 and CdS in Fig. 4.3). For example, HgS shows catalytic activity at 600 nm providing up to 0.55 μM of H_2O_2 in a non-sacrificial mode [65]. Photocatalytic activity in a sacrificial mode at 365 nm with phenol as an electron donor has been tested for a wide set of chalcogenides, including ZnS, HgS, CdS, Ga_2S_3, CdSe, CdTe and ZnTe [41]. Within this series, CdS and CdSe exhibited the best performance, generating up to 1.7 and 1.0 mM of H_2O_2, respectively. Significant amounts of hydrogen peroxide above 0.3 mM were also detected in case of HgS and Ga_2S_3 [41].

4.2.4 *Inorganic Composite Photocatalysts*

The performance of the catalysts based on oxide or chalcogenide semiconductors relies on the construction of nanocomposites with a semiconductor-metal contact. Particles of noble metals such as platinum [66–69], gold [70–72] and binary Ag-Au alloys [73], when in contact with the oxide semiconductor, increase its photocatalytic activity and light efficiency. Photocatalysts of this type show quasi-stationary concentrations of hydrogen peroxide of up to 4.3 mM [68]. Particles of noble metals enhance the light efficiency due to plasmon resonance [74], catalyze one- and two-electron reductions of molecular oxygen [69] and increase the luminous efficiency and quantum yield of the charge separation process collecting the electrons from the semiconductor conduction band [71]. In some cases, nanoparticles of noble metal were shown to lead the oxygen reduction reaction exclusively to a two-electron reduction path [70] (Fig. 4.4). In addition, the modification of the semiconductor surface with noble metals prevents the accumulation of peroxide particles on the semiconductor surface due to inertness of the noble metal. This can also be the reason for the observed inhibition of the catalytic decomposition of H_2O_2 on catalyst particles by Ag-Au alloys [73]. Nanoensembles of TiO_2 with gold and platinum show enhanced

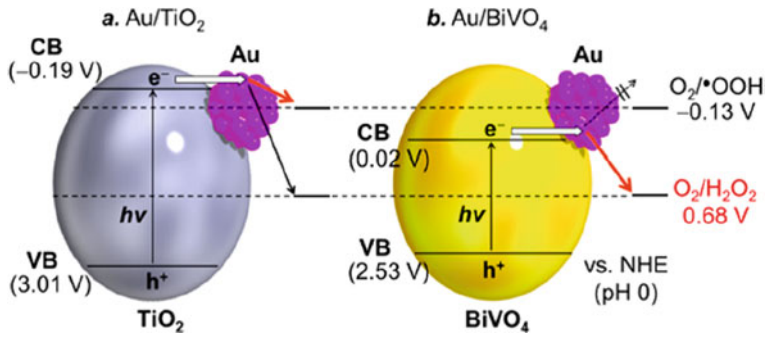

Fig. 4.4 Schematic representation of Au/TiO_2 and $Au/BiVO_4$ photocatalysts with energy diagram for photocatalysis. Adapted with permission from [70]. Copyright 2016 American Chemical Society

ORR photocatalytic performance, providing $[H_2O_2]_{QS}$ of 1.5 mM in a sacrificial mode [75, 76]. Only a subtle plasmonic resonance light utilization was observed in these cases, while the catalysis of charge transfer to O_2 is the main function of metal nanoparticles in such ensembles. The same effect is observed using polyoxymetallate covalent modification of TiO_2 surface [77]. ZnO photocatalyst may also be improved using the surface plasmon resonance of gold nanoparticles [74].

The second group of composite photocatalysts is a pair of semiconductors being in contact [78–86]. Such composites show an increase in luminous efficiency due to the electronic transitions now possible between the valence band of one semiconductor and the conduction band of another directly, or through the formation of an electron-hole pair in one semiconductor with the subsequent transition of an electron or hole to the other semiconductor. The main mechanism of such photocatalysis in most cases is photoelectrolysis, where the areas of electrode reactions are localized in different semiconductors.

The H_2O_2 formation rate on ZnO photocatalyst can be increased using this approach by dopation of ZnO with ruthenium oxide, which allows the harvesting of visible light up to 800 nm due to the narrow band gap between the conduction band of zinc oxide and the valence band of ruthenium oxide [87]. A similar effect is achieved with CdSe quantum dot sensitization [88]. Using $CoFe_2O_4$ spinel nanocrystals, double catalytic effect was achieved, improving both oxygen reduction and donor oxidation [89]. Recently, a great progress in the visible light harvesting of TiO_2 ORR photocatalysts was achieved by using nanostructured TiO_2 ensembles with quantum dots, which enhances the visible light absorption and facilitates charge separation due to Shottki effect [90]. Using highly structured TiO_2 particles, proton-form TiO_2 nanotubes modified with carbon quantum dots (Fig. 4.5), the millimolar concentrations of H_2O_2 may be achieved under 420 nm illumination [91]. WO_3-based heterojunction composites are also able to photocatalyze ORR. WO_3-melam particles exhibit high photocatalytic performance, producing up to 40 μM of H_2O_2 [92], as well as three-component composite particles, combining WO_3:TiO_2 heterojunction and WO_3:Pt surface modification.

Platinized Bi_2WO_6 [93], Bi_2O_3 surface-modified with Au nanoparticles [94] and mixed phase bismuth oxyhalides [95] also show the ORR photocatalytic performance with H_2O_2 concentrations up to 40 μM under 420–480 nm illumination. A sesame ball-like Ag_3PO_4@$CoFe_2O_4$ composite, irradiated with visible light, was found to produce up to 40 μM of H_2O_2 [96]. MoO_3/SnS_2 composite nanotubes deliver more than 120 μM of H_2O_2 under simulated sunlight [97]. The prominent photocatalytic ability was demonstrated by nanoporous-carbon supported Co_3O_4, which generates more than 1.5 mM of H_2O_2 under visible light [98]. An interesting example is composite particles, containing CdS spheres and graphene sheets modified with Pd^{II}-porphyrin and 9,10-ethynylphenylanthracene (Fig. 4.6), which provide up-conversion of photons in the red region of the spectrum and allow the use of light up to 650 nm, which increases the overall luminous efficiency of the system [83].

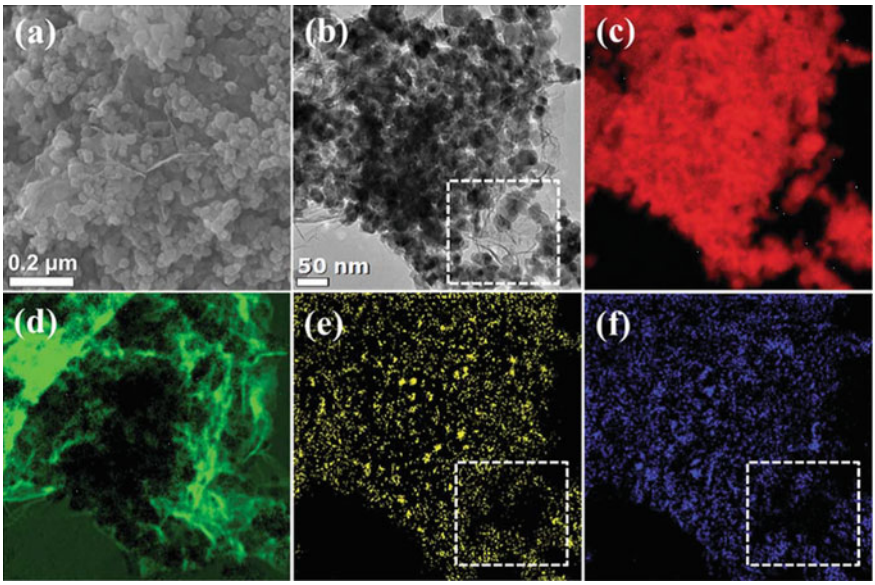

Fig. 4.5 **a** FE-SEM image and **b** TEM image of rGO/TiO_2 (including 6 wt% of rGO) after the irradiation for 3 h in the presence of cobalt and phosphate ions. **c–f** EELS mapping corresponding to panel (**b**). Red, green, yellow, and blue colour represent (**c**) titanium, (**d**) carbon, (**e**) phosphorus, and (**f**) cobalt element, respectively. Reprinted from [91], Copyright 2019, with permission from Elsevier

4.3 Carbon-Derived Photocatalysts

A broad spectrum of carbon-based materials and organic compounds demonstrates photocatalytic activity in two-electron oxygen reduction reaction. The solid state photocatalysts are presented by graphene oxide, carbon nitride and polyaromatic compounds. The molecular photocatalysts are presented mainly by anthracene, acridine and isoquinoline derivatives.

4.3.1 2D Carbon Materials

Graphene, the most simple in terms of molecular structure representative of 2D carbon materials, can enhance the photocatalytic performance of semiconductor solids similarly to nanoparticles of noble metals [99, 100]. Hybrid materials consisting of titanium oxide or cadmium sulfide in contact with graphene showed photocatalytic activity greater than the components of the materials taken separately.

Graphene oxide, which can be considered a surface O-modified graphene (Fig. 4.7), shows photocatalytic activity in two-electron oxygen reduction both as an individual component or in combination with semiconductor additives. The obtained

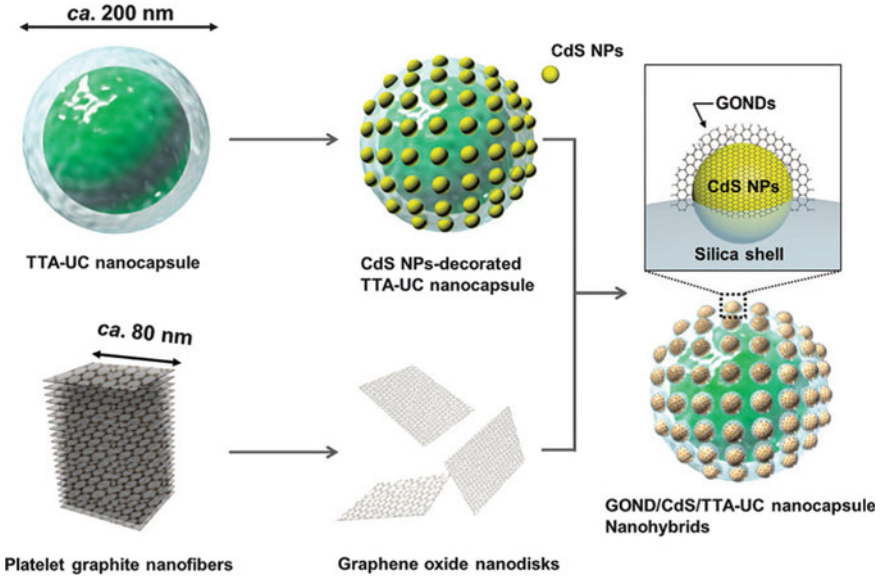

Fig. 4.6 Morphology of the composite up-conversion photocatalyst composed of CdS nanoparticles (NP) modified with graphene oxide nanodiscs (GOND). Republished with permission of The Royal Society of Chemistry from [83] Copyright 2016, permission conveyed through Copyright Clearance Center, Inc.

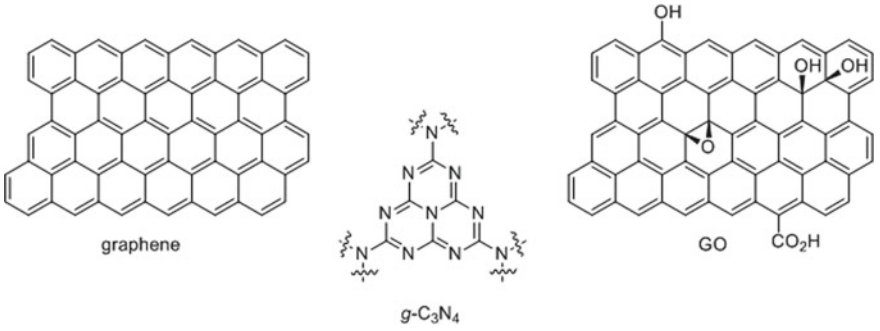

Fig. 4.7 2D carbon materials: graphene, graphene oxide (GO) and graphitic carbon nitride (g-C_3N_4)

maximum quasi-stationary concentrations of H_2O_2 comprised 1.5 mM in pure water, which could be increased to 4 mM when sacrificial reductants were used [101]. Further increase was achieved by modification of graphene oxide with cadmium polynuclear complexes, which afforded up to 7 mM of H_2O_2 under visible light irradiation [102].

Heteroatom-doped graphene quantum dots showed more modest performance as oxygen reduction catalysts, yielding up to 0.5 mM H_2O_2 concentrations [103].

The best performance within the family of carbon materials show graphitic carbon nitride photocatalysts extensively studied during the past few years [9, 104–107]. The g-C_3N_4 nanostructures (Fig. 4.7), modified with different inorganic and/or organic compounds, are able to produce millimolar quantities of H_2O_2 utilizing nearly the whole visible spectrum [108].

4.3.2 Polyaromatic Compounds

In addition to the classical inorganic semiconductors, organic and organometallic semiconductors are used for photocatalytic oxygen reduction. An important advantage of these catalysts is the possibility of fine tuning of their properties by modifying an organic molecule.

A series of p-type semiconductor cobalt, iron and zinc porphyrinates and phthalocyaninates **1**–**5** (Fig. 4.8) adsorbed on Nafion membranes was tested [109]. Irradiation of such membranes with visible light in the presence of triethylammonium perchlorate in the system leads to the formation of micromolar quasi-stationary concentrations of hydrogen peroxide on a μM scale. Better results demonstrated polythiophene with 0.1 mM H_2O_2 concentration in a non-sacrificial photocatalitic ORR.

An improved ORR photocatalytic behavior of n-type organic semiconductors was demonstrated using acene-based biscoumarins **6**-**8** (Fig. 4.8), which show the non-sacrificial H_2O_2 production under visible light with a rate up to 3.3 mg per 1 g of catalyst per 1 h [110]. Nearly the same non-sacrificial photocatalytic performance was observed using the resorcinol-formaldehyde resins as n-type semiconductors,

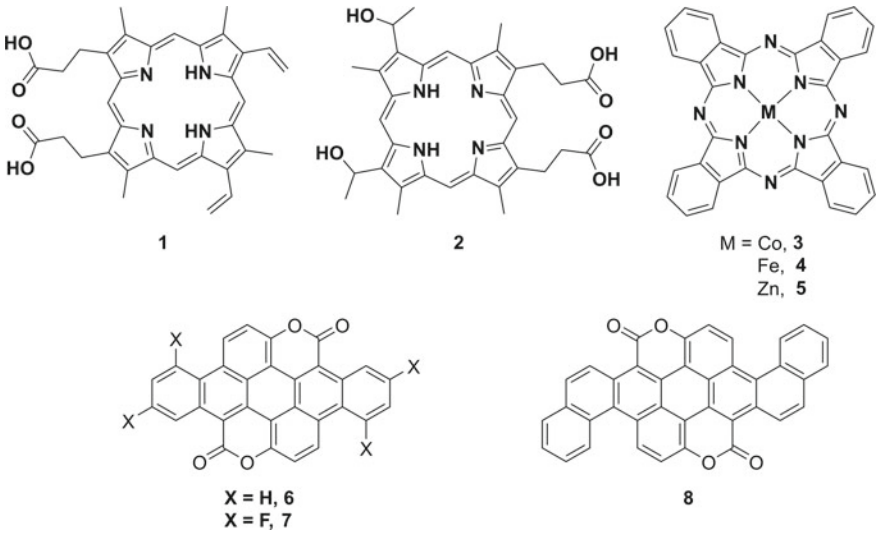

Fig. 4.8 Structure of organic semiconductors **1-8**

harvesting light up to 700 nm and producing more than 60 μM of hydrogen peroxide in water [111]. Another n-type semiconductor, perylene diimide, produced up to 3 mM hydrogen peroxide concentration with oxalate as a sacrificial electron donor [112]. Acetylene-extended triazine covalent frameworks afford up to 70 μM of H_2O_2 under the same operation conditions [113].

The semiconductive microcrystals of coordination polymer derived from Cd^{2+} and thiocyanuric acid is an interesting example of a metal complex semiconductor photocatalyst [114]. The maximum concentration of hydrogen peroxide achieved with the addition of methanol was 8.75 mM. The authors suggest a single-electron oxygen reduction mechanism.

4.3.3 *Metal Complexes with Organic Ligands as Homogeneous Photocatalysts*

Ru^{II} complexes with *N*,*N*-bidentate ligands based on bipyridyl fragment, like compounds **9** and **10** (Fig. 4.9) are well studied ORR photocatalysts with good performance [115–120]. For example, compound **9** was found to produce a hydrogen peroxide with concentration of 0.57 mM upon visible light illumination in the presence of ascorbic acid [116].

High chemical and photolytic stability, combined with a sufficiently long lifetime of the triplet excited state (600 ns) and absorption in the visible region of the spectrum (λ_{max} ~ 450 nm) make them convenient photocatalysts [121]. Kinetic studies revealed the one-electron oxygen reduction (4.2) to be the key step of Ru-photocatalyzed ORR [115]. Depending on the sacrificial donor, either dismutation (4.3) or the reduction of superoxide by sacrificial donor leads then to the formation of H_2O_2.

In order to increase the electron transfer rate from the photocatalyst to molecular oxygen, various redox mediators are widely used. The maximum concentration of hydrogen peroxide achieved using **9** as a photocatalyst and dimethyl viologen as redox mediator for one-electron oxygen reduction with the addition of formic acid was about 0.35 mM [118].

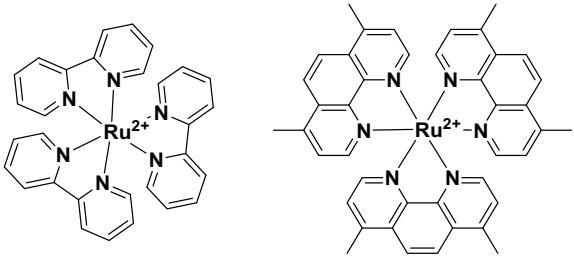

9 **10**

Fig. 4.9 Structures of Ru^{II} photocatalysts

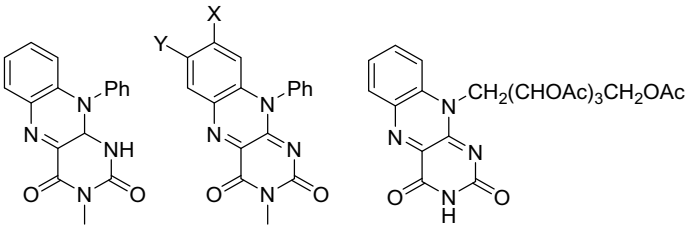

11 X = Y = H, **12**
X = Cl, Y = H, **13**
X = H, Y = NO_2, **14**
15

Fig. 4.10 Flavins **11-15**

An alternative way to enhance electron transfer is to stabilize the resulting product of one-electron O_2 reduction, the superoxide anion. Hence, ions of rare earth metals such as Sc^{3+}, Y^{3+}, Yb^{3+}, Lu^{3+} were found to co-catalyze photocatalytic ORR with ruthenium complexes by coordinating the reaction product, superoxide anion [122–125].

For non-sacrificial photocatalytic ORR, water oxidation usually represents a bottleneck of the process, which may be overcome using water oxidation catalysts. Polynuclear complex $Fe_3[Co(CN)_6]_2$ [122–124] as well as inorganic semiconductors $Ir(OH)_3$, WO_3 and $BiVO_4$ [122, 125] can enhance the Ru^{II} catalyzed ORR by mediating water oxidation. This approach allows to obtain a 0.4 mM quasi-stationary concentration of hydrogen peroxide without any oxidizable additives.

A combination of these approaches in a multicomponent system for nonsacrificial photocatalytical ORR, consisting of ruthenium-based ORR catalyst with Sc^{3+} as a co-catalyst and $NiFe_2O_4$ nanoparticle for simultaneous water oxidation, was reported to produce up to 1.4 mM H_2O_2 concentration [126].

Due to the high cost of ruthenium, cheaper alternatives are actively sought. An example can be zinc and magnesium complexes of flavins **11-14** (Fig. 4.10) or scandium and lanthanoide 2:1 complexes with flavin **15**, which also demonstrate photocatalytic activity in ORR. Under illumination with visible light, the complex of **11** with Mg^{2+} produces up to 2 mM concentration of H_2O_2 with benzylic alcohol as a sacrificial electron donor [127]. Within this series, the highest quasi-stationary concentration of hydrogen peroxide of 2.8 mM was achieved with **15**-Lu^{3+} as a photocatalyst and 4-methoxybenzyl alcohol as an oxidizable additive [128].

4.3.4 Anthraquinone Derivatives

The ability of anthraquinone to photochemically oxidize organic matter, combined with the well-known two-electron reduction of molecular oxygen by 2H-anthraquinone, inspired the application of anthraquinone derivatives in photocatalytical ORR.

In the presence of a sacrificial hydrogen donor like ethanol, anthraquinone was reported to be photoreduced to 2H-anthraquinone, which then reduces dioxygen in a two-electron reduction step similar to the dark process (Fig. 4.11). For example, a quasi-stationary concentration of hydrogen peroxide of ca. 360 mM was achieved with 2-ethylanthraquinone at exposure to simulated sunlight [129].

When no convenient hydrogen source is present, the photocatalytic process was described to proceed as one-electron oxidation of sacrificial donor followed by one-electron reduction of dioxygen (Fig. 4.11). In both cases the active form is the long-living triplet state of anthraquinone catalyst (ca. 10 μs), which either abstracts hydrogen atom from a hydrogen donor or mediates electron transfer from the reductant to dioxygen via radical anion species [130].

For practical applications, two-phase water/organic solvent systems are convenient, like water/ethyl acetate, water/toluene, water/xylene and water/mesitylene. In these systems, hydrogen peroxide formed during the reaction in the organic phase is extracted into the aqueous phase. The highest H_2O_2 concentration of 0.5 M was achieved within this series for water/mesitylene system [129].

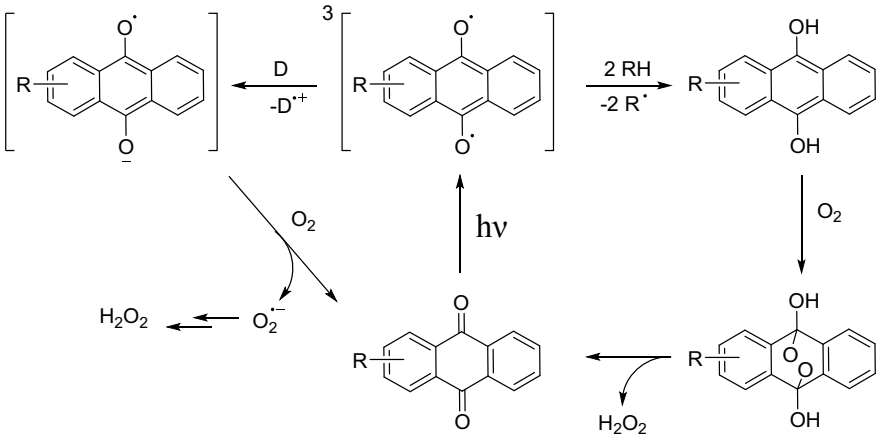

Fig. 4.11 Scheme of the photocatalytic production of hydrogen peroxide using anthraquinones

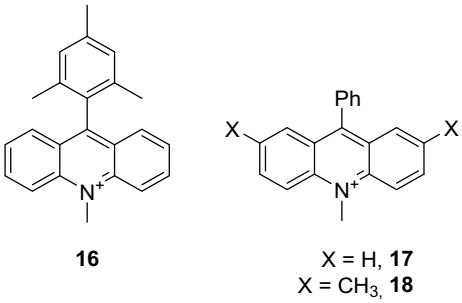

Fig. 4.12 Structures of the acridinium photocatalysts

4.3.5 Acridinium Photocatalysts

9-Aryl-10-methylacridinium derivatives (Fig. 4.12) are an interesting class of homogeneous photocatalysts, due to the long lifetime and high energy of the charge shifted state (2.37 eV for **16**) formed upon photoexcitation of these molecules [131].

The formation of hydrogen peroxide was observed as an oxygen reduction product with a yield close to quantitative in the process of photocatalytic oxidation of anthracene to anthraquinone with atmospheric oxygen catalyzed by **16** in acetonitrile upon irradiation at 430 nm [132]. The extract of coal tar, which consists mostly of anthracene, was proposed as a cheap oxidizable additive for the synthesis of hydrogen peroxide [133]. Irradiation of an aerated solution of coal tar extract and photocatalyst **16** in acetonitrile with light at 430 nm resulted in the formation of a 0.47 mM hydrogen peroxide solution. In these reactions, oxidation of the anthracene with charge separated state of **16** is the first step, followed by the electron transfer from the reduced photocatalyst to an oxygen molecule. The electron transfer from the semi-oxidized intermediate of anthracene, 10-hydroxyanthrone, leads to reduction of the superoxide to yield the hydrogen peroxide molecule, efficiently suppressing its dismutation. The formation of the hydrogen peroxide was also detected in photocatalytic oxidation of cyclohexane [134] and Fe^{II} [135] complexes with **16**.

Similar photocatalytic oxidation of methylbenzenes and benzylic alcohols to corresponding benzaldehydes with catalysts **16-18** leads to the formation of hydrogen peroxide, although the non-polarized singlet excited state is responsible for the process in case of **17** and **18** [136, 137].

The formation of the hydrogen peroxide was also detected in photocatalytic oxidation of cyclohexane and Fe^{II} complexes with **16** [134, 135].

4.3.6 Quinolinium Photocatalysts

Quinolinium (**19**-**22**) and isoquinolinium (**23**) compounds (Fig. 4.13) demonstrate both types of photoredox activity, through strongly oxidizing electronically excited singlet state and through charge-separated state.

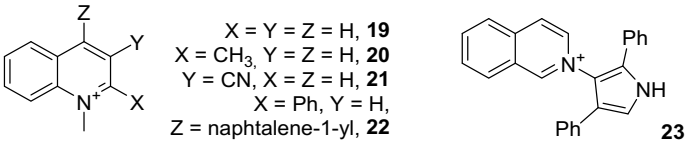

Fig. 4.13 Structures of (iso)quinolinium ORR photocatalysts

An example of the first type, compound **21**, has the first singlet excited state with oxidative potential of 2.72 V. This allows simultaneous H_2O_2 production and selective oxidative transformations of a wide range of organic sacrificial donors [138].

The photocatalytic activity of compound **21** in the acetonitrile-water-benzene system was investigated upon irradiation with light with a wavelength of 290–400 nm [138]. During the reaction, the $[H_2O_2]_{QS}$ of 15 mM was achieved, with phenol being the main oxidation product in 41% yield, 98% selectivity and 16% quantum yield. Catalysts **19**-**20** exhibit similar activity, but give lower yield and selectivity. The use of chlorobenzene instead of benzene as an oxidizable additive leads to the formation of a mixture of 4-chlorophenol and 2-chlorophenol in 27% and 3% yields with a selectivity of 31%. Along with hydrogen peroxide formation, an alkoxylation of arenes takes place, when an alcohol is used as a nucleophile instead of water [139]. Similarly, using fluoride ion as a nucleophile, fluorination of benzene can be achieved along with the formation of hydrogen peroxide [140]. The maximum concentration of hydrogen peroxide in this photocatalytic system reaches 8 mM. The reaction mechanism of ORR photocatalyzed by **21** in the presence of benzene includes preliminary one-electron oxidation of arene by the singlet excited state of **21** with subsequent one-electron transfer from the reduced catalyst to oxygen molecule. Nucleophilic addition to the resulting benzene radical-cation occurs, followed by radical quenching with oxygen molecule [138–140].

Compound **22** (Fig. 4.13) is an example of the second type of photocatalytic activity, which proceeds through the formation of the charge separated state. This molecule, due to the combination of donor and acceptor fragments, forms a charge transfer state with a lifetime of 500 fs upon photoexcitation [141]. In the photoredox catalytic cycle of oxygen reduction by oxalate ions in aqueous acetonitrile, the electronically excited **22** reduces the oxygen molecule and then the resulting dication-radical oxidizes the oxalate ion. Overall, the yield of peroxide on oxalate reaches 93% and the quantum yield is 14%. The oxalate is a prospective sacrificial electron donor as it is a by-product in wood industry and because it gives carbon dioxide as the only oxidation product.

Photocatalytic oxygen reduction by oxalate ions is sensitive to *p*H of the medium. A great enhancement of the H_2O_2 production was found with the addition of acetate ions, and the maximum concentration of hydrogen peroxide of 70 mM was reached in this case. The acetate ion was suggested to play the role of a proton transporter in acetonitrile, facilitating deprotonation of oxalic acid and protonation of a superoxide ion [142].

Compound **22** can be used also in water but in a heterogenous mode, when sorbed into a mesoporous silica-alumina sorbent [143]. The resulting composite catalyst gives a quasi-stationary concentration of hydrogen peroxide of 4 mM and a quantum yield of 10%.

Homogeneous photocatalytic ORR in aqueous solution was achieved with pyrrolo-isoquinolinium dyad **23** [144]. With this photocatalyst in an oxalate-containing aqueous solution illuminated with 420 nm light, a concentration of H_2O_2 exceeds 1 mM. The oxidation of the oxalate with the excited state of **20** was found to be the first step of the process, followed by the electron transfer to the oxygen molecule. Most probably, the active intermediate is the charge-separated state of **23**.

4.4 Conclusions

Starting from the middle of twentieth century, a wide range of classes of inorganic and organic materials were found to exhibit photocatalytic reduction of molecular oxygen to hydrogen peroxide. To improve photocatalytic ORR performance of semiconductor photocatalysts, several pathways have been formulated. To increase the luminous efficiency of the photocatalysts, the optical band gap may be narrowed by heterojunction with another semiconductors or quantum dots, or by introduction of ions or molecules which have discreet energy levels within the band gap of the semiconductor. Modification of semiconductor surface with noble metal particles enables an extensive visible light utilization via the surface plasmon resonance, while modification of semiconductor particles with dyes leads to its sensibilisation. ORR kinetics may be facilitated using surface-bound or dissolved redox mediators, for example, transition metal ions, or switched from unfavorable one-electron oxygen reduction to the two-electron process using “electron condensers”.

Alternative to inorganic semiconductors, carbon-based materials or organic compounds can be employed as photocatalysts for conversion of oxygen to hydrogen peroxide. These compounds bear fused aromatic or electron-poor heteroaromatic rings as a key structural motif. The mechanism of photocatalytic oxygen reduction using these compounds proceeds through an energy-rich electronically excited state of the catalyst, which can be of triplet or highly polarized singlet character.

References

1. R.S. Disselkamp, Energy Fuels **22**, 2771 (2008)
2. G. Goor, J. Glenneberg, S. Jacobi, J. Dadabhoy, E. Candido, *Ullmann’s Encyclopedia of Industrial Chemistry* (Wiley-VCH Verlag GmbH & Co. KGaA, 2019)
3. E. Baur, C. Neuweiler, Helv. Chim. Acta **10**, 901 (1927)
4. A.H. Mehler, Arch. Biochem. Biophys. **33**, 65 (1951)
5. S. Fukuzumi, Biochim. Biophys. Acta **1857**, 604 (2016)
6. S. Fukuzumi, Y.M. Lee, W. Nam, Chemistry **24**, 5016 (2018)

7. J. Highfield, Molecules **20**, 6739 (2015)
8. C. Wang, X. Zhang, Y. Liu, Appl. Surf. Sci. **358**, 28 (2015)
9. Z. Haider, H.-I. Cho, G.-H. Moon, H.-I. Kim, Catal. Today **335**, 55 (2019)
10. S.G. Bratsch, J. Phys. Chem. Ref. Data **18**, 1 (1989)
11. M.C. Markham, K.J. Laidler, J. Phys. Chem. **57**, 363 (1953)
12. S.B. Brown, P. Jones, A. Suggett, Anal. Chim. Acta **43**, 343 (1968)
13. T.C.J. Ovenston, W.T. Rees, Analyst **75**, 204 (1950)
14. W. Masschelein, M. Denis, R. Ledent, Water Sewage Works **124**, 69 (1977)
15. R.M. Sellers, Analyst **105**, 950 (1980)
16. M. Zhu, X. Huang, L. Liu, H. Shen, Talanta **44**, 1407 (1997)
17. A.N. Díaz, F.G. Sanchez, J.A.G. García, Anal. Chim. Acta **327**, 161 (1996)
18. W. Chen, S. Cai, Q.Q. Ren, W. Wen, Y.D. Zhao, Analyst **137**, 49 (2012)
19. A. Takahashi, K. Hashimoto, S. Kumazawa, T. Nakayama, Anal. Sci. **15**, 481 (1999)
20. S.M. Steinberg, Environ. Monit. Assess. **185**, 3749 (2013)
21. H.C. Hu, H.J. Jin, X.S. Chai, J. Chromatogr. A **1235**, 182 (2012)
22. S. Zhao, X. Zhao, Appl. Catal. B **250**, 408 (2019)
23. V. Stevanovic, S. Lany, D.S. Ginley, W. Tumas, A. Zunger, Phys. Chem. Chem. Phys. **16**, 3706 (2014)
24. J. Anderson, G.V.d.W. Chris, Rep. Prog. Phys. **72**, 126501 (2009)
25. C.F. Goodeve, Trans. Faraday Soc. **33**, 340 (1937)
26. X. Domènech, J.A. Ayllón, J. Peral, Environ. Sci. Pollut. Res. **8**, 285 (2001)
27. G. Winter, Nature **163**, 326 (1949)
28. Y. Liu, J. Han, W. Qiu, W. Gao, Appl. Surf. Sci. **263**, 389 (2012)
29. M.C. Markham, M.C. Hannan, S.W. Evans, J. Am. Chem. Soc. **76**, 820 (1954)
30. C.B. Vail, J.P. Holmquist, L. White, J. Am. Chem. Soc. **76**, 624 (1954)
31. J.C. Young, E.P. Guth, J. Am. Pharm. Assoc. **45**, 724 (1956)
32. M.C. Markham, J.C. Kuriacose, J. DeMarco, C. Giaquinto, J. Phys. Chem. **66**, 932 (1962)
33. C. Kormann, D.W. Bahnemann, M.R. Hoffmann, Environ. Sci. Technol. **22**, 798 (1988)
34. E.R. Carraway, A.J. Hoffman, M.R. Hoffmann, Environ. Sci. Technol. **28**, 786 (1994)
35. J.C. Kuriacose, M.C. Markham, J. Catal. **1**, 498 (1962)
36. M.A. Gondal, A.M. Ilyas, T.A. Fasasi, M.A. Dastageer, Z.S. Seddigi, T.F. Qahtan, M. Faiz, G.D. Khattak, Appl. Surf. Sci. **357**, 2217–2222 (2015)
37. B. Pal, M. Sharon, Toxicol. Environ. Chem. **78**, 233 (2000)
38. J.G. Calvert, K. Theurer, G.T. Rankin, W.M. MacNevin, J. Am. Chem. Soc. **76**, 2575 (1954)
39. D. Dixon, T. Healy, Aust. J. Chem. **24**, 1193 (1971)
40. J.R. Harbour, M.L. Hair, J. Phys. Chem. **83**, 652 (1979)
41. R.E. Stephens, B. Ke, D. Trivich, J. Phys. Chem. **59**, 966 (1955)
42. M.C. Markham, M.C. Upreti, J. Catal. **4**, 229 (1965)
43. G. Irick, J. Appl. Polym. Sci. **16**, 2387 (1972)
44. T.R. Rubin, J.G. Calvert, G.T. Rankin, W. MacNevin, J. Am. Chem. Soc. **75**, 2850 (1953)
45. A.L. Linsebigler, G. Lu, J.T. Yates, Chem. Rev. **95**, 735 (1995)
46. C.M. Lousada, A.J. Johansson, T. Brinck, M. Jonsson, J. Phys. Chem. C **116**, 9533 (2012)
47. B. Jenny, P. Pichat, Langmuir **7**, 947 (1991)
48. V. Diesen, M. Jonsson, J. Phys. Chem. C **118**, 10083 (2014)
49. T. Hirakawa, H. Kominami, B. Ohtani, Y. Nosaka, J. Phys. Chem. B **105**, 6993 (2001)
50. M. Mrowetz, E. Selli, New J. Chem. **30**, 108 (2006)
51. V. Maurino, C. Minero, G. Mariella, E. Pelizzetti, Chem. Commun. **20**, 2627 (2005)
52. V. Maurino, C. Minero, E. Pelizzetti, G. Mariella, A. Arbezzano, F. Rubertelli, Res. Chem. Intermed. **33**, 319 (2007)
53. G. Zuo, B. Li, Z. Guo, L. Wang, F. Yang, W. Hou, S. Zhang, P. Zong, S. Liu, X. Meng, Y. Du, T. Wang, V.A.L. Roy, Catalysts **9**, 623 (2019)
54. T. Hirakawa, Y. Nosaka, J. Phys. Chem. C **112**, 15818 (2008)
55. T. Baran, S. Wojtyła, A. Minguzzi, S. Rondinini, A. Vertova, Appl. Catal. B **244**, 303 (2019)
56. A.P. Hong, D.W. Bahnemann, M.R. Hoffmann, J. Phys. Chem. **91**, 2109 (1987)

57. H. Irie, S. Miura, K. Kamiya, K. Hashimoto, Chem. Phys. Lett. **457**, 202 (2008)
58. Y. Nosaka, S. Takahashi, H. Sakamoto, A.Y. Nosaka, J. Phys. Chem. C **115**, 21283 (2011)
59. S. Kitano, N. Murakami, T. Ohno, Y. Mitani, Y. Nosaka, H. Asakura, K. Teramura, T. Tanaka, H. Tada, K. Hashimoto, H. Kominami, J. Phys. Chem. C **117**, 11008 (2013)
60. D. Zhang, G. Xu, T. Chen, F. Chen, RSC Adv. **4**, 52199 (2014)
61. F. Shiraishi, C. Kawanishi, J. Phys. Chem. A **108**, 10491 (2004)
62. H. Goto, Y. Hanada, T. Ohno, M. Matsumura, J. Catal. **225**, 223 (2004)
63. M.C. Markham, M.C. Hannan, L. Lin, C. Coffey, B. Jones, J. Phys. Chem. **62**, 989 (1958)
64. J. Bandara, I. Guasaquillo, P. Bowen, L. Soare, W.F. Jardim, J. Kiwi, Langmuir **21**, 8554 (2005)
65. L.I. Grossweiner, J. Phys. Chem. **59**, 742 (1955)
66. W. Zhao, C. Chen, X. Li, J. Zhao, H. Hidaka, N. Serpone, J. Phys. Chem. B **106**, 5022 (2002)
67. F. Shiraishi, T. Nakasako, Z. Hua, J. Phys. Chem. A **107**, 11072 (2003)
68. M. Teranishi, S.-I. Naya, H. Tada, J. Am. Chem. Soc. **132**, 7850 (2010)
69. V.M. Daskalaki, P. Panagiotopoulou, D.I. Kondarides, Chem. Eng. J. **170**, 433 (2011)
70. H. Hirakawa, S. Shiota, Y. Shiraishi, H. Sakamoto, S. Ichikawa, T. Hirai, ACS Catal. **6**, 4976 (2016)
71. M. Teranishi, R. Hoshino, S.-I. Naya, H. Tada, Angew. Chem. Int. Ed. **55**, 12773 (2016)
72. M. Teranishi, S.-I. Naya, H. Tada, J. Phys. Chem. C **120**, 1083 (2016)
73. D. Tsukamoto, A. Shiro, Y. Shiraishi, Y. Sugano, S. Ichikawa, S. Tanaka, T. Hirai, ACS Catal. **2**, 599 (2012)
74. X. Meng, P. Zong, L. Wang, F. Yang, W. Hou, S. Zhang, B. Li, Z. Guo, S. Liu, G. Zuo, Y. Du, T. Wang, V.A.L. Roy, Catal. Commun. **134**, 105860 (2020)
75. M.V. Dozzi, L. Prati, P. Canton, E. Selli, Phys. Chem. Chem. Phys. **11**, 7171 (2009)
76. K. Kim, J. Park, H. Kim, G.Y. Jung, M.-G. Kim, ACS Catal. **9**, 9206 (2019)
77. X. Wu, X. Zhang, S. Zhao, Y. Gong, R. Djellabi, S. Lin, X. Zhao, Appl. Catal. A **591**, 117271 (2020)
78. H. Chen, W. Leng, Y. Xu, J. Phys. Chem. C **118**, 9982 (2014)
79. C. Wang, X. Zhang, B. Yuan, Y. Wang, P. Sun, D. Wang, Y. Wei, Y. Liu, Chem. Eng. J. **237**, 29 (2014)
80. X. Zong, H. Chen, B. Seger, T. Pedersen, M.S. Dargusch, E.W. McFarland, C. Li, L. Wang, Energy Environ. Sci. **7**, 3347 (2014)
81. K. Fuku, K. Sayama, Chem. Commun. **52**, 5406 (2016)
82. M. Jakešová, D.H. Apaydin, M. Sytnyk, K. Oppelt, W. Heiss, N.S. Sariciftci, E.D. Głowacki, Adv. Funct. Mater. **26**, 5248 (2016)
83. H.-I. Kim, O.S. Kwon, S. Kim, W. Choi, J.-H. Kim, Energy Environ. Sci. **9**, 1063 (2016)
84. K. Mase, M. Yoneda, Y. Yamada, S. Fukuzumi, ACS Energy Lett. **1**, 913 (2016)
85. O. Tomita, T. Otsubo, M. Higashi, B. Ohtani, R. Abe, ACS Catal. **6**, 1134 (2016)
86. T. Fukumura, S. Akane, E. Sambandan, React. Kinet. Mech. Catal. **121**, 785 (2017)
87. J.Z. Bloh, R. Dillert, D.W. Bahnemann, Phys. Chem. Chem. Phys. **16**, 5833 (2014)
88. F. Donat, S. Corbel, H. Alem, S. Pontvianne, L. Balan, G. Medjahdi, R. Schneider, Beilstein J. Nanotechnol. **8**, 1080 (2017)
89. M. Chen, Y. Xu, Langmuir **35**, 9334 (2019)
90. P. Wang, D. Li, J. Chen, X. Zhang, J. Xian, X. Yang, X. Zheng, X. Li, Y. Shao, Appl. Catal. B **160–161**, 217 (2014)
91. R. Ma, L. Wang, H. Wang, Z. Liu, M. Xing, L. Zhu, X. Meng, F.-S. Xiao, Appl. Catal. B **244**, 594 (2019)
92. Z. Jin, Q. Zhang, L. Hu, J. Chen, X. Cheng, Y.-J. Zeng, S. Ruan, T. Ohno, Appl. Catal. B **205**, 569 (2017)
93. J. Sheng, X. Li, Y. Xu, ACS Catal. **4**, 732 (2014)
94. H.Y. Jiang, K. Cheng, J. Lin, Phys. Chem. Chem. Phys. **14**, 12114 (2012)
95. G. Liu, T. Wang, S. Ouyang, L. Liu, H. Jiang, Q. Yu, T. Kako, J. Ye, J. Mater. Chem. A **3**, 8123 (2015)

96. S. Huang, Y. Xu, Q. Liu, T. Zhou, Y. Zhao, L. Jing, H. Xu, H. Li, Appl. Catal. B **218**, 174 (2017)
97. Y. Zhang, S.-J. Park, J. Mater. Chem. A **6**, 20304 (2018)
98. C. Zhu, M. Zhu, Y. Sun, Y. Zhou, J. Gao, H. Huang, Y. Liu, Z. Kang, ACS Appl. Energy Mater. **2**, 8737 (2019)
99. G.-H. Moon, W. Kim, A.D. Bokare, N.-E. Sung, W. Choi, Energy Environ. Sci. **7**, 4023 (2014)
100. S. Thakur, T. Kshetri, N.H. Kim, J.H. Lee, J. Catal. **345**, 78 (2017)
101. W.-C. Hou, Y.-S. Wang, ACS Sustain. Chem. Eng. **5**, 2994 (2017)
102. J. Xu, Z. Chen, H. Zhang, G. Lin, H. Lin, X. Wang, J. Long, Sci. Bull. **62**, 610 (2017)
103. L. Zheng, H. Su, J. Zhang, L.S. Walekar, H. Vafaei Molamahmood, B. Zhou, M. Long, Y.H. Hu, Appl. Catal. B **239**, 475 (2018)
104. Y. Shiraishi, S. Kanazawa, Y. Sugano, D. Tsukamoto, H. Sakamoto, S. Ichikawa, T. Hirai, ACS Catal. **4**, 774 (2014)
105. Y. Shiraishi, Y. Kofuji, H. Sakamoto, S. Tanaka, S. Ichikawa, T. Hirai, ACS Catal. **5**, 3058 (2015)
106. Y. Kofuji, S. Ohkita, Y. Shiraishi, H. Sakamoto, S. Tanaka, S. Ichikawa, T. Hirai, ACS Catal. **6**, 7021 (2016)
107. S. Li, G. Dong, R. Hailili, L. Yang, Y. Li, F. Wang, Y. Zeng, C. Wang, Appl. Catal. B **190**, 26 (2016)
108. L. Zhou, J. Feng, B. Qiu, Y. Zhou, J. Lei, M. Xing, L. Wang, Y. Zhou, Y. Liu, J. Zhang, Appl. Catal. B **267** (2020)
109. J. Premkumar, R. Ramaraj, J. Mol. Catal. A: Chem. **142**, 153 (1999)
110. M.K. Węcławski, M. Jakešová, M. Charyton, N. Demitri, B. Koszarna, K. Oppelt, S. Sariciftci, D.T. Gryko, E.D. Głowacki, J. Mater. Chem. A **5**, 20780 (2017)
111. Y. Shiraishi, T. Takii, T. Hagi, S. Mori, Y. Kofuji, Y. Kitagawa, S. Tanaka, S. Ichikawa, T. Hirai, Nat. Mater. **18**, 985 (2019)
112. M. Gryszel, M. Sytnyk, M. Jakesova, G. Romanazzi, R. Gabrielsson, W. Heiss, E.D. Glowacki, ACS Appl. Mater. Interfaces **10**, 13253 (2018)
113. L. Chen, L. Wang, Y. Wan, Y. Zhang, Z. Qi, X. Wu, H. Xu, Adv. Mater. **32**, e1904433 (2020)
114. H. Zhuang, L. Yang, J. Xu, F. Li, Z. Zhang, H. Lin, J. Long, X. Wang, Sci. Rep. **5**, 16947 (2015)
115. Y. Kurimura, R. Onimura, Inorg. Chem. **19**, 3516 (1980)
116. K. Yoshimi, Y. Hiroshi, M. Yuko, Bull. Chem. Soc. Jpn. **54**, 2450 (1981)
117. Y. Kurimura, M. Nagashima, K. Takato, E. Tsuchida, M. Kaneko, A. Yamada, J. Phys. Chem. **86**, 2432 (1982)
118. M. Fukushima, K. Tatsumi, S. Tanaka, H. Nakamura, Environ. Sci. Technol. **32**, 3948 (1998)
119. A. Das, V. Joshi, D. Kotkar, V.S. Pathak, V. Swayambunathan, P.V. Kamat, P.K. Ghosh, J. Phys. Chem. A **105**, 6945 (2001)
120. J. Premkumar, R. Ramaraj, J. Chem. Soc. Dalton Trans., 3667 (1998)
121. C.-T. Lin, N. Sutin, J. Phys. Chem. **80**, 97 (1976)
122. S. Kato, J. Jung, T. Suenobu, S. Fukuzumi, Energy Environ. Sci. **6**, 3756 (2013)
123. Y. Isaka, K. Oyama, Y. Yamada, T. Suenobu, S. Fukuzumi, Catal. Sci. Technol. **6**, 681 (2016)
124. J.W. Han, J. Jung, Y.-M. Lee, W. Nam, S. Fukuzumi, Chem. Sci. **8**, 7119 (2017)
125. Y. Isaka, Y. Yamada, T. Suenobu, T. Nakagawa, S. Fukuzumi, RSC Adv. **6**, 42041 (2016)
126. Y. Isaka, S. Kato, D. Hong, T. Suenobu, Y. Yamada, S. Fukuzumi, J. Mater. Chem. A **3**, 12404 (2015)
127. S. Fukuzumi, S. Kuroda, T. Tanaka, J. Am. Chem. Soc. **107**, 3020 (1985)
128. S. Fukuzumi, K. Yasui, T. Suenobu, K. Ohkubo, M. Fujitsuka, O. Ito, J. Phys. Chem. A **105**, 10501 (2001)
129. G. Xu, Y. Liang, F. Chen, J. Mol. Catal. A: Chem. **420**, 66 (2016)
130. H. Gorner, Photochem. Photobiol. Sci. **5**, 1052 (2006)
131. S. Fukuzumi, H. Kotani, K. Ohkubo, S. Ogo, N.V. Tkachenko, H. Lemmetyinen, J. Am. Chem. Soc. **126**, 1600 (2004)
132. H. Kotani, K. Ohkubo, S. Fukuzumi, J. Am. Chem. Soc. **126**, 15999 (2004)

133. H. Kotani, K. Ohkubo, S. Fukuzumi, Appl. Catal. B **77**, 317 (2008)
134. K. Ohkubo, A. Fujimoto, S. Fukuzumi, Chem. Commun. **47**, 8515 (2011)
135. T. Tsudaka, K. Ohkubo, S. Fukuzumi, Chem. Commun. **52**, 6178 (2016)
136. K. Ohkubo, K. Suga, S. Fukuzumi, Chem. Commun. **19**, 2018 (2006)
137. K. Ohkubo, K. Mizushima, R. Iwata, K. Souma, N. Suzuki, S. Fukuzumi, Chem. Commun. **46**, 601 (2010)
138. K. Ohkubo, T. Kobayashi, S. Fukuzumi, Angew. Chem. Int. Ed. **50**, 8652 (2011)
139. K. Ohkubo, T. Kobayashi, S. Fukuzumi, Opt. Express **20**, A360 (2012)
140. K. Ohkubo, A. Fujimoto, S. Fukuzumi, J. Phys. Chem. A **117**, 10719 (2013)
141. H. Kotani, K. Ohkubo, S. Fukuzumi, Faraday Discuss. **155**, 89 (2012)
142. Y. Yamada, A. Nomura, T. Miyahigashi, K. Ohkubo, S. Fukuzumi, J. Phys. Chem. A **117**, 3751 (2013)
143. Y. Yamada, A. Nomura, K. Ohkubo, T. Suenobu, S. Fukuzumi, Chem. Commun. **49**, 5132 (2013)
144. D.A. Lukyanov, L.D. Funt, A.S. Konev, A.V. Povolotskiy, A.A. Vereshchagin, O.V. Levin, A.F. Khlebnikov, Photochem. Photobiol. Sci. **18**, 1982 (2019)

Chapter 5
Rare Earth Ion Based Luminescence Thermometry

Ilya Kolesnikov and Alina Manshina

Abstract In this chapter, the contactless thermal sensors based on luminescence properties of rare earth-doped nanocrystalline phosphors are discussed. The luminescence thermometry is considered nowadays as a remote and noninvasive approach providing excellent functional parameters—high thermal sensitivity and spatial resolution, wide working temperature range and short response times. The competitive advantage of the luminescence thermometry is its applicability in specific environmental conditions like external electromagnetic field, fast-moving objects, flows and fluids of different nature. The key functional characteristics of temperature sensors are described in the chapter together with different strategies of temperature readout including variants of ratiometric approach via thermally coupled levels, Stark sublevels, spectral line position, and bandwidth and lifetime thermometry. Further progress in this direction includes stimulated market demands and industrial development of micro- and nanoelectronics, photonics, nanomedicine, micro- and nanofluidics, as well as academic interest and scientific challenge in the improvement of current intrinsic limitations. The presented analysis of emerging new directions in the field of luminescence thermometry testifies an interest in widening the working spectral range, development of multi-sensing devices based on multiple emission centers, etc. All these open fascinating prospects of luminescence thermometry in the future and development of even newer fields such as multimodal imaging with temperature monitoring, 3D temperature mapping, and temperature-supervised processes.

I. Kolesnikov (✉) · A. Manshina
Saint Petersburg State University, Saint Petersburg, Russia
e-mail: ilya.kolesnikov@spbu.ru

A. Manshina
e-mail: a.manshina@spbu.ru

K. Yamanouchi et al. (eds.), *Progress in Photon Science*, Springer Series in Chemical Physics 125, https://doi.org/10.1007/978-3-030-77646-6_5

5.1 Introduction

Temperature is one of the fundamental parameters characterizing systems, processes, and phenomena. The notion of temperature is well established from the viewpoint of thermodynamics and used for characterization of various systems (gas, liquid, solid phases, micro and macro objects) in thermodynamic equilibrium. The accurate temperature measurement is necessary for the reliable characterization and control of processes in various fields from biology and medicine to industrial production.

Direct determination of temperature is impossible, but it can be measured via control of various characteristics of bodies such as volume, pressure, conductivity, etc. that are monotonically correlated with temperature change. For convenience, the measurement methods can be classified into three categories, depending on the nature of contact which exists between the sensor and the object of analysis [1]:

- Invasive. The monitoring device is in direct contact with the medium of interest (thermistor- or thermocouple-based technologies).
- Semiinvasive. The medium of interest is treated in some manner to enable remote observation (imaging of thermally sensitive paints).
- Noninvasive. The medium of interest is observed remotely (infrared and luminescence thermography).

Traditional contact thermometers, such as liquid-filled and bimetallic thermometers, thermocouples, pyrometers, and thermistors, are generally not suitable for temperature measurements at scales below 10 μm [2–6]. Moreover, contact measurements require, in general, conductive heat transfer and thus need to reach equilibrium between the sensor and the object. This thermal connection disturbs the temperature of the sample during the measurement, especially for small systems (in which the size is small compared to that of the sensor head) [5].

The rapid technological progress and limitations of contact thermometers for small systems where the spatial resolution decreases to the submicron scale have required the development of new noncontact (semi-invasive and noninvasive) accurate thermometers with micrometric and nanometric spatial resolution [3–5, 7].

Among noninvasive spectroscopic methods for determining temperature, the luminescence thermometry is one of the most promising and accurate techniques. This method provides temperature measurements based on the monitoring of phosphor emission temperature dependence, for example, luminescence intensity (or luminescence intensity ratio, LIR, spectral line position, bandwidth, and excited state lifetime). Luminescence thermometry combines high relative thermal sensitivity ($> 1\%\ K^{-1}$) and spatial resolution (< 10 μm) in short acquisition times (<1 ms), and, as it operates remotely, works even in biological fluids, fast-moving objects, and strong electromagnetic fields [3–5]. Phosphors of different nature have been utilized as contactless thermal sensors through their light emission properties, e.g., polymers [8, 9], DNA or protein conjugated systems [10], organic dyes [11, 12], quantum dots (QDs) [13, 14] transition metals-based materials [15, 16] and rare earth-doped phosphors [17–20].

Rare earth-doped materials are stable and narrow band emitters covering the entire electromagnetic spectrum with, in general, high emission quantum yields (> 50% in the visible range) [21–23]. In the last decade, many of these thermometers have been reported covering a wide temperature range, from cryogenic (T < 100 K) to technological (up to 1200 K) values, and including chelate complexes [24], metal organic frameworks [25, 26], polymers [27], organic–inorganic hybrids [28], and inorganic nanoparticles (NPs) [29–31].

This review focuses primarily on examples of recent successful applications of different temperature dependent luminescence parameters for rare earth-doped inorganic micro and nanoparticles and analysis of future trends in the field of luminescence thermometry.

5.2 Temperature Sensor Performance and Characteristics

For reliable and reproducible temperature monitoring, temperature sensors should be chemically and thermally stable. This is a general requirement to a sensor as a device. As for the estimation of the temperature sensor performance and the comparison of different luminescence thermometers, the following parameters are used:

- thermal sensitivity;
- temperature resolution;
- repeatability and reproducibility.

Absolute (S_a) and relative (S_r) thermal sensitivities are the most common characteristics. The absolute thermal sensitivity shows the absolute change of chosen thermometric parameter with temperature variation and is defined as follows:

$$S_a = \frac{d\Lambda}{dT} \tag{5.1}$$

It is obvious from (5.1) that S_a depends on the absolute Λ value, which can be significantly changed by manipulating the calculation procedure. Therefore, absolute thermal sensitivity cannot be used for fair comparison among different thermometry systems (e.g. mechanical or electrical thermometers) [3]. To compare thermometers irrespective to their nature and sensing parameter, the relative thermal sensitivity is introduced. S_r shows normalized change of chosen thermometric parameter with temperature variation and is defined as follows:

$$S_r = \frac{1}{\Lambda}\frac{d\Lambda}{dT} \tag{5.2}$$

Another important thermometric parameter is the temperature resolution, which provides information about accuracy of thermal sensing that can be derived using this

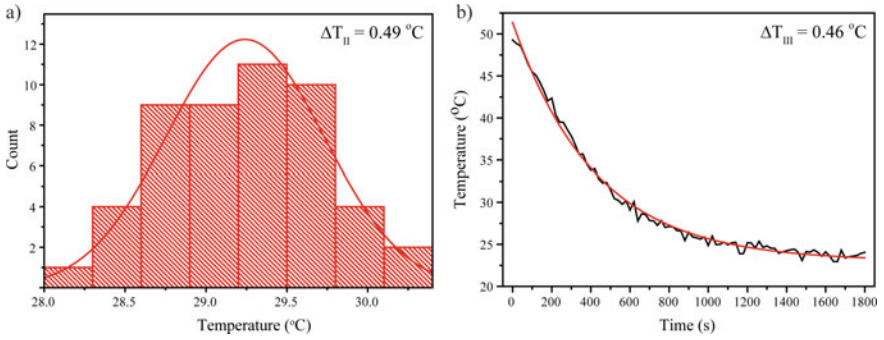

Fig. 5.1 Temperature resolution of YVO_4:Nd^{3+} 3 at.% obtained from **a** acquisition of several consecutive emission spectra at a fixed temperature (ΔT_{II}) and **b** analysis of the thermal relaxation process (ΔT_{III}) [32]

material. There are several experimental techniques to obtain the temperature resolution, which were discussed and compared in our previous work [32]. The temperature resolution can be calculated from calibration curve ($\Delta T_I = \frac{1}{S_r}\frac{\delta\Lambda}{\Lambda}$), from acquisition of several consecutive emission spectra at a fixed temperature (ΔT_{II}), and from the analysis of the thermal relaxation process (ΔT_{III}). It was found that the temperature resolution obtained from abovementioned independent methods gives similar values. For example, temperature resolutions of YVO_4:Nd^{3+} 3 at.% thermometer were determined as follows: $\Delta T_I = 0.72$ °C, $\Delta T_{II} = 0.49$ °C, $\Delta T_{III} = 0.46$ °C (Fig. 5.1) [32].

One interesting strategy to quantify the minimum temperature uncertainty of the thermometer was reported by Alicki and Leitner, in which the spin-boson model was applied and size and system dependent properties were used [33]. For solid-state nanothermometers, the relative fluctuation in temperature is linked to the number of atoms in the sample (N) and its Debye temperature (T_D):

$$\Delta T = \left(\frac{4T}{3\sqrt{3}T_D} e^{\frac{3T_D}{8T}}\right)\frac{1}{\sqrt{N}}T \tag{5.3}$$

For T_D in the range 100–2000 K, the term in parenthesis changes between 0.9 and 1.3, meaning that the order of magnitude of the temperature resolution is determined by $\Delta T = \frac{T}{\sqrt{N}}$ [33], which means that the minimum achievable ΔT is fundamentally controlled by the size of the thermal sensor. In quantum metrology, it is known that for nonentangled particles, the precision $\delta\theta$ of a general quantity θ scales with the inverse of the number of particles (N_P) $\delta\theta = \frac{1}{\sqrt{N_P}}$ [34], a relation called shot-noise scaling (for entangled states, however, Heisenberg-scaling applies and $\delta\theta$ is inversely proportional to N_P). As N_P is proportional to N, the last formula supports the result of the model derived by Alicki and Leitner [33]. There are very few examples reporting the thermal resolution of luminescent thermometers as a function of its size. One case is Alaulamie's work [35] that examined experimentally the correlation between

particle size and the temperature resolution based on the temperature readouts of Er^{3+}-doped up-conversion nanoparticle clusters of different sizes (ranging from 1 to 9 μm). Briefly, the larger the cluster size the higher the signal-to-noise ratio, leading to better temperature resolution (low standard deviation value). The experimental data present an unequivocal increase of the temperature uncertainty as the cluster size decreases according to presented equations.

Thermal sensitivity and *temperature resolution* are important parameters, which take into account both the potential of the temperature probes and the limitation of the experimental setup; it is still possible that other factors contribute to a lower temperature accuracy, such as systematic errors. Repeatability and reproducibility are the two components of precision in a measurement system, and are the major concerns in sensor engineering. Since the great majority of industrial and scientific applications require continuous monitoring, it is critical to achieve the same response under the same external stimulus.

Repeatability refers to the variation in repeat measurements made under identical conditions. A given quantity is considered repeatable if different measurements made using the same instrument or method, over a certain period, give the same results. Variability in measurements made on the same subject in a repeatability study can then be ascribed only to errors due to the measurement process itself [36].

Reproducibility, on the other hand, refers to the variation in measurements of the same measurand carried out under modified conditions [37]. The changing conditions may be due to different measurement methods or instruments being used, measurements being made by different observers, or measurements being made over a period of time within which the "error-free" level of the measurand could undergo nonnegligible change [36].

The repeatability of a thermometric probe indicates the accord between its ability to evaluate the temperature in comparison with a reference temperature probe (a thermocouple, for instance). An acceptable repeatability coefficient can be obtained when the deviation relative to the average measured temperature is lower than double standard deviation of the data. This criterion ensures that, for stochastic processes, 95% of the measurements are less than two standard deviations away from the mean value of temperature.

In a typical procedure, the repeatability of a thermal probe is estimated by cycling the temperature in a given interval, ensuring that each measurement is performed with the probe in thermal equilibrium with the temperature controller. The repeatability of a thermometer's readout upon temperature cycling can be quantified using the expression:

$$R = 1 - \frac{\max(\Delta_c - \Delta_i)}{\Delta_c} \tag{5.4}$$

where Δ_c and Δ_i represent, respectively, the thermometric parameter's mean value and the thermometric parameter measured at each temperature.

Another key feature of the thermometer readout is the ability to reproduce the same results, even when different detectors are employed or the measurements are made in

different ways. Although the reproducibility of a thermometer cannot be numerically quantified, statistical analysis may be used if distinct calibration procedures are significantly different. If the same calibration curve can be obtained in different measurements within the experimental uncertainties of the fitting parameters, it can be concluded than the thermometer produces reproducible readouts under the tested conditions.

5.3 Luminescence Intensity Ratio

Generally, the emission intensity of a given transition is sensitive to temperature changes due to the following mechanisms:

- Population redistribution over electronic levels according to the Boltzmann statistics;
- Temperature-activated quenching mechanisms (e.g., cross-relaxation between electronic levels);
- Nonradiative deactivations (the electrons relax from excited states to the ground state generating heat, instead of light);
- Phonon-assisted Auger conversion processes.

Luminescence thermometers based on the intensity of a single transition are highly dependent of eventual illumination oscillations, signal-to-noise detection, absorption and scatter cross-sections, and local fluctuations on the phosphor concentration. As recursive calibration procedures are not compatible with end-user applications, a ratio of intensities must be employed [2, 5].

The ratiometric thermometry exploits the relative change in the intensity ratio of two independent energy-close transitions. Both emission lines can be generated from a single luminescent center (single-center thermometers), or they can result from two distinct emitting centers (dual-center thermometers) [3, 4]. To date, majority of the reported ratiometric luminescence thermometers are single-center thermometers.

In single-center ratiometric thermometers, Δ (or LIR) is defined using the emission intensities of the $|2\rangle \rightarrow |0\rangle$ (I_2) and $|1\rangle \rightarrow |0\rangle$ (I_1) transitions, where $|0\rangle$ denotes the ground level and $|1\rangle$ and $|2\rangle$ the two thermally coupled excited levels (level $|2\rangle$ is more energetic than level $|1\rangle$) [38–40],

$$\Delta = \frac{I_2}{I_1} = \frac{A_{02} h \nu_{02} N_2}{A_{01} h \nu_{01} N_1} \tag{5.5}$$

where N_1 and N_2 are the populations of the $|1\rangle$ and $|2\rangle$ levels, ν_{01} and ν_{02} are the frequencies of the $|1\rangle \rightarrow |0\rangle$ and $|2\rangle \rightarrow |0\rangle$ transitions, and A_{01} and A_{02} are the total spontaneous emission rates from levels $|1\rangle$ and $|2\rangle$ to level $|0\rangle$. If the depopulation of the $|1\rangle$ and $|2\rangle$ energy levels involves other energy levels beyond $|0\rangle$, (5.5) must be corrected by the β_2/β_1 ratio, where β_i ($i = 1, 2$) are the branching ratios of the $|i\rangle$ level, i.e., the percentage of the total emission from the thermalized level ($|1\rangle$ or

$|2\rangle$) to the final $|0\rangle$ state. If the two high-energy levels are in thermal equilibrium (they are called "thermally coupled levels," with energy separations of the order of the thermal energy kT), N_1 and N_2 are related by

$$N_2 = \frac{g_2}{g_1} N_1 \exp\left(-\frac{\Delta E}{kT}\right) \tag{5.6}$$

where g_1 and g_2 are the degeneracies of the two levels and ΔE is the energy gap between the barycenters of the $|1\rangle \rightarrow |0\rangle$ and $|2\rangle \rightarrow |0\rangle$ emission bands. Equation (5.5) is, thus, written as

$$\Delta = \frac{g_2 A_{02} h\nu_{02}}{g_1 A_{01} h\nu_{01}} \exp\left(-\frac{\Delta E}{kT}\right) = B \exp\left(-\frac{\Delta E}{kT}\right) \tag{5.7}$$

with $B = \frac{g_2 A_{02} h\nu_{02}}{g_1 A_{01} h\nu_{01}}$. The two light-emitting levels cannot be too separated in energy, otherwise its thermalization is not detected. Typically, they are considered "thermally coupled" (e.g., in a thermodynamically quasi equilibrium state) for ΔE ranging from 200 to 2000 cm^{-1} [41]. As thermally coupled levels could be two excited electron energy levels or ground electronic energy levels, or two Stark sublevels.

Technically, LIR is calculated as the ratio between integral intensities of two emission transitions. This standard calculation technique can be named peak-to-peak ratio. It was found that temperature change sometimes affects the valley between emission bands more significantly than the bands themselves. Thus, monitoring peak-to-valley ratio could result in more sensitive thermal sensing in such a case. Comparison of peak-to-peak and peak-to-valley ratios would be conducted in terms of thermometric performances.

5.3.1 Excited Thermally Coupled Levels

An example of using excited thermally coupled levels for ratiometric thermometry in wide temperature range of 123–873 K is descried below, in which thermal sensing was performed with YVO_4:Nd^{3+} 2.4 at.% NPs [42]. Room temperature excitation and emission spectra of YVO_4:Nd^{3+} 2.4 at.% NPs are presented in Fig. 5.2a. As can be seen, excitation spectrum consists of bands situated at 420–442, 455–490, 500–550, 550–640, and 670–700 nm, which are ascribed to the transitions from ground state $^4I_{9/2}$ to higher levels $^2D_{5/2}$, $^4G_{9/2} + {}^4G_{11/2} + {}^2K_{15/2}$, $^4G_{7/2} + {}^4G_{9/2} + {}^2K_{13/2}$, $^4G_{5/2} + {}^4G_{7/2} + {}^2H_{11/2}$, $^4F_{9/2}$, respectively [43, 44]. Emission spectrum consists of narrow lines attributed to the $^4F_{3/2} - {}^4I_{9/2}$ (870–925 nm) and $^4F_{5/2} + {}^2H_{9/2} - {}^4I_{9/2}$ (790–850 nm) transitions. The energy levels scheme of Nd^{3+} ion in YVO_4 host displaying thermally coupled $^4F_{3/2}$ and $^4F_{5/2} + {}^2H_{9/2}$ levels is presented in Fig. 5.2b.

The temperature dependence of emission spectrum of YVO_4:Nd^{3+} 2.4 at.% NPs is shown in Fig. 5.3a. One can see that intensity ratio between $^4F_{5/2} - {}^4I_{9/2}$ (808 nm)

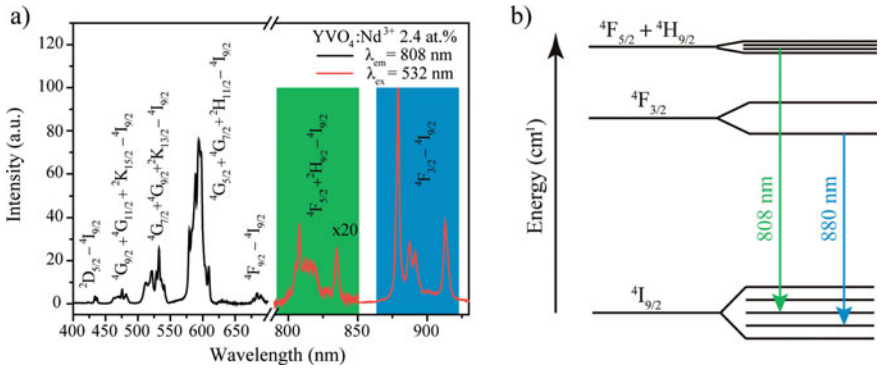

Fig. 5.2 **a** Excitation (black) and emission (red) spectra of YVO_4:Nd^{3+} 2.4 at.% NPs (λ_{em} = 880 nm, λ_{ex} = 532 nm) at room temperature; **b** energy levels scheme of Nd^{3+} ion in YVO_4 host [42]

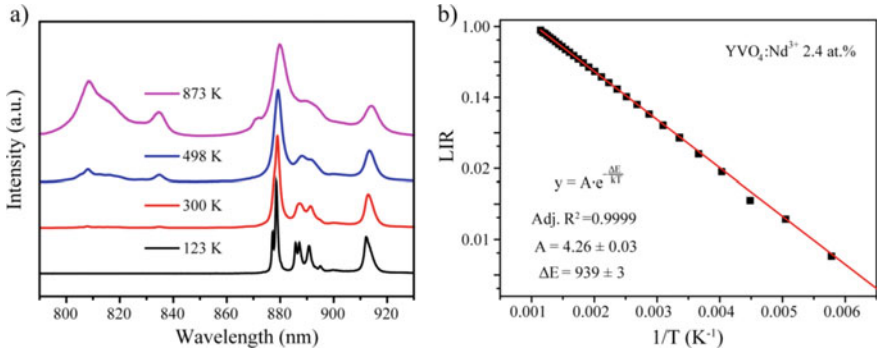

Fig. 5.3 **a** Emission spectra of YVO_4:Nd^{3+} 2.4 at.% at different temperatures (T = 123 K; 300 K; 498 K; 873 K); **b** temperature dependence of LIR between the emission peaks at 808 nm ($^4F_{5/2} - {}^4I_{9/2}$) and 880 nm ($^4F_{3/2} - {}^4I_{9/2}$) for YVO_4:Nd^{3+} 2.4 at. % NPs [42]

and $^4F_{3/2} - {}^4I_{9/2}$ (880 nm) transitions is significantly changed and can be used as thermometric parameter. Taking into account the energy gap between the excited levels and (5.7), we can write $\Delta = \frac{I_{808}}{I_{880}} = A \cdot \exp\left(-\frac{\Delta E}{kT}\right)$. Figure 5.3b shows evolution of LIR as a function of temperature on semi-logarithmic scale. The observed experimental data is accurately fitted by the exponential Boltzmann formula with Adj. R^2 = 0.99. Therefore, monitoring this spectral ratio could provide information about temperature around YVO_4:Nd^{3+} NPs and could be used for different applications.

Relative thermal sensitivity of YVO_4:Nd^{3+} 2.4 at.% NPs obtained according to (5.2) was found to be 1.5% K^{-1}. This value is comparable with other Nd^{3+} based thermometers. For example, sensitivity of Gd_2O_3:Nd^{3+} NPs based on LIR between $^4F_{5/2} - {}^4I_{9/2}$ and $^4F_{3/2} - {}^4I_{9/2}$ transitions was determined to be 1.75% K^{-1} at 288 K [45]. Nd^{3+}-doped $NaYF_4$ microcrystals showed maximum sensitivity of 1.12% K^{-1} at the temperature 500 K [46]. In works [47] and [48], the authors presented $CaWO_4$ and

La_2O_2S bulk powders doped with Nd^{3+} ions, and the maximum of S_r was about 0.3% K^{-1} at the temperature 668 K and 1.1% K^{-1} at the temperature 358 K, respectively.

As YVO_4:Nd^{3+} 2.4 at.% NPs can be used for thermal sensing in a wide temperature range, temperature resolution was obtained at significantly different temperatures (313 and 673 K) suitable for biological and technical applications. Temperature resolutions calculated from calibration curves were determined to be 0.5 K and 1.2 K for 313 K and 673 K temperatures, respectively. The temperature resolution of other Nd^{3+} based thermometers were reported as follows: 0.14 K at 288 K (Gd_2O_3:Nd^{3+}) [45], 2 K at 298 K (LaF_3:Nd^{3+}), [49] 1.13 K at 313 K ($LiNdP_4O_{12}$) [50]. So, we can draw a conclusion that the thermometric performances of YVO_4:Nd^{3+} 2.4 at.% NPs is comparable with other Nd^{3+}-doped thermal sensors.

Another example of contactless ratiometric sensing based on the LIR between transitions originated from two thermally-coupled excited electron levels is shown by Dy^{3+}-doped YVO_4 nanophosphors [51]. Normalized emission spectra of YVO_4:Dy^{3+} 1 at.% nanopowders measured at different temperatures (298, 423 and 673 K) are presented in Fig. 5.4a. The observed emission lines are originated from electron transitions from $^4I_{15/2}$ and $^4F_{9/2}$ excited states with energy separation of about 1000 cm^{-1} (Fig. 5.4b). According to definition, $^4I_{15/2}$ and $^4F_{9/2}$ are thermally coupled levels, and therefore, a ratiometric approach for transitions from these excited states can be utilized to determine the local temperature. The LIR between $^4I_{15/2} - {}^6H_{15/2}$ and $^4F_{9/2} - {}^6H_{15/2}$ transitions ($LIR_{455/480}$), as well as the ratio between $^4I_{15/2} - {}^6H_{15/2}$ and $^4F_{9/2} - {}^6H_{13/2}$ transitions ($LIR_{455/575}$) were used for thermal sensing.

The variations of the LIR values of YVO_4:Dy^{3+} 1 at.% nanocrystalline powders as a function of the temperature are presented in Fig. 5.5a, b. Temperature induced

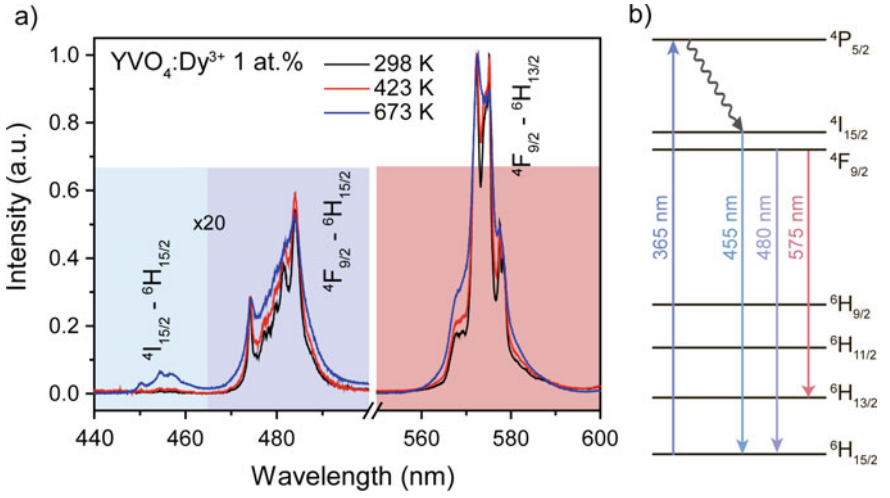

Fig. 5.4 Normalized emission spectra of **a** YVO_4:Dy^{3+} 1 at.% and **b** YVO_4:Dy^{3+} 2 at.% nanopowders at different temperatures. The colored areas are used for the integral intensity ratio calculations. **c** Energy levels scheme of YVO_4:Dy^{3+} nanophosphors [51]

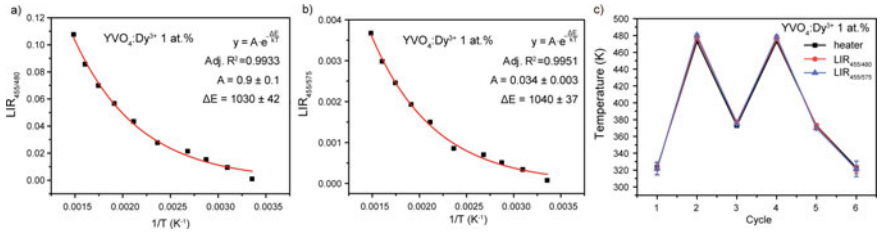

Fig. 5.5 Luminescence intensity ratio **a** $LIR_{455/480}$ and **b** $LIR_{455/575}$ of $YVO_4:Dy^{3+}$ 1 at.% nanopowders as a function of temperature [51]

change of LIR is caused by electron re-distribution at the energy levels according to the Boltzmann formula (5.7).

Performance of $YVO_4:Dy^{3+}$ 1 at.% thermometer is studied in terms of thermal sensitivities, temperature resolution, and repeatability. The observed temperature dependences of S_a and S_r demonstrate opposite behavior: the temperature increase leads to a gradual growth of S_a and a monotonic decline of S_r. As the temperature dependence in both LIRs originate from the same excited levels: $^4I_{15/2}$ and $^4F_{9/2}$, it is not surprising that the maximal relative thermal sensitivity ($T = 298$ K) for $LIR_{455/480}$ and $LIR_{455/575}$ ratios is similar: 1.8% K^{-1} ($YVO_4:Dy^{3+}$ 1 at.%). However, the absolute thermal sensitivities differ significantly: 0.039 K^{-1} at 673 K ($LIR_{455/480}$) and 0.0013 K^{-1} at 673 K ($LIR_{455/575}$). Compared to Er^{3+}, Tm^{3+} or Nd^{3+} ions, the use of dysprosium ions for temperature sensing are relatively rare. Among other Dy^{3+} single doped materials, the obtained S_r values are comparable to the values reported in the literature: 1.7% K^{-1} for $BaYF_5:Dy^{3+}$ NPs [52], 1.6% K^{-1} for $Gd_2Ti_2O_7:Dy^{3+}$ NPs [53], 1.7% K^{-1} for YAG:Dy^{3+} microcrystals [54], 1.7% K^{-1} and 1.3% K^{-1} for Dy:Y$(acac)_3$ and Dy:Y$(acac)_3$(phen) molecular crystals, respectively [55].

Temperature resolution of $YVO_4:Dy^{3+}$ 1 at.% thermometer was estimated from consecutive emission spectra measured at fixed heating stage temperature. Due to the rather wide temperature sensing region, ΔT was obtained for 323 and 473 K. The obtained value lay in the range of 3–7 K depending on the measured temperature and the luminescence intensity ratio used.

Repeatability of $YVO_4:Dy^{3+}$ thermometer was tested over cyclic heating-cooling measurements (Fig. 5.5c). During the experiment, we increased and decreased the temperature within the thermal range of 323–473 K. Black squares indicate the actual temperature of heater, whereas red circles and blue triangles present temperature obtained with $LIR_{455/480}$ and $LIR_{455/575}$ luminescence intensity ratio, respectively. Taking into account temperature uncertainties, we can conclude that the considered $YVO_4:Dy^{3+}$ nanopowder has good repeatability: temperatures obtained using optical thermometry are repeated from cycle to cycle and they are in good agreement with the actual heater temperature.

5.3.2 Ground Thermally Coupled Levels

In addition to excited levels with energy gap not exceeding 2000 cm^{-1}, the thermoequilibrium between the two ground energy levels can be used for ratiometric thermometry. This strategy was successfully demonstrated using $^7F_0$, $^7F_1$, and $^7F_2$ europium ground levels in $YVO_4:Eu^{3+}$ nanophosphors [56]. It was notably the first demonstration of thermal sensing based on excitation spectra of luminescence nanoparticles.

Excitation spectra of $YVO_4:Eu^{3+}$ 16 at.% NPs monitored at forced electric dipole transition $^5D_0$–$^7F_4$ (698 nm) measured at different temperatures are shown in Fig. 5.6a. The studied temperature range was 299–466 K. These spectra consist of many bands, which can be used for thermal sensing based on electron population redistribution of low lying levels. As $^7F_0$, $^7F_1$, and $^7F_2$ levels are situated within 2000 cm^{-1}, the following luminescence lines were utilized to calculate LIR: $^7F_0$–$^5D_1$ (526 nm), $^7F_1$–$^5D_1$ (537 nm), $^7F_2$–$^5D_1$ (555 nm), $^7F_1$–$^5D_0$ (593 nm), and $^7F_2$–$^5D_0$ (613 nm) (Fig. 5.6b). LIRs based on thermal electron population redistribution between $^7F_0$ and $^7F_1$, $^7F_0$ and $^7F_2$, $^7F_1$ and $^7F_2$ levels were compared. Moreover, effect of excited level on LIR sensing properties was also studied. The following

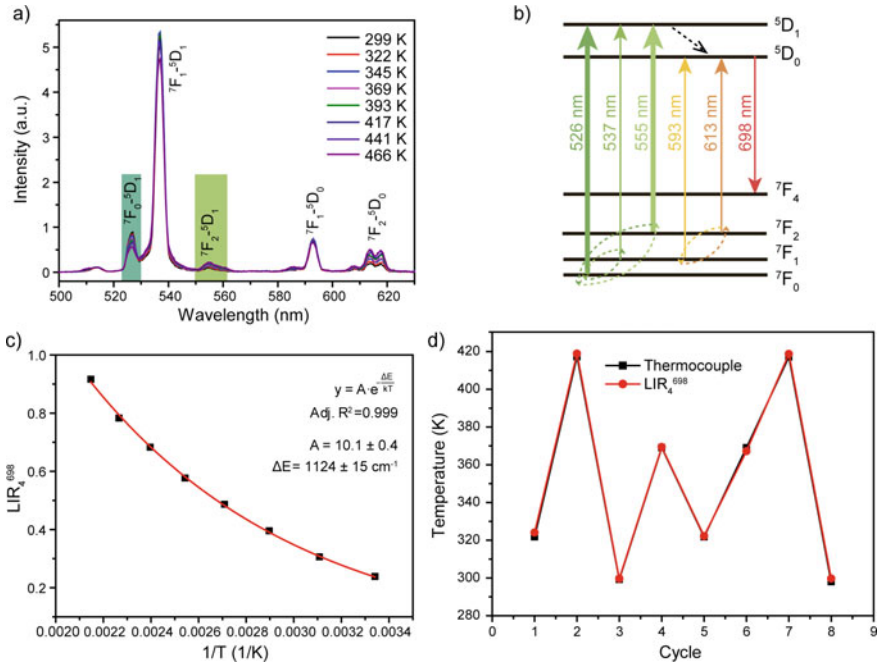

Fig. 5.6 **a** Excitation spectra of $YVO_4:Eu^{3+}$ 16 at.% NPs obtained at different temperatures (λ_{em} = 698 nm); **b** thermal sensing scheme based on excitation spectra of $^5D_0$–$^7F_4$ transition, **c** temperature evolution of luminescence intensity ratio LIR_4^{698}; **d** complex heating-cooling cycles [56]

luminescence intensity ratios were calculated: $^7F_1$–$^5D_1$/$^7F_0$–$^5D_1$ (LIR_1^{698}), $^7F_1$–$^5D_0$/$^7F_0$–$^5D_1$ (LIR_2^{698}), $^7F_2$–$^5D_1$/$^7F_0$–$^5D_1$ (LIR_3^{698}), $^7F_2$–$^5D_0$/$^7F_0$–$^5D_1$ (LIR_4^{698}), $^7F_2$–$^5D_1$/$^7F_1$–$^5D_1$ (LIR_5^{698}), and $^7F_2$–$^5D_0$/$^7F_1$–$^5D_1$ (LIR_6^{698}). Integral intensity of each band was collected within spectral range equal to spectral slit width during measurement (3 nm). In all cases experimental data were fitted by the exponential function (5.7), which confirmed that LIR thermal dependence is governed by a Boltzmann process. All suggested LIRs are suitable to provide thermal sensing. A comparison of the effective gap ΔE_{eff} obtained from the fitting procedure led to a conclusion that LIR_4^{698} has the best thermometric performances among all calculated $LIRs_4^{698}$. A calibration curve of the most promising R_4^{698} for YVO_4:Eu^{3+} 16 at.% nanophosphor is shown in Fig. 5.6c. The highest S_r value of YVO_4:Eu^{3+} 16 at.% NPs was 1.25% K^{-1} at 298 K, while S_a achieved 0.00475 K^{-1} at 466 K. Temperature resolution was found to be 1 K at 323 K, which was obtained from the calibration curve. To monitor the repeatability, a thermal cycling experiment with YVO_4:Eu^{3+} 16 at.% nanophosphor, where the temperature was determined in consecutive complex heating-cooling cycles, was carried out. The temperature was defined by two independent methods: luminescence nanothermometry (LIR_4^{698}) and thermocouple measurements. As can be seen from Fig. 5.6d, measured and calculated temperatures are in good agreement taking into account thermal uncertainties.

5.3.3 Stark Sublevels

LIR can be calculated not only by using different excited or ground electronic levels, but also by utilizing different Stark sublevels. As the energy gap between Stark sublevels is less than that between the electronic levels, relative sensitivity of thermometers based on this approach is lower. However, some thermometry applications require two emission bands used for LIR calculation within a certain spectral region, for example, biological optical transparency windows, which is of crucial importance for medicine and biology. This requirement can be fulfilled by Nd^{3+}-doped Y_2O_3 NPs possessing emission peaks originated from different Stark sublevels and situated in both first (650–950 nm) and second (1000–1350 nm) biological windows (BW) [57]. Detailed emission spectra of Y_2O_3:Nd^{3+} 1 at.% NPs at different temperatures (26.5 and 58.5 °C) measured in the spectral range of 870–922 nm (I-BW) are presented in Fig. 5.7a. The luminescence intensity ratio between $^4F_{3/2}(2) - {}^4I_{9/2}(3)$ and $^4F_{3/2}(1) - {}^4I_{9/2}(3)$ (hereafter denoted as LIR_1^I) was chosen for nanothermometry (Fig. 5.7b), because it should have a temperature dependence in biological range due to the value of the energy gap between the Stark sublevels. As can be seen, the emission lines used for thermal sensing are well resolved, thus, a deconvolution analysis is not required. Temperature evolution of LIR_1^I demonstrated a monotonous pseudo-linear trend within the studied temperature range (Fig. 5.7c). The observed pseudo-linear trend appeared from usual Boltzmann function with small energy gap in the narrow temperature range.

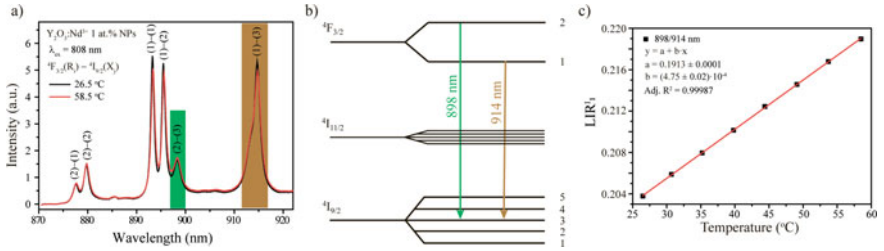

Fig. 5.7 **a** Emission spectra of Y_2O_3:Nd^{3+} 1 at.% nanoparticles obtained at two different temperatures ($\lambda_{ex} = 808$ nm); **b** energy levels scheme of transition $^4F_{3/2}(R_i) - {}^4I_{9/2}(X_j)$ for Nd^{3+} ion in the Y_2O_3 host; **c** luminescence intensity ratios LIR_1^I as a function of temperature [57]

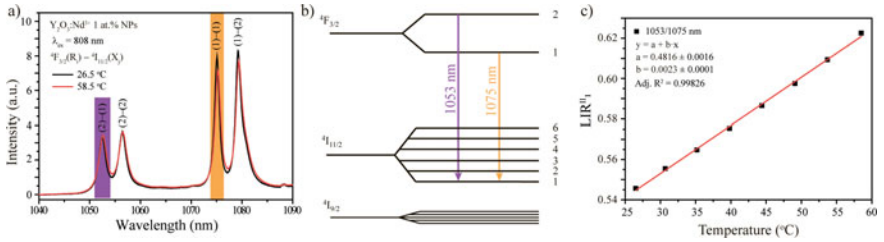

Fig. 5.8 **a** Emission spectra of Y_2O_3:Nd^{3+} 1 at.% nanoparticles obtained at different temperatures ($\lambda_{ex} = 808$ nm); **b** energy levels scheme of transition $^4F_{3/2}(R_i) - {}^4I_{11/2}(Y_k)$ for Nd^{3+} ion in the Y_2O_3 host; **c** luminescence intensity ratios LIR_1^{II} as a function of temperature [57]

Thermal sensing using Y_2O_3:Nd^{3+} 1 at.% NPs was also performed in the II-BW. Detailed emission spectra at different temperatures (26.5 and 58.5 °C) measured in the spectral range of 1040–1090 nm are presented in Fig. 5.8a. Nanothermometry was based on the luminescence intensity ratio between $^4F_{3/2}(2) - {}^4I_{11/2}(1)$ and $^4F_{3/2}(1) - {}^4I_{11/2}(1)$ (hereafter denoted as LIR_1^{II}) (Fig. 5.8b). Figure 5.8c showed LIR_1^{II} as a function of temperature from which a pseudo-linear behavior was observed.

The relative thermal sensitivities of Y_2O_3:Nd^{3+} 1 at.% NPs were found to be 0.23 and 0.43% $°C^{-1}$ for Stark sublevels LIR_1^I and LIR_1^{II}, respectively. Careful examination of earlier reported Stark sublevel-based LIR for other Nd^{3+}-doped thermometers ($NaYF_4$, YAG, $YNbO_4$, LaF_3, YVO_4, $KGd(WO_4)_2$, CaF_2) led to a conclusion that among NIR-to-NIR nanothermometers, Y_2O_3:Nd^{3+} nanophosphor demonstrates the best relative thermal sensitivity. Sub-degree temperature resolution (0.2 and 0.5 °C for LIR_1^I and LIR_1^{II}, respectively) makes Nd^{3+}-doped Y_2O_3 NPs prospective candidates for accurate thermal sensing.

5.3.4 Peak-to-Valley Calculation

As it was demonstrated in the previous paragraphs, ratiometric thermal sensing can be successfully performed using emission transition originated from different Stark sublevels despite the much lower relative thermal sensitivity compared to that of the different electronic levels. To enhance thermal sensitivity, a new strategy based on the monitoring of peak-to-valley ratio was developed [32].

Normalized emission spectra generated upon 808 nm excited YVO_4:Nd^{3+} 3 at.% NPs obtained at 26 and 58 °C are shown in Fig. 5.9a. A temperature increase results in the increase of the relative contribution of the $^4F_{3/2}(2) - {}^4I_{11/2}(3)$ transition due to temperature induced population of $^4F_{3/2}(2)$ Stark sublevel [58]. The intensity ratio of $^4F_{3/2}(1) - {}^4I_{11/2}(1)$ (1064.8 nm) and $^4F_{3/2}(2) - {}^4I_{11/2}(3)$ (1072 nm) transitions (hereafter denoted as LIR_3) has been previously used for nanothermometry [58]. As it can be clearly seen from Fig. 5.9, temperature change also significantly affects relative intensity of "valleys" centered at 1066.3 and 1063.7 nm. Therefore, luminescence intensity ratios between the largest peak at 1064.8 nm and the valley at 1066.3 nm (LIR_1) or the valley at 1063.7 nm (LIR_2) were used for thermal calibration to enhance thermal sensitivity.

The intensity ratio demonstrated a monotonous pseudo-linear trend in the biophysical temperature range (25–60 °C) for all LIRs (Fig. 5.10). Strictly speaking, luminescence intensity ratio should be fitted by the exponential Boltzmann formula, but it was much more convenient to use a linear function to define local temperature from the observed ratio [59–61].

Calculated thermal sensitivities for different LIRs gave the following values: 0.35, 0.32 and 0.20% K^{-1}. A simple analysis showed that the new strategy for LIR calculation (peak-to-valley) results in a remarkable enhancement up to 1.75 of the thermal sensitivity compared to standard approach (peak-to-peak). Moreover, the new strategy also significantly improved another important thermometric

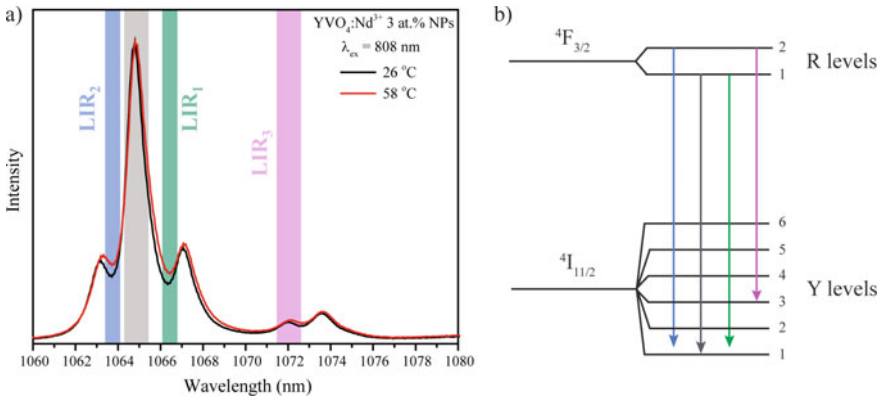

Fig. 5.9 **a** Normalized emission spectra of YVO_4:Nd^{3+} 3 at.% NPs obtained at different temperatures ($\lambda_{ex} = 808$ nm); **b** energy levels scheme of Nd^{3+} ion in the YVO_4 host [32]

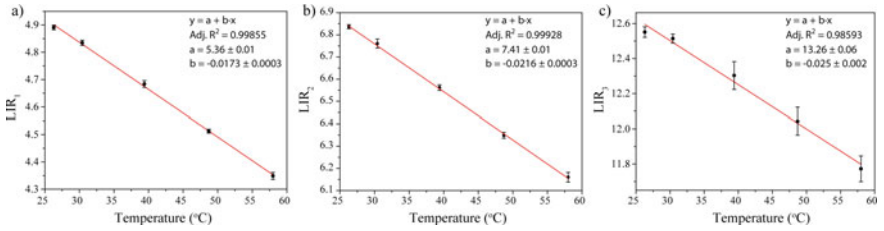

Fig. 5.10 **a** Evolution of the integral intensity ratio between emission peak 1064.8 nm and valley 1066.3 nm; **b** evolution of the integral intensity ratio between emission peak 1064.8 nm and valley 1063.7 nm; **c** evolution of the integral intensity ratio between 1064.8 and 1072 nm emission peaks. Red line corresponds to the best fitting [32]

performance, temperature resolution. ΔT was obtained using all three techniques described above. However, here we provide calibration curve method. It was found that the temperature resolution of YVO_4:Nd^{3+} 3 at.% equals 0.6, 0.7 and 2.3 °C, when monitoring LIR_1, LIR_2 and LIR_3, respectively. We can therefore conclude that the peak-to-valley strategy enhances accuracy of thermal sensing of NIR-to-NIR ratiometric thermometer by 4 times.

5.4 Spectral Line Position Thermometry

This technique is based on the analysis of the spectral positions of the emission lines, which are unequivocally determined by the energy separation between the two electronic levels involved in the emission. Any temperature change leads to modifications in the arrangement of the lattice ions surrounding rare earth ion and, therefore, to a crystal field modification which results in a shift in the emission lines. Temperature reading can be achieved by an accurate spectral analysis of the emission lines. Typically, in the physiological range, these temperature-induced shifts are small but they can be recognized when dealing with rare earth ions characterized by narrow emission lines, such as neodymium [62].

Generally, an increase in temperature leads to the red shift of the emission line positions. When the crystal temperature is increased, the energy levels and, therefore, the spectral lines broaden, invariably as the higher phonon modes are occupied. Since there are many high-lying energy levels which couples, an energy level is normally lowered. Further, it is usually the case that the temperature dependence of higher levels is larger than for lower levels because of smaller energy denominators. As a result, the spectral lines are observed to shift normally to the longer wavelengths when the temperature is increased [63, 64]. Thermal shifts to the blue can be caused by thermal expansion of the crystal lattice due to the changes of crystalline-field strength and impurity-level energies. Such shifts were observed for some transitions of Nd^{3+} in the soft hydrated crystal $Pr(NO_3)_3 \cdot 6H_2O$. However, such thermal expansion is negligible in hard ionic crystals [63, 64].

The shift of the emission line is usually associated with the electron–phonon coupling effect, which results from the fact that at higher temperatures, host vibration modes introduce random perturbation of the ion's local environment [65]. According to the phonon theory [66, 67], the line position is affected by the crystal strain inhomogeneity, direct one-phonon processes, multiphonon processes, and Raman phonon scattering processes. As found in earlier studies [64, 68], thermal shift is mainly governed by electron–host interaction effect associated with Raman scattering, and therefore the simplified theoretical expressions for the line shift can be written in the following form [69]:

$$\upsilon = \upsilon_0 + \alpha\left(\frac{T}{\Theta_D}\right)^4 \int_0^{\Theta_D/T} \frac{x^3}{e^x - 1} dx \tag{5.8}$$

where υ_0, α, Θ_D represent the initial line position (determined at low temperature, in this paper at 123 K), the electron–host coupling parameter, and the effective Debye temperature, respectively.

Spectral line position thermometry was demonstrated by use of YVO_4:Nd^{3+} 2.4 at % NPs possessing narrow emission lines [70]. Normalized emission spectra of this phosphor obtained at different temperatures in a wide range of 123–873 K are shown in Fig. 5.11a. The position of the most intensive emission band, which is attributed to the transition between the Stark levels of the $^4F_{3/2}$ and $^4I_{11/2}$ states was chosen as a temperature dependent parameter. The growth of temperature from 123 to 873 K caused monotonical red shift of the emission line position which can be perfectly fitted by (5.8) (red curve in Fig. 5.11b).

It should be noted that, in spite of its clear physical meaning, the aforementioned function cannot be used for thermal sensing due to its complexity and inability

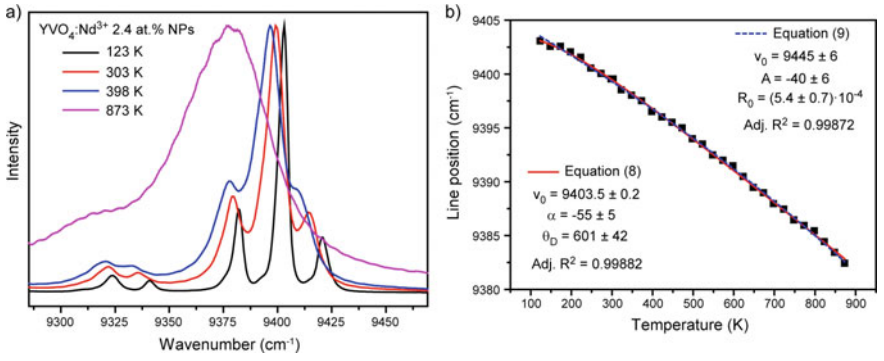

Fig. 5.11 **a** Normalized emission spectra of $^4F_{3/2} - {}^4I_{11/2}$ transition obtained at different temperatures (123–873 K); **b** line position of $^4F_{3/2}$ (R_1) $- {}^4I_{11/2}$ (Y_1) transition as a function of temperature [70]

to derive temperature as a function of spectral shift. Therefore, a simple exponential expression was suggested for fitting the observed line shift as a function of temperature:

$$\upsilon = \upsilon_0 + A \cdot e^{R_o T} \tag{5.9}$$

Both fitting procedures resulted in similar values of adjusted R^2: 0.99882 and 0.99872 for (5.8) and (5.9), respectively. Therefore, the proposed fitting function allows us to use a spectral shift of emission line for thermal sensing.

Relative thermal sensitivity based on line shift of YVO_4:Nd^{3+} 2.4 at % NPs was found to be 0.75% K^{-1} at 303 K, which is much higher than S_r of $LiLaP_4O_{12}$:Nd^{3+} 1% NPs (0.47% K^{-1}) and $LiNdP_4O_{12}$ NPs (0.003% K^{-1}).

5.5 Bandwidth Thermometry

Emission line bandwidth is determined by the properties of the material such as the degree of disorder and temperature. Generally, the emission lines of phosphors broaden as the temperature increases. This is ascribed to the intrinsic vibrations of the lattice exhibiting homogeneous broadening, which depends sensitively on temperature or to the presence of different optical centers and defects exhibiting inhomogeneous broadening, which depends only slightly on temperature. Detailed analysis of thermally-induced broadening in rare earth-doped inorganic NPs as well as temperature sensing based on line bandwidth is demonstrated in [71].

Bandwidth is affected by the same processes which influence line position. According to the phonon theory [66], the width of energy level is given by:

$$\Delta\upsilon = \Delta\upsilon^{strain} + \Delta\upsilon^{D} + \Delta\upsilon^{M} + \Delta\upsilon^{R} \tag{5.10}$$

The first term, $\Delta\upsilon^{strain}$, is the width due to the crystal strains. The second term, $\Delta\upsilon^{D}$, is the width due to direct one-phonon process between the selected energy level and other nearby levels, and consists of a temperature-independent part, which is due to a spontaneous one-phonon emission, and a temperature-dependent part. The third term, $\Delta\upsilon^{M}$, is the contribution to the width from the multiphonon emission processes, which are temperature independent. The last term, $\Delta\upsilon^{R}$ represents the width for the Raman multiphonon process associated with phonon scattering by impurity ions [72]. It should be noted that the first term represents inhomogeneous broadening with a Gaussian line shape due to crystal strains, whereas the other terms give rise to homogeneous broadening with a Lorentzian line shape. Since different line shapes are expected for several broadening mechanisms, simple summation of (5.4) is a rough approximation, and a line shape composed of both homogeneous and inhomogeneous parts can be represented by a Voigt profile [73]. If it is necessary, line width may be resolved into homogeneous and inhomogeneous contributions by using the numerical tables prepared by Posener [74].

It was earlier found that the main contribution to line broadening is Raman scattering process which consists of the absorption of one phonon and the emission of another phonon without changing the electronic state of the ion [64, 72]. In this case, the width of the energy level can be given by following expression:

$$\Delta\upsilon = \Delta\upsilon_0 + \overline{\alpha}\left(\frac{T}{\Theta_D}\right)^7 \int_0^{\Theta_D/T} \frac{x^6 e^x}{(e^x - 1)^2} dx \tag{5.11}$$

where $\Delta\upsilon_0$ is the initial linewidth, $\overline{\alpha}$ is the coupling coefficient for the electron–phonon interaction, and Θ_D is the effective Debye temperature.

Normalized emission spectra of Y_2O_3:Nd^{3+} 1 at.% NPs obtained at different temperatures in a wide range of 123–873 K are presented in Fig. 5.12a. Bandwidth of $^4F_{3/2}(R_1)$–$^4I_{11/2}(Y_1)$ transition was monitored to obtain thermal sensing. Due to the proximity of other emission lines, deconvolution procedure was performed to define the exact bandwidth. An evolution of the full width at half maximum (FWHM) of the emission line as a function of temperature is presented in Fig. 5.12b. Experimental data were approximated with (5.11) with previously defined effective Debye temperature $\Theta_D = 538$ K. Similar to line position sensing, (5.11) was not suitable for the calibration of the luminescence thermometer. Therefore, the experimental data were perfectly fitted with simple exponential expression:

$$\Delta\upsilon = \Delta\upsilon_0 + A \cdot e^{R_o T} \tag{5.12}$$

Bandwidth relative thermal sensitivity of Y_2O_3:Nd^{3+} 1 at % NPs was 0.36% K^{-1} at 298 K, which is comparable with S_r of other Nd^{3+}-doped nanothermometers: $LiLaP_4O_{12}$:Nd^{3+} 1% (0.32% K^{-1}), $LiNdP_4O_{12}$ (0.46% K^{-1}) and YVO_4:Nd^{3+} 2.4 at.% (0.14% K^{-1}). Temperature sensing based on bandwidth demonstrated superior accuracy in a wide temperature range: 0.2 K at 323 K and 0.5 K at 498 K. It is

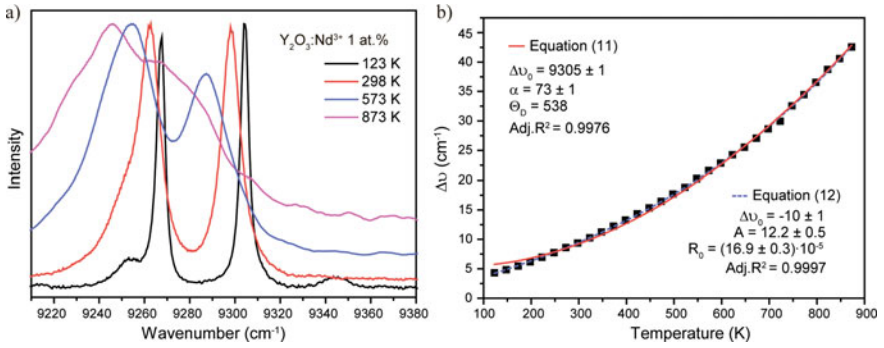

Fig. 5.12 **a** Normalized emission spectra of $^4F_{3/2} - {}^4I_{11/2}$ transition obtained at different temperatures (123–873 K); **b** FWHM of $^4F_{3/2}$ $(R_1) - {}^4I_{11/2}$ (Y_1) transition as a function of temperature [71]

noteworthy that the temperature resolution was found using acquisition and analysis of consecutive photoluminescence spectra.

5.6 Lifetime Thermometry

In contrast to the temperature readout from the intensity of a single emission line, the determination of temperature from the emission lifetime is not really compromised by changes in measurement conditions. Additionally, it is not affected by the inhomogeneity of the probe material. Lifetime measurements have better detection limits than the measurements of intensity, which is important for high-temperature applications and, generally, they present smaller uncertainties compared to those in measurements of intensity [75]. Lifetime-based thermometry, like the ratiometric intensity method, is self-referencing, but it needs the observation of just one emission line. The drawbacks of lifetime measurements are that they require relatively expensive equipment, and, compared to the emission intensity, a longer time to collect experimental data and a more complex processing of emission decay data to derive lifetime values. In addition, the temperature change of the excited state lifetime of rare earth ions generally shows two regimes, which can be easily understood from following equation:

$$\tau(T) = \frac{\tau_r(T)}{1 + \tau_r(T) \cdot k_{nr}(T)} \tag{5.13}$$

where τ and τ_r are the observed and radiative lifetime, k_{nr} is nonradiative decay rate. At low temperatures, where the values of the nonradiative rate are negligible, the lifetime is equal to the radiative lifetime, $\tau \cong \tau_r$. The radiative lifetime only slightly changes with temperature: $\tau_r(T) = \tau_{r0} exp(-\alpha T)$, where α is the phenomenological parameter of order 10^{-4} K^{-1} or less. Therefore, at low temperatures, lifetime only slightly decreases with temperature increase or does not change at all. As a consequence, the lifetime method is practically insensitive to temperature changes in this range. At higher temperatures, the nonradiative decay rate sharply increases, leading to a steep decrease in observed lifetime. The temperature point of the transition between two regions essentially depends on the energy difference between excited levels of rare earth ions and the closest lower energy level or charge-transfer band, and on the phonon energy of the host material. Examples of lifetime temperature dependences of some rare earth-doped metal oxides and salts are shown in Fig. 5.13. The temperature region of lifetime insensitivity presents a major obstacle to its use. This region frequently covers the physiologically relevant temperature range and thus prevents the use of the majority of lifetime based thermal sensors in biomedicine. On the other hand, in the high temperature region, lifetime method is very sensitive. It is worthy of note that the uncertainties in decay times are generally smaller than those in emission intensities and that the current technology facilitates measurements of very short decay times. Therefore, the lifetime sensing technique has the potential

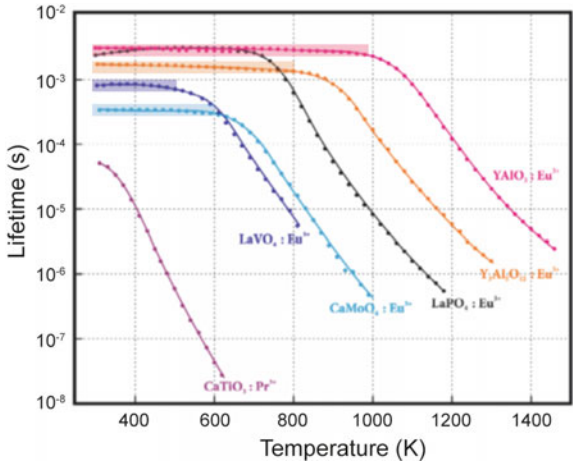

Fig. 5.13 Temperature dependences of lifetime of some lanthanide-doped metal oxides and salts. Shadowed areas show temperature insensitive regions [76]

to present better temperature resolutions than intensity-based measurements and has larger high-temperature operating bounds.

By analyzing the data from Fig. 5.13, one can conclude that Pr^{3+} ions display better lifetime temperature dependence in 300–400 K range compared with Eu^{3+} ions. $LiPr(PO_3)_4$ was tested by Gharouel et al. as lifetime-based contactless thermometer within 298–363 K temperature range [77]. Emission spectra of $LiPr(PO_3)_4$ sample normalized to $^3P_0$–$^3F_2$ transition as a function of temperature obtained upon laser excitation at 488 nm are presented in Fig. 5.14a. In this wavelength region, there are two distinct emission bands attributed to the $^3P_0$–$^3H_6$ and $^3P_0$–$^3F_2$ transitions respectively. The temperature increase results in a more pronounced decline in $^3P_0$–$^3H_6$ intensity compared with that of $^3P_0$–$^3F_2$. Fluorescence decay curves from $^3P_0$ energy level of Pr^{3+} ions registered at different temperatures upon pulsed laser excitation at 488 nm are shown in Fig. 5.14b. The luminescence decay curves demonstrated an exponential behavior in the entire temperature range. Figure 5.14c represents the temperature evolution of the normalized decay time, $\tau_{norm}(T)$, defined

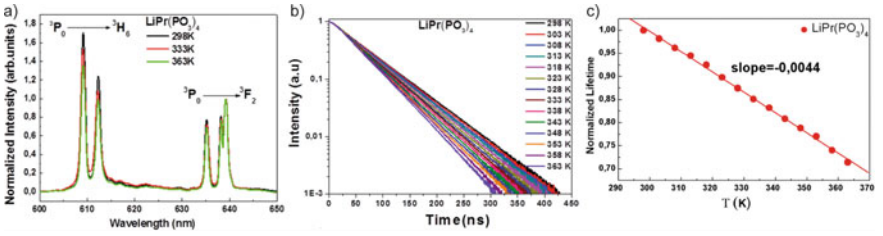

Fig. 5.14 **a** Emission spectra of $LiPr(PO_3)_4$ sample as a function of temperature obtained under laser excitation at 488 nm, **b** fluorescence decay curves of $^3P_0$ level recorded at different temperatures upon 488 nm laser excitation, **c** normalized $^3P_0$ lifetime as a function of the temperature [77]

as $\tau_{norm}(T) = \tau(T)/\tau$ (298 K). The luminescence lifetimes versus temperature monotonically decreased in 298–363 K temperature range and followed a linear behavior ($\tau = a + bT$).

Lifetime-based thermal sensitivity of $LiPr(PO_3)_4$ sample was 0.62% K^{-1}, which was approximately in the same order of magnitude than the sensitivities of previously investigated praseodymium and chromium-doped lifetime based thermometers (0.59% K^{-1} for $NaPr(PO_3)_4$, 0.50% K^{-1} for Cr^{3+}:$Y_3Al_5O_{12}$, 0.83% K^{-1} for Cr^{3+}:$LiAl_5O_8$). The temperature resolution of $LiPr(PO_3)_4$ was determined to be 0.8 K, much higher than those obtained for different lifetime thermometeric sensors such as BaClF:Sm^{3+} ($\Delta T = 5$ °C) [78], Er^{3+}-doped fibers ($\Delta T = 4$ °C) [79], and Cr^{3+}:Al_2O_3 ($\Delta T \approx 2.4$ K) [80].

5.7 Conclusion and Perspectives

The analysis presented in the chapter demonstrated that temperature has become a measurable characteristic at micro- and nanoscale owing to the colossal progress in the technique of luminescence thermometry. The luminescence thermometry relies on high thermal sensitivity of luminescence characteristics such as luminescence intensity, spectral line position, bandwidth, and excited state lifetime, of various materials—from organic dyes to rare earth-doped nanophosphors. The latter objects seem to be the most promising among others. They provide a wide measurable temperature range (from cryogenic to technological values) due to narrow emission lines, high thermal and chemical stability. The current record parameters of luminescence temperature sensors combine high relative thermal sensitivity (> 1% K^{-1}), thermal resolution (~ 0.1 °C) and spatial resolution (< 10 μm) with short acquisition times (< 100 ms). These high performance features are provided both by the use of rare earth-doped phosphors as temperature sensors and by the ratiometric thermometry approach that exploits the relative change in the intensity ratio of two energy-close transitions. The important feature of the ratiometric thermometry discussed in the chapter is the consideration of the thermodynamically quasi-equilibrium state, the so called thermally coupled levels, with energy difference from 200 to 2000 cm^{-1}. In practice, the ratiometric approach can be realized by excited or ground electronic energy levels and two Stark sublevels. Moreover, various readout strategies can be used, such as peak-to-peak and peak-to-valley ratios. Other variants of readout strategy can be realized by means of monitoring the spectral position of the emission lines, bandwidth, and lifetime. Each strategy offers its own advantage and applicability in the specific field.

In such a way, the progress of luminescence thermometry resulted in the creation of breakthrough technologies in various areas of application such as micro- and nanoelectronics, micro- and nanofluidics, photonics, and nanomedicine. As a feedback of the technological progress, new challenges towards luminescence temperature sensors appeared that are connected with requests for further improvement of parameters and broadening of the areas of application. In spite of the already achieved and

extraordinary temperature performance of luminescence thermal sensors, there are urgent tasks that can be prioritized. First of all, the spectral range of the luminescence thermometry has to be widened to NIR emissions correlated with optical windows in biological tissues that is of great importance to application in biomedicine. Another interesting problem to be solved is connected with the fundamental development of the luminescence thermometry by considering alternative strategies such as ratiometric approach based on non-thermally coupled levels and the use of multiple emission centers (couples of different rare earth ions or combinations of rare earth ions with other luminescent elements). The next very ambitious and very promising task is combining the fields of luminescence microscopy and luminescence thermometry. The current achievements of luminescence microscopy allow visualization of objects below the resolution of a light microscope, resulting in in vivo noninvasive study of ongoing biological processes and 3D optical tomographic reconstructions. Integration of luminescence microscopy and thermometry in mutual technological protocol will provide multimodal spectral diagnostics with potency of 3D visualization and thermal mapping with micro- and nanoscale resolution. It should be noted that other variants of dual- or multi-sensing devices with thermometric functionalities are also promising and realizable. Further progress in fundamental and applied luminescence thermometry is inevitably approaching.

Acknowledgements This research has been performed in "Center for Optical and Laser materials research".

References

1. P.R.N. Childs, J.R. Greenwood, C.A. Long, Review of temperature measurement. Rev. Sci. Instrum. **71**, 2959–2978 (2000)
2. C.D.S. Brites, A. Millán, L.D. Carlos, Lanthanides in luminescent thermometry. Handb. Phys. Chem. Rare Earths **49**, 339–427 (2016). https://doi.org/10.1016/bs.hpcre.2016.03.005
3. C.D.S. Brites, P.P. Lima, N.J.O. Silva et al., Thermometry at the nanoscale. Nanoscale **4**, 4799–4829 (2012). https://doi.org/10.1039/c2nr30663h
4. D. Jaque, F. Vetrone, Luminescence nanothermometry. Nanoscale **4**, 4301 (2012). https://doi.org/10.1039/c2nr30764b
5. X. Wang, O.S. Wolfbeis, R.J. Meier, Luminescent probes and sensors for temperature. Chem. Soc. Rev. **42**, 7834–7869 (2013)
6. S. Uchiyama, A. Prasanna de Silva, K. Iwai, Luminescent molecular thermometers. J. Chem. Educ. **83**, 720 (2006)
7. Y. Yue, X. Wang, Nanoscale thermal probing. Nano Rev. **3**, 11586 (2012)
8. S. Uchiyama, N. Kawai, A.P. de Silva, K. Iwai, Fluorescent polymeric AND logic gate with temperature and pH as inputs. J. Am. Chem. Soc. **126**, 3032–3033 (2004)
9. K. Okabe, N. Inada, C. Gota et al., Intracellular temperature mapping with a fluorescent polymeric thermometer and fluorescence lifetime imaging microscopy. Nat. Commun. **3**, 705 (2012)
10. J.S. Donner, S.A. Thompson, M.P. Kreuzer et al., Mapping intracellular temperature using green fluorescent protein. Nano Lett. **12**, 2107–2111 (2012)
11. P. Löw, B. Kim, N. Takama, C. Bergaud, High-spatial-resolution surface-temperature mapping using fluorescent thermometry. Small **4**, 908–914 (2008)

12. C. Paviolo, A.H.A. Clayton, S.L. McArthur, P.R. Stoddart, Temperature measurement in the microscopic regime: a comparison between fluorescence lifetime-and intensity-based methods. J. Microsc. **250**, 179–188 (2013)
13. H.D.A. Santos, D. Ruiz, G. Lifante et al., Time resolved spectroscopy of infrared emitting Ag_2S nanocrystals for subcutaneous thermometry. Nanoscale **9**, 2505–2513 (2017)
14. S. Kalytchuk, O. Zhovtiuk, S.V. Kershaw et al., Temperature-dependent exciton and trap-related photoluminescence of CdTe quantum dots embedded in a NaCl matrix: implication in thermometry. Small **12**, 466–476 (2016)
15. J. Ueda, M. Back, M.G. Brik et al., Ratiometric optical thermometry using deep red luminescence from $^4T_2$ and ^2E states of Cr^{3+} in $ZnGa_2O_4$ host. Opt. Mater. (Amst) **85**, 510–516 (2018)
16. E. Glais, V. Đorđević, J. Papan et al., $MgTiO_3$: Mn^{4+} a multi-reading temperature nanoprobe. RSC Adv. **8**, 18341–18346 (2018)
17. A. Benayas, B. del Rosal, A. Pérez-Delgado et al., Nd: YAG near-infrared luminescent nanothermometers. Adv. Opt. Mater. **3**, 687–694 (2015)
18. L. Marciniak, A. Bednarkiewicz, K. Elzbieciak, NIR–NIR photon avalanche based luminescent thermometry with Nd^{3+} doped nanoparticles. J. Mater. Chem. C **6**, 7568–7575 (2018)
19. O. Savchuk, J.J. Carvajal, L.G. De la Cruz et al., Luminescence thermometry and imaging in the second biological window at high penetration depth with Nd:KGd $(WO_4)_2$ nanoparticles. J. Mater. Chem. C **4**, 7397–7405 (2016)
20. I.E. Kolesnikov, E.V. Golyeva, E. Lähderanta et al., Ratiometric thermal sensing based on Eu^{3+}-doped YVO4 nanoparticles. J. Nanopart. Res. **18**, 354 (2016). https://doi.org/10.1007/s11051-016-3675-8
21. J.-C.G. Buenzli, S.V. Eliseeva, Intriguing aspects of lanthanide luminescence. Chem. Sci. **4**, 1939–1949 (2013)
22. K. Binnemans, Lanthanide-based luminescent hybrid materials. Chem. Rev. **109**, 4283–4374 (2009)
23. J. Feng, H. Zhang, Hybrid materials based on lanthanide organic complexes: a review. Chem. Soc. Rev. **42**, 387–410 (2013)
24. C.D.S. Brites, P.P. Lima, N.J.O. Silva et al., A luminescent molecular thermometer for long-term absolute temperature measurements at the nanoscale. Adv. Mater. **22**, 4499–4504 (2010). https://doi.org/10.1002/adma.201001780
25. Z. Wang, D. Ananias, A. Carné-Sánchez et al., Lanthanide-organic framework nanothermometers prepared by spray-drying. Adv. Funct. Mater. **25**, 2824–2830 (2015)
26. J. Rocha, C.D.S. Brites, L.D. Carlos, Lanthanide organic framework luminescent thermometers. Chem. Eur. J. **22**, 14782–14795 (2016)
27. S. Arai, S. Takeoka, S. Ishiwata et al., Micro-thermography in millimeter-scale animals by using orally-dosed fluorescent nanoparticle thermosensors. Analyst **140**, 7534–7539 (2015)
28. E.N. Cerón, D.H. Ortgies, B. del Rosal et al., Hybrid nanostructures for high-sensitivity luminescence nanothermometry in the second biological window. Adv. Mater. **27**, 4781–4787 (2015). https://doi.org/10.1002/adma.201501014
29. O.A. Savchuk, P. Haro-Gonzalez, J.J. Carvajal et al., Er:Yb:NaY_2F_5O up-converting nanoparticles for sub-tissue fluorescence lifetime thermal sensing. Nanoscale **6**, 9727–9733 (2014)
30. K. Trejgis, A. Bednarkiewicz, L. Marciniak, Engineering excited state absorption based nanothermometry for temperature sensing and imaging. Nanoscale **12**, 4667–4675 (2020)
31. I.E. Kolesnikov, E.V. Golyeva, M.A. Kurochkin et al., Nd^{3+}-doped YVO4 nanoparticles for luminescence nanothermometry in the first and second biological windows. Sens. Actuators B Chem. **235**, 287–293 (2016). https://doi.org/10.1016/j.snb.2016.05.095
32. I.E. Kolesnikov, A.A. Kalinichev, M.A. Kurochkin et al., New strategy for thermal sensitivity enhancement of Nd^{3+}-based ratiometric luminescence thermometers. J. Lumin. **192**, 40–46 (2017). https://doi.org/10.1016/j.jlumin.2017.06.024
33. R. Alicki, D.M. Leitner, Size-dependent accuracy of nanoscale thermometers. J. Phys. Chem. B **119**, 9000–9005 (2015)

34. G. Tóth, I. Apellaniz, Quantum metrology from a quantum information science perspective. J. Phys. A Math. Theor. **47**, 424006 (2014)
35. A.A. Alaulamie, Nanoscale temperature measurement of phase transition in water using novel optical thermometry techniques (2017)
36. J.W. Bartlett, C. Frost, Reliability, repeatability and reproducibility: analysis of measurement errors in continuous variables. Ultrasound Obstet. Gynecol. Off. J. Int. Soc. Ultrasound Obstet. Gynecol. **31**, 466–475 (2008)
37. B.N. Taylor, C.E. Kuyatt, Guidelines for evaluating and expressing the uncertainty of NIST measurement results (1994)
38. S.A. Wade, S.F. Collins, G.W. Baxter, Fluorescence intensity ratio technique for optical fiber point temperature sensing. J. Appl. Phys. **94**, 4743–4756 (2003)
39. M.D. Shinn, W.A. Sibley, M.G. Drexhage, R.N. Brown, Optical transitions of Er^{3+} ions in fluorozirconate glass. Phys. Rev. B **27**, 6635 (1983)
40. S.F. León-Luis, U.R. Rodríguez-Mendoza, P. Haro-González et al., Role of the host matrix on the thermal sensitivity of Er^{3+} luminescence in optical temperature sensors. Sens. Actuators B Chem. **174**, 176–186 (2012)
41. A.H. Khalid, K. Kontis, 2D surface thermal imaging using rise-time analysis from laser-induced luminescence phosphor thermometry. Meas. Sci. Technol. **20**, 25305 (2009)
42. A.A. Kalinichev, M.A. Kurochkin, E.V. Golyeva et al., Near-infrared emitting YVO4:Nd^{3+} nanoparticles for high sensitive fluorescence thermometry. J. Lumin. **195**, 61–66 (2018). https://doi.org/10.1016/j.jlumin.2017.11.024
43. I.E. Kolesnikov, D.V. Tolstikova, A.V. Kurochkin et al., Concentration effect on structural and luminescent properties of YVO_4:Nd^{3+} nanophosphors. Mater. Res. Bull. **70**, 799–803 (2015). https://doi.org/10.1016/j.materresbull.2015.06.023
44. J.B. Gruber, D.K. Sardar, K.L. Nash, R.M. Yow, Comparative study of the crystal-field splitting of trivalent neodymium energy levels in polycrystalline ceramic and nanocrystalline yttrium oxide. J. Appl. Phys. **102**, 23103 (2007)
45. S. Balabhadra, M.L. Debasu, C.D.S. Brites et al., Boosting the sensitivity of Nd^{3+}-based luminescent nanothermometers. Nanoscale **7**, 17261–17267 (2015)
46. X. Tian, X. Wei, Y. Chen et al., Temperature sensor based on ladder-level assisted thermal coupling and thermal-enhanced luminescence in $NaYF_4$:Nd^{3+}. Opt. Express **22**, 30333–30345 (2014)
47. W. Xu, Q. Song, L. Zheng et al., Optical temperature sensing based on the near-infrared emissions from Nd^{3+}/Yb^{3+} codoped $CaWO_4$. Opt. Lett. **39**, 4635–4638 (2014)
48. G. Jiang, X. Wei, S. Zhou et al., Neodymium doped lanthanum oxysulfide as optical temperature sensors. J. Lumin. **152**, 156–159 (2014)
49. U. Rocha, C. Jacinto da Silva, W. Ferreira Silva et al., Subtissue thermal sensing based on neodymium-doped LaF_3 nanoparticles. ACS Nano **7**, 1188–1199 (2013)
50. L. Marciniak, K. Prorok, A. Bednarkiewicz et al., Water dispersible $LiNdP_4O_{12}$ nanocrystals: new multifunctional NIR–NIR luminescent materials for bio-applications. J. Lumin. **176**, 144–148 (2016). https://doi.org/10.1016/j.jlumin.2016.03.034
51. I.E. Kolesnikov, A.A. Kalinichev, M.A. Kurochkin et al., Structural, luminescence and thermometric properties of nanocrystalline YVO_4:Dy^{3+} temperature and concentration series. Sci. Rep. **9**, 2043 (2019). https://doi.org/10.1038/s41598-019-38774-6
52. Z. Cao, S. Zhou, G. Jiang et al., Temperature dependent luminescence of Dy^{3+} doped $BaYF_5$ nanoparticles for optical thermometry. Curr. Appl. Phys. **14**, 1067–1071 (2014)
53. S. Ćulubrk, V. Lojpur, S.P. Ahrenkiel et al., Non-contact thermometry with Dy^{3+} doped $Gd_2Ti_2O_7$ nano-powders. J. Lumin. **170**, 395–400 (2016)
54. L.M. Chepyga, A. Osvet, C.J. Brabec, M. Batentschuk, High-temperature thermographic phosphor mixture YAP/YAG:Dy^{3+} and its photoluminescence properties. J. Lumin. **188**, 582–588 (2017)
55. B.R. Anderson, R. Gunawidjaja, H. Eilers, Dy^{3+}-doped yttrium complex molecular crystals for two-color thermometry in heterogeneous materials. J. Lumin. **188**, 238–245 (2017)

56. I.E. Kolesnikov, A.A. Kalinichev, M.A. Kurochkin et al., Ratiometric optical thermometry based on emission and excitation spectra of YVO_4:Eu^{3+} nanophosphors. J. Phys. Chem. C **123**, 5136–5143 (2019)
57. I.E. Kolesnikov, A.A. Kalinichev, M.A. Kurochkin et al., Y_2O_3:Nd^{3+} nanocrystals as ratiometric luminescence thermal sensors operating in the optical windows of biological tissues. J. Lumin. **204**, 506–512 (2018). https://doi.org/10.1016/j.jlumin.2018.08.050
58. I.E. Kolesnikov, E.V. Golyeva, A.A. Kalinichev et al., Nd^{3+} single doped YVO_4 nanoparticles for sub-tissue heating and thermal sensing in the second biological window. Sens. Actuators B Chem. **243**, 338–345 (2017). https://doi.org/10.1016/j.snb.2016.12.005
59. E. Carrasco, B. del Rosal, F. Sanz-Rodríguez et al., Intratumoral thermal reading during photothermal therapy by multifunctional fluorescent nanoparticles. Adv. Funct. Mater. **25**, 615–626 (2015). https://doi.org/10.1002/adfm.201403653
60. A. Benayas, B. del Rosal, A. Pérez-Delgado et al., Nd:YAG near-infrared luminescent nanothermometers. Adv. Opt. Mater. **3**, 687–694 (2015). https://doi.org/10.1002/adom.201400484
61. U. Rocha, C. Jacinto, K.U. Kumar et al., Real-time deep-tissue thermal sensing with sub-degree resolution by thermally improved Nd^{3+}:LaF_3 multifunctional nanoparticles. J. Lumin. **175**, 149–157 (2016). https://doi.org/10.1016/j.jlumin.2016.02.034
62. B. del Rosal, E. Ximendes, U. Rocha, D. Jaque, In vivo luminescence nanothermometry: from materials to applications. Adv. Opt. Mater. **5**, 1600508 (2017)
63. S.A. Johnson, H.G. Freie, A.L. Schawlow, W.M. Yen, Thermal shifts in the energy levels of LaF_3:Nd^{3+}. JOSA **57**, 734–737 (1967)
64. T. Kushida, Linewidths and thermal shifts of spectral lines in neodymium-doped yttrium aluminum garnet and calcium fluorophosphate. Phys. Rev. **185**, 500–508 (1969). https://doi.org/10.1103/PhysRev.185.500
65. Ł Marciniak, A. Bednarkiewicz, D. Hreniak, W. Strek, The influence of Nd^{3+} concentration and alkali ions on the sensitivity of non-contact temperature measurements in $ALaP_4O_{12}$:Nd^{3+} (A = Li, K, Na, Rb) nanocrystalline luminescent thermometers. J. Mater. Chem. C **4**, 11284–11290 (2016). https://doi.org/10.1039/c6tc03396b
66. X. Chen, B. Di Bartolo, Phonon effects on sharp luminescence lines of Nd^{3+} in $Gd_3Sc_2Ga_3O_{12}$ garnet (GSGG). J. Lumin. **54**, 309–318 (1993)
67. A. Kiel, Temperature-dependent line width of excited states in crystals. I. Line broadening due to adiabatic variation of the local fields. Phys. Rev. **126**, 1292 (1962)
68. D.K. Sardar, R.M. Yow, Inter-stark energy levels and effects of temperature on sharp emission lines of Nd^{3+} in $LiYF_4$. Phys. Status Solidi A Appl. Res. **173**, 521–534 (1999)
69. D.K. Sardar, R.M. Yow, Optical characterization of inter-stark energy levels and effects of temperature on sharp emission lines of Nd^{3+} in $CaZn_2Y_2Ge_3O_{12}$. Opt. Mater. (Amst) **10**, 191–199 (1998)
70. I.E. Kolesnikov, A.A. Kalinichev, M.A. Kurochkin et al., YVO_4:Nd^{3+} nanophosphors as NIR-to-NIR thermal sensors in wide temperature range. Sci. Rep. **7**, 18002 (2017). https://doi.org/10.1038/s41598-017-18295-w
71. I.E. Kolesnikov, A.A. Kalinichev, M.A. Kurochkin et al., Bifunctional heater-thermometer Nd^{3+}-doped nanoparticles with multiple temperature sensing parameters. Nanotechnology **30**, 145501 (2019). https://doi.org/10.1088/1361-6528/aafcb8
72. D.K. Sardar, R.M. Yow, Stark components of $^4F_{3/2}$, $^4I_{9/2}$ and $^4I^{11/2}$ manifold energy levels and effects of temperature on the laser transition of Nd^{3+} in YVO_4. Opt. Mater. (Amst) **14**, 5–11 (2000)
73. B. Di Bartolo, R.H. Silsbee, Optical interactions in solids. Am. J. Phys. **37**, 756–757 (1969)
74. D.W. Posener, The shape of spectral lines: tables of the Voigt profile. Aust. J. Phys. **12**, 184–196 (1959)
75. M.D. Chambers, D.R. Clarke, Doped oxides for high-temperature luminescence and lifetime thermometry. Annu. Rev. Mater. Res. **39**, 325–359 (2009)
76. J. Brübach, C. Pflitsch, A. Dreizler, B. Atakan, On surface temperature measurements with thermographic phosphors: a review. Prog. Energy Combust. Sci. **39**, 37–60 (2013)

77. S. Gharouel, L. Labrador-Páez, P. Haro-González et al., Fluorescence intensity ratio and lifetime thermometry of praseodymium phosphates for temperature sensing. J. Lumin. **201**, 372–383 (2018)
78. J.S. McCormack, Remote optical measurement of temperature using luminescent materials. Electron. Lett. **17**, 630–631 (1981)
79. Z.Y. Zhang, K.T.V. Grattan, A.W. Palmer et al., Fluorescence decay-time characteristics of erbium-doped optical fiber at elevated temperatures. Rev. Sci. Instrum. **68**, 2764–2766 (1997)
80. H.C. Seat, J.H. Sharp, Dedicated temperature sensing with c-axis oriented single-crystal ruby (Cr/sup 3+: Al/sub 2/O/sub 3/) fibers: temperature and strain dependences of R-line fluorescence. IEEE Trans. Instrum. Meas. **53**, 140–154 (2004)

Chapter 6
Optical Monitoring of Single Molecule Dynamics of RNA in Living Cells

Hideaki Yoshimura and Takeaki Ozawa

Abstract Live-cell optical imaging is a powerful approach to monitor the intracellular localization and dynamics of the molecules of interest for elucidating the mechanism of physiological function. Single-molecule imaging is a unique technique that provides information on the dynamics and association/dissociation of each molecule inside living cells. Despite having monitored a variety of biomolecules in living cells, live-cell imaging of RNA, which is an important component of living systems, has not been performed intensively. This can be attributed to the lack of techniques available for the optical labeling of RNA inside living cells. This review introduces labeling methods and microscopic techniques for monitoring RNA in living cells, focuses on an example of single-molecule imaging of a long non-coding RNA TERRA (telomeric repeat-containing RNA) using mPUM-technology, an RNA labeling method, along with the investigation of a single-molecule RNA imaging system in living cells.

Abbreviations

EGFP	Enhanced green fluorescent protein
FRET	Förster resonance energy transfer
PAMmer	PAM-presenting DNA oligonucleotide (PUM: protospacer adjacent motif)
PUM-HD	Pumilio homology domain. TERRA: telomeric repeat-containing RNA
TIRF	Total internal reflection fluorescence

H. Yoshimura (✉) · T. Ozawa
Department of Chemistry, School of Science, The University of Tokyo, 7-3-1 Hongo, Bunkyo-ku, Tokyo 113-0033, Japan
e-mail: hideaki@chem.s.u-tokyo.ac.jp

T. Ozawa
e-mail: ozawa@chem.s.u-tokyo.ac.jp

K. Yamanouchi et al. (eds.), *Progress in Photon Science*, Springer Series in Chemical Physics 125, https://doi.org/10.1007/978-3-030-77646-6_6

6.1 Introduction

Living cells consist of a myriad of biomolecule such as proteins, nucleic acids, lipids, and sugars. As a simple mixture of all the molecules involved in the living cells would not reconstitute such a cell, appropriate assembly, localization, and dynamics of these molecules are required for the generation and maintenance of the cellular lives. To understand the mechanism of living cells with respect to molecules, optical imaging is the most direct approach for observation such molecules in living cells. Optical microscopy, especially fluorescence microscopy, has been frequently used to visualize molecules in living samples owing to its non-invasiveness. Another advantage of fluorescence microscopy, apart from non-invasiveness, is selectivity to monitor fluorescence-tagged target molecules. A variety of fluorescent probes have been developed in recent decades for labeling and monitoring target molecules in living cells [1, 2]. Certain dyes that emit fluorescence upon binding to double-stranded nucleic acids are used to visualize DNA in living cells. Ions such as Ca^{2+} are visualized by probes obtained via organic synthesis that generate fluorescence during chelation of target ions [3] and protein-based probes that result in conformational change upon binding to Ca^{2+} and release FRET (Förster resonance energy transfer) signal [4]. Proteins in living cells can be conjugated with fluorescent proteins using genetic engineering techniques.

RNA is also an important element in living cells along with DNA, ions, and proteins. As described by the biological central dogma, RNA that functions as messenger RNA (mRNA) is produced via the transcription of genes in chromosomal DNA and transports genetic information for protein production. Previously mRNA was characterized only as a messenger of the genetic information, and attention was not paid to the intracellular localization and dynamics of mRNA. However, certain examples have been reported, in which the intracellular localization of mRNA plays important roles in physiological events [5, 6]. For instance, β-actin mRNA concentrates in leading edges involving lamellipodia, and filopodia of cells that are expanding and migrating upon stimulation with external growth and/or chemotactic signals [7–9]. This localization of β-actin mRNA supports rapid pseudopodia formation and cell expansion for quick response to external signals. Apart from mRNA, non-coding RNAs have also been implicated in various physiological processes. Among various species of non-coding RNAs, long non-coding RNAs (lncRNAs) exhibit crucial roles in cellular functions, such as gene regulation and genome stability [10].

Despite the importance of intracellular RNA localization and dynamics, techniques for visualizing RNAs in living cells are still developing, and hence the investigation of RNA based on its intracellular dynamics has been delayed. Under such circumstances, certain technologies have been developed recently for labeling and monitoring the RNA of interest. In this chapter, optical techniques that contribute to the visualization of RNA dynamics in living cells, such as microscopic methods and optical probe technologies, are introduced. Examples of single-molecule imaging of

RNA in living cells based on one of the technologies, named mPUM technology, are explained.

6.2 RNA Labeling Methods for Live-Cell Optical Imaging

Several techniques for RNA labeling in living cells have been developed to monitor RNA localization, dynamics, and functions (Fig. 6.1) [11, 12]. The most popular method for RNA visualization in cell samples under an optical microscope is the fluorescence *in situ* hybridization method, in which the target RNA is hybridized with a fluorescence-labeled oligonucleotide probe. However, this method requires washing of excess probes and is limited for use in chemically fixed and permeabilized cell samples. To overcome these limitations, a technique was developed using an oligonucleotide-based tool known as molecular beacon [13–15]. The molecular beacon has a stem-loop hairpin structure and its 5′ and 3′ ends are conjugated with a fluorescent dye and a quencher, respectively. The fluorescent dye is located close to the quencher. Hence, the fluorescence is quenched in the absence of target RNA. In the presence of the target RNA, the stem-loop hairpin region dissociates and attaches to the target RNA sequence, leading to the separation of the fluorescence dye from the quencher and subsequent recovery of its fluorescence. Fluorogenic RNA aptamer is another nucleotide-based RNA probe that has recently been developed as a tool for RNA detection in living cells. The aptamer is an RNA molecule that specifically captures a nonfluorescent dye and converts it into the fluorescent form. As a typical example, an RNA aptamer "Spinach" captures an enhanced green fluorescent protein (EGFP) fluorophore-resembling dye 24-2-DFHBI and emits fluorescence [16–18].

In addition to oligonucleotide-based RNA probes, certain protein-based RNA probes have also been developed [19, 20]. The MS2 system is the most widely used

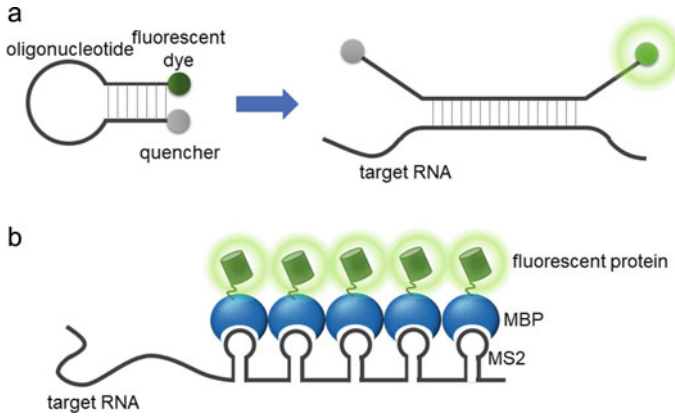

Fig. 6.1 Schematics of **a** molecular beacon and **b** MS2 system

method for labeling the RNA of interest using a protein-based probe. In the MS2 system, a repeat of a bacteriophage-derived RNA tag called MS2 is fused to the 3′ terminus of the target RNA. The MS2 region is specifically recognized and captured by MS2-binding proteins (MBP). In the MS2 system employed for monitoring the target RNA, MBP is fused to a fluorescent protein (FP) and introduced into the sample cells. In addition, the target RNA fused with an MS2 repeat sequence is expressed in the cells. The MBP-FP accumulates in the MS2 repeat region, and can be visualized as a bright fluorescent spot under a fluorescence microscope. This system originally existed only in bacteriophages. Hence, it has been used to label the RNA of interest in mammalian cells without off-target interactions with other RNAs. Another potential candidate for providing a platform for protein-based RNA probes is the Cas protein. Clustered regularly interspaced short palindromic repeats (CRISPR)/Cas systems have been typically used to target double-stranded DNA; however, several modifications have been obtained to alter the systems for targeting RNAs. Nelles et al. developed a fusion protein with GFP and dCas9 that incorporated a single guide RNA and PAMmer (PAM-presenting DNA oligonucleotide) that hybridizes to a target RNA [21]. The localization of β-actin mRNA in fixed cells was visualized using this method.

6.3 Design of the PUM-HD-Based RNA Probes

PUM-HD is an RNA-binding protein domain derived from human PUMILIO1 that binds to an 8-base RNA sequence of 5′-UGUAU(orC)AUA-3′ (Fig. 6.2) [22, 23]. Examinations performed with crystallography demonstrated that PUM-HD has eight repeated motifs, each capturing an RNA base via the interactions of hydrogen bonds

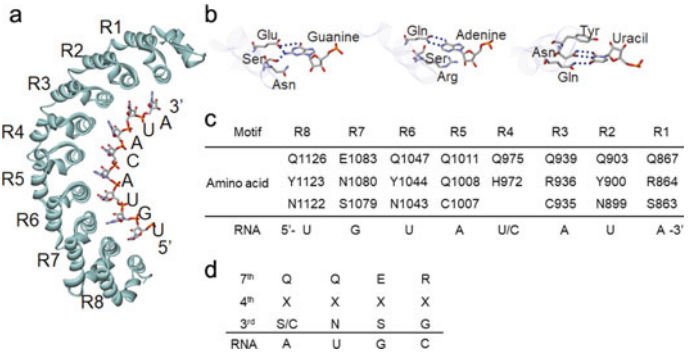

Fig. 6.2 RNA recognition by PUM-HD [27]. **a** The structure of a PUM-HD and a recognized 8-base RNA. **b** RNA recognition by three amino acids in a repeat motif of PUM-HD. **c** The three amino acid combination in each repeat motif of wild type PUM-HD and the recognized RNA base. **d** Relationship between recognized RNA bases and the combination of three amino acids in the repeat motif

and van der Waals forces [24, 25]. Based on crystallographic studies, three amino acids at the third, fourth, and seventh positions in one helix of the motif were identified to be involved in these interactions with the RNA base, and hence in determining the specificity of the RNA base. Therefore, site-directed mutageneses of these three amino acids, especially on the third and seventh positions, alters the RNA base for recognition by the motif, and custom-designed PUM-HD mutants that recognize a specific 8-base RNA sequence can be prepared [24, 26–28]. Although no motifs recognize a cytosine base in the wild-type PUM-HD, several investigations with random mutations on the three amino acids have discovered a motif that recognizes a cytosine base [29]. The dissociation constant between a PUM-HD mutant (mPUM) and the eight-base sequence RNA identified is typically in the order of nM when the RNA initiates 5′-UGU-3′ at the 5′ terminus, and ~ 100 nM when the 5′ terminus is not 5′-UGU-3′ [24].

As a single mPUM can be considered to recognize an 8-base RNA sequence, the specificity of the target RNA sequence is 4^8, which might not fulfill required specificity for labeling to a target RNA in mammalian cells by using only a single mPUM species. One of the approaches employed in solving the potential off-target problem of mPUM is the use of a fluorescent protein reconstitution method [8, 9, 30]. In this method, the two split fragments of a fluorescent protein are fused to a pair of proteins of interest. When the pair of proteins approach each other, the fluorescent protein-fragments are brought into proximity, leading to the reconstitution of the full-length fluorescent protein and restoration of its fluorescence. Using this method, mPUM-based probes can be designed to recognize target RNA specifically. Two mPUM molecules that recognize different but adjacent regions in a target RNA are prepared and subsequently conjugated with N- and C-terminal fluorescent protein fragments. After both mPUMs bind to the target regions in the RNA of interest, the fragments of fluorescent protein come in proximity and reconstitute to form the fluorescent protein. In this design, the probe does not emit fluorescence without binding to the target RNA. Moreover, a 16-base sequence in the target RNA is required to be recognized by the probe system for emitting fluorescence signals, leading to sufficient selectivity for observing a specific RNA molecule in mammalian cells.

6.4 Microscope Setup for Single-Molecule Imaging of RNA in Living Cells

Fluorescent probes based on the reconstitution of split fluorescent protein are applied not only for conventional and confocal fluorescence microscope imaging but also for single-molecule fluorescence imaging to monitor the dynamics of the target molecules in real-time. The PUM-HD-based RNA probe also has the potential to label the RNA of interest for monitoring its single-molecule dynamics [8, 9, 31]. However, the RNA is typically localize in the cytosol and/or the nucleus, whereas the targets for single-molecule imaging comprise primarily the membrane molecules as

the total internal reflection illumination typically used for single-molecule imaging can irradiate the regions located in the vicinity of the plasma membrane. Hence, special techniques are required for the illumination of cells with a low background fluorescence signal in single RNA molecule imaging. Our microscopy setup for single-molecule imaging inside a cell sample is explained below.

Microscope systems for single-molecule RNA detection inside a cell are typically designed based on the total internal reflection fluorescence (TIRF) microscope (Fig. 6.3). We constructed a home-build TIRF microscope system that employs excitation laser optics to illuminate the sample, and detection optics for the separation of emitted fluorescence light based on the wavelength followed by detection with respective sCMOS cameras. Using this system, simultaneous dual- and triple-color fluorescence imaging of the RNA of interest and an associated protein labeled with another fluorescent dye can be conducted [27, 31].

Excitation optics is the most important aspect of the microscopic system for single-molecule RNA imaging as the incidence angle of the excitation laser light on the sample is required to be modulated. The samples were illuminated by evanescent light that reaches the sample with a depth of approximately 150 nm from the coverslip in the TIRF microscopic visualizations. Under such excitation conditions, most of the intracellular molecules, including RNAs are not illuminated. Hence, they are

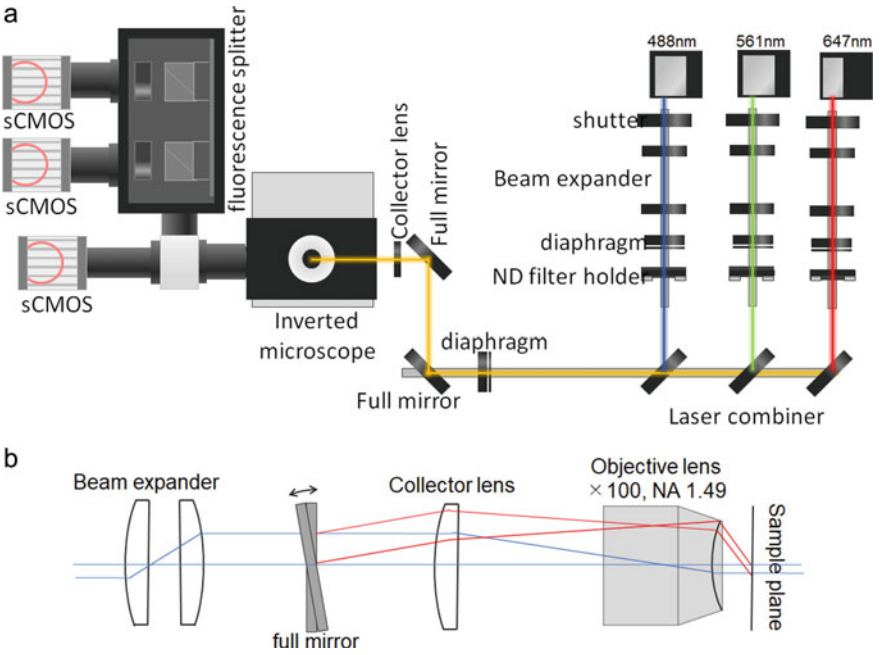

Fig. 6.3 Microscope setup for single molecule RNA observation [27]. **a** Overall picture of the microscope system used in RNA single molecule imaging. **b** Light path adjustment for TIRF and oblique illumination

invisible with the excitation during complete TIRF illumination. Highly inclined illumination or oblique illumination, in which the laser beam demonstrates a large incidence angle but smaller than the total internal reflection, deepen the illumination area and enables the monitoring of intracellular molecules with low background fluorescence [32].

The optical apparatus for excitation in the TIRF microscope system developed by us was composed of diode lasers, mechanical shutters, beam expanders consisting of a pair of convex lenses, neutral density (ND) filters, laser combiners, full mirrors, and a collector lens [27]. These components were placed on a vibration removal table along with a microscope and a detection system. The mechanical shutters were placed in front of the lasers. The two convex lenses in a beam expander exhibited a focus distance of 10 mm and 200 mm, respectively, which increases the diameter of the laser beam increased 20 times. The intensity of the laser lights was modulated via ND filters and combined using a dichroic mirror that act as a laser combiner. The laser light was introduced to the collector lens that focuses the laser light on the back focal plane of the objective lens. Subsequently, the laser beam is emitted from the objective lens as parallel light. The full mirror was placed 250 mm away from the collector lens with focus distance of 250 nm. This means that the mirror and collector lens are situated in a conjugate position. Alteration of the mirror angle slides the laser beam position after passing through the collector lens despite being kept parallel to the optical axis, making the incident angle of the laser beam on the sample to be oblique illumination that penetrates into the sample cell.

6.5 Application of PUM-HD for Monitoring RNA in Living Cells

The mPUM-based probe has been recently used for monitoring telomeric repeat-containing RNA (TERRA), which is a non-coding RNA, to investigate its mechanism [31]. TERRA is the transcription product obtained from the terminal region of the chromosomal DNA called telomeres [33–36]. TERRA consists of a subtelomeric region along with the telomeric-repeat region, and is implicated in telomere maintenance. Two different models have been proposed for explaining the mechanism of TERRA in the maintenance and regulation of telomeres: a scaffold model, which proposes that TERRA included in the ribonucleoprotein (RNP) complexes on a telomere aiding in their stabilization [37]; and a decoy model, which suggests that the protein components in the RNP complexes are transported or removed by TERRA [38]. Single-molecule monitoring of TERRA dynamics around a telomere in living cells would provide critical information for evaluating the true mechanistic model of the TERRA function.

TERRA has a unique repetitive region with multiple 5′-UUAGGG-3′ sequences derived from a telomere [33]. Our TERRA probe was designed to address this region [31]. The TERRA probe consists of three domains: an EGFP N-terminal, an mPUM

designed to capture a 5′-UUAGGGUU-3′ sequence (mPUMt), and an EGFP C-terminal fragment. Three repeats of a nuclear localization signal sequence are fused to the N-terminus of the probe owing to the nuclear localization of TERRA. In the presence of TERRA, multiple probe molecules accumulate on the unique repetitive region. The EGFP N-terminal fragment in the probe and the C-terminal fragment of the next probe come in close proximity, leading to the reconstitution of EGFP and emission of fluorescence. Although many reconstituted fluorescent proteins are expected to be generated on a TERRA molecule because of the large number of telomeric repeats in TERRA, most of the observed fluorescent spots included a single fluorescent molecule, confirmed by single-step photobleaching and analysis of the distribution of fluorescence intensity of the spots. This suggested that mPUMt did not penetrate and attach to a G-quartet structure, which is formed by the telomeric repeats, but only captured the flexible terminal region of TERRA.

Using the developed mPUMt-based probe, endogenous TERRA was monitored with an oblique illumination microscope in the living U2OS cells. The U2OS cells express the mPUMt-based TERRA probe as well as a SNAP-fused telomere marker protein TRF1 that enables the simultaneous monitoring of TERRA and telomeres. Many TERRA was visualized in a diffuse motion in the nucleus, whereas telomeres were almost static in the resulting movie. We observed two modes of the TERRA motion, namely diffusive and stationary upon detailed analysis of the movie. In addition, TERRA demonstrated localization of a substantial part to a region about 1 μm apart from a telomere. However, the remaining portion was colocalized with a telomere. This suggested the presence of a scaffold for capturing TERRA in this region.

To investigate the function of the TERRA in the region around a telomere, triple-color single-molecule imaging of TERRA, telomere, and telomere-associated proteins was conducted with an oblique illumination microscope equipped with a triple-color fluorescence separating detection system. The telomere-related protein, HP1, which is included in the scaffold model, and hnRNPA1, which is a potential target in the decoy model, were observed. In addition, H2A that reportedly does not interact with TERRA, was adopted as a negative control. In this observation, TERRA and telomere-related proteins were observed in a diffusive motion, whereas the telomeres were almost static, in accordance with the results obtained with dual-color imaging. Colocalization with TERRA was detected in all three telomere-related proteins. Consequently, the colocalization duration time was analyzed. For H2A with which interaction with TERRA has not been reported, the colocalization with TERRA can be considered as an accidental overlapping, and the colocalization duration was less than 0.2 s. The colocalization duration for HP1 and TERRA was comparable to that of H2A and TERRA, whereas the duration of hnRNPA1-TERRA colocalization was significantly longer than that of H2A-TERRA. Thus, hnRNPA1 was identified as an interacting partner of TERRA. A radial distribution analysis demonstrated that the interaction between hnRNPA1 and TERRA was concentrated in the area approximately 1–1.5 μm apart from a telomere. On initiation of this colocalization, diffusive hnRNPA1 molecules arrived and interacted with a static TERRA in the area. Based on the results from single-molecule imaging, a potential model for the function of

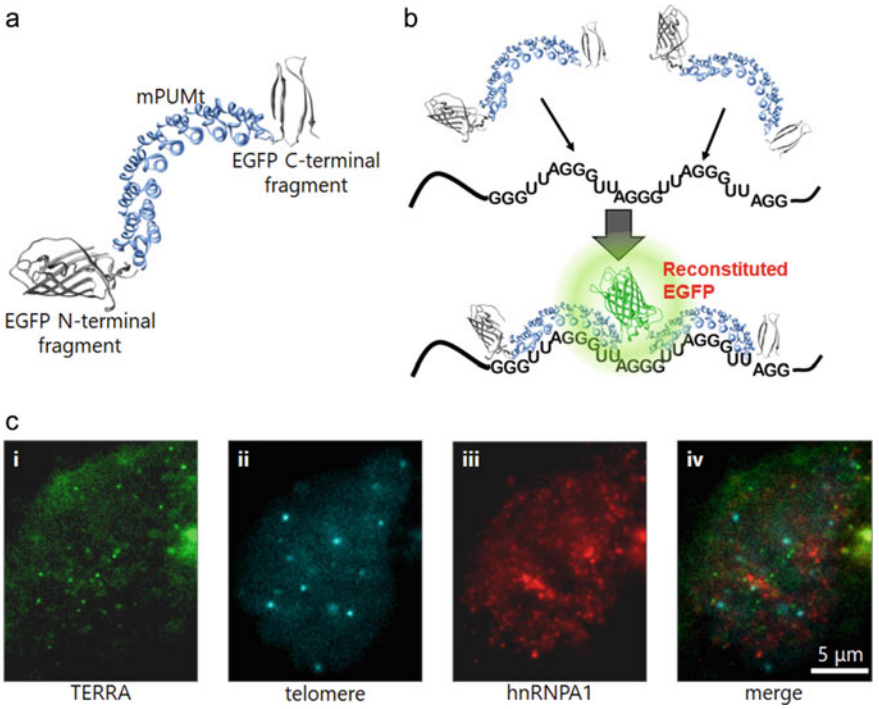

Fig. 6.4 Single molecule observation of TERRA [31]. **a** A schematic of mPUM-based TERRA probe. **b** Principle to detect TERRA by the mPUM-based probe. **c** Obtained single molecule fluorescence images of TERRA, telomere, and hnRNPA1

TERRA was proposed. The hnRNPA1 was originally located in an RNP complex on a telomere. When TERRAs appear around the telomere and form a scaffold, hnRNPA1 is captured with the TERRA scaffold upon release from telomeres. Subsequently, the component of the RNP is altered leading to a change in state of the telomere and the on/off regulation of the function of telomere maintenance. While further analyses of the dynamics and biochemical properties of TERRA and the associated molecules are required to obtain proof of this hypothesis, these results are achieved by development of the TERRA probe based on mPUM and split EGFP reconstitution techniques and unique of a single-molecule imaging approach (Fig. 6.4).

6.6 Perspective

The single-molecule RNA imaging study using a probe based on mPUM and split fluorescent protein techniques was used to obtain unique information different from previous biochemical experiments. Single-molecule imaging provides information that other methods cannot discern. However, certain limitations can be attributed on

the single-molecule RNA imaging using the probe introduced here. The observation time is limited to just a few second owing to photobleaching and the lack of quantitativity due to the irreversibility of fluorescent protein reconstitution. In order to apply the mPUM technology to different situation of RNA imaging analysis from short-term single-molecule imaging, some technical variations are expected. An approach for introducing such modifications is to swap the split fluorescent protein portion with other protein tools. For instance, quantitative RNA probes could be designed using a split luciferase reconstitution technique [30] or a fluorescent protein FAST [39], whose reconstitution reactions are reversible. When higher specificity of the target RNA is required, a modified mPUM consisting of 14 or 16 repeated motifs can be applied to the design of mPUM-based RNA probes [29]. Thus, the mPUM-based probe has a potential to modify the design to fit with the requirements of the investigations.

The evolution of microscopic methods will improve RNA imaging in living cells. The study introduced above used an oblique illumination technique. Hence, the resulting data are two-dimensional (2D) images, whereas RNA demonstrates three-dimensional (3D) diffusion in the cells. Recently, several techniques have been developed to obtain 3D fluorescence images in living cells. One such method for developing 3D images is based on the use of 2D diffraction grating to separate fluorescence light to multiple beams and to induce different areas on an image sensor [40]. The respective area has an image of the sample at obtained different depths. By the combination of such images, a 3D image is constructed. Another method to create a 3D image is based on the use of a light sheet as the excitation source. The use of lattice light sheet is a technique for obtaining high-resolution 3D images [41, 42]. Such techniques involving modified detection and excitation optical systems will support the 3D observation of the motility of target molecules in living cells.

In conclusion, the properties of mPUM, such as design flexibility and specificity for the target RNA sequence have been used for protein-based tools for live-cell optical imaging of RNAs. Even the single-molecule dynamics of an RNA of interest can be visualized in living cells combining the mPUM technology and optical microscope techniques. With further development of these technologies in the near future, the molecular mechanisms of RNA function in living cells can be elucidated.

Acknowledgements This work was supported by the Japan Society for the Promotion of Science (JSPS) KAKENHI (Grants-in-Aid for Scientific Research (B) 16H04162 and 19H02745 to H.Y., and Grants-in-Aid for Scientific Research (A) 19H00900 to T.O.) and CREST (JPMJCR1752 to T.O.) from Japan Science and Technology (JST).

References

1. T. Ozawa, H. Yoshimura, S.B. Kim, Advances in fluorescence and bioluminescence imaging. Anal. Chem. **85**(2), 590–609 (2013)
2. E.A. Specht, E. Braselmann, A.E. Palmer, A critical and comparative review of fluorescent tools for live-cell imaging. Annu. Rev. Physiol. **79**, 93–117 (2017)

3. N.K. Roopa, M. Kumar, V. Bhalla, Design and applications of small molecular probes for calcium detection. Chem. Asian J. **14**(24), 4493–4505 (2019)
4. T. Rose, P.M. Goltstein, R. Portugues, O. Griesbeck, Putting a finishing touch on GECIs. Front. Mol. Neurosci. **7**, 88 (2014)
5. A.R. Buxbaum, G. Haimovich, R.H. Singer, In the right place at the right time: visualizing and understanding mRNA localization. Nat. Rev. Mol. Cell Biol. **16**(2), 95–109 (2015)
6. K.C. Martin, A. Ephrussi, mRNA localization: gene expression in the spatial dimension. Cell **136**(4), 719–730 (2009)
7. C. Eliscovich, S.M. Shenoy, R.H. Singer, Imaging mRNA and protein interactions within neurons. Proc. Natl. Acad. Sci. **114**(10), E1875–E1884 (2017)
8. T. Yamada, H. Yoshimura, A. Inaguma, T. Ozawa, Visualization of nonengineered single mRNAs in living cells using genetically encoded fluorescent probes. Anal. Chem. **83**(14), 5708–5714 (2011)
9. H. Yoshimura, A. Inaguma, T. Yamada, T. Ozawa, Fluorescent probes for imaging endogenous beta-actin mRNA in living cells using fluorescent protein-tagged pumilio. ACS Chem. Biol. **7**(6), 999–1005 (2012)
10. L.L. Chen, Linking long noncoding RNA localization and function. Trends Biochem. Sci. **41**(9), 761–772 (2016)
11. F. Tomoike, H. Abe, RNA imaging by chemical probes. Adv. Drug Deliv. Rev. **147**, 44–58 (2019)
12. M.O. Urbanek, P. Galka-Marciniak, M. Olejniczak, W.J. Krzyzosiak, RNA imaging in living cells—methods and applications. RNA Biol. **11**(8), 1083–1095 (2014)
13. D.Y. Vargas, K. Shah, M. Batish, M. Levandoski, S. Sinha, S. Marras, A.E. Salvatore, P. Schedl, S. Tyagi, Single-molecule imaging of transcriptionally coupled and uncoupled splicing. Cell **147**(5), 1054–1065 (2011)
14. D.P. Bratu, B.J. Cha, M.M. Mhlanga, F.R. Kramer, S. Tyagi, Visualizing the distribution and transport of mRNAs in living cells. Proc. Natl. Acad. Sci. USA **100**(23), 13308–13313 (2003)
15. B. Turner-Bridger, M. Jakobs, L. Muresan, H.H.-W. Wong, K. Franze, W.A. Harris, C.E. Holt, Single-molecule analysis of endogenous β-actin mRNA trafficking reveals a mechanism for compartmentalized mRNA localization in axons. Proc. Natl. Acad. Sci. **115**(41), E9697–E9706 (2018)
16. W.Q. Ong, Y.R. Citron, S. Sekine, B. Huang, Live cell imaging of endogenous mRNA using RNA-based fluorescence "turn-on" probe. ACS Chem. Biol. **12**(1), 200–205 (2017)
17. J.S. Paige, K.Y. Wu, S.R. Jaffrey, RNA mimics of green fluorescent protein. Science **333**(6042), 642–646 (2011)
18. D. Guet, L.T. Burns, S. Maji, J. Boulanger, P. Hersen, S.R. Wente, J. Salamero, C. Dargemont, Combining spinach-tagged RNA and gene localization to image gene expression in live yeast. Nat. Commun. **6**, 8882 (2015)
19. J. Dictenberg, Genetic encoding of fluorescent RNA ensures a bright future for visualizing nucleic acid dynamics. Trends Biotechnol. (2012)
20. E. Tutucci, M. Vera, J. Biswas, J. Garcia, R. Parker, R.H. Singer, An improved MS2 system for accurate reporting of the mRNA life cycle. Nat. Methods **15**, 81 (2017)
21. D.A. Nelles, M.Y. Fang, M.R. O'Connell, J.L. Xu, S.J. Markmiller, J.A. Doudna, G.W. Yeo, Programmable RNA tracking in live cells with CRISPR/Cas9. Cell **165**(2), 488–496 (2016)
22. G. Lu, S.J. Dolgner, T.M. Hall, Understanding and engineering RNA sequence specificity of PUF proteins. Curr. Opin. Struct. Biol. **19**(1), 110–115 (2009)
23. T.M. Hall, De-coding and re-coding RNA recognition by PUF and PPR repeat proteins. Curr. Opin. Struct. Biol. **36**, 116–121 (2016)
24. C.G. Cheong, T.M.T. Hall, Engineering RNA sequence specificity of Pumilio repeats. Proc. Natl. Acad. Sci. **103**(37), 13635–13639 (2006)
25. X. Wang, J. McLachlan, P.D. Zamore, T.M.T. Hall, Modular recognition of RNA by a human Pumilio-homology domain. Cell **110**(4), 501–512 (2002)
26. H. Yoshimura, T. Ozawa, Chapter three—monitoring of rna dynamics in living cells using PUM-HD and fluorescent protein reconstitution technique, in *Methods in Enzymology*, vol. 572, eds. by G.S. Filonov, S.R. Jaffrey (Academic Press, 2016), pp. 65–85

27. H. Yoshimura, T. Ozawa, Real-time fluorescence imaging of single-molecule endogenous noncoding RNA in living cells. Methods Mol. Biol. **1649**, 337–347 (2018)
28. H. Yoshimura, Live cell imaging of endogenous RNAs using Pumilio homology domain mutants: principles and applications. Biochemistry **57**(2), 200–208 (2018)
29. A. Filipovska, M.F. Razif, K.K. Nygard, O. Rackham, A universal code for RNA recognition by PUF proteins. Nat. Chem. Biol. **7**(7), 425–427 (2011)
30. H. Yoshimura, T. Ozawa, Methods of split reporter reconstitution for the analysis of biomolecules. Chem. Rec. **14**(3), 492–501 (2014)
31. T. Yamada, H. Yoshimura, R. Shimada, M. Hattori, M. Eguchi, T.K. Fujiwara, A. Kusumi, T. Ozawa, Spatiotemporal analysis with a genetically encoded fluorescent RNA probe reveals TERRA function around telomeres. Sci. Rep. **6**, 38910 (2016)
32. M. Tokunaga, N. Imamoto, K. Sakata-Sogawa, Highly inclined thin illumination enables clear single-molecule imaging in cells. Nat. Methods **5**(2), 159–161 (2008)
33. C.M. Azzalin, P. Reichenbach, L. Khoriauli, E. Giulotto, J. Lingner, Telomeric repeat containing RNA and RNA surveillance factors at mammalian chromosome ends. Science **318**(5851), 798–801 (2007)
34. C.M. Roake, S.E. Artandi, Approaching TERRA firma: genomic functions of telomeric noncoding RNA. Cell **170**(1), 8–9 (2017)
35. M. Graf, D. Bonetti, A. Lockhart, K. Serhal, V. Kellner, A. Maicher, P. Jolivet, M.T. Teixeira, B. Luke, Telomere length determines TERRA and R-Loop regulation through the cell cycle. Cell **170**(1), 72–85.e14 (2017)
36. H.P. Chu, C. Cifuentes-Rojas, B. Kesner, E. Aeby, H.G. Lee, C. Wei, H.J. Oh, M. Boukhali, W. Haas, J.T. Lee, TERRA RNA Antagonizes ATRX and protects telomeres. Cell **170**(1), 86–101.e16 (2017)
37. Z. Deng, J. Norseen, A. Wiedmer, H. Riethman, P.M. Lieberman, TERRA RNA binding to TRF2 facilitates heterochromatin formation and ORC recruitment at telomeres. Mol. Cell **35**(4), 403–413 (2009)
38. R.L. Flynn, R.C. Centore, R.J. O'Sullivan, R. Rai, A. Tse, Z. Songyang, S. Chang, J. Karlseder, L. Zou, TERRA and hnRNPA1 orchestrate an RPA-to-POT1 switch on telomeric single-stranded DNA. Nature **471**(7339), 532–536 (2011)
39. A.G. Tebo, A. Gautier, A split fluorescent reporter with rapid and reversible complementation. Nat. Commun. **10**(1), 2822 (2019)
40. S. Abrahamsson, J. Chen, B. Hajj, S. Stallinga, A.Y. Katsov, J. Wisniewski, G. Mizuguchi, P. Soule, F. Mueller, C. Dugast Darzacq, X. Darzacq, C. Wu, C.I. Bargmann, D.A. Agard, M. Dahan, M.G. Gustafsson, Fast multicolor 3D imaging using aberration-corrected multifocus microscopy. Nat. Methods **10**(1), 60–63 (2013)
41. B.-C. Chen, W.R. Legant, K. Wang, L. Shao, D.E. Milkie, M.W. Davidson, C. Janetopoulos, X.S. Wu, J.A. Hammer, Z. Liu, B.P. English, Y. Mimori-Kiyosue, D.P. Romero, A.T. Ritter, J. Lippincott-Schwartz, L. Fritz-Laylin, R.D. Mullins, D.M. Mitchell, J.N. Bembenek, A.-C. Reymann, R. Böhme, S.W. Grill, J.T. Wang, G. Seydoux, U.S. Tulu, D.P. Kiehart, E. Betzig, Lattice light-sheet microscopy: imaging molecules to embryos at high spatiotemporal resolution. Science **346**(6208), 1257998 (2014)
42. L. Balagopalan, J. Yi, T. Nguyen, K.M. McIntire, A.S. Harned, K. Narayan, L.E. Samelson, Plasma membrane LAT activation precedes vesicular recruitment defining two phases of early T-cell activation. Nat. Commun. **9**(1), 2013 (2018)

Chapter 7
Angular Momentum Conversion of the Light Beams in Three-Wave Mixing Processes in the Bulk and on the Surface of Isotropic Chiral Medium

K. S. Grigoriev, I. A. Perezhogin, V. A. Diukov, and V. A. Makarov

Abstract The interconversion and total conservation of spin and orbital components of angular momentum of light is analytically considered in various nonlinear optical processes in isotropic chiral medium, such as sum frequency and second harmonic generation on the surface and in the bulk of the medium. The nonlocality of nonlinear response and the symmetry break in its near surface layer were taken into account, and for each process the selection rules for interacting photons were derived.

7.1 Introduction

The idea that light possesses not only linear but angular momentum (AM) as well was firstly proposed by J.H. Poynting himself [1]. Further discussions on the components of this angular momentum, their gauge invariance, quantum explanation etc. were particularly difficult, and this topic was usually avoided in experimental physics. Only in the early 90s, when the paper [2] about the angular momentum of paraxial light was written, the interest in this topic started to grow. It was shown that paraxial light beams can carry AM, because their electric and magnetic fields are not entirely transverse. Due to the spatial finiteness of the beams, a small longitudinal component of the

K. S. Grigoriev (✉) · V. A. Diukov · V. A. Makarov
Physics Faculty, Moscow State University, Leninskie Gory 1, Moscow, Russia
e-mail: ksgrigoriev@ilc.edu.ru

V. A. Diukov
e-mail: diukov.va16@physics.msu.ru

V. A. Makarov
e-mail: vamakarov@phys.msu.ru

I. A. Perezhogin
Technological Institute for Superhard and Novel Carbon Materials, Centralnaya 7a, Troitsk, Russia

I. A. Perezhogin · V. A. Makarov
International Laser Center, Moscow State University, Leninskie Gory 1, Moscow, Russia

K. Yamanouchi et al. (eds.), *Progress in Photon Science*, Springer Series in Chemical Physics 125, https://doi.org/10.1007/978-3-030-77646-6_7

electric field appears, the complex amplitude of which is related to the transverse amplitude $\mathbf{E}_\perp$ as follows:

$$E_z = \mathrm{i}k^{-1}\,\mathrm{div}\,\mathbf{E}_\perp, \tag{7.1}$$

where k is the wavenumber of the beam. The presence of the longitudinal component of the field makes the Poynting vector slightly non-parallel to the beam axis, and its transverse flow may create non-zero longitudinal projection of the optical AM. In paraxial optics, it is separated into two distinctive parts. The first is called orbital angular momentum (OAM), caused by the transverse flow of electromagnetic energy density in the cross-section of the beam and commonly present in the beams containing phase singularities (optical vortices). The second is called spin angular momentum (SAM), and it is associated with the polarization of the beam. It is maximal for the circularly polarized beams and zero for the linearly polarized ones.

Light beams with AM became an important tool in many branches of modern applied optics, including manipulation of the micro-particles [3, 4], spectroscopy [5, 6], quantum information science [7–9], precision measurements [10], material processing [11] and telecommunication [12]. The behavior of light with angular momentum is also actively studied in nonlinear optics [13–21]. One of the key problems in the nonlinear interaction of light and matter is the conservation of the light AM and possible interconversion between its spin and orbital parts. Typically, OAM and SAM are treated separately, because the synchronism is achieved only with certain polarization states of the interacting light beams. However, this requirement is not necessary in isotropic nonlinear media, e.g. chiral liquids with nonlocal optical response. It was shown that sum frequency and second harmonic generation can be achieved in this kind of medium for basically any polarization state of the input light, and the relations between the spin and orbital parts of AM of the beams were revealed. The chapter outlines the contents of our previous publications [22–24] and presents a comparative description of the AM conversion of the light beams in three-wave mixing processes in the bulk and on the surface of nonlinear isotropic medium.

7.2 Bulk Sum-Frequency Generation

Consider two monochromatic paraxial beams at the frequencies ω_1 and ω_2 collinearly propagating in isotropic chiral medium along the same axis Oz (Fig. 7.1). Within undepleted pump approximation (UPA) we assume that pump beams propagate linearly in the isotropic medium and the evolution of their transverse complex amplitudes $\mathbf{E}_{m\perp}$ is described by ordinary parabolic equations:

$$2\mathrm{i}\tilde{k}_m \partial_z \mathbf{E}_{m\perp} + \left(\partial_x^2 + \partial_y^2\right)\mathbf{E}_{m\perp} = 0. \tag{7.2}$$

Here and further, the number $m = 1, 2$ indicates the characteristics of the mth beam, $\tilde{k}_m = n_m\omega_m/c$, where n_m are real refractive indices of the medium at the correspond-

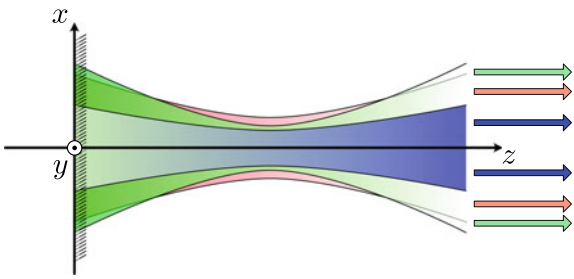

Fig. 7.1 Scheme of collinear sum-frequency generation in the bulk of isotropic medium (in the region $z \geq 0$). The pump beams are shown in red and green and the signal beam is shown in blue

ing frequencies and c is the speed of light. To study the AM transformations we will focus on a particular set of (7.2) solutions, namely, Laguerre-Gaussian modes with circular polarization. Their scalar envelopes $\Lambda_n^{(l)}$ are given by the following expression in cylindrical coordinates (r, φ, z):

$$\Lambda_n^{(l)}(\rho_m, \varphi, \beta_m) = \frac{\rho_m^{|l|}}{\beta_m^{n+|l|+1}} L_n^{(|l|)}\left(\frac{\rho_m^2}{\beta_m}\right) \exp\left(\mathrm{i}l\varphi - \frac{\rho_m^2}{\beta_m}\right). \tag{7.3}$$

The modes are characterized by two integers: the azimuthal index l and the radial index $n \geq 0$. The dimensionless coordinates are their own for each beam: $\rho_m = r/w_m$ and $\beta_m(z) = 1 + \mathrm{i}(z - z_0)/z_m$, where w_m is the waist size and $z_m = \tilde{k}_m w_m^2/2$ is the diffraction length of the mth beam. For the sake of simplicity, we will assume that z_0 is the same for all modes of both beams. Regardless of the index n, the z-projection of the OAM of all photons in mode (7.3) is equal to $l\hbar$. The transverse polarization state of the modes are given by unit constant vectors of right-hand circular polarization $\mathbf{e}_R = (\mathbf{e}_x + \mathrm{i}\mathbf{e}_y)/\sqrt{2}$ or left-hand circular polarization $\mathbf{e}_L = \mathbf{e}_R^*$, where $\mathbf{e}_x$ and $\mathbf{e}_y$ are the orthogonal unit vectors, perpendicular to the propagation axis of the beams. The z-projection of the SAM of the circularly polarized mode is $s\hbar$, where $s = 1$ is for the right-hand polarization and $s = -1$ for the left-hand polarization.

The beam at the sum frequency $\omega_3 = \omega_1 + \omega_2$ is generated by the solenoidal part of the medium nonlinear polarization field with the complex amplitude $\mathbf{P}^{(\mathrm{s})}$. The transverse amplitude $\mathbf{E}_{3\perp}$ of the signal beam is the solution of the following heterogeneous parabolic equation [23]:

$$2\mathrm{i}\tilde{k}_3 \partial_z \mathbf{E}_{3\perp} + \left(\partial_x^2 + \partial_y^2\right)\mathbf{E}_{3\perp} = -\frac{4\pi\omega_3^2}{c^2}\mathbf{P}_\perp^{(\mathrm{s})} \exp(\mathrm{i}\Delta k z), \tag{7.4}$$

where $\tilde{k}_3 = n_3\omega_3/c$ and the wavevector mismatch $\Delta k = \tilde{k}_3 - \tilde{k}_1 - \tilde{k}_2$. We assume that the field at the sum frequency does not exist at the border of the medium, so that $\mathbf{E}_3(x, y, 0) = 0$. It is necessary to separate the solenoidal part of the medium polarization $\mathbf{P}^{(\mathrm{s})}$ instead of using the total field $\mathbf{P}$, because the former consist of transverse Fourier harmonics, and only they can generate a free electromagnetic

wave in the bulk of the medium. In paraxial approximation the separation of the solenoidal part is done in a simple way:

$$\mathbf{P}_{\perp}^{(s)} = \mathbf{P}_{\perp} + \mathrm{i}(\tilde{k}_1 + \tilde{k}_2)^{-1}\nabla_{\perp} P_z, \tag{7.5}$$

where $\nabla_{\perp} = \mathbf{e}_x\partial_x + \mathbf{e}_y\partial_y$.

In isotropic chiral medium the external symmetry group of the quadratic response tensor is $\infty\infty$ and the complex amplitude of the nonlinear polarization vector $\mathbf{P}$ is proportional to the vector product of the amplitudes of pump beams [25]

$$\mathbf{P} = \chi_0[\mathbf{E}_1 \times \mathbf{E}_2], \tag{7.6}$$

where χ_0 is a material constant, which is equal to zero if the medium is not chiral. Note that (7.6) makes use of total complex amplitudes, including their small longitudinal projections (7.1). The substitution of (7.6) to (7.5) yields the relation between the fields of the pump beam and the solenoidal part of the medium polarization vector in a form of the following convolution:

$$P_{3\zeta}^{(s)} = (\tilde{k}_1 + \tilde{k}_2)^{-1}\left(d^{(1)}_{\zeta\eta\xi\theta}E_{2\xi}\partial_\theta E_{1\eta} + d^{(2)}_{\zeta\eta\xi\theta}E_{1\eta}\partial_\theta E_{2\xi}\right). \tag{7.7}$$

Here, instead of Cartesian x and y, Greek indices take values R and L and summation is performed over repeated indices. The combinations $E_{mR} = (E_{mx} - \mathrm{i}E_{my})/\sqrt{2}$ and $E_{mL} = (E_{mx} + \mathrm{i}E_{my})/\sqrt{2}$ are the amplitudes of circularly polarized components of the pump beams (their projections onto the basis $\mathbf{e}_R$, $\mathbf{e}_L$) and special transverse differential operators $\partial_R = \partial_L^* = (\partial_x + \mathrm{i}\partial_y)/\sqrt{2}$ are used. Note that the terms, proportional to "classical" products $E_{1\eta}E_{2\xi}$, are absent in (7.7), which essentially makes the response of the medium non-local. Below we list all non-zero coefficients of the tensors $d^{(m)}_{\zeta\eta\xi\theta}$:

$$d^{(1)}_{RLRL} = -d^{(1)}_{LRLR} = \chi_0\tilde{k}_2/\tilde{k}_1; \quad d^{(2)}_{RRLL} = -d^{(2)}_{LLRR} = -\chi_0\tilde{k}_1/\tilde{k}_2; \tag{7.8}$$

$$d^{(1)}_{RRLL} = -d^{(1)}_{LLRR} = -d^{(2)}_{RLRL} = d^{(2)}_{LRLR} = \chi_0; \tag{7.9}$$

$$d^{(m)}_{RRRR} = -d^{(m)}_{LLLL} = d^{(m)}_{RRLL} + d^{(m)}_{RLRL}. \tag{7.10}$$

To understand the conversions of light AM in collinear sum-frequency generation, we need to analyze the action of operators $\partial_{R,L}$ on Laguerre-Gaussian modes in (7.3):

$$\partial_R\Lambda_n^{(l)} = w_m^{-1}\sqrt{2}(n+1)\Lambda_{n+1}^{(l+1)}, \quad l < 0, \tag{7.11}$$

$$\partial_R\Lambda_n^{(l)} = -w_m^{-1}\sqrt{2}\Lambda_n^{(l+1)}, \quad l \geq 0, \tag{7.12}$$

$$\partial_L\Lambda_n^{(l)} = -w_m^{-1}\sqrt{2}\Lambda_n^{(l-1)}, \quad l \leq 0, \tag{7.13}$$

$$\partial_L \Lambda_n^{(l)} = w_m^{-1}\sqrt{2}(n+1)\Lambda_{n+1}^{(l-1)}, \quad l > 0. \tag{7.14}$$

Essentially, operators $\partial_{R,L}$ are raising and lowering the azimuthal index of Laguerre-Gaussian mode by unity. As it follows from (7.7), if two pump beams are single modes with indices l_1 and l_2, the dependence of products $E_{2\xi}\partial_\theta E_{1\eta}$ and $E_{1\xi}\partial_\theta E_{2\eta}$ on polar angle φ is $\exp[\mathrm{i}(l_1 + l_2 \pm 1)]$, where the sign is determined by the operator ∂_θ. Solving (7.4) by Green function method, we retain the same angular dependencies in the field at the sum-frequency, since the Green function of (7.4)

$$\mathrm{Gr}(x, y, z) = -\frac{\mathrm{i}\tilde{k}_3}{2\pi z}\exp\left(\frac{\mathrm{i}\tilde{k}_3(x^2+y^2)}{2z}\right) \tag{7.15}$$

does not depend on φ. We will show in detail which modes are generated for each possible combination of polarization states of pump beams and how their AM is transformed during the process of SFG:

- "Right+Right". When both pump beams are right-hand circularly polarized ($s_1 = s_2 = 1$), only two summands with coefficients $d^{(m)}_{RRRR}$ are left in (7.7). Therefore, the azimuthal index of all generated modes is $l_3 = l_1 + l_2 + 1$. The polarization of the signal beam is right-handed as well, so the spin index $s_3 = s_1 + s_2 - 1$. As a result, we have the equality $l_1 + s_1 + l_2 + s_2 = l_3 + s_3$.
- "Left+Left". The mixing of two left-hand circularly polarized beams ($s_1 = s_2 = -1$) is described by coefficients $d^{(m)}_{LLLL}$. The azimuthal index l_3 is less than $l_1 + l_2$ by unity. However, the spin indes $s_3 = -1$ is greater than $s_1 + s_2$ by unity. Thus, the equality $l_1 + s_1 + l_2 + s_2 = l_3 + s_3$ is also valid.
- "Right+Left". In the case of opposite beam polarizations ($s_1 = -s_2 = 1$), two different transverse modes are generated at the sum frequency. They are described by the coefficients $d^{(m)}_{RRLL}$ and $d^{(m)}_{LRLR}$ respectively. The first mode is right-hand polarized ($s_3 = 1 = s_1 + s_2 + 1$) and its azimuthal index is $l_3 = l_1 + l_2 - 1$ due to the action of the operator ∂_L. The second one is left-hand polarized ($s_3 = -1 = s_1 + s_2 - 1$), but its azimuthal index is $l_3 = l_1 + l_2 + 1$. For each mode the same equality $l_1 + s_1 + l_2 + s_2 = l_3 + s_3$ is valid, as well as for the modes described by $d^{(m)}_{LLRR}$ and $d^{(m)}_{RLRL}$ that are generated in the case $s_1 = -s_2 = -1$.

It is readily seen that there are two relations $l_3 = l_1 + l_2 \pm 1$, $s_3 = s_1 + s_2 \mp 1$ if the photons in incident beams are in the states with single OAM, defined by indices l_m, and single SAM, defined by s_m. The z-projection of neither SAM nor OAM of the signal photon is equal to the sum of the corresponding projections of the pump photons. However, the total AM of the signal photon, which is the sum of its OAM and SAM, is indeed the sum of total AM of the pump photons. The above scenarios of the interaction of the photons are illustrated in Fig. 7.2. Even if the pump beams consist of many transverse modes and have non-uniform polarization, the above statements are valid for each pair of their interacting circularly polarized Laguerre-Gaussian modes.

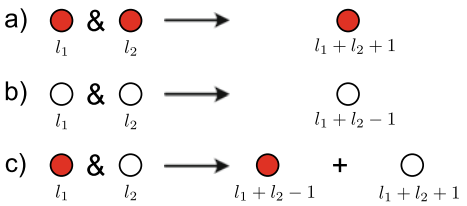

Fig. 7.2 Schematic illustration of selection rules in the bulk SFG, when two fundamental photons have **a** the same positive SAM projections, **b** the same negative SAM projections, **c** different SAM projections on the propagation direction. Filled (open) circles represent the photons of pump and signal beams with positive (negative) SAM projections, the corresponding OAM indices are written below the circles

Although the total AM is conserved when considering separate acts of three-photon mixing with well-defined OAM and SAM, the corresponding conservation law is generally not fulfilled for the quantum mean values of total AM, sometimes called "AM-per-photon" in a semiclassical manner. This AM can be calculated as the ratio of total AM of the whole signal beam and "the number of photons" in it, which is the energy of the beam divided by $\hbar\omega_3$. Consider one of the simplest example of SFG process, when pump beams are elliptically polarized Gaussian modes with the vector complex amplitudes

$$\mathbf{E}_m = 2^{-1/2}\left(\sqrt{1+\sigma_m}\mathrm{e}^{-\mathrm{i}\Psi_m}\mathbf{e}_R + \sqrt{1-\sigma_m}\mathrm{e}^{\mathrm{i}\Psi_m}\mathbf{e}_L\right)\Lambda_0^{(0)}(\rho_m, \varphi, \beta_m). \quad (7.16)$$

Here σ_m are the values of normalized third Stokes parameter, defining the ellipticity degrees of the beam polarizations, and Ψ_m are the angles between the major axes of the ellipses and the x-axis in the beams cross-sections. From the quantum point of view, the photon of the pump beams are in the superposition of two states ($l = 0$; $s = 1$) and ($l = 0$; $s = -1$), so that quantum mean value of the total AM of the mth beam is $\hbar\sigma_m$. According to (7.7), the mixing of these beams yields four different transverse modes in the signal beam, namely ($l = 1$; $s = 1$), ($l = -1$; $s = -1$), ($l = -1$; $s = 1$) and ($l = 1$; $s = -1$). The coefficients of these modes were found in [22] as well as the quantum mean value of the total AM of the signal beam:

$$\frac{\hbar(\sigma_1 + \sigma_2)}{1 - \frac{\tilde{k}_1\tilde{k}_2}{(\tilde{k}_1+\tilde{k}_2)^2}\left[1 - \sigma_1\sigma_2 - \cos 2\Psi\sqrt{(1-\sigma_1^2)(1-\sigma_2^2)}\right]}. \quad (7.17)$$

Here $\Psi = \Psi_2 - \Psi_1$ is the angle between the major axes of the polarization ellipses of the pump beams. It is clearly seen, that "AM per photon" of the signal beam is equal to the sum $\hbar(\sigma_1 + \sigma_2)$ only if this sum is zero or $\pm 2\hbar$. In all other cases, there is a discrepancy between these two quantities, which depends even on the relative orientation of the pump beams (Fig. 7.3). This discrepancy can be ascribed to the fact that the coefficients of the four modes in the signal beam are determined by their own laws, e.g. by the ratio of the wavevectors of the pump beams and that each of

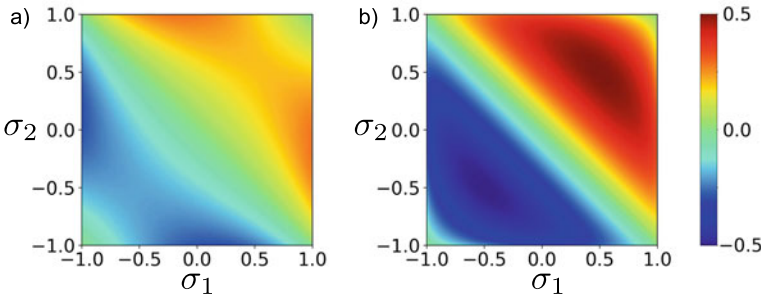

Fig. 7.3 The difference between total AM-per-photon of a signal beam at the sum frequency and the sum of total AM-per-photon of two elliptically polarized Gaussian pump beams expressed in units of $\hbar$ and plotted over their normalized third Stokes parameters σ_1 and σ_2. The plots are made for two different angles $\Psi = \pi/4$ (**a**) and $\Psi = \pi/2$ (**b**) between the major axes of the polarization ellipses of the pump beams. The ratio of their wavenumbers $\tilde{k}_2/\tilde{k}_1 = 2$

the modes with zero total AM ($(l = 1; s = -1)$ and $(l = -1; s = 1)$) is generated by two different combinations of input photons: $s_1 = -s_2 = 1$ and $s_1 = -s_2 = -1$, and these two processes interfere with each other. For this reason, the energy of these modes is different for different values of Ψ, while total AM of the signal beam does not depend on this parameter [22]. Overall, this leads to the different values of "AM-per-photon" of the signal beam.

7.3 Surface Sum-Frequency Generation

Consider two monochromatic beams collinearly incident from vacuum on the surface of an isotropic chiral medium along the axis Oz, perpendicular to the medium surface (Fig. 7.4). The transverse complex amplitude of incident beams are the solutions of parabolic equations

$$2\mathrm{i}k_m \mathbf{E}_{m\perp} + \left(\partial_x^2 + \partial_y^2\right)\mathbf{E}_{m\perp} = 0, \tag{7.18}$$

where $k_m = \omega_m/c$. Using these equations, we can write the spatial distribution of the incident field complex amplitude, taking into account the propagation factor $\exp(\mathrm{i}k_m z)$, as the following Fourier integral

$$\mathbf{E}_{m\perp}\exp(\mathrm{i}k_m z) = \int \hat{\mathbf{E}}_m(\mathbf{k}_\perp)\exp\left[\mathrm{i}\mathbf{k}_\perp\mathbf{r}_\perp + \mathrm{i}k_m\left(1 - \frac{|\mathbf{k}_\perp|^2}{2k_m^2}\right)z\right]\mathrm{d}\mathbf{k}_\perp. \tag{7.19}$$

Equation (7.19) actually represents the propagating field as a superposition of plane waves with slightly non-collinear wavevectors which, in accordance with paraxial approximation, have small transverse projections $\mathbf{k}_\perp$ and thus, slightly modified z-projection. We consider the absolute value of $\hat{\mathbf{E}}_{m\perp}$ to decrease fast enough with the increase of $|\mathbf{k}_\perp|$; therefore integration in (7.19) is done over all values of $\mathbf{k}_\perp$.

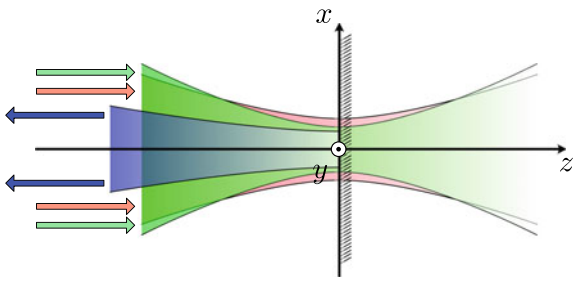

Fig. 7.4 Scheme of reflective sum-frequency generation from the surface of isotropic medium (in the region $z \geq 0$). The incident pump beams are shown in red and green and the reflected signal beam is shown in blue

To find the field of the reflected beam at the sum-frequency, we will evaluate the contribution of each pair of Fourier harmonics $\hat{\mathbf{E}}_1(\mathbf{k}_{1\perp})$ and $\hat{\mathbf{E}}_2(\mathbf{k}_{2\perp})$ to the spatial Fourier spectrum of the signal field and then integrate the result over $\mathbf{k}_{1\perp}$ and $\mathbf{k}_{2\perp}$ and perform inverse Fourier transform.

Since the signal beam is generated by the nonlinear polarization of the medium, we have to find the amplitude of the transmitted Fourier harmonics $\hat{\mathbf{E}}_m^{(t)}$. In the case of normal incidence, their transverse components are simply $\hat{\mathbf{E}}_{m\perp}$ multiplied by $2/(1+n_m)$. The small longitudinal projection of the transmitted waves is found by a transversality constraint: $\hat{E}_{mz}^{(t)} = -\left(\mathbf{k}_{m\perp} \cdot \hat{\mathbf{E}}_{m\perp}^{(t)}\right)/\tilde{k}_m$, where $\tilde{k}_m = n_m k_m$. The complex amplitude $\hat{\mathbf{P}}$ of the corresponding Fourier harmonic of medium polarization vector can be found by the same material equation (7.6), in the right-hand part of which the complex amplitudes $\hat{\mathbf{E}}_m^{(t)}$ are used. The polarization of the medium generates two waves inside it. The first one is a non-transverse wave with the complex amplitude $\hat{\mathbf{E}}_N$ and wavevector $\mathbf{k}_N = \mathbf{k}_{3\perp} + (\tilde{k}_1 + \tilde{k}_2)\mathbf{e}_z$, where $\mathbf{k}_{3\perp} = \mathbf{k}_{1\perp} + \mathbf{k}_{2\perp}$. The second one is a transverse wave with the complex amplitude $\hat{\mathbf{E}}_O$ and wavevector $\mathbf{k}_{1\perp} + \mathbf{k}_{2\perp} + \tilde{k}_3\mathbf{e}_z$, where $\tilde{k}_3 = n_3(k_1 + k_2)$. The amplitude $\hat{\mathbf{E}}_N$ can be found by direct solution of the Maxwell equations

$$\hat{E}_{Ni} = -\frac{4\pi}{n_3^2}\frac{\tilde{k}_3^2\delta_{ij} - k_{Ni}k_{Nj}}{\tilde{k}_3^2 - k_N^2}\hat{P}_j, \tag{7.20}$$

where summation is performed over repeated index j and δ_{ij} is the Kronecker symbol. To find the amplitude $\hat{\mathbf{E}}_O$ and the amplitude of the Fourier harmonic of the reflected field $\hat{\mathbf{E}}_3$ we have to use the boundary conditions for the field at the sum frequency:

$$\hat{\mathbf{E}}_{3\perp} - \hat{\mathbf{E}}_{O\perp} = \hat{\mathbf{E}}_{N\perp}, \tag{7.21}$$

$$\hat{\mathbf{E}}_{3z} - n_3^2\hat{\mathbf{E}}_{Oz} = n_3^2\hat{\mathbf{E}}_{N\perp} + 4\pi\hat{P}_z, \tag{7.22}$$

$$k_3\left(\hat{\mathbf{E}}_{3\perp} + n_3\hat{\mathbf{E}}_{O\perp}\right) = \mathbf{k}_{3\perp}(\hat{E}_{Nz} + \hat{E}_{Oz} - \hat{E}_{3z}) - (\tilde{k}_1 + \tilde{k}_2)\hat{\mathbf{E}}_{N\perp} \tag{7.23}$$

and transversality constraints $\hat{E}_{Oz} = -\left(\mathbf{k}_{3\perp} \cdot \hat{\mathbf{E}}_{O\perp}\right)/\tilde{k}_3$ and $\hat{E}_{3z} = \left(\mathbf{k}_{3\perp} \cdot \hat{\mathbf{E}}_{3\perp}\right)/k_3$, where $k_3 = k_1 + k_2$. The transverse projection $\hat{\mathbf{E}}_{3\perp}$, obtained from (7.21)–(7.23) is expressed as follows:

$$\hat{\mathbf{E}}_3 = -\frac{4\pi\mathcal{M}}{1+n_3}\left(\hat{\mathbf{P}}_{3\perp} + \mathbf{k}_{3\perp}\hat{P}_z/\tilde{k}_3\right). \tag{7.24}$$

Here $\mathcal{M} = k_3/(\tilde{k}_1 + \tilde{k}_2 + \tilde{k}_3)$. After integrating (7.24) over $\mathbf{k}_{1\perp}$ and $\mathbf{k}_{2\perp}$ and inverse Fourier transform of this integral one obtains the transverse distribution of the reflected field at the sum-frequency in the cross-section $z = 0$. The reflected beam propagates along the opposite direction to the incident beam and for this reason we will use another system of Cartesian unit vectors $\mathbf{e}_{x1} = -\mathbf{e}_x$, $\mathbf{e}_{y1} = \mathbf{e}_y$, $\mathbf{e}_{z1} = -\mathbf{e}_z$ to analyze it. The relation between the incident and reflected fields can be written as the convolution, similar to (7.7),

$$E_{3\zeta} = \mathcal{M}D_0\tilde{k}_3^{-1}\left(d^{(1)}_{\zeta\eta\xi\theta}\tilde{E}_{2\xi}\tilde{\partial}_\theta E_{1\eta} + d^{(2)}_{\zeta\eta\xi\theta}\tilde{E}_{1\eta}\tilde{\partial}_\theta E_{2\xi}\right), \tag{7.25}$$

where $D_0 = 16\pi\left[(1+n_1)(1+n_2)(1+n_3)\right]^{-1}$. The Greek notation in (7.25) is the same as in (7.7), but the components of the reflected field refer to its own coordinate system: $E_{3R} = (E_{3x_1} - \mathrm{i}E_{3y_1})/\sqrt{2}$ and $E_{3L} = (E_{3x_1} + \mathrm{i}E_{3y_1})/\sqrt{2}$. The tildes in (7.25) are needed for the coordination between two systems. They indicate that in order to obtain the amplitude of the reflected field in the point (x_1, y_1), we have to make use of the amplitudes of the incident field and their derivatives in the point $(-x_1, y_1)$. This coordinate transformation results in the reverting the sign of index l of any Laguerre-Gaussian mode of the beam: $\tilde{\Lambda}^{(l)}_n = (-1)^{|l|}\Lambda^{(-l)}_n$. All the non-zero coefficients $d^{(1)}_{\zeta\eta\xi\theta}$ form a following set:

$$d^{(1)}_{LRRR} = -d^{(1)}_{RLLL} = \chi_0\tilde{k}_3/\tilde{k}_1; \quad d^{(2)}_{RLLL} = -d^{(2)}_{LRRR} = \chi_0\tilde{k}_3/\tilde{k}_2; \tag{7.26}$$

$$d^{(1)}_{RLRR} = d^{(2)}_{LLRL} = -d^{(1)}_{LRLL} = -d^{(2)}_{RRLR} = \chi_0; \tag{7.27}$$

$$d^{(1)}_{RRLR} = -d^{(1)}_{LLRL} = d^{(1)}_{RLLL} - d^{(1)}_{RLRR}; \tag{7.28}$$

$$d^{(2)}_{RLRR} = -d^{(2)}_{LRLL} = d^{(2)}_{RLLL} - d^{(2)}_{RRLR}. \tag{7.29}$$

Analyzing the terms with different coefficients as was done in the previous section, we can separate them into three groups. The first one, $d^{(m)}_{LRRR}$, corresponds to the generation of the modes with indices $l_3 = -l_1 - l_2 - 1$ and $s_3 = -s_1 - s_2 + 1$. The second one, $d^{(m)}_{RLLL}$, corresponds to the generation of the modes with indices $l_3 = -l_1 - l_2 + 1$ and $s_3 = -s_1 - s_2 - 1$. The other nonzero coefficients also describe

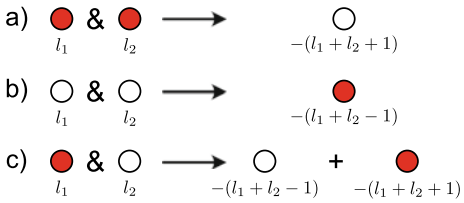

Fig. 7.5 Schematic illustration of selection rules in the surface SFG, when two fundamental photons have **a** the same positive SAM projections, **b** the same negative SAM projections, **c** different SAM projections on the propagation direction. Filled (open) circles represent the photons of pump and signal beams with positive (negative) SAM projections, the corresponding OAM indices are written below the circles

contribution to the modes with the same relations between OAM and SAM indices (Fig. 7.5). All the processes listed above obey the same conservation rule $l_3 + s_3 = -(l_1 + s_1) - (l_2 + s_2)$. This rule has a different form compared to the rule of the bulk SFG. However, this is only because different coordinate systems are used to describe the incident pump beams and the reflected signal beam. The physical entity of the new rule remains the same: the z-projection of total AM of the signal photon is equal to the sum of z-projections of total AM of the pump photons for each possible combination of indices l_m and s_m.

In the process of reflective SFG the nonlinear signal might also be caused by the symmetry breaking of the near-surface layer of the medium [26]. Commonly, the account for this effect is done by altering the material equation (7.6):

$$\hat{P}_i = \chi^{(S)}_{ijk} \hat{E}^{(t)}_{1j} \hat{E}^{(t)}_{2k}. \tag{7.30}$$

The external symmetry group of the surface response tensor $\chi^{(S)}_{ijk}$ is the same as that the surface of the medium (in our case, the group ∞). Using the new material equation, one can calculate the amplitude of the signal generated in the near-surface layer of the medium:

$$E^{(S)}_{3\zeta} = \mathrm{i}\mathcal{M} D_0 \tilde{k}_3^{-1} \left(d^{(1)}_{\zeta\eta\xi\theta} \tilde{E}_{2\xi} \tilde{\partial}_\theta E_{1\eta} + d^{(2)}_{\zeta\eta\xi\theta} \tilde{E}_{1\eta} \tilde{\partial}_\theta E_{2\xi} \right). \tag{7.31}$$

The coefficients $d^{(m)}_{\zeta\eta\xi\theta}$ are expressed through six of seven nonzero components of the tensor $\chi^{(S)}_{ijk}$: $\chi^{(S)}_{zxx} = \chi^{(S)}_{zyy} = \chi_1$, $\chi^{(S)}_{xxz} = \chi^{(S)}_{yyz} = \chi_3$, $\chi^{(S)}_{xzx} = \chi^{(S)}_{yzy} = \chi_4$, $\chi^{(S)}_{xyz} = -\chi^{(S)}_{yxz} = \chi_5$, $\chi^{(S)}_{yzx} = -\chi^{(S)}_{xzy} = \chi_6$, $\chi^{(S)}_{zxy} = -\chi^{(S)}_{zyx} = \chi_7$. The set of non-zero coefficients, however, is the same as the bulk response of the medium:

$$d^{(1)}_{RLRR} = \left(d^{(1)}_{LRLL}\right)^* = d^{(2)}_{LLRL} = \left(d^{(2)}_{RRLR}\right)^* = -\chi_1 - \mathrm{i}\chi_7, \tag{7.32}$$

$$d^{(1)}_{RLLL} = \left(d^{(1)}_{LRRR}\right)^* = \tilde{k}_3(\chi_4 + \mathrm{i}\chi_6)/\tilde{k}_1, \tag{7.33}$$

$$d^{(2)}_{RLLL} = \left(d^{(2)}_{LRRR}\right)^* = \tilde{k}_3(\chi_3 - \mathrm{i}\chi_5)/\tilde{k}_2, \tag{7.34}$$

$$d^{(1)}_{RRLR} = \left(d^{(1)}_{LLRL}\right)^* = d^{(1)}_{RLLL} + \left(d^{(1)}_{RLRR}\right)^*, \tag{7.35}$$

$$d^{(2)}_{RLRR} = \left(d^{(2)}_{LRLL}\right)^* = d^{(2)}_{RLLL} + \left(d^{(2)}_{RRLR}\right)^*. \tag{7.36}$$

For this reason, the interconversion of SAM and OAM obeys the same rules that were previously stated for the case of a purely bulk response.

The modification (7.30) to material equation, though being phenomenologically reasonable, does not always reflect the physics of the light–matter interaction correctly. For example, when the nonlinear response of the medium is spatially nonlocal, the boundary conditions (7.21)–(7.23) are incorrect. In the presence of spatial dispersion the average thickness of the transition surface layer h_1 can be comparable with the wavelengths of interacting waves [27]. An original method to account for this transition layer was developed in [26, 27]. The method retained the assumption of negligibly thin border of the medium by modification of the boundary conditions (7.21)–(7.23). These modification eventually sum up in the additional term in the expression (7.24), which is phenomenologically equivalent to the component with the tensor $\chi^{(S)}_{ijk}$ in (7.30) (but without the factor $\mathcal{M}$). Besides, qualitatively new terms appear in this material equation that describe the nonlocal part of the medium response:

$$\hat{P}_i = \gamma^{(1)}_{ijln}\hat{E}^{(t)}_{2l}\left(\mathrm{i}k^{(t)}_{1n}\right)\hat{E}^{(t)}_{1j} + \gamma^{(2)}_{ijln}\hat{E}^{(t)}_{1j}\left(\mathrm{i}k^{(t)}_{2n}\right)\hat{E}^{(t)}_{2l}, \tag{7.37}$$

where $\mathbf{k}^{(t)}_m = \mathbf{k}_{m\perp} + \tilde{k}_m\mathbf{e}_z$. In (7.37) the tensors of nonlocal quadratic nonlinearity $\gamma^{(m)}_{ijln}$ have an external symmetry group $\infty\infty$. Their nonzero components are expressed through constants $\gamma^{(m)}_{1,2,3}$: $\gamma^{(m)}_{ijji} = \gamma^{(m)}_1$, $\gamma^{(1)}_{iijj} = \gamma^{(1)}_2$, $\gamma^{(2)}_{ijij} = \gamma^{(2)}_2$, $\gamma^{(1)}_{ijij} = \gamma^{(1)}_3$, $\gamma^{(2)}_{iijj} = \gamma^{(2)}_3$, $\gamma^{(m)}_{iiii} = \gamma^{(m)}_1 + \gamma^{(m)}_2 + \gamma^{(m)}_3$, where $i, j = x, y, z$ and $i \neq j$. The contribution of the nonlocal response to the reflected field at the sum frequency may still be represented as in (7.25) and (7.31):

$$E^{(D)}_{3\zeta} = \mathcal{M}D_0\left(d^{(1)}_{\zeta\eta\xi\theta}\tilde{E}_{2\xi}\tilde{\partial}_\theta E_{1\eta} + d^{(2)}_{\zeta\eta\xi\theta}\tilde{E}_{1\eta}\tilde{\partial}_\theta E_{2\xi}\right). \tag{7.38}$$

The nonzero coefficients $d^{(m)}_{\zeta\eta\xi\theta}$ form the same set as in the cases described above:

$$d^{(1)}_{RLRR} = d^{(1)}_{LRLL} = \gamma^{(1)}_a + \gamma^{(1)}_2;\ d^{(1)}_{RLLL} = d^{(1)}_{LRRR} = \gamma^{(1)}_b + \gamma^{(1)}_2; \tag{7.39}$$

$$d^{(2)}_{RRLR} = d^{(2)}_{LLRL} = \gamma^{(1)}_a + \gamma^{(2)}_2;\ d^{(2)}_{RLRR} = d^{(2)}_{LRLL} = \gamma^{(2)}_a + \gamma^{(2)}_b; \tag{7.40}$$

$$d^{(m)}_{RLLL} = d^{(m)}_{LRRR} = \gamma^{(m)}_b + \gamma^{(m)}_2. \tag{7.41}$$

Here $\gamma^{(1)}_a = (1 + \tilde{k}_1/\tilde{k}_3)\gamma^{(1)}_1 + \tilde{k}_2\gamma^{(2)}_1/\tilde{k}_3, \gamma^{(1)}_b = -\tilde{k}_2\gamma^{(2)}_2/\tilde{k}_1, \gamma^{(2)}_a = (1 + \tilde{k}_2/\tilde{k}_3)\gamma^{(2)}_1 + \tilde{k}_1\gamma^{(1)}_1/\tilde{k}_3$ and $\gamma^{(2)}_b = -\tilde{k}_1\gamma^{(1)}_2/\tilde{k}_2$. Therefore, the details of AM transformation with its total value conservation remain unchanged.

7.4 Second-Harmonic Generation

In this section we consider a degenerate case of sum-frequency generation in both off-surface and in-bulk generation of the signal beam. In the case when only one pump beam falls on the border of the medium, a series of simplifications to (7.25), (7.31) and (7.38) are made. First of all, the terms $d^{(m)}_{\zeta\eta\xi\theta}\tilde{E}_{2\xi}\tilde{\partial}_\theta E_{1\eta}$ and $d^{(m)}_{\zeta\eta\xi\theta}\tilde{E}_{1\eta}\tilde{\partial}_\theta E_{2\xi}$ sum up to a single term $d_{\zeta\eta\xi\theta}\tilde{E}_\xi\tilde{\partial}_\theta E_\eta$, where $d_{\zeta\eta\xi\theta} = d^{(1)}_{\zeta\eta\xi\theta} + d^{(2)}_{\zeta\eta\xi\theta}$ and $\mathbf{E}$ is the complex amplitude of the pump beam. Second, the additional permuttation symmetry of the material tensors implies several important constraints on their components. The constant χ_0 becomes zero, which indicates that SHG process is forbidden in the bulk of centrosymmetric media in dipole approximation. There also appear additional conditions $\chi_4 = \chi_3$, $\chi_6 = -\chi_5$, $\chi_7 = 0$ and $\gamma^{(1)}_{1,2} = \gamma^{(2)}_{1,2} \equiv \gamma_{1,2}/2$. Finally, the refractive indices n_1 and n_2 become the same, as well as the wavenumbers k_1 and k_2.

The above simplifications lead to interesting changes in the nonlocal quadratic response of the medium. The list of non-zero coefficients $d_{\zeta\eta\xi\theta}$ becomes shorter:

$$d_{RRLR} = d_{LLRL} = (1 + n_1/n_3)\gamma_1 - \gamma_2, \tag{7.42}$$

$$d_{RLRR} = d_{LRLL} = (1 + n_1/n_3)\gamma_1 + \gamma_2. \tag{7.43}$$

and it is clearly seen that only photons with opposite circular polarization are allowed to interact. In the case when the incident beam is purely circularly polarized, the nonlinear signal from the medium is absent. However, in case of homogeneous elliptical polarization of the beam, i.e. when $E_R = F(x, y, z)\sqrt{(1 + \sigma)/2}$ and $E_L = F(x, y, z)\sqrt{(1 - \sigma)/2}$ the intensity of the signal beam is proportional to the constant γ_1:

$$E_{3R,L} = \mathcal{M}D_0\gamma_1\sqrt{1 - \sigma_1^2}\,(1 + n_1/n_3)\,F\partial_{R,L}F \tag{7.44}$$

When considering in-bulk second harmonic generation caused by the nonlocality of nonlinear response, it is worth mentioning that the part of nonlinear signal, proportional to the component γ_1 does not appear. From 7.37, it can be seen that the part of the medium polarization vector $\mathbf{P}$ proportional to γ_1 is a purely potential field, and is not a solenoidal one. Therefore, it is not necessary to take into account γ_1 when describing the bulk three-wave mixing (see (7.5)). Consequently, it is easy to show that the nonlinear signal is not generated in the bulk of the medium for any polarization state of the pump beam, unless it is not different in different points of its cross-section [28].

7.5 Conclusion

We have analytically studied the interaction between spin and orbital angular momenta of two coaxial circularly polarized light beams with Laguerre–Gaussian profiles and the beam at the sum frequency, generated in their nonlinear mixing in the bulk and on the surface of an isotropic chiral medium within the undepleted pump approximation. The mathematical expressions we obtained revealed different scenarios of pairwise interaction between the transverse modes of the pump beams with different values of spin and orbital angular momenta and these scenarios were interpreted in classical and quantum ways. While the projection of the total angular momentum of interacting photons on the axis of the interacting beams is conserved, the sum of neither spin nor orbital angular momenta of the pump photons are equal to the corresponding part of the angular momentum of the signal photon. The general expressions for the generated field at the sum frequency are shown to have the same form for different nonlinearity mechanisms: the local and nonlocal bulk responses and the response of the near-surface layer of the medium.

Acknowledgements The authors acknowledge financial support from the Russian Foundation for Basic Research (Grant No. 19-02-00069) and Foundation for the Advancement of Theoretical Physics and Mathematics "Basis".

References

1. J.H. Poynting, Proc. R. Soc. A **82**, 560 (1909). https://doi.org/10.1098/rspa.1909.0060
2. L. Allen, M. Beijersbergen, R. Spreeuw, J.P. Woerdman, Phys. Rev. A **45**, 8185 (1992). https://doi.org/10.1103/PhysRevA.45.8185
3. A.A. Kovalev, V.V. Kotlyar, A.P. Porfirev, Opt. Lett. **41**(11), 2426 (2016). https://doi.org/10.1364/OL.41.002426
4. M. Mestre, F. Diry, B. Lesegno, L. Pruvost, Eur. Phys. J. D **57**, 87 (2010). https://doi.org/10.1140/epjd/e2010-00005-0
5. K.A. Forbes, D.L. Andrews, Opt. Lett. **43**(3), 435 (2018). https://doi.org/10.1364/OL.43.000435
6. C.T. Schmiegelow, J. Schulz, H. Kaufmann, T. Ruster, U.G. Poschinger, F. Schmidt-Kaler, Nat. Commun. **7**, 12998 EP (2016). https://doi.org/10.1038/ncomms12998
7. J.T. Barreiro, N.K. Langford, N.A. Peters, P.G. Kwiat, Phys. Rev. Lett. **95** (2005). https://doi.org/10.1103/PhysRevLett.95.260501
8. R. Fickler, G. Campbell, B. Buchler, P.K. Lam, A. Zeilinger, Proc. Natl. Acad. Sci. USA **113**(48), 13642 (2016). https://doi.org/10.1073/pnas.1616889113
9. J.C. Garcia-Escartin, P. Chamorro-Posada, Phys. Rev. A **86** (2012). https://doi.org/10.1103/PhysRevA.86.032334
10. Z.Y. Zhou, Y. Li, D.S. Ding, W. Zhang, S. Shi, B.S. Shi, Opt. Lett. **39**(17), 5098 (2014). https://doi.org/10.1364/OL.39.005098
11. J. Hamazaki, R. Morita, K. Chujo, Y. Kobayashi, S. Tanda, T. Omatsu, Opt. Express **18**(3), 2144 (2010). https://doi.org/10.1364/OE.18.002144
12. D.K. Nguyen, O. Pascal, J. Sokoloff, A. Chabory, B. Palacin, N. Capet, Radio Sci. **50**, 1165 (2015). https://doi.org/10.1002/2015RS005772
13. R.N. Lanning, Z. Xiao, M. Zhang, I. Novikova, E.E. Mikhailov, J.P. Dowling, Phys. Rev. A **96** (2017). https://doi.org/10.1103/PhysRevA.96.013830

14. D. Wei, J. Guo, X. Fang, D. Wei, R. Ni, P. Chen, X. Hu, Y. Zhang, W. Hu, Y.Q. Lu, S.N. Zhu, M. Xiao, Opt. Express **25**(10), 11556 (2017). https://doi.org/10.1364/OE.25.011556
15. Y. Wang, D. Wei, Y. Zhu, X. Huang, X. Fang, W. Zhong, Q. Wang, Y. Zhang, M. Xiao, Appl. Phys. Lett. **109**(8) (2016). https://doi.org/10.1063/1.4961694
16. D.N. Vavulin, A.A. Sukhorukov, Phys. Rev. A **96** (2017). https://doi.org/10.1103/PhysRevA.96.013812
17. N. Kravets, E. Brasselet, Phys. Rev. A **97** (2018). https://doi.org/10.1103/PhysRevA.97.013834
18. X.Y.Z. Xiong, A. Al-Jarro, L.J. Jiang, N.C. Panoiu, W.E.I. Sha, Phys. Rev. B **95** (2017). https://doi.org/10.1103/PhysRevB.95.165432
19. G. Li, L. Wu, K.F. Li, S. Chen, C. Schlickriede, Z. Xu, S. Huang, W. Li, Y. Liu, E.Y.B. Pun, T. Zentgraf, K.W. Cheah, Y. Luo, S. Zhang, Nano Lett. **17**(12), 7974 (2017). https://doi.org/10.1021/acs.nanolett.7b04451. PMID: 29144753
20. M. Beresna, P.G. Kazansky, Yu. Svirko, M. Barkauskas, R. Danielius, Appl. Phys. Lett. **95**(12) (2009). https://doi.org/10.1063/1.3232235
21. D.F. Gordon, B. Hafizi, A. Ting, Opt. Lett. **34**(21), 3280 (2009). https://doi.org/10.1364/OL.34.003280
22. I.A. Perezhogin, K.S. Grigoriev, N.N. Potravkin, E.B. Cherepetskaya, V.A. Makarov, Laser Phys. Lett. **14**(8) (2017). https://doi.org/10.1088/1612-202x/aa77a3
23. K.S. Grigoriev, I.A. Perezhogin, V.A. Makarov, Opt. Lett. **43**(21), 5182 (2018). https://doi.org/10.1364/OL.43.005182
24. K.S. Grigoriev, V.A. Diukov, V.A. Makarov, Opt. Lett. **45**(2), 276 (2020). https://doi.org/10.1364/OL.45.000276
25. J.A. Giordmaine, Phys. Rev. **138**, A1599 (1965). https://doi.org/10.1103/PhysRev.138.A1599
26. S. Volkov, N. Koroteev, V. Makarov, Quantum Electron. **25**, 1183 (1995). https://doi.org/10.1070/QE1995v025n12ABEH000562
27. A.A. Golubkov, V.A. Makarov, Phys. Uspekhi **38**(3), 325 (1995)
28. K.S. Grigoriev, N.Y. Kuznetsov, E.B. Cherepetskaya, V.A. Makarov, Opt. Express **25**(6), 6253 (2017). https://doi.org/10.1364/OE.25.006253

Chapter 8
CARS Diagnostics of Molecular Fluid Phase Behavior in Nanoporous Glasses

Vladimir G. Arakcheev, Alexei N. Bekin, and Vyacheslav B. Morozov

Abstract Coherent anti-Stokes Raman scattering (CARS) spectroscopy is applied to study the dense phases composition and detailed features of the phase state of carbon dioxide filling pores of nanoporous glass samples (2 and 3.5 nm mean pore radii) in a wide pressure range at sub-critical and supercritical temperatures. Each of the phases is identified by the spectral shift of the CO_2 line corresponding to the Q-branch peak of the Raman band at 1388 cm^{-1}. It is demonstrated that at sub-critical temperatures − 6 and − 13 °C the surface adsorbed monolayer and the polymolecular layers adsorbed above it can be spectroscopically distingushed from each other. Moreover, the spectrum of the polymolecular layers is found to be noticeably shifted from that of the liquid phase, making these two similar phases also well distinguishable. After the onset of condensation, the spectrum of the appearing liquid phase is at least threefold broader than that of the bulk liquid. As the pressure increases, it narrows down to the value of the bulk liquid. The observed narrowing reflects enlargement of the liquid clusters from primarily sub-nanometric and nanometric size ones with a significant fraction of molecules, constituting the outer border and interacting with the non-uniform environment, to finally infinite-size homogeneous liquid filling the pore network. The density of supercritical cabon dioxide confined in the pores at isochoric heating (from 30 to 68 °C) determined by the measurements of the Raman shift shows a significant (~ 30%) increase in the vicinity of the bulk critical temperature and asymptotically decreases at higher temperatures. The obtained results demonstrate that CARS diagnostics can be used for precise characterization of subcritical and supercritical carbon dioxide phase composition under the conditions of nanoconfinement.

V. G. Arakcheev · A. N. Bekin · V. B. Morozov (✉)
Faculty of Physics, M.V. Lomonosov Moscow State University, 119991 Moscow, Russia
e-mail: morozov@phys.msu.ru

V. G. Arakcheev
e-mail: arakcheev@physics.msu.ru

A. N. Bekin
e-mail: bekin.aleksey@physics.msu.ru

K. Yamanouchi et al. (eds.), *Progress in Photon Science*, Springer Series in Chemical Physics 125, https://doi.org/10.1007/978-3-030-77646-6_8

8.1 Introduction

Adsorption of molecular substances in natural and synthetic nanoporous materials is the subject of intense applied and fundamental research over the recent decades. Nanoporous materials have been attracting much attention among researchers because of the progressively expanding sphere of their advanced and promising applications in catalysis [1], waste treatment [2], purification of blood [3], antibacterial therapy [4], implant creation [5], fuel cell technologies [6], microelectronics and optics [7]. A vast scope of their practical applications is related to natural gas storage facilities based on natural [8, 9] and artificial [10, 11] porous reservoirs for later consumption. Special interest is connected with development of advanced porous adsorbents designed exclusively for carbon dioxide capture and storage [12–14] as well as with use of captive carbon dioxide for displacement and enhancing recovery of hydrocarbons [15, 16]. Of significant practical interest are the pores of large surface-to-volume ratios up to hundreds and even thousands square meters per gram namely, micropores (pore radius $r < 2$ nm) and mesopores (2 nm $< r <$ 50 n). Due to strong space restrictions, the adsorption in micro- and mesoporous materials is the most complicated to be described, especially in the vicinity of the critical point of the filler.

Supercritical fluids (SCF) are extremely capable for penetrating into bulk porous substrates including those with the pore size of down to nanometer scale due to unique properties such as high permeability and low viscosity. Owing to inherent high dissolving power, SCF is used as a chemical reagent or a transport medium in the wide range of technological applications. Among the variety of SCFs, the most popular SCF is supercritical carbon dioxide ($scCO_2$) [17–23] because it is widespread, inexpensive, non-toxic, and non-flammable. Its critical values of temperature (~ 31 °C) and pressure (~ 73 atm) are easy to be achieved.

Fluids confined in small pores with a nanometer scale diameter show phase behavior essentially different from those in a bulk volume. The real mechanisms of adsorption are difficult to be understood and remain the subject of ongoing discussions as represented by different interpretations of empirically observed effects. Actually, the experimental data are typically represented as adsorption isotherms obtained using volumetric, gravimetric [24, 25] and nuclear magnetic resonance [26, 27] methods. The results were interpreted based on theoretical and numerical analyses based on a set of fundamental assumptions on both the properties of the pores and the adsorption physical and chemical mechanisms. The problem can be solved with no difficulty in the cases of relatively large nanopores with clear morphology and reasonably simple network topology as well as nanopores whose pore walls are sufficiently flat or at least regular so that there are only a small amount of geometrical and chemical defects. In these cases, the density of the absorbed liquid or the density of SCF, which cannot be measured directly, is considered to be equal to the density in the bulk volume. However, in the case of small pores, a similar approximation may not be adopted because the strong confinement exerts a significant influence on a local molecular environment and requires adequate interpretations [28–34].

Indeed, the lack of clear understanding of the roles of factors determining the strong confinement can result in multiple interpretations of the experimental data.

It is true that a complex adsorption pattern in pores deep below the surface of the nanoporous material can in principle be clarified using an experimental approach with which we directly probe the molecules in nanopores, and thus can shed extra light upon specific features of the confined molecular medium. However, in general, without having a priori knowledge of the porous network properties or relying on a certain adsorption model, it is a difficult task to extract detailed information from the experimental data. It seems that Raman spectroscopy is promising for these purposes because Raman scattering signals generated at the adsorbate confined in nanopores can be detected by Raman spectroscopic measurements, thus providing direct information about the density of the adsorbate. In principle, the local environment around molecules affects their vibrations, and therefore, the density of gas, liquid, or SCF influences the shift and linewidth of a Raman band. The results obtained earlier for CO_2 by CARS spectroscopy showed that the spectrum of the Raman band at 1388 cm^{-1} linearly moves with density toward low Raman shifts as the density of the bulk gas, liquid [35] or SCF [36] increases. Simply speaking, the phases appearing in the pores can be identified by their specific shift and linewidth of a chosen Raman band.

Previous studies [37–44] showed the capabilities of CARS in the characterization of fluid adsorption in mesoporous glass with pores of several nanometers in radius. In particular, initial spectroscopic observations of carbon dioxide surface adsorption [37] and condensation [38, 39] were then supported by calculations based on the model of capillary condensation [40] leading to a good quantitative agreement for the pores of two different sizes [41].

At the same time, the studies on CO_2 confined in mesoporous glass showed that the spectral contributions of gas and liquid phases [3–34, 37–39] as well as that of the surface-adsorbed layers [38–40] can be easily identified in the measured spectra by a significant relative Raman shift. Moreover, the spectroscopic method appeared to be precise enough to distinguish the spectral contribution of the first surface-adsorbed layer from that of the polymolecular layers absorbed upon the surface-adsorbed layer [41] as well as to observe appearance of the SCF phase in the pores and distinguish the spectral contribution of the SCF phase from that of the compressed gas [42], providing an opportunity to observe a critical point shift under the conditions of nanoconfinement. The results obtained at relatively low pressures, corresponding to submonolayer coverage of the pore wall, showed the capability of the CARS spectroscopy to detect and identify relatively small amounts of both the surface adsorbate [39] and the liquid-like phase [40]. However, because of a weak signal from the liquid-like phase, it remained unknown whether the liquid-like phase can be spectroscopically distinguishable from the bulk liquid or not. Therefore, the nature of the liquid-like phase, which was found to appear at pressure that is several times smaller than the capillary condensation pressure, remained unclear. A further study [45] showed that there are distinct spectroscopic contributions of the first surface-adsorbed layer and the subsequent polymolecular layers and that the phase of multimolecular liquid clusters aggregating in pores and the phase of

condensed liquid filling the pores are distinguished from each other by their spectral widths. The term "liquid clusters" means the clusters that can be the seeds of a molecular fluid. The liquid clusters formed initially at the boundary of the liquid-like phase develop with increasing pressure from small droplets into larger droplets and form capillary bridges, which merge and flow into the pores to fill finally the entire pore volume. In [46], from the analysis of spectroscopic data obtained for $scCO_2$ at isochoric heating in two different mesoporous glass samples at temperatures above 30 °C and those obtained for bulk carbon dioxide, it was demonstrated that the density in the pores appears to be significantly higher by about 30% in the vicinity of the bulk critical temperature. In the present chapter, we discuss recent results obtained in our group, in combination with the development in the CARS spectroscopic measurement techniques, to study the characteristic features of carbon dioxide, especially its phase behavior under conditions of nanoporous confinement starting from submonolayer coverage on the pore walls through molecular multilayers, clusterization, infinite condensation within the nanoporous samples and up to essentially supercritical conditions. Based on the achieved understanding, possible scenarios for further research will be introduced with a clear justification. The CARS spectroscopic approach we have been developing looks promising as a method with which we can examine directly the molecular medium confined deeply inside natural and artificial nanoporous substrates.

8.2 Materials and Methods

8.2.1 Carbon Dioxide at Near the Critical Point Conditions

Carbon dioxide is one of the principal atmospheric gases. In view of its growing importance in supercritical technologies [18–20] as well as of the ongoing exploration for efficient approaches for CO_2 capture [12–14] to diminish the effect of greenhouse gases, a development of advanced tools for the diagnostics of its phase state in the region around the critical point under conditions of nanoporous confinement has been awaited.

Figure 8.1 illustrates a typical phase diagram for a single substance. A supercritical fluid is a medium whose temperature and pressure exceed the critical values: ~ 31 °C and 72.8 atm, respectively, for CO_2. The coexisting curve between the triple point and the critical point divides the liquid and gas states. At the critical point, the gaseous and liquid phases merge and become indistinguishable. This is why supercritical fluids take the intermediate position between gases and liquids in terms of their properties. As the pressure and/or density increase, the meniscus of the liquid gradually disappears till the system becomes homogeneous [20]. A further rise in the pressure or temperature does not lead to a phase state change. The region around the critical point thus includes the phase transition between gas and liquid as well as the phase transitions to the supercritical fluid state.

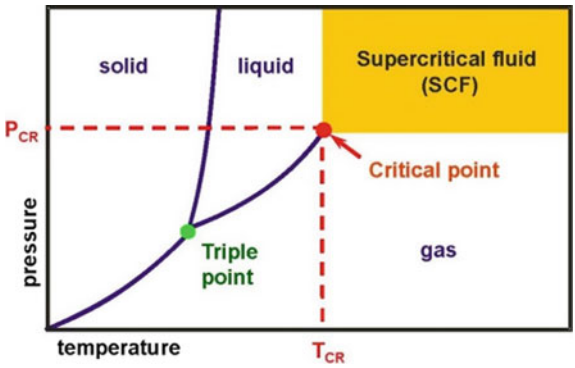

Fig. 8.1 Typical phase diagram of a chemical substance

Based on the available data on thermodynamic properties of bulk carbon dioxide, its equation of state was investigated in the great detail [47]. The calculation examples of the pressure-density relationship of bulk carbon dioxide at the temperatures near the critical value are presented in Fig. 8.2. The horizontal parts of the curves below the critical temperature represent the coexistence of the gas and liquid phases. The region above the critical point corresponds to the supercritical state. The conditions of nanoconfinement and the interaction with the pore walls can significantly change the equation of state and the critical point position in different areas of the pore volume. Due to the inhomogeneous pore structure, physical and chemical defects of the surface walls etc., carbon dioxide occupying the nanoporous host can take various coexisting phase states. Analysis of the latter using Raman can provide useful detailed information related to phase composition features.

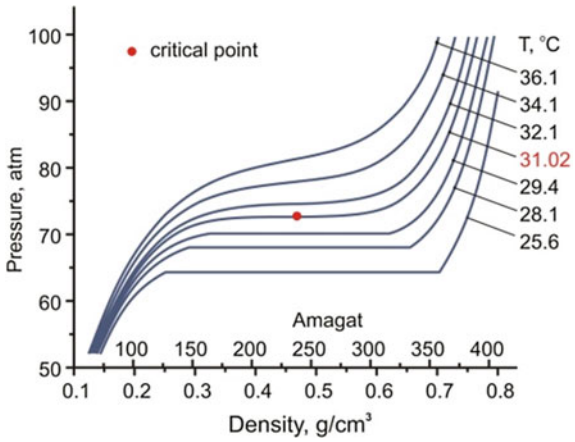

Fig. 8.2 Pressure-density relationship of bulk carbon dioxide at the temperatures around the critical value

8.2.2 Raman Spectrum

The structure of molecular rovibrational levels and the spectral lines of CO_2 have been studied well [48]. In gas phase Raman spectroscopy, the Fermi dyad of the two vibrational modes $\nu_1 + 2\nu_2$ appearing as the two Q-branch peaks at 1285 and 1388 cm^{-1} has been known well as a spectral signature of CO_2 since the early days of Raman spectroscopy [49, 50]. A large number of studies were reported on the determination of the molecular constants and the vibrational level energies [51–54] including the energy separation between the 02^00 and 10^00 levels forming the Fermi dyad [55, 56]. After the laser technologies were introduced into molecular spectroscopy, quite natural attempts were made to use two intense peaks as spectral markers to probe CO_2 in near-critical and supercritical conditions in particular [57–59]. With the development of nonlinear Raman spectroscopy, bringing a variety of excellent experimental approaches with high resolution and sensitivity, the main attention was paid to the study of the structure of vibrational–rotational spectra of the Q-branches starting from the lowest densities [60–65]. Thorough theoretical models were developed to describe the transformation of spectra due to collisional dephasing and rotational energy transfer [62, 63]. The two doublet branches demonstrate essentially different spectral shapes. The 1285 cm^{-1} branch has relatively broad rotational spectrum (~ 0.5 cm^{-1} on $1/e^2$ level) while the 1388 cm^{-1} branch rotational structure is much narrower (~ 0.011 cm^{-1}). At density ~ 0.2 amagat, the rotational structure of the 1388 cm^{-1} branch collapses, and, when the density exceeds 1 amagat, the broadening is induced by the collisional dephasing [62] and the branch is observed as a single homogeneously broadened line with the linewidth determined mainly by the gas density. To the contrary, the spectral contour of the 1285 cm^{-1} branch retains the extra broadening attributed to the rotational structure [63]. The broadening mechanisms are clearly manifested when time-domain approach is used instead of the frequency-domain approach [66–69] and the pulse response in the time domain was analyzed. The Doppler effect, rotational energy transfer (spectral exchange [66]) and collisional dephasing are easily recognized in time-domain for the narrow 1388 cm^{-1} band [66, 67, 69], while "this band will never be resolved by usual Doppler limited Raman spectroscopies" [63]. At high densities, the time-domain approach becomes less informative, while the studies in which time-domain and frequency-domain measurements are combined become rather fruitful [68, 69]. The results of the measurements for the 1285 cm^{-1} line and those of the model calculations showed that the contribution of the extended rotational structure can remain noticeable in comparison with the total line width up to the highest gas densities. Indeed, the results obtained by frequency-domain CARS for CO_2 at room and near critical temperature [35, 36] demonstrate that the 1285 cm^{-1} line is broader by ~ 30% than the 1388 cm^{-1} line at the densities up to 180 amagat in the high-pressure gas phase and up to 320 amagat in the liquid phase. At temperatures below the critical value, the spectral behavior is similar. When the density increases from 320 to 400 amagat, the width of the 1285 cm^{-1} line gradually decreases from ~ 2.2 cm^{-1} to ~ 1.7 cm^{-1}, which is approximately equal to the width of the 1388 cm^{-1} line.

Considering this complicated density behaviour of the linewidth of the 1285 cm^{-1} line, it is obviously more reasonable to use the other line at 1388 cm^{-1} as a spectral marker for the investigation of the spectral behavior at nanoporous confinement. On the other hand, in the investigation of the density enhancement, density fluctuations [70–72], and clusterization [73] in neat supercritical CO_2, both of the components in the Fermi dyad were used in Raman spectroscopy.

8.2.3 Nanoporous Samples and Thermal High-Pressure CO_2 Cell

Mesoporous glass samples of two types were used in the experiment for comparison. The first is made of Vycor glass with the mean pore radius of 2 nm, the porosity of ~ 28% and the internal surface area of ~ 200 m^2/g [74] and has the cross dimensions of 4 × 4 mm^2 and the length of 9 mm. Another sample is made of DV-1M glass [75] with the mean pore radius of 3.5 nm, the porosity of ~ 26%, the internal surface area of ~ 100 m^2/g and has the cross dimensions of 6 × 6 mm^2 and the length of 10 mm. To eliminate the admixtures adsorbed from the atmosphere, the samples are annealed at 600 °C for several hours until just before the experiment is started. Immediately after the annealing procedure, the sample is installed inside the high pressure cell. The cell is made of stainless steel and has two quartz glass windows with the distance of 12 mm between them. The internal volume of the cell is about 2 cm^3. Compression of CO_2 (99.99% purity) is performed by means of a piston compressor with a 200 ml volume. The pressure is measured with the precision of 0.1 bar. The temperature in the cell can be adjusted with the precision of ~ 0.2 °C using a thermo-stabilizing duralumin shell equipped with a set of Peltier elements adopted to reverse the operating mode.

8.2.4 CARS Spectrometer

A general scheme of the experimental setup is shown in Fig. 8.3. Details of the specifications of the laser light sources have been described in our recent reports [44–46]. The pulses of the second harmonic of the Nd:YAG laser (LS-2134D-C3, Lotis TII) are used as the pump and probe radiations (532 nm, 10 ns, ~ 0.2 mJ). An optical parametric oscillator (LT-2215-PC, Lotis TII) pumped by the third harmonic of another Nd:YAG laser (LS-2147, Lotis TII) is used as a tunable source of the Stokes radiation (the central wavelength ~ 574 nm, 12 ns, ~ 1 mJ). The polarizations of the pump, Stokes, and probe beams are parallel to each other. The difference frequency is tuned to a CO2 vibrational resonance at 1388 cm^{-1}. The pump and the Stokes beams are focused into the nanoporous sample using a lens with a focal length

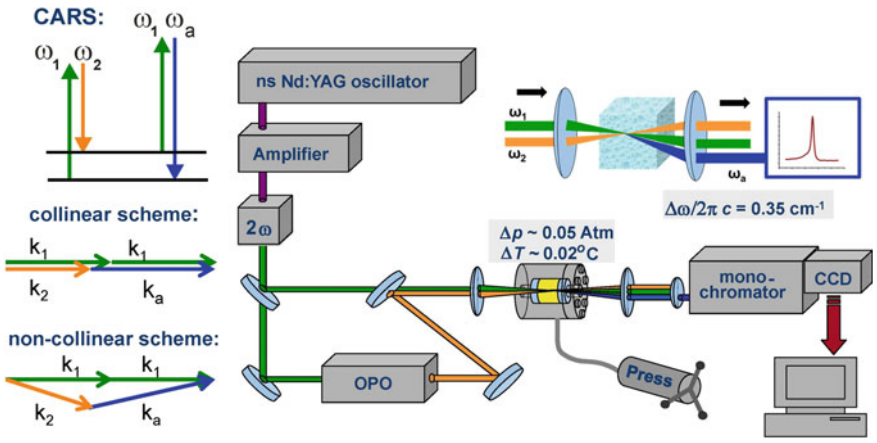

Fig. 8.3 General scheme of the experimental setup. Laser beams are focused inside the cell with the nanoporous sample and filled with the carbon dioxide. The insert at the top right shows the beams crossing deep inside the sample when the noncollinear scheme is used. On the left side of the picture: the level energy diagram of CARS is on the top; the phase matching conditions for the wave vectors are shown below for the collinear and non-collinear geometries

of 17 cm. Both collinear and non-collinear CARS geometries can be realized in the experiments.

Phase matching conditions are well satisfied for the collinear geometry as long as the cell is filled with a bulk gas with the refractive index closed to 1. The non-collinear geometry with the crossing angle within ~ 1° provides better phase matching in the case of nanoporous sample and facilitates the observation of local CARS signals from molecules in pores located far below from the surface of the sample. If the CARS geometry is collinear, the CARS signals from the beam waist zone in the nanoporous sample can be rather weak. On the other hand, the anti-Stokes signals originating from CO_2 filling the gaps between the nanoporous sample and the cell window can be strong because of the favorable phase matching. The bright peak originating from the bulk gas is indeed a parasitic signal, but it can be used as a reference signal for the frequency calibration procedure. It should be noted that the signals from the gas and the condensed phase may cover the frequency range wider than 20 cm^{-1}, which is several times broader than the Stokes beam bandwidth. During the CARS spectrum accumulation, the central wavelength of the Stokes radiation is varied in steps of ~ 0.1 nm in the wavelength range from 573.8 to 574.8 nm, and a total of 100 shots accumulated at each wavelength provides homogeneous biharmonic excitation in the range from 1375 to 1400 cm^{-1}. A pair of monochromators, that is, a double diffraction-grating monochromator (MDR-6U, LOMO) and a monochromator/spectrograph (GMS-850-U2C, Lotis TII), working in the additive-dispersion mode, and a matrix detector are used to record the spectrum of the anti-Stokes signal. The shape of the apparatus function is close to Gaussian with the full-width at half-maximum of ~ 0.35 cm^{-1}.

8.2.5 CARS Signal Analysis

Measured CARS spectra may consist of several interfering contributions: resonant CARS signals originating from the different phases of CO_2 and a nonresonant background CARS signals generated mainly by the nanoporous glass substrate. The spectral profiles are analyzed using the scalar theory of CARS, in which the profile of the anti-Stokes signal is expressed as [76, 77]:

$$I_a(\omega_1 - \omega_2) \propto \left|\lambda_R^{(3)} + \lambda_{NR}^{(3)}\right|^2 I_1 I_2 I_p \tag{8.1}$$

where $\lambda_R^{(3)} = \lambda_R^{(3)}(\omega_1 - \omega_2)$ and $\lambda_{NR}^{(3)}$ are the coefficients of resonant and nonresonant nonlinear-optical interactions, I_1, I_2, I_p, I_a are the intensities of the pump, Stokes, probe, and anti-Stokes radiations, the ω_1 and ω_2 are the pump and Stokes frequencies, respectively. If more than one phase of molecular species coexist in the interaction volume, the resonant part $\lambda_R^{(3)}$ represents a coherent sum of their respective contributions. Assuming a Lorentzian profile for each resonant contribution, the resonant part can be calculated as [76–78]

$$\lambda_R^{(3)} = \sum_k \frac{\overline{\lambda}_k^{(3)}}{-i - \Delta_k} \quad \Delta_k = (\omega_1 - \omega_2 - \Omega_k)/\Gamma_k \tag{8.2}$$

where $\overline{\lambda}_k^{(3)}$ is the relative amplitude of the spectral component k and Δ_k is the frequency detuning of the biharmonic pump from the Raman resonance normalized to the linewidth Γ_k. Within the framework, each of the resonant components is associated with a specific carbon dioxide phase that is present in the system of the confined media. The validity of such an analysis of the spectral manifestations of the processes of adsorption [37] and capillary condensation in nanopores [38, 39] was supported by calculations based on a capillary condensation model, yielding a good quantitative agreement with experimental results for the samples with different mean pore radii [40, 41]. Figure 8.4 demonstrates an example of the results for the CARS spectrum obtained using the collinear geometry in carbon dioxide in the Vycor glass at − 11 °C [44]. The analysis shows that the liquid-like phase is observed in the pores at pressure well below the bulk saturation pressure. Making measurements at reasonably low temperatures allows distinguishing the spectral contributions of the gas and liquid phases. The sharp high-frequency peak at 1388 cm^{-1} corresponds to the gas phase within the pores and, mainly, in the gaps between the porous sample and the cell windows. The broad low-frequency peak centered at ~ 1382 cm^{-1} and extending towards the lower frequency side is attributed to carbon dioxide molecules adsorbed on the pore walls and strongly interacting with the surface. The strong middle peak at 1385.5 cm^{-1} indicates the appearance of the liquid-like phase in the pores. The

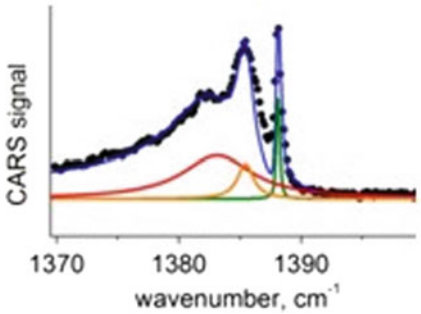

Fig. 8.4 Example of experimental spectrum (dots) obtained in the carbon dioxide in Vycor glass at pressure 19.7 atm and temperature − 11 °C using the collinear geometry [44]. The respective spectral contributions of gaseous (green), surface adsorbed (red) and liquid-like phases (orange) are plotted with the solid curves

respective spectral contributions attributed to the different phases are indicated by the solid lines.

8.3 Experimental Observations and Discussion

8.3.1 Surface-Adsorbed and Polymolecular Layers, Formation of Liquid Clusters

To focus on the recognition of coexisting phases in the process of pore filling and to obtain additional information regarding the spectral manifestation of different stages of the adsorption process, the CARS spectra of carbon dioxide in the Vycor glass were measured at − 13 and − 6 °C in a wide pressure range covering the pressure at which the transition occurs from partial coverage of the pore walls to condensation in the entire volume of the nanoporous sample [45]. The measurements were made using the non-collinear CARS scheme in the Vycor glass. The non-collinear geometry allowed improvement of the locality and sensitivity conditions, so that a distinct signal was observed even at low pressure of 1.7 atm. The observed spectral changes were qualitatively similar at these temperatures, so the line shapes and the phase behavior were examined in detail at − 6 °C. The only difference between the two conditions at different temperatures were the pressure values at which the condensation occurs as discussed below.

The spectra obtained (Fig. 8.5) exhibit clearly asymmetric shape originating from the interference between the resonant and non-resonant parts of the CARS signal. The resonant contribution is caused by the molecules in the pores of the sample. The nonresonant background is attributed to both the molecules and the glass matrix, but the contribution of the latter can be considered to be dominant. The observed

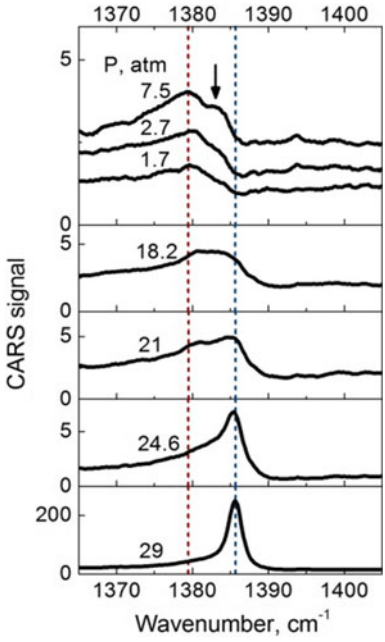

Fig. 8.5 CARS spectra of the carbon dioxide Q-branch 1388 cm^{-1} measured at isothermal adsorption in Vycor glass at − 6 °C. The pressure values are shown for each spectrum. The red dashed vertical line (left) indicates the approximate position of the peaks of the surface adsorbate and the blue dashed vertical line (right) indicates that of the liquid phase; the arrow points to the small spectral peak appearing at the low pressures just between the two dashed lines

changes in the line shape with the pressure reflects the changes in the composition of the adsorbate phases. It is true that a relative weight of the nonresonant part is important in the spectral fitting procedure, but the non-resonant part affects only weakly the positions and amplitudes of the spectral peaks. Therefore, the positions and amplitudes are regarded as those obtained by a visual and intuitive analysis.

In particular, there is a visually distinguished broad peak at ~ 1380 cm^{-1} which grows with pressure in the range from 1.7 to 7.5 atm as shown in the top frame of Fig. 8.5. In our previous study [44] using collinear CARS, this peak was observed and was ascribed to the surface adsorbed layer because it dominated at low pressures and no distinct additional structures were identified. Obviously, the low-pressure range corresponds to a slightly sloping part of adsorption isotherm [79] which reflects the adsorption of carbon dioxide molecules on the pore walls without condensation in the pore volume.

Another evident observation is a bright peak at ~ 1385 cm^{-1}, which starts appearing at 21 atm, becomes dominant, and finally grows ~ 50-fold in intensity at 29 atm as the pressure approaches the bulk saturation pressure as shown in the three lowest frames of Fig. 8.5. This peak observed previously at the different temperatures [37–40, 43, 44] is caused by the liquid phase appearing through the condensation in the pores, which is consistence with the steeper part of the adsorption isotherm [79]. The present measurements using non-collinear CARS yielded more detailed picture of the spectral changes. It is clearly seen in the pressure range from 1.7 to 7.5 atm that the spectral profiles show the additional component that looks like a bulge (indicated by an arrow), appearing between the positions of the two peaks considered above.

The bulge, which obviously represents an additional minor phase, grows with pressure faster than the broad low-frequency peak attributed to the surface adsorbed layer. Furthermore, the present spectra clearly show that this additional peak is noticeably red-shifted from the spectrum of liquid, suggesting that its origin is different from the molecules in the liquid phase as will be discussed below. It should be noted in Fig. 8.5 that the right wing of the peak corresponding to the liquid phase in the pores at 29 atm is significantly narrower than the right wings in the capillary condensation stage at 18.2, 21, an 24.6 atm.

It should be mentioned here that the CARS spectra recorded at reasonably low pressures and those recorded at higher pressures approaching the bulk saturation value show the respective distinctive structures that can be qualitatively interpreted as will be explained below. On the contrary, the line shapes observed in the "middle" pressure range (see, for example, the spectrum at 18.2 atm in Fig. 8.5) exhibit a broad profile with no distinctive peak structures, which can be interpreted as a result of the merging of more than two different contributions of the phases coexisting with comparable amounts.

First, we focus on the CARS spectra recorded at the pressures in the range from 1.7 to 7.5 atm. The results of the line-shape fitting of the resonant part of the CARS spectra with a single component and those with two components are illustrated in Fig. 8.6a, b, respectively. It can be seen clearly that the two component model (Fig. 8.6b) gives better agreement with the recorded spectral profiles.

The results of the numerical fitting show that the Raman shifts of the two peaks are ~ 1381 and ~ 1384 cm^{-1} and their linewidths are ~ 5.5 and ~ 3 cm^{-1}, respectively. The Raman shifts and the linewidths do not vary so much in the low-pressure range [45], suggesting that the respective peaks originate from different kind of phases of the molecular system, which are present in the pores at the low pressures at which only surface adsorption is expected to take place. Based on these observations, we attribute the low frequency peak at ~ 1381 cm^{-1}, dominating at the lowest pressures, to the first surface-adsorbed layer, which interacts directly with the pore walls. A specificity of the first layer of CO_2 adsorbed in Vycor was observed in an earlier study [79], where

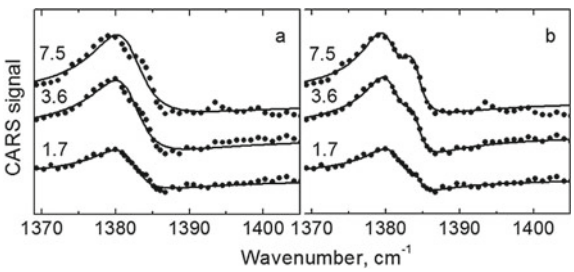

Fig. 8.6 CARS spectra measured at the relatively low pressures (circles) and the results of numerical fits to the resonant part (solid line) with a single component (**a**) and two components (**b**). The pressure values (in atmospheres) are indicated for each spectrum. The experimental uncertainties are smaller than the size of the dots [45]

the surface density of carbon dioxide was estimated not to be equal to that estimated from the bulk liquid density. Moreover, the molecular area of the CO_2 molecules on the pore wall surface was estimated as somewhat smaller than that calculated for the bulk molecules. A more likely interpretation was suggested [79] that the adsorbate molecules in a complete monolayer (surface adsorbed layer) pack in essentially the same way as in the solid. Therefore, it is expected that the interaction between CO_2 molecules and the glass surface has a significant influence on the first layer and its magnitude is strong enough to modify the molecular vibrations, leading to the pronounced red shift of the first layer peak from 1385.6 cm^{-1}, corresponding to the peak position of the bulk liquid at the lowest density at the temperature 29.5 °C [35] according to the aquation of state [47]. For the same reasons, the high-frequency peak at 1384 cm^{-1} is attributed to the polymolecular layers, that is, the multilayers adsorbed upon the first layer. Indeed, the peak becomes apparent at higher pressures as compared with the low frequency peak, indicating that the second group of molecules appears only in the presence of the first one. Another finding we have to mention here is that the Raman shift is closer to the one of the bulk liquid than to that of the first surface adsorbed layer (1381 cm^{-1}). In fact, the molecules constituting the polymolecular layers are densely packed and predominantly interact with the neighboring molecules in a similar manner as in the bulk liquid. For this reason, the polymolecular layers are naturally expected to have the density equal to the liquid density and are considered to be liquid-like [80]. At the same time, the relative Raman shift of the polymolecular layers peak from the bulk liquid peak is noticeably large, being almost as much as the linewidth 1.55 cm^{-1} observed earlier in the bulk liquid [35] and to a half of the linewidth 3 cm^{-1} of polymolecular layers peak itself obtained in the current research. Therefore, the spectral contributions of the polymolecular layers and the liquid can be discriminated from each other, and the relative shift is large enough to identify the phases present in the pores. The observed relative shift is most probably related to the indirect influence of the glass surface on the polymolecular layers that modifies the molecular vibrational levels in a similar manner as in the first layer, but the extent of the shift is smaller than that induced in the first layer. The peaks of both the first layer and the polymolecular layers are significantly broader than the peak of the bulk liquid. The broadening can most probably be ascribed to the inhomogeneity of the considered layers. Indeed, the first layer is affected by geometrical defects and/or chemical heterogeneity of the pore wall, which are always present in the nanoporous glass. The inhomogeneity of the polymolecular layers is attributed to a nonuniform local environment of the molecules due to the small thickness of the layers, in which a large part of the molecules constitute the outer fluide boundary to the void pore volume. It should be noted that the total fraction of the polymolecular phase, in principle, can be estimated based on the ratio of the peak intensities.

As illustrated above, in the CARS spectra recorded at low pressures, the two resonant components are identified at ~ 1381 and ~ 1384 cm^{-1}. The low-frequency peak is obviously attributed to the first adsorbed layer because it dominates at the lowest pressures at which the pore wall coverage is significantly below the monolayer coverage [79]. The high-frequency peak whose Raman shift is close to that of the

bulk liquid is attributed to the liquid-like polymolecular layers adsorbed upon the surface-adsorbed layer. The detailed analysis of the spectral line shape has revealed that the peak assigned to the polymolecular layers is noticeably red shifted from the spectral peak of the bulk liquid at 1385.6 cm^{-1}. Thus, the two groups of adsorbed molecules, that is, the molecules in the first molecular layer and the molecules in the polymolecular layer, can be spectroscopically identified and discriminated from each other as well as from the liquid phase.

Next, we examined the CARS spectra recorded in the high pressure range, at which the volume of the pores is being filled by the liquid phase. When the pressure was increased, the spectral peak of the liquid phase starts appearing and its contribution becomes prevailing at 21 atm. The fitting confirmed [45] that the Raman shift of the peak whose intensity increases with the pressure increase is equal to the shift, 1385.6 cm^{-1}, for the bulk liquid. Therefore, the peak is undoubtedly attributed to the liquid filling the volume of the pores, and the observed growth reflects the progress in the condensation. At the same time, the pressure dependence of the linewidth (Fig. 8.7) provides a more precise view on the condensation pattern. The peak linewidth at 21 atm is ~ 5 cm^{-1} and it becomes narrower as the pressure increases and reached the bulk liquid value of 1.55 cm^{-1} at 29 atm. This shows that the liquid phase appearing in the pores undergoes a certain transformation.

To explain the observed behavior, we have to take into account that condensation starts in the smallest pores or other small voids that are present in the porous network. At first, carbon dioxide molecules with the nanometer size in all the three dimensions, having a large surface-to-volume ratio, start appearing in the liquid. Therefore, a significant fraction of the molecular clusters constitute the surface bordering mostly to the empty pore volume. This makes small clusters less homogeneous in comparison with the bulk liquid, leading to larger spectral broadening. As the pressure is increased, the clusters grow in size and merge into larger ones and become more homogeneous, so that the surface-to-volume ratio decreases. For this reason, the narrowing of the corresponding spectral peak is attributed to the transition of the nanometer size clusters to infinitely large clusters, that is, the bulk liquid, filling the entire volume of the pores. A similar narrowing is observed at

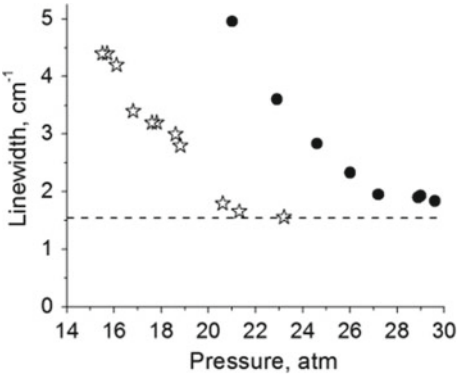

Fig. 8.7 Linewidth of the liquid phase spectrum obtained for − 6 °C (filled circles) and − 13 °C (open stars). Dashed line indicates the value in the bulk liquid [45]

− 13 °C, but the pressure range in which the narrowing occurs is shifted to the lower pressure side by about 6 atm than at − 6 °C as shown in Fig. 8.7. The pressure shift is consistent with the general theory of capillary condensation [81, 82] by which earlier experimental results on condensation of CO_2 in Vycor glass at different temperatures were interpreted [37–40, 43, 44]. This shows that the peak at ~ 1386 cm^{-1} is securely attributed to the liquid phase filling the volume of the pores and not to any kind of liquid-like surface adsorbate because the liquid-like surface adsorbate is not expected to be strongly affected by the temperature. The results of the CARS measurements at the low and high pressure ranges show that the two different phenomena, that is, the surface adsorption and the condensation, occur in the nanometer size pores. The analysis of the line shape has revealed spectral characteristics of the surface-adsorbed layer, the polymolecular layers, and the liquid phase. The normalized spectral contributions of each of the three phases are shown in Fig. 8.8.

It is clearly visible in Fig. 8.8 that the neighboring peaks significantly overlap, which makes it difficult to extract the contributions of the respective phases especially when their spectral intensities are close to each other. The analysis above was made for the two specific pressure regions in which the spectral changes can mainly be attributed to two of the three considered mechanisms while the spectral changes in the "middle" pressure range from 7.5 to 21 atm at − 6 °C has not been examined above. To extract the information from the spectra recorded at the "middle" pressure range, it becomes necessary to use additional data to be obtained by another experimental techniques [24–27], which will facilitate an analysis of spectra composed of more than two components.

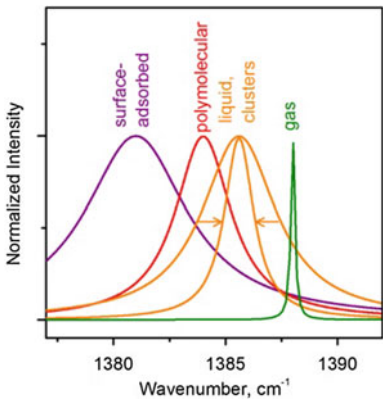

Fig. 8.8 Normalized spectra of the different phases of CO_2 in Vycor glass: surface-adsorbed layer (purple line), polymolecular layers (red line), and liquid clusters/liquid phase (orange lines). The horizontal arrows show the observed narrowing of the spectrum when the pressure is increased. The gas phase spectrum (green line) is shown for comparison

8.3.2 *Supercritical Carbon Dioxide Density in Pores*

The density variation of supercritical carbon dioxide confined in nanoporous glass at isochoric heating in the temperature range from 30 to 68 °C has been investigated using non-collinear CARS [46] in two nanoporous samples with the mean pore radius of 2 nm [74] and 3.5 nm [75]. In the measurements, the heating started from 30 °C, which is the subcritical temperature in the bulk carbon dioxide, but is supercritical for the condition of nanoporous confinement because the critical temperature significantly decreases in small mesopores [79]. Indeed, the spectral contribution of supercritical phase of CO_2 confined in mesoporous glass was earlier observed at 30.5 °C [42]. When the measurements started from 30 °C, the pressure was set to be 73.8 atm and the cell remains closed during the experiment. According to the equation of state for CO_2 [47], this provides the bulk density in the cell of 335 amagat, which is noticeably higher than the bulk critical density 238 amagat, leading to the supercritical conditions at the higher temperature above 30 °C.

The spectra recorded during the isochoric heating (Fig. 8.9) showed a clear single peak centred at around 1385.5 cm^{-1} whose shape does not vary noticeably when the temperature increases. The peak can be attributed mainly to $scCO_2$ filling the central area of the pores.

As was discussed above as well as in the previous works [43, 45], the asymmetry of the spectral shape reflects the interference between the contribution of surface adsorbed molecules whose frequency is shifted towards the smaller frequency side and the contribution of the non-resonant background, attributed mainly to the nanoporous glass material.

The fits obtained using (8.1) and (8.2) show a good agreement with the CARS spectra (Fig. 8.10a). The fitting results demonstrate that the spectral contributions of both the surface adsorbate, centred at ~ 1382 cm^{-1}, and the nonresonant background are much smaller than the large peak of $scCO_2$ (Fig. 8.10b) filling the pore volume.

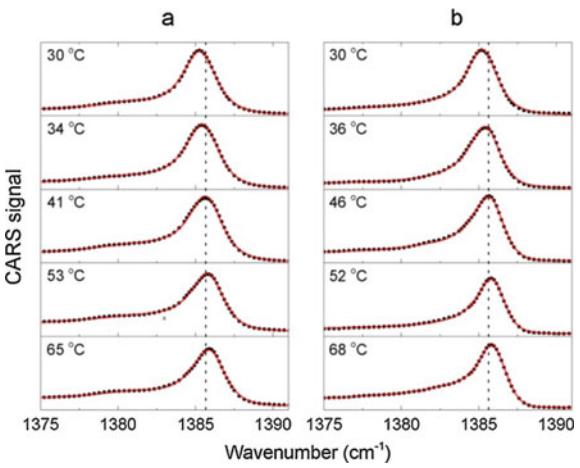

Fig. 8.9 The temperature dependence of the CARS spectra (dots) measured with isochoric heating of scCO2 confined to the pores of 2 nm (**a**) and 3.5 nm (**b**) in the radius and the fits (solid line) calculated using the two-component model for the resonant part [46]

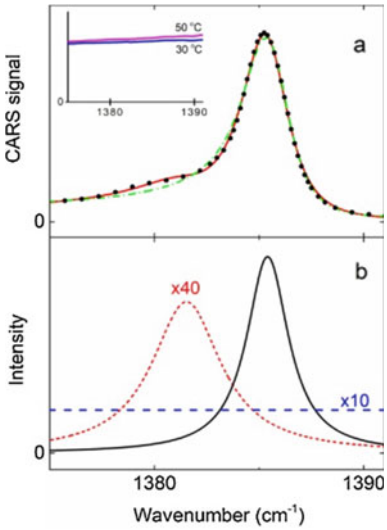

Fig. 8.10 **a** CARS spectrum (dots) measured in $scCO_2$ confined in the pores of 2 nm radius at 30 °C and the fits obtained using a single component (green dash-dotted line) and a two components (red solid line) for the resonant part [46]. **b** The spectral contributions of $scCO_2$ filling the volume of the pores (black solid line), CO_2 adsorbed on the pore walls (red short dashed line) and the nonresonant background (blue dashed line). The latter two are shown multiplied by 40 and 10, respectively. The insert shows CARS spectra of an empty nanoporous sample measured at 30 °C (blue solid line) and 50 °C (magenta solid line)

At the same time, the contribution of the surface adsorbed layer cannot be neglected. If it is neglected the fitting exhibits a certain deviation in the left wing from the experimentally observed profile (Fig. 8.10a). The insert in Fig. 8.10a demonstrates that the empty nanoporous sample yields the CARS signal representing only the nonresonant background with no peaks in the spectral range of interest. Similar signal behaviour was observed in samples with the mean pore radii of 2 and 3.5 nm. Both of the spectra at 30 and 50 °C exhibit a slight increase towards higher frequencies and the slope at 50 °C is slightly larger than at 30 °C.

Figure 8.9 clearly shows for both of the samples that the spectra gradually move towards the higher wavenumber side when the temperature increases. The most pronounced shift is observed in the range between 30 and 45 °C, which is close enough to the critical temperature of the bulk liquid. It seems clear that the shift is associated with a change in the $scCO_2$ density. The results obtained in the earlier study on the bulk CO_2 [35] showed that the Raman shift linearly decreases with density $scCO_2$ at 33 °C. Moreover, the Raman shifts observed at different temperatures in the liquid [40, 41, 43, 44] and in the supercritical [42] phases confined in the mesopores were similar to the Raman shift in the bulk. Therefore, the Raman shift can serve as a marker of the density of $scCO_2$ in the pores at different temperatures.

The results of rather simple measurements performed for the bulk $scCO_2$ showed two important aspects. First, the peak does not shift at the isochoric heating at the

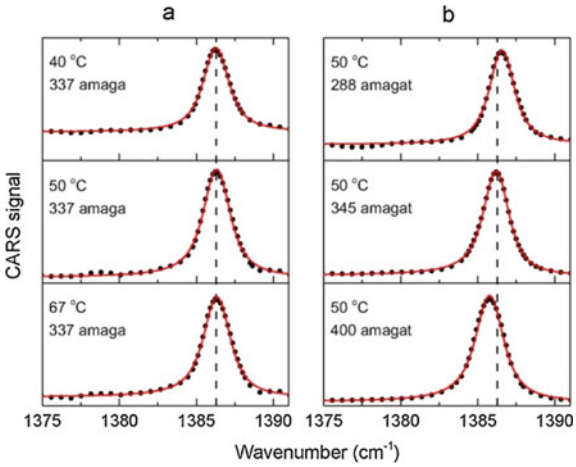

Fig. 8.11 CARS spectra (dots) measured for bulk scCO2 at the isochoric heating (**a**) and the isothermal compression (**b**). The fits (solid line) calculated using the single-component model for the resonant part. The temperature and density values are shown for the respective spectra [46]

similar density in the same temperature range (Fig. 8.11a). Therefore, the spectral shift observed under the nanoconfinement cannot be interpreted as a temperature effect. Second, the isothermal compression of bulk $scCO_2$ is accompanied by a noticeable shift of the CARS spectrum towards the low frequency side (Fig. 8.11b). The fitting shows that the density dependence of the Raman shift is close to linear and the specific spectral shift is $-$ 0.006 cm^{-1}/amagat, which is consistent with the previous data [35].

Another set of measurements was performed at the isothermal compression under conditions of nanoconfinement to observe the spectral variation when the density increases (Fig. 8.12).

The temperature is chosen far below the bulk critical value to avoid any near-critical effects. The results clearly show that the peak profile shifts towards the lower wavenumber side when the pressure increases linearly and the spectral shift obtained is similar to that obtained for the bulk liquid [35]. Therefore, the Raman shift of CO_2 under nanoconfinement shows quantitatively similar behavior to that in the bulk liquid.

Thus, the spectral behavior observed at isochoric heating of $scCO_2$ in the mesopores (Fig. 8.9) clearly shows that the density decreases when the temperature increases from 30 to 68 °C. The density can be estimated using the specific spectral shift of $-$ 0.006 cm^{-1}/amagat obtained both for the bulk liquid and for the liquid under the nanoconfinement. Figure 8.13 illustrates the temperature dependence of the spectral shift and the corresponding density values. With the increase in temperature, the density decreases and asymptotically approaches the average value for the bulk liquid and scCO2 equal to 335 amagat. At the same time, the density is $\sim$ 450 amagat at 30 °C, exceeding the average bulk density in the cell by more than 100 amagat. It can be concluded that the density in the pores exceeds the density in the bulk at the temperatures close enough to the bulk critical value.

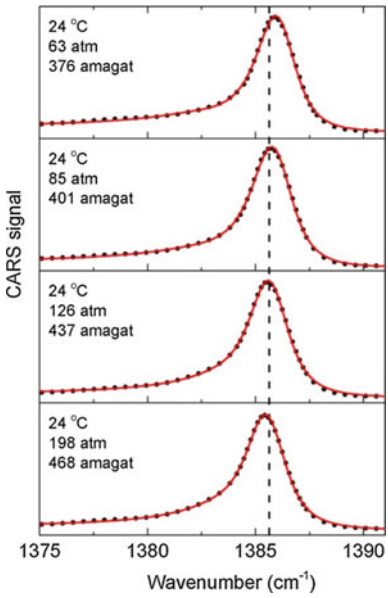

Fig. 8.12 CARS spectra (dots) measured at the isothermal compression of CO_2 confined to the pores of 3.5 nm in radius and the fits (solid line) obtained using the two-component model for the resonant part [46]. The values of the temperature, pressure and density are shown for the respective spectra

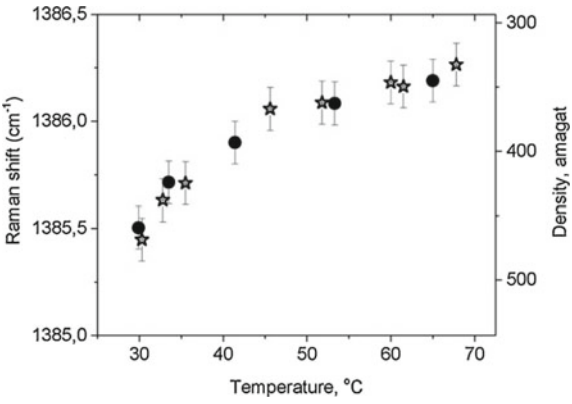

Fig. 8.13 Temperature dependences of the Raman shift and the density for scCO2 confined to the pores whose radii are 2 nm (dots) and 3.5 nm (open stars) [46]

It should be noted, that the temperature dependences of the density obtained for the two types of porous glass were indistinguishable. Probably, the conditions of nanoconfinement are similar enough and more precise experiments are necessary to identify differences.

The results show that the equation of state of scCO2 is significantly modified under conditions of nanoconfinement at temperatures that are not far from the bulk critical value. For instance, at 35 °C, which is undoubtedly supercritical temperature both in the nanopores and in the bulk, the density of 420 amagat, observed at $\sim$ 88 atm in the pores, is achieved in the bulk at $\sim$ 156 atm [47], which is almost twice as large as in the nanopores. At the same time, at 68 °C, the behavior in the bulk and that under

the nanoconf inement are similar. Therefore, a significant densification observed in the pores in the vicinity of bulk critical point is attributed to the near-critical effects taking place under the nanoconfinement.

Thus, we can conclude that CARS spectroscopic measurements applied to the analysis of the phase composition of carbon dioxide filling the nanoporous glass samples affords better understanding and visual explication of the phenomenon. Figure 8.14 illustrates the main stages of the process of the pore filling interpreted on the basis of the vibrational Raman spectra analysis. In the initial stage (a) when the pores are being filled with a relatively low density gas, the deposition of the surface adsorbed monolayer contributing to the CARS signal takes place. As the first layer covers significantly large areas of the pore walls, polymolecular layers can be adsorbed upon the first layer. As the pressure increases (b), the first monolayer becomes almost full while the polymolecular layers (multilayers) are developed. Then, the liquid clusters formation starts and gradual pores are being filled gradually (c). The molecules constituting the cluster surface are in the different environment in

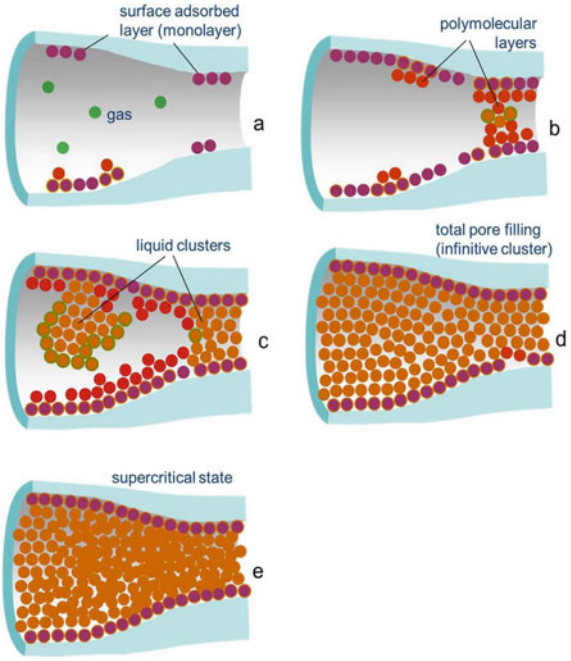

Fig. 8.14 Sketch illustrating the pore filling process: **a** the first surface adsorbed layer (purple) deposited from the gas (green) phase; **b** progress in the polymolecular layer formation (red); **c** the clusterization in the narrowest pores and on the predominately concave pore walls. (The cluster surface molecules are indicated in green round circles.); **d** the entire pore volume are filled with the liquid phase molecules (orange); **e** the supercritical state, in which the density enhancement proceeds starting from the narrowest pores. The surface adsorbed molecular layer is covered by the next molecular layers as shown in orange circles (**a**–**e**), indicating possible spectral differences in comparison with the molecules in the uncovered first surface adsorbed layer

comparison with the molecules in the cluster core and thus exhibit a different spectral shift. The smallest the size of the clusters becomes, the larger the surface-to-volume ratio becomes. This characteristic heterogeneous nature of the small clusters leads to the larger spectral peak broadening than that of the infinite liquid. The larger the size of the clusters becomes, the smaller the spectral broadening becomes. As the clusters grow in size further, the pores are finally filled with the liquid phase (d), while the surface adsorbed layer is still present. Supercritical conditions induce further the density increase (e), which starts occurring from the smallest size pores. It should be noted that the surface adsorbed layer, covered by the next molecular layers, can be, in principle, spectrally different from the uncovered first molecular layer. For example, the linewidth ~ 3.9 cm^{-1} of the lower-frequency shifted peak attributed to the molecules adsorbed on the wall surface at supercritical conditions (Fig. 8.10b) is smaller by the factor of ~ 1.4 than the linewidth ~ 5.5 cm^{-1} obtained from the calculations illustrated in Fig. 8.8, and is ascribed specifically to the molecules adsorbed on the surface from the gas phase. The obtained spectral shifts, 1382 cm^{-1} [46] (Fig. 8.10b) and 1381 cm^{-1} [45] (Fig. 8.8) are also slightly different. Because the contribution of the lower-frequency peak is much smaller than the contribution of the main peak (Fig. 8.9b), the errors of the shift and linewidth of the lower-frequency surface adsorbed layer peak can be very large, further measurements and calculations with higher precision will be necessary.

Obviously, the pattern presented in Fig. 8.14 is somewhat simplified. However, it can instil scenarios for new clarifying experiments. For example, (a) the samples with narrower pores could emphasize the role of nanoconfinement; (b) some special experiments can be set up to articulate the connection of the critical point shift with the nanopores size, (c) the properties of the first surface-adsorbed layer can be examined by the comparison of the cases with different exterior environments: the free space, the polymolecular phase, the subcritical liquid phase, and the supercritical phase. Generally speaking, more precise characterisations can be achieved even for the cases in which more than two different phases coexist if additional considerations are taken into account based on a comparative analysis using results to be obtained by other related and alternative techniques [24–27].

8.4 Conclusion

Precise characterization of the dense subcritical and supercritical phases of carbon dioxide under the conditions of nanoconfinement has been achieved by the diagnostic analysis of the CARS spectra of the glass samples with pores whose radius is of the order of several nanometers. The CARS measurements have been made in a wide pressure range at sub-critical and supercritical temperatures. The appearance of the different phases has been identified by the spectral line shifts corresponding to the Q-branch peak at 1388 cm^{-1} of the vibrational transition of CO_2. It has been clearly demonstrated that, at the sub-critical temperatures of − 6 and − 13 °C, the surface adsorbed monolayer and the polymolecular layers adsorbed upon the surface

adsorbed monolayer can be spectroscopically distingushed from each other. The spectral peak of the polymolecular layers was found to be noticably shifted from that of the liquid phase and appeared between the peak attributed to the surface adsorbed monolayer and that attributed to the liquid phase. At the pressure above the condensation onset, the spectral peak appearing at the liquid phase frequency was at least threefold broader than that of the bulk liquid. With the pressure increase, the peak width became narrower and reached the value in the bulk liquid. This narrowing reflects the enlargement of the liquid clusters from those in the primarily sub-nanometer and nanometer size with a significantly large fraction of molecules constituting the outer border and interacting with the non-uniform environment to the infinitely large homogeneous liquid filling the pore network. The density of supercritical cabon dioxide confined in the pores at isochoric heating (from 30 to 68 °C) determined by measuring the Raman shift exhibited a significant (~ 30%) increase in the vicinity of the bulk critical temperature, and then, asymptotically decreased to the average level in the bulk $scCO_2$ equal to 335 amagat at higher temperatures. The present CARS approach we have developed have shown potential applicability for the investigation of the adsorption processes of molecules in mesoporous and microporous materials, and will afford a complementary technique to the traditionally available methods such as volumetric, gravimetric and nuclear magnetic resonance techniques. The experimental data we obtained will be useful for the description of the structure of confined adsorbate, which can also be a multicomponent mixture, and thus, leading to a deeper insight into the interplay of different adsorption mechanisms and to the verification of theoretical models.

From the view point of applications, the presented spectroscopic technique has promising perspectives in the investigation of adsorption processes of mixtures of different molecular species in bulk nanoporous reservoirs. One of the applications of greatest practical interest is the characterization of the displacement of light hydrocarbons by carbon dioxide in shales and other related geological structures. Although real nanoporous solid materials of a practical interest are generally opaque, transparent materials with pores of the similar size like porouse glasses, silicon aerogels etc. can be used instead for modeling in the different stages of the applications along this direction.

Acknowledgements The authors greatly appreciate the support from the Russian Foundation for Basic Research (grant 19-02-00978), Moscow State University Program of Development, and the organizing committee of the STEPS program.

References

1. D.K. Dutta, B.J. Borah, P.P. Sarmah, Recent advances in metal nanoparticles stabilization into nanopores of montmorillonite and their catalytic applications for fine chemicals synthesis. Catal. Rev. **57**(3), 257–305 (2015). https://doi.org/10.1080/01614940.2014.1003504
2. N.Z. Logar, V. Kaučič, Nanoporous materials: from catalysis and hydrogen storage to wastewater treatment. Acta Chim. Slov. **53**(2), 117–135 (2006)

3. D.J. Malik, C. Webb, R.G. Holdich, J.J. Ramsden, G.L. Warwick, I. Roche, D.J. Williams, A.W. Trochimczuk, J.A. Dale, N.A. Hoenich, Synthesis and characterization of size-selective nanoporous polymeric adsorbents for blood purification. Sep. Purif. Technol. **66**(3), 578–585 (2009). https://doi.org/10.1016/j.seppur.2009.01.016
4. Á. Szegedi, M. Popova, K. Yoncheva, J. Makk, J. Mihály, P. Shestakova, Silver- and sulfadiazine-loaded nanostructured silica materials as potential replacement of silver sulfadiazine. J. Mater. Chem. B **2**(37), 6283–6292 (2014). https://doi.org/10.1039/C4TB00619D
5. M.A. Massa, C. Covarrubias, M. Bittner, I.A. Fuentevilla, P. Capetillo, A. Von Marttens, J.C. Carvajal, Synthesis of new antibacterial composite coating for titanium based on highly ordered nanoporous silica and silver nanoparticles. Mater. Sci. Eng. C **45**, 146–153 (2014). https://doi.org/10.1016/j.msec.2014.08.057
6. J. Tang, J. Liu, N.L. Torad, T. Kimura, Y. Yamauchi, Tailored design of functional nanoporous carbon materials toward fuel cell applications. Nano Today **9**(3), 305–323 (2014). https://doi.org/10.1016/j.nantod.2014.05.003
7. N. Hüsing, U. Schubert, *Aerogels, Ullmann's Encyclopedia of Industrial Chemistry*, 2nd edn. (Wiley, VCH, Weinheim, 2006).
8. F. Hao, H. Zou, Y. Lu, Mechnisms of shale shale gas storage: Implictions for shale gas exploration in China. AAPG Bull. **97**(8), 1325–1346 (2013). https://doi.org/10.1306/02141312091
9. D.J.K. Ross, R.M. Bustin, The importance of shale composition and pore structure upon gas storage potential of shale gas reservoirs. Mar. Pet. Geol. **26**(6), 916–927 (2009). https://doi.org/10.1016/j.marpetgeo.2008.06.004
10. K.V. Kumar, K. Preuss, M.-M. Titirici, F. Rodríguez-Reinoso, Nanoporous materials for the onboard storage of natural gas. Chem. Rev. **117**(3), 1796–1825 (2017). https://doi.org/10.1021/acs.chemrev.6b00505
11. R.E. Morris, P.S. Wheatley, Gas storage in nanoporous materials. Angew. Chem. Int. Ed. **47**(27), 4966–4981 (2008). https://doi.org/10.1002/anie.200703934
12. A. Modak, S. Jana, Advances in porous adsorbents for CO_2 capture and storage, in *Carbon Dioxide Chemistry, Capture and Oil Recovery*. Chapter 9 (2018). https://doi.org/10.5772/intechopen.70796
13. R. Bera, M.Ansari, A. Alam, N. Das, Nanoporous azo polymers (NAPs) for selective CO_2 uptake. J. CO_2 Util. **28**, 385–392 (2018). https://doi.org/10.1016/j.jcou.2018.10.016
14. D.M. D'Alessandro, B. Smit, J.R. Long, Carbon dioxide capture: prospects for new materials. Angew. Chem. Int. Ed. **49**(35), 6058–6082 (2010). https://doi.org/10.1002/anie.201000431
15. A. Saghafi, H. Javanmard, K. Pinetown, Study of coal gas wettability for CO_2 storage and CH_4 recovery. Geofluids **14**(9), 310–325 (2014). https://doi.org/10.1111/gfl.12078
16. T.J. Hughes, A. Honari, B.F. Graham, A.S. Chauhan, M.L. Johns, E.F. May, CO_2 sequestration for enhanced gas recovery: New measurements of supercritical CO_2–CH_4 dispersion in porous media and a review of recent research. Int. J. Greenh. Gas Contr. **9**(1), 457–468 (2012). https://doi.org/10.1016/j.ijggc.2012.05.011
17. D. Sanli, S.E. Bozbag, C. Erkey, Synthesis of nanostructured materials using supercritical CO_2: Part I. Physical transformations. J. Mater. Sci. **47**(7), 2995–3025 (2011). https://doi.org/10.1007/s10853-011-6054-y
18. . C.A. Eckert, B.L. Knutson, P.G. Debenedetti, Supercritical fluids as solvents for chemical and materials processing. Nature **383**(6598), 313–318 (1996). https://doi.org/10.1038/383313a0
19. T. Matsuda, Recent progress in biocatalysis using supercritical carbon dioxide. J. Biosci. Bioeng. **115**(3), 233–241 (2013). https://doi.org/10.1016/j.jbiosc.2012.10.002
20. A.I. Cooper, Polymer synthesis and processing using supercritical carbon dioxide. J. Mater. Chem. **10**(2), 207–234 (2000). https://doi.org/10.1039/A906486I
21. X. Han, M. Poliakoff, Continuous reactions in supercritical carbon dioxide: problems, solutions and possible ways forward. Chem. Soc. Rev. **41**(8), 1428–1436 (2012). https://doi.org/10.1039/C2CS15314A
22. A. Zhang, Q. Zhang, H. Bai, L. Li, J. Li, Polymeric nanoporous materials fabricated with supercritical CO_2 and CO_2-expanded liquids. Chem. Soc. Rev. **43**(20), 6938–6953 (2014). https://doi.org/10.1039/C4CS00100A

23. S.E. Bozbag, D. Sanli, C. Erkey, Synthesis of nanostructured materials using supercriticalCO_2: Part II. Chemical transformations. J. Mater. Sci. **47**(7), 3469–3492 (2012). https://doi.org/10.1007/s10853-011-6064-9
24. S. Brunnauer, The adsorption of gases and vapors, in *Physical Adsorption*, vol. 1 (Princeton University Press, Princeton, 1943)
25. M.M. Dubinin, B.P. Bering, V.V. Serpinskii, B.N. Vasil'ev, in *Surface Phenomena in Chemistry and Biology*, eds. by J.F. Danielli, R.G. A. Pankhurst, A.C. Riddiford (Pergamon Press, London, 1958), p. 172
26. R. Valiullin, S. Naumov, P. Galvosas, J. Karger, H.-J. Woo, F. Porcheron, P.A. Monson, Exploration of molecular dynamics during transient sorption of fluids in mesoporous materials. Nature **443**(7114), 965–968 (2006). https://doi.org/10.1038/nature05183
27. S. Naumov, R. Valiullin, P.A. Monson, J. Karger, Probing memory effects in confined fluids via diffusion measurements. Langmuir **24**(13), 6429–6432 (2008). https://doi.org/10.1021/la801349y
28. H.-J. Woo, P.A. Monson, Phase behavior and dynamics of fluids in mesoporous glasses. Phys. Rev. E **67**(4), 041207(17) (2003). https://doi.org/10.1103/PhysRevE.67.041207
29. M. R. Deinert, J.-Y. Parlange, Dynamics of crater formations in immersed granular materials. Phys. Rew. E, **79**(2), 021202(7) (2009). https://doi.org/10.1103/PhysRevE.79.021301
30. K. Morishige, Nature of adsorption hysteresis in cylindrical pores: effect of pore corrugation. J. Phys. Chem. C **120**(39), 22508–22514 (2016). https://doi.org/10.1021/acs.jpcc.6b07764
31. A.C. Mitropoulos, K.L. Stefanopoulos, E.P. Favvas, E. Vansant, N.P. Hankins, On the formation of nanobubbles in Vycor porous glass during the desorption of halogenated hydrocarbons. Sci. Rep. **5**(1), 10943(12) (2015). https://doi.org/10.1038/srep10943
32. P.I. Ravikovitch, A.V. Neimark, Experimental confirmation of different mechanisms of evaporation from ink-bottle type pores: equilibrium, pore blocking, and cavitation. Langmuir **18**(25), 9830–9837 (2002). https://doi.org/10.1021/la026140z
33. T. Hiratsuka, H. Tanaka, M.T. Miyahara, Critical energy barrier for capillary condensation in mesopores: hysteresis and reversibility. J. Chem. Phys. **144**(16), 164705(8) (2016). https://doi.org/10.1063/1.4947243
34. Y.H. Zeng, L. Prasetyo, S.J. Tan, C. Fan, D.D. Do, D. Nicholson, On the hysteresis of adsorption and desorption of simple gases in open end and closed end pores. Chem. Ing. Sci. **158**, 462–479 (2016). https://doi.org/10.1016/j.ces.2016.10.048
35. V.G. Arakcheev, V.B. Morozov, Narrowing of the vibrational spectrum under compression of liquid carbon dioxide. JETP Lett. **90**(7), 524–529 (2009). https://doi.org/10.1134/S0021364009190060
36. V.G. Arakcheev, V.N. Bagratashvili, A.A. Valeev, V.B. Morozov, V.K. Popov, Broadening peculiarities of vibrational bands in the spectrum of carbon dioxide close to the critical temperature. Rus. J. Phys. Chem. B **4**(8), 1245–1251 (2010). https://doi.org/10.1134/S1990793110080117
37. V.G. Arakcheev, V.N. Bagratashvili, S.A. Dubyanskiy, V.B. Morozov, A.N. Olenin, V.K. Popov, V.G. Tunkin, A.A. Valeev, D.V. Yakovlev, Vibrational line shapes of liquid and sub-critical carbon dioxide in nano-pores. J. Ram. Spectr. **39**(6), 750–755 (2008). https://doi.org/10.1002/jrs.1974
38. V.G. Arakcheev, V.N. Bagratashvili, A.A. Valeev, V.B. Morozov, A.N. Olenin, V.K. Popov, V.G. Tunkin, Broadening of vibrational spectra of carbon dioxide upon absorption and condensation in nanopores. Moscow Univ. Phys. Bull. **63**(6), 388–392 (2008). https://doi.org/10.3103/S0027134908060052
39. V.G. Arakcheev, A.A. Valeev, V.B. Morozov, A.N. Olenin, CARS diagnostics of molecular media under nanoporous confinement. Las. Phys. **18**(12), 1451–1458 (2008). https://doi.org/10.1134/S1054660X08120128
40. V.G. Arakcheev, A.A. Valeev, V.B. Morozov, I.R. Farizanov, Phase behavior of the molecular medium in nanopores and vibrational spectra structure transformation. Moscow. Univ. Phys. Bull. **66**(2), 147–154 (2011). https://doi.org/10.3103/S0027134911020032
41. O.V. Andreeva, V.G. Arakcheev, V.N. Bagratashvili, V.B. Morozov, V.K. Popov, A.A. Valeev, CARS diagnostics of fluid adsorption and condensation in small mesopores. J. Ram. Spectr. **42**(9), 1747–1753 (2011). https://doi.org/10.1002/jrs.2979

42. V.G. Arakcheev, V.B. Morozov, CARS diagnostics of fluid phase behavior in small mesopores at near-critical temperatures. J. Ram. Spectr. **44**(10), 1363–1368 (2013). https://doi.org/10.1002/jrs.4289
43. V.G. Arakcheev, V.B. Morozov, Vibrational spectra of carbon dioxide adsorbed on nanopores walls at supermonolayer and submonolayer coverage. J. Raman Spectrosc. **45**(7), 501–506 (2014). https://doi.org/10.1002/jrs.4453
44. V.G. Arakcheev, A.N. Bekin, V.B. Morozov, CARS detection of liquid-like phase appearance in small mesopores. Las. Phys. **27**(11), 115701(6) (2017). https://doi.org/10.1088/1555-6611/aa8cd8
45. V.G. Arakcheev, A.N. Bekin, V.B. Morozov, Spectroscopic characterization of adsorbate confined in small mesopores: distinction of first surface-adsorbed layer, polymolecular layers, and liquid clusters. J. Raman Spectrosc. **49**(12), 1945–1952 (2018). https://doi.org/10.1002/jrs.5491
46. V. Arakcheev, A. Bekin, V. Morozov, Spectroscopic characterization of supercritical carbon dioxide density change under isochoric heating in mesoporous glass. J. Sup. Crit. Fl. **143**, 353–357 (2019). https://doi.org/10.1016/j.supflu.2018.09.014
47. R. Span, W. Wagner, A new equation of state for carbon dioxide covering the fluid region from the triple-point temperature to 1100 K at pressures up to 800 MPa. J. Phys. Chem. Ref. Data **25**(6), 1509–1596 (1996). https://doi.org/10.1063/1.555991
48. G. Herzberg, *Molecular Spectra and Molecular Structure II. Infrared and Raman Spectraof Polyatomic Molecules*, 2nd edn. (Krieger, Malabar, Florida, 1991)
49. F. Rasetti, Raman effect in gases. Nature **123**(3093), 205 (1929). https://doi.org/10.1038/123205a0; F. Rasetti, Selection rules in the Raman effect. Nature **123**(3107), 757–759 (1929). https://doi.org/10.1038/123757c0
50. E. Fermi, Über den Ramaneffekt des Kohlendioxyds. Z. Physik **71**(3–4), 250–259 (1931). https://doi.org/10.1007/BF01341712
51. C.P. Courtoy, G. Herzberg, Effect of fermi resonance on the centrifugal stretching constants in CO_2. J. Chem. Phys. **23**(5), 975–976 (1955). https://doi.org/10.1063/1.1742161
52. H.E. Howard-Lock, B.P. Stoicheff, Raman intensity measurements of the fermi diad ν_1, $2\nu_2$ in $12CO_2$ and $^{13}CO_2$. J. Mol. Spectr. **37**(2), 321–326 (1971). https://doi.org/10.1016/0022-2852(71)90302-X
53. B.P. Stoicheff, High resolution Raman spectroscopy of gases: XI. Spectra of CS_2 and CO_2. Can. J. Phys. **36**(2), 218–230 (1958). https://doi.org/10.1139/p58-026
54. H.L. Welsh, P.E. Pashler, B.P. Stoicheff, Density effects in the Raman spectrum of carbon dioxide. Can. J. Phys. **30**(2), 99–110 (1952). https://doi.org/10.1139/p52-009
55. G. Amat, M. Pimbert, On Fermi resonance in carbon dioxide. J. Mol. Spectrosc. **16**(2), 278–290 (1965). https://doi.org/10.1016/0022-2852(65)90123-2
56. H.R. Gordon, T.K. McCubbin, The 2.8-micron bands of CO_2. J. Mol. Spectr. **19**(1–4), 137–154 (1966). https://doi.org/10.1016/0022-2852(66)90237-2
57. R.B. Wright, C.H. Wang, Density effect on the Fermi resonance in gaseous CO_2 by Raman scattering. J. Chem. Phys. **58**(7), 2893–2895 (1973). https://doi.org/10.1063/1.1679594
58. Y. Garrabos, R. Tufeu, B. Le Neindre, G. Zalczer, D. Beysens, Rayleigh and Raman scattering near the critical point of carbon dioxide. J. Chem. Phys. **72**(8), 4637–4651 (1980). https://doi.org/10.1063/1.439706
59. C.G. Deacon, M.J. Clouter, H. Kiefte, High resolution Raman spectra of near-critical CO_2. J. Chem. Phys. **83**(1), 446 (1985). https://doi.org/10.1063/1.449789
60. C.M. Roland, W.A. Steele, Rotation–vibration CARS spectra of the $2\nu_2$ mode in CO_2 gas. J. Chem. Phys. **74**(5), 2733–2739 (1981). https://doi.org/10.1063/1.441441
61. J. Baran, A. Grofcsik, W.J. Jones, Motional narrowing in the $\nu_1/2\nu_2$ Fermi resonance diad of CO_2. Mol. Phys. **45**(6), 1291–1297 (1982). https://doi.org/10.1080/00268978200101001
62. B. Lavorel, G. Millot, R. Saint-Loup, H. Berger, L. Bonamy, J. Bonamy, D. Robert, Study of collisional effects on band shapes of the $\nu_1/2\nu_2$ Fermi dyad in CO_2 gas with stimulated Raman spectroscopy. I. Rotational and vibrational relaxation in the $2\nu_2$ band. J. Chem. Phys. **93**(4), 2176–2184 (1990). https://doi.org/10.1063/1.459049

63. B. Lavorel, G. Millot, R. Saint-Loup, H. Berger, L. Bonamy, J. Bonamy, D. Robert, Study of collisional effects on band shapes of the $\nu_1/2\nu_2$ Fermi dyad in CO_2 gas with stimulated Raman spectroscopy. II. Simultaneous line mixing and Dicke narrowing in the $\nu 1$ band. J. Chem. Phys. **93**(4), 2185–2191 (1990). https://doi.org/10.1063/1.459050
64. C. Roche, G. Millot, R. Chaux, R. SaintLoup, Rotational and vibrational relaxation of the $\nu_1/2\nu_2$ Fermi dyad in CO_2 gas from Raman-infrared double resonance experiments. J. Chem. Phys. **103**(4), 2863–2870 (1995). https://doi.org/10.1063/1.467600
65. G. Millot, C. Roche, State-to-state vibrational and rotational energy transfer in CO_2 gas from time-resolved raman–infrared double resonance experiments. J. Ram. Spectr. **29**(4), 313–320 (1998). https://doi.org/10.1002/(SICI)1097-4555(199804)29:4%3c313::AID-JRS242%3e3.0.CO;2-R
66. D.S Kuznetsov, V.B Morozov, A.N Olenin, V.G Tunkin, High resolution study of 1388 cm^{-1} CO_2 vibration by time-domain CARS: spectral exchange and Dicke effect. **257**(1), 117–122 (2000). https://doi.org/10.1016/S0301-0104(00)00125-7
67. V. Morozov, S. Mochalov, A. Olenin, V. Tunkin, A. Kouzov, Density evolution of the picosecond time-domain CARS responses from carbon dioxide gas. J. Ram. Spect. **34**(12), 983–988 (2003). https://doi.org/10.1002/jrs.1097
68. V.G. Arakcheev, V.V. Kireev, V.B. Morozov, A.N. Olenin, V.G. Tunkin, A.A. Valeev, D.V. Yakovlev, Collisionally induced dephasing and rotational energy transfer in the CO_2 Fermi dyad 'red' Q-branch 1285 cm^{-1}. J. Ram. Spectr. **38**(8), 1038–1045 (2007). https://doi.org/10.1002/jrs.1780
69. V.G. Arakcheev, V.V. Kireev, V.B. Morozov, A.N. Olenin, V.G. Tunkin, A.A. Valeev, D.V. Yakovlev, Collisionally induced dephasing and rotational energy transfer in the CO_2 Fermi dyad 'blue' Q-branch 1388 cm^{-1}. J. Ram. Spectr. **38**(8), 1046–1051 (2007). https://doi.org/10.1002/jrs.1783
70. H. Nakayama, K. Saitow, M. Sakashita, K. Ishii, K. Nishikawa, Raman spectral changes of neat CO_2 across the ridge of density fluctuation in supercritical region. Chem. Phys. Lett. **320**(3–4), 323–327 (2000). https://doi.org/10.1016/S0009-2614(00)00249-9
71. V.G. Arakcheev, V.N. Bagratashvili, A.A. Valeev, V.M. Gordiyenko, V.V. Kireev, V.B. Morozov, A.N. Olenin, V.K. Popov, V.G. Tunkin, D.V. Yakovlev, Linewidths and shifts of carbon dioxide CARS spectra near the critical point. J. Ram. Spectr. **34**(12), 952–956 (2003). https://doi.org/10.1002/jrs.1098
72. M.I. Cabaço, S. Longelin, Y. Danten, M. Besnard, Local density enhancement in supercritical carbon dioxide studied by Raman spectroscopy. J. Phys. Chem. A **111**(50), 12966–12971 (2007). https://doi.org/10.1021/jp0756707
73. M.I. Cabaço, M. Besnard, S. Longelin, Y. Danten, Evolution with the density of CO_2 clustering studied by Raman spectroscopy. J. Mol. Liq. **153**(1), 15–19 (2010). https://doi.org/10.1016/j.molliq.2009.09.007
74. T.H. Elmer, Porous and reconstructed glasses, in ceramics and glasses, in: *Engineered Materials Handbook*, vol. 4, ed. by S.J. Schneider (ASM International, Cleveland, Ohio, 1992)
75. O.V. Andreeva, I.E. Obyknovennaya, E.R. Gavrilyuk, A.A. Paramonov, A.P. Kushnarenko, Silver-halide photographic materials based on nanoporous glasses. J. Opt. Technol. **72**(12), 916–922 (2005). https://doi.org/10.1364/JOT.72.000916
76. S.A. Akhmanov, N.I. Koroteev, *Methods of Nonlinear Optics in Light Scattering Spectroscopy* (Nauka, Moscow, 1981). (in Russian)
77. G.L. Eesley, *Coherent Raman Spectroscopy* (Pergamon Press, London, 1981).
78. R.J. Hall, Coherent anti-Stokes Raman spectroscopic modeling for combustion diagnostics. Opt. Eng. **22**(3), 322–329 (1983). https://doi.org/10.1117/12.7973113

79. C.G.V. Burgess, D.H. Everett, S. Nuttall, Adsorption of carbon dioxide and xenon by porous glass over a wide range of temperature and pressure-applicability of the Langmuir case VI equation. Langmuir **6**(12), 1734–1738 (1990). https://doi.org/10.1021/la00102a004
80. S. Brunauer, P.H. Emmett, E. Teller, J. Am. Chem. Soc. **60**(2), 309–319 (1938). https://doi.org/10.1021/ja01269a023
81. W. Thomson, Proc. R. Soc. Edinburgh **7**, 63 (1870); Phil. Mag. **42**, 448 (1871)
82. S.J. Gregg, K.S.W. Sing, *Adsorption, Surface Area and Porosity* (Academic Press, New York, 1982).

Chapter 9
Contemporary Discoveries in the Copper Octacyanidometallate Photomagnetic Assemblies

Olaf Stefanczyk, Koji Nakabayashi, and Shin-ichi Ohkoshi

Abstract In this chapter, the concept of photomagnetic effect in copper(II)-octacyanidometallate(IV) systems and its various aspects have been introduced. Multifunctional cyanido-bridged metal assemblies attract much attention due to their great importance for fundamental research as well as their potential application in various technologies. Among the numerous advantages of this type of assemblies, the vast structural diversity should be distinguished, as it allows for various electronic states by a combination of metal ions and ligand, resulted in their functionalities. The most excellent examples of such materials are photomagnetic compounds revealing switching between different magnetic states by stimulation with electromagnetic radiation. Herein, various Cu^{II}-$[M^{IV}(CN)_8]^{4-}$ complexes with unique characters of photoinduced magnetization, milestones in understanding the mechanism of photomagnetic behavior and the impact of various factors on their photomagnetic phenomena are presented.

9.1 Introduction

Modern chemistry focuses on the elaboration of innovative functional materials and the discovery of new physical phenomena, which can broaden our knowledge and possibly beget new areas of science [1, 2]. Among the available pool of known chemical compounds, multifunctional molecular materials which consist of metal complexes have attracted significant attention by offering several incredible advantages such as the possibility of introducing desirable function at the design stage,

O. Stefanczyk · K. Nakabayashi · S. Ohkoshi (✉)
Department of Chemistry, School of Science, The University of Tokyo, 7-3-1 Hongo, Bunkyo-ku, Tokyo 113-0033, Japan
e-mail: ohkoshi@chem.s.u-tokyo.ac.jp

O. Stefanczyk
e-mail: olaf@chem.s.u-tokyo.ac.jp

K. Nakabayashi
e-mail: knakabayashi@chem.s.u-tokyo.ac.jp

K. Yamanouchi et al. (eds.), *Progress in Photon Science*, Springer Series in Chemical Physics 125, https://doi.org/10.1007/978-3-030-77646-6_9

easiness of synthesis and modification, structural diversity with various topologies [3], the prospect of postsynthetic modification, ability to respond to chemical and physical external stimuli [4, 5], and the most motivating possibility of observing physical cross-effects. All these benefits we owe to the modular construction of these materials based on different combinations of metal cations and ligands which provide various structures and intrinsic functionalities.

Since the beginning of the millennium, multifunctional molecule-based magnetic materials have celebrated a series of great successes in broadening our knowledge about new physical phenomena including novel cross-effects [3, 6, 7]. Scientists were able to combine magnetic phenomena of long-range magnetic ordering (extended two- (2D) and three-dimensional (3D) coordination polymers), slow magnetic relaxation (discrete complexes and clusters, and low-dimensional coordination polymers), or spin transition (monometallic spin crossover and bimetallic charge transfer systems) with other functionalities (e.g. luminescence, nonlinear optical activity, ferroelectricity, conductivity, porosity/sorption). This unique approach resulted in the invention of remarkable materials revealing new magneto-optical cross-effects [8] of magnetic circular dichroism (MCD) in cyanido-bridged Mn^{II}-$[Cr^{III}(CN)_6]^{3-}$ and Mn^{II}-$[Nb^{IV}(CN)_8]^{4-}$ ferrimagnets [9, 10], magneto-chiral dichroism (MChD) in an oxalate-bridged Mn^{II}-Cr^{III} ferromagnet [11], and magnetization-induced second harmonic generation (MSHG) in a cyanido-bridged Co^{II}-$[Cr^{III}(CN)_6]^{3-}$ [12], Mn^{II}-$[Nb^{IV}(CN)_8]^{4-}$ [13, 14] and Mn^{II}-$[Mo^{I}(CN)(NO)]^{3-}$ ferrimagnets [15], and an oxalate-bridged Mn^{II}-Cr^{III} ferromagnet [16]. All compounds exhibit enhancement of nonlinear optical signals by the onset of long-range magnetic ordering below the critical temperature. Besides, nonlinear optical active chiral magnets are worth to emphasize other luminescent magnets combining nontrivial magnetic characteristics with luminescence phenomena [17–20]. Other noteworthy classes of assemblies are systems revealing simultaneously ferroelectricity and ferromagnetism [21, 22], and superionic conductivity and ferromagnetism—V^{II}/Co^{II}-$[Cr^{III}(CN)_6]_{2/3}\cdot zH_2O$ [23]. Last but not least, there is also successively explored family of compounds showing diverse magnetic response towards sorption and desorption of solvents from gas and liquid phases known as porous magnets and solvatomagnets, respectively [18, 24–29].

Currently, the rapid development of research on photomagnets, molecular magnets revealing change of their magnetic states in the response to external stimuli by electromagnetic radiation (i.e. ultraviolet, visible, and near infrared lights), is also observed. The vast majority of them can be classified as systems showing: organic ligand isomerization or open/close switching with a change of spin state, e.g., stilbenoid complexes, diarylethene type ligands; valence tautomerism, e.g., Co^{II} catecholate; metal-centered thermal spin transition, e.g., Fe^{II}, Mn^{III} spin crossover (SCO) and $[M^{IV}(CN)_8]^{4-}$ (M^{IV} = Mo, W) complexes; metal-to-metal charge transfer (MMCT), e.g., Prussian blue analogues (PBAs); and metal-to-ligand charge transfer (MLCT), e.g., $Na_2[Fe(CN)_5(NO)]\cdot 2H_2O$ and its analogues [30–32]. More importantly, photomagnetic complexes after excitation with light can show the most of nontrivial magnetic behaviors including long-range magnetic ordering [33–36], slow magnetic relaxation [37], or spin transition [38–40], which can be also merged

with other functionalities leading to multifunctional photomagnets [41]. At this point, it is noteworthy to emphasize two multifunctional photomagnets showing spin-crossover-induced SHG, light-reversible spin-crossover, long-range magnetic ordering, and photoswitching of MSHG–$Fe_2[Nb(CN)_8](4\text{-bromopyridine})_8 \cdot 2H_2O$ [42] and a photoswitchable polar magnet that exhibits superionic conduction and SHG–$Cs_{1.1}Fe^{II}_{0.95}[Mo^{I}(CN)_5(NO)] \cdot 4H_2O$ [43].

Another aspect which is important to take into consideration during elucidation of photomagnetic materials is the fact that adding the next factor—excitation light, extends the number of additional experimental parameters that should be carefully considered in research (e.g. light wavelength, intensity, time of irradiation, conditions at which experiment is conducted). Furthermore, the light can also activate diverse mechanisms of photoexcitation which is very exciting but also very challenging to analyze. An excellent example of photomagnetic materials, which can be used in the construction of multifunctional materials, and revealing intricate mechanisms of photomagnetic effect, are Cu^{II}-$[Mo^{IV}(CN)_8]^{4-}$ assemblies [44–50]. Historically, the first attempt to explain the observed photomagnetic phenomenon has been done based on light-induced Metal-to-Metal Charge-Transfer (MMCT) mechanism in Cu^{II}-Mo^{IV} pair [51, 52]. However, because of reported results [53–58], the second mechanism of the Light-Induced Excited Spin-State Trapping (LIESST) effect on $[Mo^{IV}(CN)_8]^{4-}$ anion is also considered. In this work, we would like to guide readers through intriguing research on photomagnetic effect in Cu^{II}-M^{IV} systems.

9.2 Role of the Octacyanidometallate Type in the Photomagnetic Effect

The concept of investigation of the substitution molybdenum for tungsten in photomagnetic copper(II)-octacyanidomolybdate(IV) systems has been considered since the discovery of the phenomenon. Up to the present time, the verification of this idea was unattainable, despite a relatively large number of octacyanidotungstate(IV)-based assemblies [3]. Merely a few works report trials of photoirradiation of Cu(II)-W(IV) samples with light corresponding to absorption bands of these compounds [59]. Unfortunately, none of these studies exhibited any change of magnetic properties upon external stimuli by the visible light. This indicated that this type of assemblies does not present a photomagnetic effect. However, the most recent studies for Mn(II)-W(IV) coordination polymers [53, 54], describing an observation of photomagnetic phenomenon on octacyanidotungstate(IV), again raised expectations for further research.

Presently, there has been a significant step forward in the topic of photomagnetism in Cu(II)-W(IV) assemblies. As a result of self-assembly of two complex salts $[Cu(ida)(H_2O)_2]_n$ (ida^{2-} = iminodiacetate) and $K_4[M(CN)_8] \cdot 2H_2O$ (M = Mo, W), novel layered $K_4\{[Cu^{II}(ida)]_2[M^{IV}(CN)_8]\} \cdot 4H_2O$ (M^{IV} = Mo, W) coordination polymers have been formed (Fig. 9.1) [60]. Both assemblies are isostructural and they are

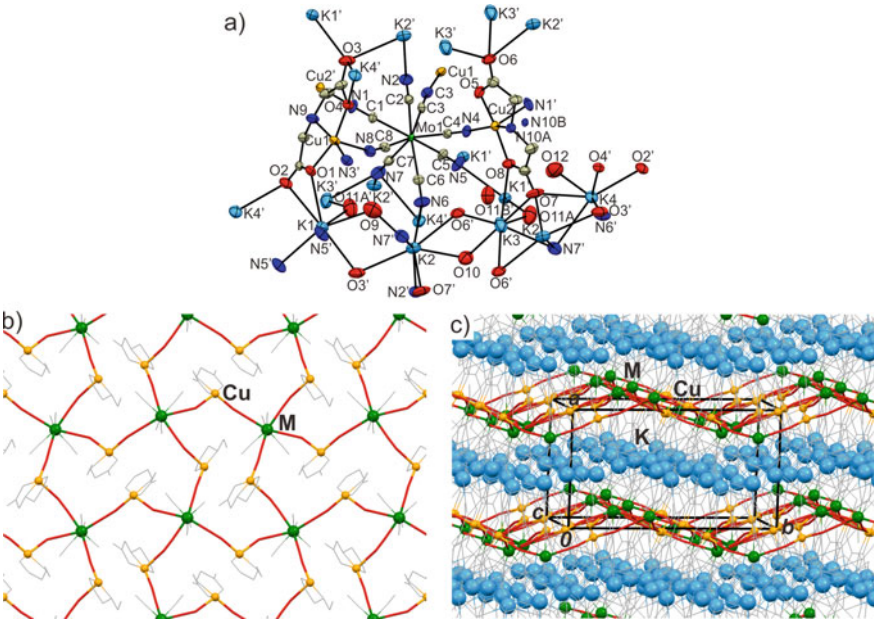

Fig. 9.1 **a** Structural unit of $K_4\{[Cu^{II}(ida)]_2[Mo^{IV}(CN)_8]\}\cdot 4H_2O$. **b** Structure of single layer with cyanido-bridges. **c** Crystal packing. Colors used: K—blue balls; Cu—yellow balls; Mo/W—green balls; bridging CN^-—red sticks; water, ida, and terminal CN^-—gray wireframe. In all figures, hydrogen atoms were omitted for clarity. Reprinted with permission from Inorg. Chem. **59**, 4292 (2020). Copyright 2020 American Chemical Society

rare cases of transition metal complexes with imino acids and polycyanidometallates. Their structures are constructed of a negatively-charged cyanido-bridged square grid with deformed 8-metallic units sandwiching potassium cations and water molecules layers in the analogy to the previously obtained $Cs_2Cu^{II}{}_7[Mo^{IV}(CN)_8]_4\cdot 6H_2O$ system [48]. Additionally, these newly obtained materials characterize complex hydrogen-bond networks and weak Coulomb interactions between potassium cations and lone pairs on oxygen atoms of water molecules and ida^{2-} anions stabilizing their crystal structures. It is also worth highlighting that $K_4\{[Cu^{II}(ida)]_2[M^{IV}(CN)_8]\}\cdot 4H_2O$ coordination polymers adopt two-dimensional topologies which have a greater preference for clearly exhibiting the photomagnetic effect.

Reflectance spectroscopy of $K_4\{[Cu^{II}(ida)]_2[M^{IV}(CN)_8]\}\cdot 4H_2O$ in UV–visible and near-IR regions revealed that structures of both spectra are comparable and complex which can be deconvoluted into ten Gaussian components. All this absorption bands can be assigned to ligand field bands of two symmetry independent $[Cu(ida)(NC)_2]$ units (600–800 nm region), ligand field bands of octacyanidometallate (330–500 nm region), and ligand field and metal-to-ligand charge-transfer bands of $[M(CN)_8]^{4-}$ and to ligand-to-metal charge-transfer bands of $[Cu(ida)(NC)_2]$ units (below 300 nm). Interestingly, all maxima of absorption bands of molybdenum analog are shifted to higher energy. This interpretation of both spectra was applied in the

choice of the excitation wavelengths: 532 and 473 nm laser lines—to observe possible the metal-to-metal charge-transfer photomagnetic effect in the Cu^{II}-M^{IV} pairs, and 407 nm light—to detect prospective Light-Induced Excited Spin-State Trapping in the M^{IV} centers.

Preliminary magnetic studies confirmed that both compounds in their ground state show paramagnetic behavior originating from copper(II) centers with single unpaired electrons ($S_{Cu(II)} = 1/2$, $g_{Cu(II)} = 2.05$) separated by bridging diamagnetic octacyanidometallate anions ($S_{M(IV)} = 0$). At low temperatures, Cu(II) centers interacting antiferromagnetically via the superexchange mechanism giving almost identical magnetic coupling constant zJ' of -0.27 and -0.25 cm^{-1} for Mo and W compounds, respectively. The next photomagnetic experiments for both systems with 407, 473, 532, 658, 705, and 804 nm laser lines have been conducted, however, the response was detected only for excitations with 407 nm. The $K_4\{[Cu^{II}(ida)]_2[Mo^{IV}(CN)_8]\}\cdot 4H_2O$ complex after 24 h of irradiation exhibited 30% increase of product of magnetic susceptibility in the $\chi_M T(T)$ plot and 6% augment of magnetization in the $M(H)$ curve in respect to its initial paramagnetic state (Fig. 9.2). These values are slightly lower than determined ones for other previously reported layered photomagnetic materials. Nonetheless, it is more important to emphasize the first observation of the photomagnetic effect in Cu^{II}-$[W^{IV}(CN)_8]^{4-}$ entities. After 24 h of irradiation with

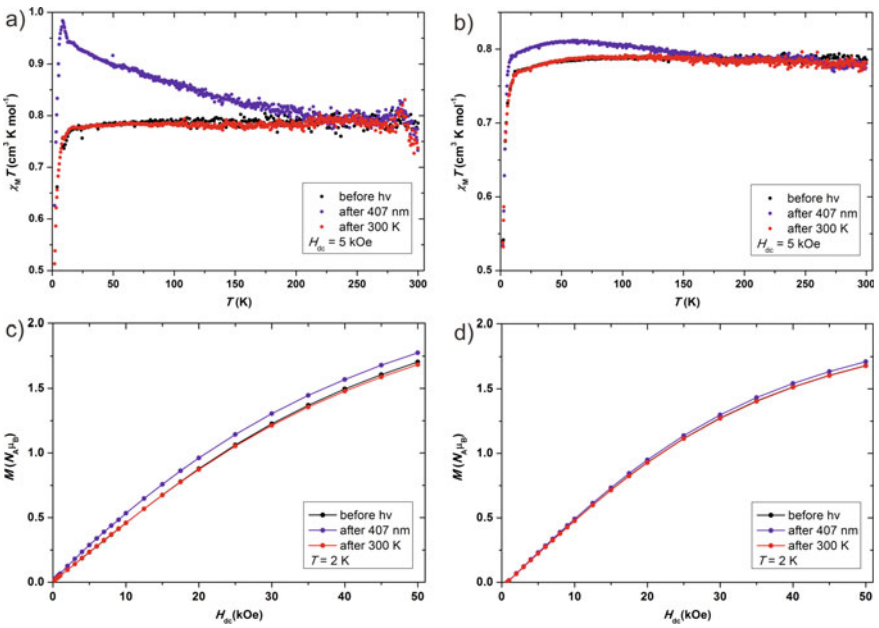

Fig. 9.2 The $\chi_M T(T)$ plots for $K_4\{[Cu^{II}(ida)]_2[M^{IV}(CN)_8]\}\cdot 4H_2O$ (M = Mo—**a**, and W—**b**) before, after excitation with 407 nm light for 24 h, and after thermal relaxation at 300 K; and corresponding $M(H)$ plots determined in the same way for Mo (**c**) and W (**d**) systems. Reprinted with permission from Inorg. Chem. **59**, 4292 (2020). Copyright 2020 American Chemical Society

407 nm light, the growth of $\chi_M T$ and M reached 3 and 2%, respectively. These small but non-negligible values are very important since they motivate further research in the field of photoswitchable materials and they could help in the development of more efficient and stable systems. Additionally, it is also worth highlighting that $\chi_M T(T)$ curves for both compounds differ in shape and relaxation temperature above which compound relax to its initial state before photoirradiation. The $\chi_M T(T)$ plot for octacyanidomolybdate-based system has a clear maximum around 9 K and monotonously diminished up to 230 K while the plot for tungsten analogue has very broad peak up to 160 K without an obvious maximum. The 70 K difference in relaxation temperature demands more studies to confirm if it is common for systems with diverse octacyanidometallates.

Furthermore, the possible mechanism of photomagnetic effect in $K_4\{[Cu^{II}(ida)]_2[M^{IV}(CN)_8]\}\cdot 4H_2O$ (M^{IV} = Mo, W) have been considered based on the most recent knowledge in this research field. Nowadays, two possible mechanisms of photomagnetic phenomenon in Cu(II)-Mo(IV) are advocated. Primarily, this unique phenomenon has been interpreted in the term of light-induced Metal-to-Metal Charge-Transfer (MMCT) mechanism in which spins are reorganized within isolated polynuclear molecules in the course of the following photoreaction: $\{Cu^{II}$ $(S = ½)$-N≡C-Mo^{IV} $(S = 0)$-$[N\equiv C\text{-}Cu^{II}$ $(S = ½)]_n\} \rightarrow \{Cu^{I}$ $(S = 0)$-N≡C-Mo^{V} $(S = ½)$-$[N\equiv C\text{-}Cu^{II}$ $(S = ½)]_n\}$. Consequently, a ferromagnetic coupling within Mo^{V} $(S = ½)$-$[N\equiv C\text{-}Cu^{II}$ $(S = ½)]_n$ units occurred resulting in the formation of local magnetic domains and a maximum in the product of magnetic susceptibility and temperature ($\chi_M T$) *versus* temperature plots. This concept correlated with the most experimental data, however, there was a controversy associated with the unexplained 10% or more increase of magnetic signal at low temperature in high fields after irradiation which ought not to be observed in systems with an invariant number of spins. In response to this inconsistency, a counter-proposals mechanism, explaining photomagnetic effect by means of Light-Induced Excited Spin-State Trapping (LIESST) in the Mo^{IV} centers, has been proposed. In this case the excitation with visible light leads to change of low-spin $Mo^{IV}{}_{LS}$ $(S = 0)$ closed shell singlet centers to high-spin $Mo^{IV}{}_{HS}$ $(S = 1)$ triplet state one, generating $\{Cu^{II}$ $(S = ½)$-N≡C-$Mo^{IV}{}_{HS}$ $(S = 1)$-$[N\equiv C\text{-}Cu^{II}$ $(S = ½)]_n\}$ domains. This idea soon attracted considerable attention and found supporters. Detailed analysis of available data for Cu(II)-Mo(IV) assembly suggested that observed effect can be explained well by LIESST with minor contribution of MMCT mechanism. This conclusion is supported by facts that ligand field bands of $[Mo(CN)_8]^{4-}$ as well as metal-to-ligand charge-transfer bands in Cu^{II}-$[Mo(CN)_8]^{4-}$ pairs can be activated by 407 nm light excitation, and the 6% increase of magnetization in $M(H)$ curve can be achieved only for LIESST mechanism, however, the expected $\chi_M T$ value of 0.9 cm^3 K mol^{-1} at low temperatures will be insufficient to explain observed signal without taking into account minor contribution of MMCT mechanism. Due to lower efficiency of photomagnetic effect in case of Cu^{II}-$[W(CN)_8]^{4-}$ system analysis of mechanism is more challenging and it gave two possible answers that photomagnetic process is related to low efficient LIESST effect on W(IV) or low efficient MMCT mechanism which requires further investigation.

9.3 Influence of Excitation Wavelength on the Mechanism of Photomagnetic Effect and Photoreversibility

An alternative way to tune photomagnetic characteristics of copper(II)-octacyanidomolybdate(IV) compounds are the adjustment of irradiation wavelength. This simple approach allows for the direct enhance of the phenomenon efficiency as well as to generate photoreversibility-phenomenon in which compounds switch back to their ground magnetic state by external stimuli with electromagnetic waves.

The most extensive studies on the influence of different excitation lights on photomagnetic effects have been performed for complex cyanido-bridged molecular ribbon $[Cu^{II}(bapa)]_2[Mo^{IV}(CN)_8]\cdot 7H_2O$, where bapa = bis(3-aminopropyl)amine [46]. This compound is built of two types of complex nodes: trigonal bipyramidal $\{[Cu(bapa)]_3[Mo(CN)_8]_2\}^{2-}$ and rhomboidal $\{[Cu(bapa)]_2[Mo(CN)_8]_2\}^{4-}$ units which are linked through $[Cu(bapa)]^{2+}$ complex ions (Fig. 9.3). Furthermore, hydrogen-bond networks stabilize the structure due to interactions between cyanides organic ligands and water molecules. Moreover, this assembly displays one of the highest complexities among the 1-D chains based on 3d metals with octacyanidometallates and other cyanido bridged complexes.

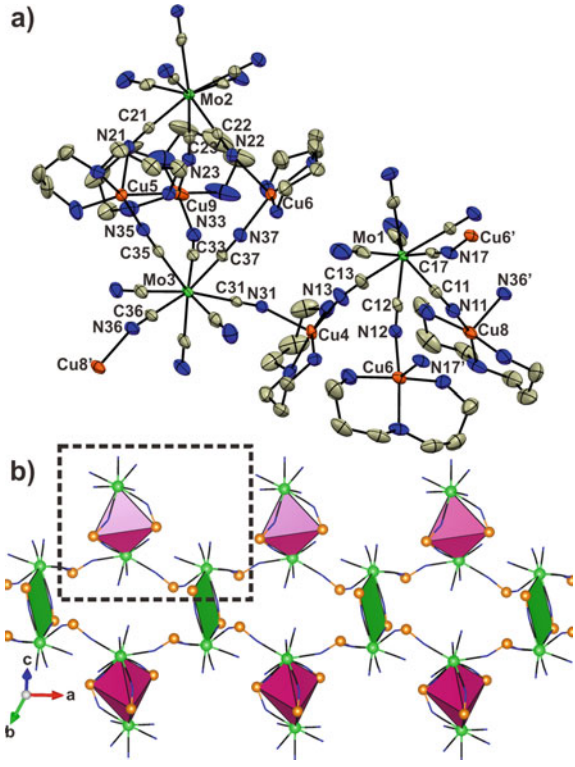

Fig. 9.3 **a** Structural unit of $[Cu^{II}(bapa)]_2[Mo^{IV}(CN)_8]\cdot 7H_2O$. **b** Skeleton of the 1-D ribbon. In both figures, hydrogen atoms and water molecules were omitted for clarity. Reproduced from J. Mater. Chem. C **3**, 8712 (2015) with permission from The Royal Society of Chemistry

Solid state UV–Vis-NIR absorption spectroscopy of $[Cu^{II}(bapa)]_2[Mo^{IV}(CN)_8]\cdot 7H_2O$ revealed several absorption bands assigned to the ligand field bands of $[Cu(bapa)]^{2+}$ complexes with diverse geometries (650–900 nm region), the metal-to-metal charge-transfer band in the Cu^{II}-Mo^{IV} pairs (band around 466 nm), and the ligand field bands of the $[Mo(CN)_8]^{4-}$ in UV region. This assignment agrees with previous observations for other Cu^{II}-$[Mo^{IV}(CN)_8]^{4-}$ systems. The provided interpretation of the spectrum was utilized for the choice of irradiation lights for photomagnetic studies.

From magnetic properties, $[Cu^{II}(bapa)]_2[Mo^{IV}(CN)_8]\cdot 7H_2O$ is ordinary paramagnet, built of copper(II) centers ($S_{Cu(II)} = 1/2$, $g_{Cu(II)} \approx 2.0$) linked by diamagnetic octacyanidomolybdate(IV) anions, revealing very weak antiferromagnetic coupling at low temperature. Nonetheless, this material is a textbook example of the multi-wavelength light-responsive photomagnet. The photomagnetic effect in $[Cu^{II}(bapa)]_2[Mo^{IV}(CN)_8]\cdot 7H_2O$ can be induced by photoexcitation with monochromatic light (405 and 532 nm), and remarkably, with polychromatic white light (Fig. 9.4). This phenomenon is seen as more than 50% and around 43% increase of $\chi_M T$ values after almost one day of illumination with mono- and polychromatic lights, respectively, and it generated several percent increases of saturation magnetization at 1.8 K for all of the light sources (Fig. 9.5). Additionally, it is worth to underline that $\chi_M T(T)$ curves for photoexcited metastable state show similar shapes with maxima around 10 K and monotonous decay up to relaxation temperature around 250 K, above which the sample returns to its initial paramagnetic state.

Complementary photomagnetic research done at 100 K with 405 nm excitation light was also the first attempt for systematic examination of the cause of temperature at which compound is irradiated on the characteristics of photomagnetic phenomenon in the hybrid inorganic–organic compound. This successful experiment revealed no significant difference in results of studies at 10 and 100 K suggesting that the

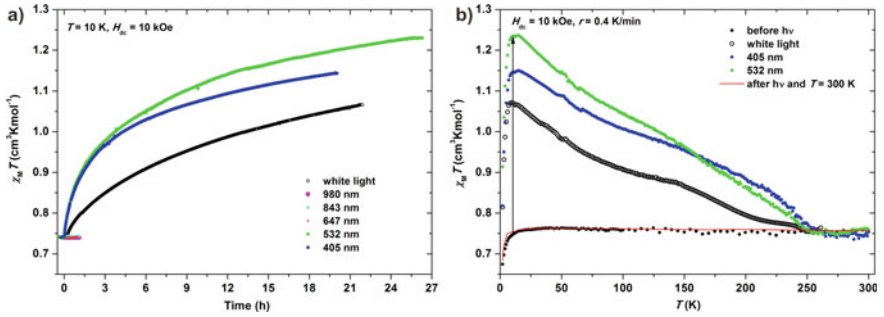

Fig. 9.4 **a** The $\chi_M T$(time) plots of $[Cu^{II}(bapa)]_2[Mo^{IV}(CN)_8]\cdot 7H_2O$ during excitation at 10 K with selected wavelengths and polychromatic white light. **b** The $\chi_M T(T)$ curves before and after excitations with different light sources, and after heating to 300 K. Reproduced from J. Mater. Chem. C **3**, 8712 (2015) with permission from The Royal Society of Chemistry

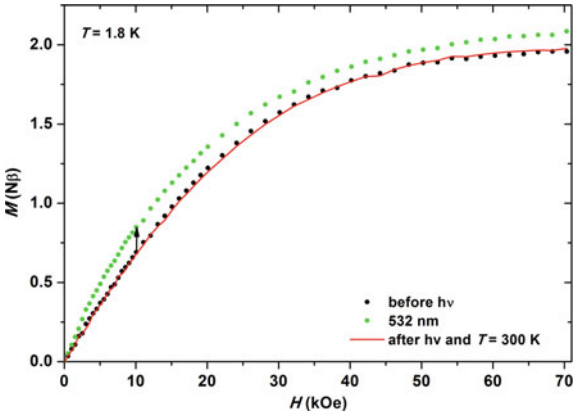

Fig. 9.5 The $M(H)$ plot at 1.8 K for $[Cu^{II}(bapa)]_2[Mo^{IV}(CN)_8]\cdot 7H_2O$ before and after excitation with a 532 nm laser line, and after heating to 300 K. Reproduced from J. Mater. Chem. C **3**, 8712 (2015) with permission from The Royal Society of Chemistry

same magnetic species have been formed and it opens the possibility of commercial use of this material using liquid nitrogen cooling systems (Fig. 9.6). Finally, $[Cu^{II}(bapa)]_2[Mo^{IV}(CN)_8]\cdot 7H_2O$ has been also tested for the photoreversibility effect (Fig. 9.7). In the first stage, a positive photomagnetic effect was induced with the use of green light. After it, using the sequence of light sources (647, 843, and 980 nm) for which no photomagnetic effect was found, the magnetic signal partial reduction was forced. This photoreversible effect has been canceled by repeated illumination with a green light.

The mechanism of photomagnetic and photoreversible processes have been analyzed in the context of two previously mentioned LIESST and MMCT mechanisms. However, the mechanism could not be clearly defined due to insufficient

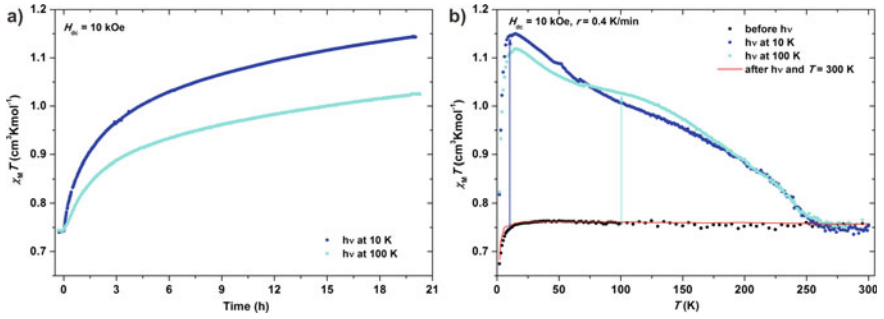

Fig. 9.6 **a** The $\chi_M T$(time) plots of $[Cu^{II}(bapa)]_2[Mo^{IV}(CN)_8]\cdot 7H_2O$ during excitation at 10 and 100 K with 405 nm light. **b** The $\chi_M T(T)$ curves before and after excitations with a 405 nm light done at T = 10 and 100 K, and after heating to 300 K. Reproduced from J. Mater. Chem. C **3**, 8712 (2015) with permission from The Royal Society of Chemistry

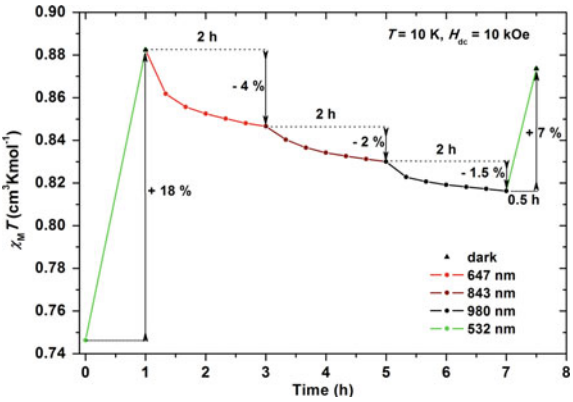

Fig. 9.7 The $\chi_M T$(irradiation time) plots of the photoreversible process at 10 K during subsequent irradiation with 532, 647, 843, and 980 nm laser lines. Reproduced from [46] with permission from The Royal Society of Chemistry

experimental evidence and the high complexity of the system. It was only found out that the mechanism was probably associated mainly with LIESST one with a minor contribution of MMCT process.

Another instance of photomagnetic material reveling photoreversibility-phenomenon is cyanido-bridged layered $[Cu^{II}(cyclam)]_2[Mo^{IV}(CN)_8]\cdot 10H_2O$ coordination polymer, where cyclam = 1,4,8,11-tetraazacyclodecane [34]. The crystal structure consists of neutral square grids with deformed 8-metallic units separated by water molecules stabilized by hydrogen-bond interactions with cyclam ligands and terminal cyanides (Fig. 9.8).

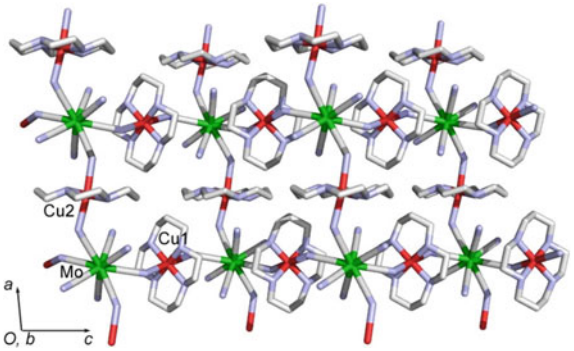

Fig. 9.8 Structure of $[Cu^{II}(cyclam)]_2[Mo^{IV}(CN)_8]\cdot 10H_2O$ single layer with cyanido-bridges. Water molecules are omitted for clarity. Reproduced from Chem. Lett. **38**, 338 (2009) with permission from The Chemical Society of Japan (CSJ)

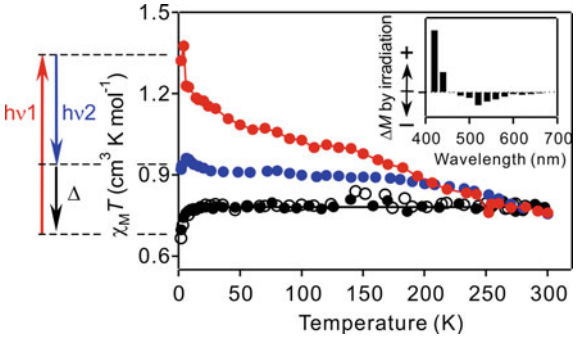

Fig. 9.9 The $\chi_M T(T)$ curves before (white circles), after 410 nm irradiation for 60 min (red circles), after 658 nm irradiation for 300 min (blue circles), and after thermal treatment at 300 K (black circles). Solid black line is to guide the eye. Inset: Wavelength of the laser light *vs.* the change in magnetization. Reproduced from Chem. Lett. **38**, 338 (2009) with permission from The Chemical Society of Japan (CSJ)

This compound before photoirradiation is a paramagnetic system with isolated copper(II) centers ($S_{Cu(II)} = 1/2$, $g_{Cu(II)} \approx 2.0$) showing weak antiferromagnetic interactions below 30 K which is similar to other Cu^{II}-$[Mo^{IV}(CN)_8]^{4-}$ systems. Successive irradiation of the sample with 410 nm blue light at 3 K leads to the monotone increase of magnetization and consecutively to appearance of the broad peak in the $\chi_M T(T)$ curve with maxima around 10 K which continuously decrease up to relaxation temperature above 250 K. Further heating induces complete recovery of sample to their primary paramagnetic state. But even more interestingly, if the sample in its photoinduced metastable state is illuminated with 658 nm red light, the $\chi_M T$ value diminishes partially, however no lower than the level before the photomagnetic experiment (Fig. 9.9). This photoreversible process was also observed in infrared spectroscopy as a modulation structure and intensities of the CN^- stretching frequency bands upon irradiation with different lights and heating up. Photoirradiation of $[Cu^{II}(cyclam)]_2[Mo^{IV}(CN)_8]\cdot 10H_2O$ with 410 nm blue light at 3 K led to a decrease in the intensity of all IR bands in $\nu(C{\equiv}N)$ region, then the application of 658 nm red light increased bands intensities, and finally, the sample reset to its initial state after 3–300–3 K heating and cooling cycle.

Finally, the results of both magnetic and spectroscopic studies were analyzed in the term of light-induced Metal-to-Metal Charge-Transfer (MMCT) mechanism of photomagnetic effect in this compound (Fig. 9.10). The increase of magnetic signal and decrease of the CN^- stretching bands intensities during irradiation with blue light have been interpreted as a consequence of the photoinduced electron transfer from Mo^{IV} to Cu^{II} in the course of the following photoreaction: $[Cu^{II}(cyclam)]_2[Mo^{IV}(CN)_8]\cdot 10H_2O \rightarrow [Cu^{II}(cyclam)]_{2x}[Cu^{I}(cyclam)]_x[Mo^{IV}(CN)_8]_{1-x}[Mo^{V}(CN)_8]_x\cdot 10H_2O$, where $S_{Cu(II)} = S_{Mo(V)} = ½$ and $S_{Cu(I)} = S_{Mo(IV)} = 0$, while revers effects originate in photoinduced back electron transfer by illumination with red light or by thermal treatment.

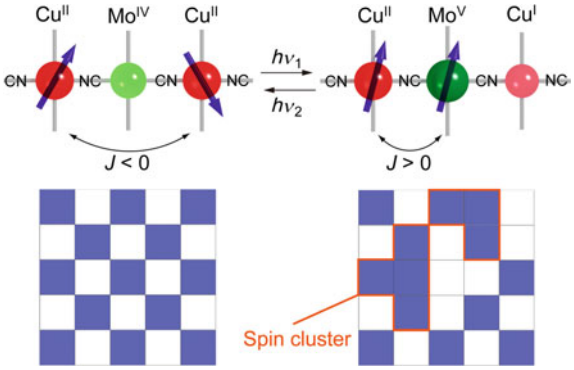

Fig. 9.10 Probable scheme of the photoreversible effect. The diagram shows 2-D Cu-Mo grid layer. Blue and white squares indicate S = 1/2 and S = 0, respectively. Reproduced from Chem. Lett. **38**, 338 (2009) with permission from The Chemical Society of Japan (CSJ)

It is also worth mentioning another experiment for $[Cu^{II}(cyclam)]_2[Mo^{IV}(CN)_8]\cdot 10H_2O$ which has been focused on detection of the 410-nm light photoswitching effect at near-room temperature using infrared spectroscopy [61]. As a result, the change in the intensity of bands in the $\nu(C{\equiv}N)$ region has been observed (Fig. 9.11). A thorough analysis of the data has shown that the photogenerated metastable phase thermally relaxed to the initial state with a half-life time of 27, 69, and 170 s at 293, 283, and 273 K in series which is shorter than a single magnetic measurement period. Near-room temperature photoswitching

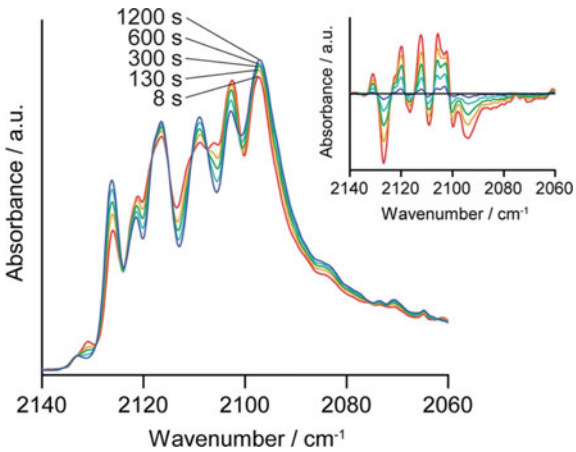

Fig. 9.11 Time dependence of the IR spectra of $[Cu^{II}(cyclam)]_2[Mo^{IV}(CN)_8]\cdot 10H_2O$ at 273 K after excitation. Inset: differential IR spectra before and after light irradiation. Reproduced with permission from AIP Advances 3, 042,133 (2013). Copyright 2013 American Chemical Society

is an essential matter in the field of optical functional materials. This model assembly is useful for the demonstration of high-temperature photoswitching material.

So far presented works showed photoswitching between initial paramagnetic state and metastable photoexcited paramagnetic state. At this point, it is necessary to distinguish another three-dimensional cyanido-bridged coordination polymer $Cu^{II}_2[Mo^{IV}(CN)_8]\cdot 8H_2O$ demonstrating a unique photomagnetic effect [47]. The crystal structure of this material consists of Mo-crosslinked square grids with distorted 4-metallic units and channels field with crystallization and coordination water molecules.

In their ground state $Cu^{II}_2[Mo^{IV}(CN)_8]\cdot 8H_2O$ is paramagnet with weak antiferromagnetic interactions at low-temperature region showing the metal-to-metal charge-transfer band between Mo^{IV}-CN-Cu^{II} and Mo^{V}-CN-Cu^{I} around 480 nm in UV-vis spectrum. Irradiation of the sample with 473 nm blue light at 3 K for 165 min caused the growth of magnetization and the manifestation of a spontaneous magnetization with a Curie temperature (T_C) of 25 K (Fig. 9.12) and magnetic hysteresis with the coercive field of 34 Oe which disappear completely after thermal treatment above 250 K and cooling to 3 K. Moreover, further photomagnetic studies for $Cu^{II}_2[Mo^{IV}(CN)_8]\cdot 8H_2O$ exhibit that the phenomenon can be induced by using laser light below 520 nm (Fig. 9.13), conversely, the light with lower energy is responsible for photoreversible effect. It is worth emphasizing that successive application of 658, 785, and 840 nm lights for photoreversibility studies resulted in complete recovery of initial paramagnetic state without heating above relaxation temperature (Fig. 9.12). These essential observations have also been confirmed in spectroscopic measurements. Infrared spectroscopy for $Cu^{II}_2[Mo^{IV}(CN)_8]\cdot 8H_2O$ revealed that the band at 2170 cm^{-1}, corresponding to Mo^{IV}-CN-Cu^{II}, diminish upon excitation with 473 nm and entirely restore after heating above 250 K. In case of UV-vis absorption

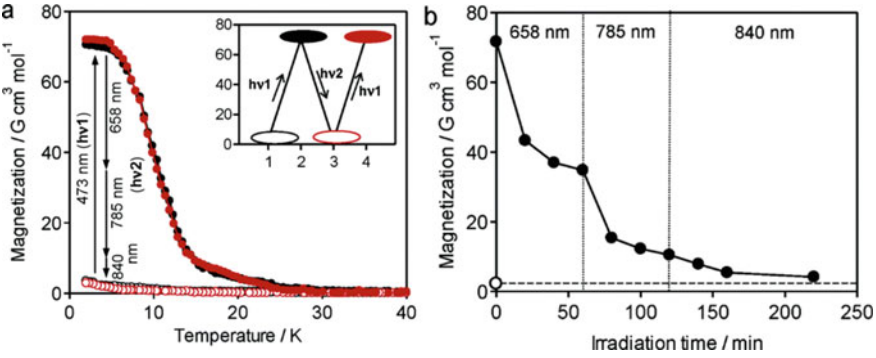

Fig. 9.12 **a** The $M(T)$ plots before (black open circle), after irradiation with 473 nm light (black closed circle), after subsequent irradiation with 658, 785 and 840 nm lights (red open circle) and the second irradiation with 473 nm light (red closed circle). **b** The M(irradiation time) plots of the photoreversible process at 3 K during subsequent irradiation with 473, 658, 785 and 840 nm laser lines. Reprinted with permission from J. Am. Chem. Soc. **128**, 270 (2006). Copyright 2006 American Chemical Society

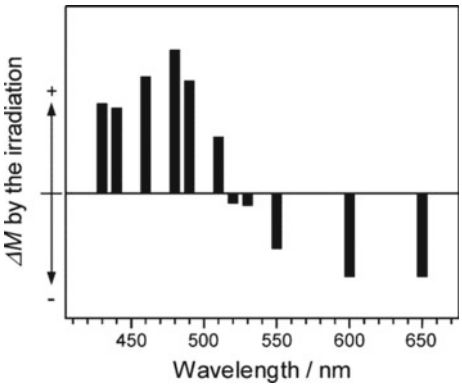

Fig. 9.13 Wavelength of the laser light *vs.* the change in magnetization. Reprinted with permission from J. Am. Chem. Soc. **128**, 270 (2006). Copyright 2006 American Chemical Society

spectroscopy, the response towards 473 nm laser light is also noted. Before irradiation, the spectrum of the compound comprises of the metal-to-ligand charge-transfer bands of $[M(CN)_8]^{4-}$ (250 nm), the ligand field bands of octacyanidometallate (370 and 400 nm), the metal-to-metal charge-transfer band (483 nm) and the ligand field bands of Cu(II) (637, 719 and 855 nm). The irradiation caused the reduction of band intensities and a new broad band to appear in the 600–900 nm region, the opposite characteristics are observed after irradiation with 658, 785 and 840 nm lights sequence or warming above 250 K. This indicates that the new band around 710 nm is the reverse metal-to-metal charge-transfer band from Mo^{V}-CN-Cu^{I} and Mo^{IV}-CN-Cu^{II} species.

All of the evidence indicates that the observed photomagnetic effect is a result of blue light-induced MMCT between ground paramagnetic state $\{Cu^{II}Mo^{IV}Cu^{II}\}_n$ and metastable state $\{Cu^{II}Mo^{V}Cu^{I}\}_n$, showing long-range magnetic ordering due to the photoinduced formation of the extended network of ferromagnetically coupled Mo^{V}-CN-Cu^{II} linkages (Fig. 9.14). This effect can be reversed by heating above the temperature at which the metastable state spontaneously relaxes or by utilizing light corresponding to the photogenerated reverse-MMCT band.

9.3.1 Influence of Photoexcitation Temperature

As already indicated, the parameters of photomagnetic effects can be amplified or weakened at the synthesis stage and by the precise selection of the excitation light wavelengths. Moreover, preliminary investigations for $[Cu^{II}(bapa)]_2[Mo^{IV}(CN)_8]\cdot 7H_2O$ set a new direction for research, which is to broaden knowledge about the influence of temperature at which sample is photoexcited [46]. This work showed that there is no significant difference in the results of photomagnetic studies after excitation at 10 and 100 K (Fig. 9.6).

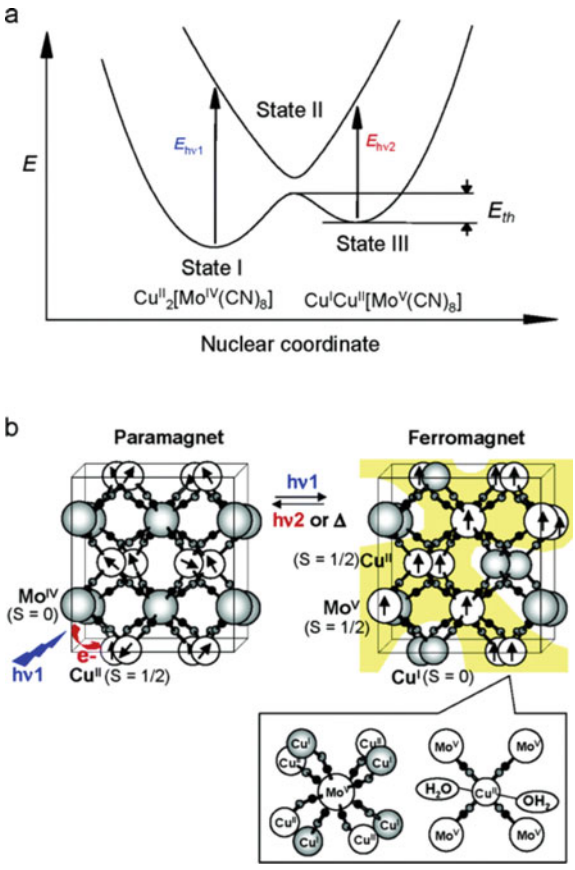

Fig. 9.14 **a** Possible energy diagrams of a class II mixed-valence compound. **b** Probable scheme of the photoreversible effect. The yellow areas show a possible route for the ferromagnetic spin alignment. Reprinted with permission from J. Am. Chem. Soc. **128**, 270 (2006). Copyright 2006 American Chemical Society

Advanced research in this topic has been conducted for a model trinuclear V-shape molecule $[Cu^{II}(enpnen)]_2[Mo^{IV}(CN)_8]\cdot 6.75H_2O$, enpnen = *N,N'*-bis(2-aminoethyl)-1,3-propanediamine (Fig. 9.15) [44]. This system has shown that photomagnetic effect in Cu^{II}-$[Mo^{IV}(CN)_8]^{4-}$ compounds should be analyzed as a combination of both competing MMCT and LIESST effects (Fig. 9.16). Furthermore, this research also unveiled that the ratio between them is correlated with the temperature at which photoexcitation is conducted (Fig. 9.17). At low temperatures, the major part of the magnetic signal is associated to MMCT mechanism with a minor few percent contribution of LIESST. The increase of the temperature leads to diminish and to complete disappearance of MMCT contribution at 100 and 150 K, respectively, without significant change of the fraction of LIESST component. Excitation at 200 K generates only a small contribution of LIESST part.

Detailed analysis of extensive magnetic data for $[Cu^{II}(enpnen)]_2[Mo^{IV}(CN)_8]\cdot 6.75H_2O$ using three models: model "0" for the initial unperturbed ground state $\{Cu^{II}$ (S = ½)-N≡C-$Mo^{IV}{}_{LS}$ (S = 0)-[N≡C-Cu^{II} (S = ½)]$_n$}, model "1" for the MMCT metastable excited state $\{Cu^{I}$ (S =

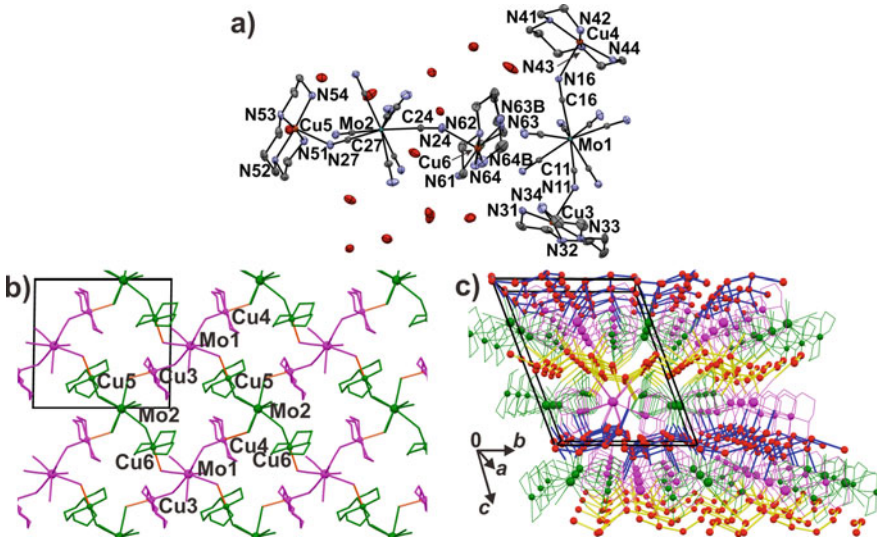

Fig. 9.15 **a** Structural unit of $[Cu^{II}(enpnen)]_2[Mo^{IV}(CN)_8]\cdot 6.75H_2O$. **b** Supramolecular interactions within layers. **c** Crystal packing. Adapted with permission from Inorg. Chem. **57**, 8137 (2018). Copyright 2018 American Chemical Society

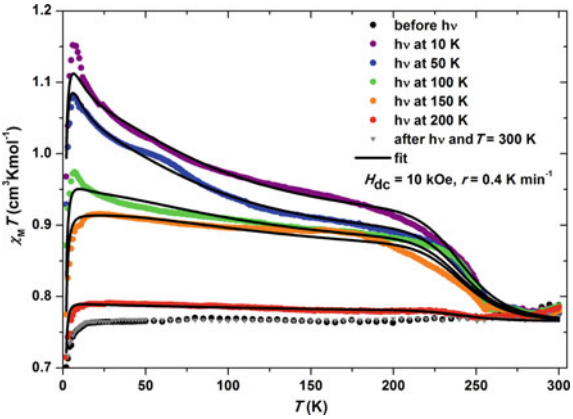

Fig. 9.16 The $\chi_M T(T)$ plots for $[Cu(enpnen)]_2[Mo(CN)_8]\cdot 6.75H_2O$ before and after excitation with 405 nm laser line performed at diverse temperatures, and after heating to 300 K. Solid lines are fits of a model representing the three assumed possible states after irradiation. Adapted with permission from Inorg. Chem. 57, 8137 (2018). Copyright 2018 American Chemical Society

0)-N≡C-Mo^V (S = ½)-[N≡C-Cu^{II} (S = ½)]$_n$}, and model "2" for the LIESST metastable excited state {Cu^{II} (S = ½)-N≡C-$Mo^{IV}{}_{HS}$ (S = 1)-[N≡C-Cu^{II} (S = ½)]$_n$} has been performed (Fig. 9.17). Models "1" and "2" were described by following Hamiltonians: $\hat{H}_1 = -J_1\hat{S}_{Mo}\cdot\hat{S}_{Cu} + g\mu_B\left(\hat{S}_{Cu}+\hat{S}_{Mo}\right)\cdot\vec{H}$ and

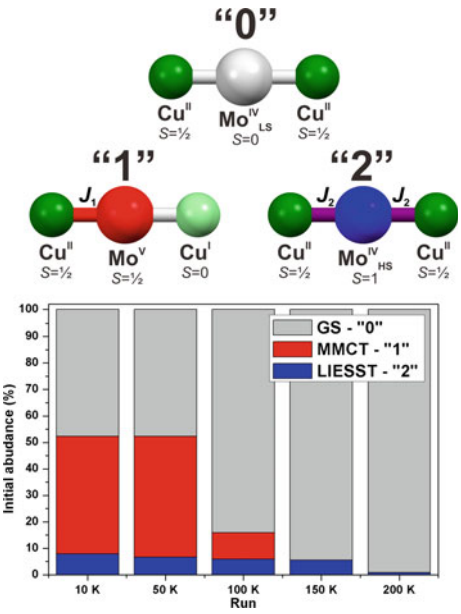

Fig. 9.17 Schematic of the ground state—model "0", the MMCT excited state—model "1" and the LIESST state—model "2", and fractions of the model "0" (GS), model "1" (MMCT) and model "2" (LIESST) states for the irradiation of $[Cu^{II}(enpnen)]_2[Mo^{IV}(CN)_8]\cdot 6.75H_2O$ at different temperatures. Adapted with permission from Inorg. Chem. **57**, 8137 (2018). Copyright 2018 American Chemical Society

$\hat{H}_2 = -J_2\hat{S}_{Mo}\cdot\left(\hat{S}_{Cu1}+\hat{S}_{Cu2}\right)+g\mu_B\left(\hat{S}_{Cu1}+\hat{S}_{Cu2}+\hat{S}_{Mo}\right)\cdot\vec{H}$, respectively, where ${J_1}^{\mathrm{MMCT}}$ and ${J_2}^{\mathrm{LIESST}}$ denote superexchange coupling constants between the Mo^V ($S = ½$) and residual Cu^{II} ($S = ½$) centers, and the ${Mo^{IV}}_{HS}$ ($S = 1$) and Cu^{II} ($S = ½$) centers, respectively, and a single average Landé factor g. As a result of fits, $\chi_M T(T)$ and $M(H)$ curves after excitations at different temperature have been reproduced with the general good compatibility between the observed and calculated values, and ${J_1}^{\mathrm{MMCT}}$ and ${J_2}^{\mathrm{LIESST}}$ values of 11 cm^{-1} and 109 cm^{-1}, respectively, and $g = 2.13(2)$ were determined. Furthermore, these fits revealed that the lifetime of photoinduced MMCT metastable state at low temperature and the relaxation energy barrier ($\Delta_1 \approx 100$ K) are sufficient to treat it as a stable state for long period, however, at higher temperatures (around 100 K) it spontaneously returns to the ground state within the experiment time span. The identical relaxation effect but at the higher temperature (around 200 K) is remarked for LIESST metastable state due to higher energy barrier ($\Delta_2 \approx 4400$ K) and larger value of the high-temperature limit of the lifetime. The estimated threshold temperature of the decay of the metastable state process is 243(7) K which is in agreement with the experimentally evaluated relaxation temperature of 255 K. Finally, these calculations also provided reliable information about the fractions of each model achieved in each experimental conditions. Concluding, this work broaden knowledge about the potential mechanism of photomagnetic effect in Cu^{II}-$[Mo^{IV}(CN)_8]^{4-}$ systems and it stressed the impact of experimental conditions (temperature) on the result of photomagnetic studies which was barely investigated.

This chapter gathers the most vivid examples of experimental factors impacting on photomagnetic effect in Cu^{II}-$[M^{IV}(CN)_8]^{4-}$ complexes. Here, we show that the exchange of octacyanidomolybdate with octacyanidotungstate can modify the intensity of photomagnetic signals and relaxation temperatures. Furthermore, the influence of irradiation wavelength and photoexcitation temperature has been also studied, resulting in the observation that different photomagnetic responses and phenomena mechanisms can be controlled at the level of experiment design. These findings will allow researchers to consider novel factors allowing for more sophisticated control of photomagnetic characteristics.

References

1. L. Ouahab (ed.), *Multifunctional Molecular Materials* (Pan Stanford, Singapore, 2013).
2. S.M. Mukhopadhyay (ed.), *Nanoscale Multifunctional Materials: Science and Applications* (Wiley, New Jersey, 2012)
3. B. Nowicka, T. Korzeniak, O. Stefańczyk, D. Pinkowicz, S. Chorąży, R. Podgajny, B. Sieklucka, Coord. Chem. Rev. **256**, 1946 (2012)
4. S. Ohkoshi, in *Progress in Photon Science: Basics and Applications (Springer Series in Chemical Physics Book 115)*. ed. by K. Yamanouchi (Springer International Publishing AG, Cham, 2017), p. 263
5. K. Nakabayshi, S. Ohkoshi, S. Chorazy, in *Progress in Photon Science: Recent Advances (Springer Series in Chemical Physics Book 119)*. ed. by K. Yamanouchi, S. Tunik, V. Makarov (Springer International Publishing AG, Cham, 2019), p. 453
6. M. Reczyński, K. Nakabayashi, S. Ohkoshi, Tuning the Optical Properties of Magnetic Materials. Eur. J. Inorg. Chem. (2020). https://doi.org/10.1002/ejic.202000428
7. H. Tokoro, S. Ohkoshi, Dalton Trans. **40**, 6825 (2011)
8. C. Train, M. Gruselle, M. Verdaguer, Chem. Soc. Rev. **40**, 3297 (2011)
9. S. Chorazy, R. Podgajny, W. Nitek, T. Fic, E. Görlich, M. Rams, B. Sieklucka, Chem. Commun. **49**, 6731 (2013)
10. K. Inoue, K. Kikuchi, M. Ohba, H. Okawa, Angew. Chem. Int. Ed. **42**, 4810 (2003)
11. C. Train, R. Gheorghe, V. Krstic, L.-M. Chamoreau, N.S. Ovanesyan, G.L.J.A. Rikken, M. Gruselle, M. Verdaguer, Nat. Mater. **7**, 729 (2008)
12. T. Nuida, T. Matsuda, H. Tokoro, S. Sakurai, K. Hashimoto, S. Ohkoshi, J. Am. Chem. Soc. **127**, 11604 (2005)
13. D. Pinkowicz, R. Podgajny, W. Nitek, M. Rams, A.M. Majcher, T. Nuida, S. Ohkoshi, B. Sieklucka, Chem. Mater. **23**, 21 (2011)
14. Y. Tsunobuchi, W. Kosaka, T. Nuida, S. Ohkoshi, CrystEngComm **11**, 2051 (2009)
15. M. Komine, K. Imoto, Y. Miyamoto, K. Nakabayashi, S. Ohkoshi, Eur. J. Inorg. Chem. **1367** (2018).
16. C. Train, T. Nuida, R. Gheorghe, M. Gruselle, S. Ohkoshi, J. Am. Chem. Soc. **131**, 16838 (2009)
17. J. Wang, J. Zakrzewski, M. Heczko, M. Zychowicz, K. Nakagawa, K. Nakabayashi, B. Sieklucka, S. Chorazy, S. Ohkoshi, J. Am. Chem. Soc. **142**, 3970 (2020)
18. Y. Xin, J. Wang, M. Zychowicz, J. Zakrzewski, K. Nakabayashi, B. Sieklucka, S. Chorazy, S. Ohkoshi, J. Am. Chem. Soc. **141**, 18211 (2019)
19. S. Chorazy, J.J. Zakrzewski, M. Reczynski, K. Nakabayashi, S. Ohkoshi, B. Sieklucka J. Mater. Chem. C **7**, 4164 (2019)
20. E. Chelebaeva, J. Larionova, Y. Guari, R.A.S. Ferreira, L.D. Carlos, F.A. Almeida Paz, A. Trifonov, C. Guerin, Inorg. Chem. **48**, 5983 (2009)

21. E. Pardo, C. Train, H. Liu, L.M. Chamoreau, B. Dhkil, K. Boubekeur, F. Lloret, K. Nakatani, H. Tokoro, S. Ohkoshi, M. Verdaguer, Angew. Chem. Int. Ed. **51**, 8356 (2012)
22. S. Ohkoshi, H. Tokoro, T. Matsuda, H. Takahashi, H. Irie, K. Hashimoto, Angew. Chem. Int. Ed. **46**, 3238 (2007)
23. S. Ohkoshi, K. Nakagawa, K. Tomono, K. Imoto Y. Tsunobuchi, H. Tokoro, J. Am. Chem. Soc. **132**, 6620 (2010)
24. S. Ohkoshi, A. Namai, H. Tokoro, Coord. Chem. Rev. **380**, 572 (2019)
25. O. Stefanczyk, S. Ohkoshi, Chem. Eur. J. **25**, 15963 (2019)
26. K.K. Orisaku, O. Stefanczyk, S. Ohishi, N. Ozaki, Y. Miyamoto, K. Imoto, S. Ohkoshi, Chem. Eur. J. **25**, 11066 (2019)
27. M. Reczynski, B. Nowicka, C. Nather, M. Koziel, K. Nakabayashi, S. Ohkoshi, B. Sieklucka, Inorg. Chem. **57**, 13415 (2018)
28. M. Reczyński, S. Chorazy, B. Nowicka, B. Sieklucka, S. Ohkoshi, Inorg. Chem. **56**, 179 (2017)
29. S. Ohkoshi, K. Arai, Y. Sato, K. Hashimoto, Nat. Mater. **3**, 857 (2004)
30. B. Sieklucka, D. Pinkowicz (eds.), *Molecular Magnetic Materials: Concepts and Applications* (Wiley-VCH, Wienheim, 2017)
31. M.A. Halcrow, *Spin-Crossover Materials: Properties and Applications* (Wiley, Chichester, 2013).
32. P. Gütlich, Y. Garcia, T. Woike, Coord. Chem. Rev. **219–221**, 839 (2001)
33. S. Ohkoshi, K. Imoto, Y. Tsunobuchi, S. Takano, H. Tokoro, Nat. Chem. **3**, 564 (2011)
34. H. Tokoro, K. Nakagawa, K. Nakabayashi, T. Kashiwagi, K. Hashimoto, S. Ohkoshi, Chem. Lett. **38**, 338 (2009)
35. S. Ohkoshi, Y. Hamada, T. Matsuda, Y. Tsunobuchi, H. Tokoro. Chem. Mater. **20**, 3048 (2008)
36. S. Ohkoshi, S. Ikeda, T. Hozumi, T. Kashiwagi, K. Hashimoto, J. Am. Chem. Soc. **128**, 5320 (2006)
37. C. Mathonière, H.-J. Lin, D. Siretanu, R. Clérac, J.M. Smith J. Am. Chem. Soc. **135**, 19083 (2013)
38. C. Mathoniere, Eur. J. Inorg. Chem. **248** (2018)
39. E.S. Koumousi, I.-R. Jeon, Q. Gao, P. Dechambenoit, D.N. Woodruff, P. Merzeau, L. Buisson, X. Jia, D. Li, F. Volatron, C. Mathonière, R. Clérac, J. Am. Chem. Soc. **136**, 15461 (2014)
40. O.N. Risset, P.A. Quintero, T.V. Brinzari, M.J. Andrus, M.W. Lufaso, M.W. Meisel, D.R. Talham, J. Am. Chem. Soc. **136**, 15660 (2014)
41. S. Ohkoshi, H. Tokoro, Accounts Chem. Res. **45**, 1749 (2012)
42. S. Ohkoshi, S. Takano, K. Imoto, M. Yoshikiyo, A. Namai, H. Tokoro, Nat. Photonics **8**, 65 (2014)
43. S. Ohkoshi, K. Nakagawa, K. Imoto, H. Tokoro, Y. Shibata, K. Okamoto, Y. Miyamoto, M. Komine, M. Yoshikiyo, A. Namai. Nat. Chem. **12**, 338 (2020)
44. O. Stefańczyk, R. Pełka, A.M. Majcher, C. Mathonière, B. Sieklucka, Inorg. Chem. **57**, 8137 (2018)
45. Y. Umeta, S. Chorazy, K. Nakabayashi, S. Ohkoshi, Eur. J. Inorg. Chem. **1980** (2016)
46. O. Stefańczyk, A.M. Majcher, M. Rams, W. Nitek, C. Mathonière, B. Sieklucka, J. Mater. Chem. C **3**, 8712 (2015)
47. S. Ohkoshi, H. Tokoro, T. Hozumi, Y. Zhang, K. Hashimoto, C. Mathonière, I. Bord, G. Rombaut, M. Verelst, C. Cartier dit Moulin, F. Villain, J. Am. Chem. Soc. **128**, 270 (2006)
48. T. Hozumi, K. Hashimoto, S. Ohkoshi, J. Am. Chem. Soc. **127**, 3864 (2005)
49. X.-D. Ma, T. Yokoyama, T. Hozumi, K. Hashimoto, S. Ohkoshi, Phys. Rev. B **72**, 094107(6) (2005)
50. J.-M. Herrera, V. Marvaud, M. Verdaguer, J. Marrot, M. Kalisz, C. Mathonière, Angew. Chem. Int. Ed. **43**, 5468 (2004)
51. G. Rombaut, M. Verelst, S. Golhen, L. Ouahab, C. Mathonière, O. Kahn, Inorg. Chem. **40**, 1151 (2001)
52. S. Ohkoshi, N. Machida, Y. Abe, Z.J. Zhong, K. Hashimoto, Chem. Lett. **4**, 312 (2001)
53. X. Qi, S. Pillet, C. de Graaf, M. Magott, E.-E. Bendeif, P. Guionneau, M. Rouzières, V. Marvaud, O. Stefańczyk, D. Pinkowicz, C. Mathonière, Angew. Chem. Int. Ed. **59**, 3117 (2020)

54. M. Magott, M. Reczyński, B. Gaweł, B. Sieklucka, D. Pinkowicz, J. Am. Chem. Soc. **140**, 15876 (2018)
55. M. Magott, O. Stefanczyk, B. Sieklucka, D. Pinkowicz, Angew. Chem. Int. Ed. **43**, 13283 (2017)
56. N. Bridonneau, J. Long, J.-L. Cantin, J. von Bardeleben, S. Pillet, E.-E. Bendeif, D. Aravena, E. Ruiz, V. Marvaud, Chem. Commun. **51**, 8229 (2015)
57. S. Brossard, F. Volatron, L. Lisnard, M.-A. Arrio, L. Catala, C. Mathonière, T. Mallah, C. Cartier dit Moulin, A. Rogalev, F. Wilhelm, A. Smekhova, P. Sainctavit, J. Am. Chem. Soc. **134**, 222 (2012)
58. M.-A. Arrio, J. Long, C. Cartier dit Moulin, A. Bachschmidt, V. Marvaud, A. Rogalev, C. Mathonière, F. Wilhelm, P. Sainctavit, J. Phys. Chem. C **114**, 593 (2010)
59. O. Stefańczyk, M. Rams, A.M. Majcher, C. Mathonière, B. Sieklucka, Inorg. Chem. **53**, 3874 (2014)
60. O. Stefanczyk, S. Ohkoshi, Inorg. Chem. **59**, 4292 (2020)
61. Y. Umeta, H. Tokoro, N. Ozaki, S. Ohkoshi. AIP Adv. **3**, 042133 (2013)

Chapter 10
Element-Specific Spin States in Heusler-Alloy Compounds Probed by X-Ray Magnetic Spectroscopy

Jun Okabayashi, Kazuya Z. Suzuki, and Shigemi Mizukami

Abstract Recent progress of x-ray magnetic circular dichroism (XMCD) studies for Heusler alloy compounds which are expected as high spin-polarized materials is summarized. For some Heusler alloys forming X_2YZ compositions, where X and Y are transition-metal (TM) elements and Z is non-TM element, the element-specific magnetic properties by XMCD are investigated to understand the electronic structures. At first, a principle of XMCD spectroscopy is introduced. Second, the research interests in Heusler alloys are explained. Then, the results of XMCD for equatorial $XX'YZ$ composited Heusler-type spin-gapless semiconductor CoMnFeSi and CoFeCrAl are discussed considering the atomic ordering. Further, the case both X and Y are Mn and Z is Ga, Mn_3Ga, is also discussed with the interfacial thermal diffusion probed by XMCD.

10.1 Introduction

Since the discovery of magneto-optical techniques using synchrotron radiation, the electronic and magnetic states in solids are widely investigated for functional magnetic materials. Several techniques have been developed for spectroscopy, diffraction, scattering, and microscopy including space and time resolutions. Among them, the most distinctive features for magnetic investigations using synchrotron radiation are the element-specific studies for magnetic materials, which unveil the intrinsic electronic and magnetic properties in the materials. The magneto-optical Kerr effect (MOKE) is well known referred to as 'Faraday effect' which originates

J. Okabayashi (✉)
Research Center for Spectrochemistry, The University of Tokyo, Tokyo, Japan
e-mail: jun@chem.s.utokyo.ac.jp

K. Z. Suzuki · S. Mizukami
WPI-Advanced Institute for Materials Research, Tohoku University, Sendai, Japan

Center for Spintronics Research Network (CSRN), Tohoku University and Center for Science and Innovation in Spintronics (CSIS), Tohoku University, Sendai, Japan

K. Yamanouchi et al. (eds.), *Progress in Photon Science*, Springer Series in Chemical Physics 125, https://doi.org/10.1007/978-3-030-77646-6_10

from the difference in absorption coefficients between right- and left-circularly polarized lights, leading to magnetic circular dichroism (MCD) [1]. For the incident beam, the ultra-violet region has been utilized with optical polarizer. Since the initial and final states are not decomposed in the visible regions, magnetic excitations from localized core levels can be a direct probe detecting the occupied and unoccupied states in electronic and magnetic states. By using synchrotron radiation beams, in particular, circularly polarized beams in the soft- and hard-x-ray regions, magneto-optical techniques with MCD using circularly polarized x-rays have been extensively developed, referred as x-ray MCD (XMCD) techniques [2]. Therefore, the difference in x-ray absorption spectroscopy (XAS) between different polarized beams is defined as XMCD.

In the x-ray absorption measurements, there are several detection types as transmission, electron yield, and fluorescent yield mode. During the absorption processes, transmission geometry is the most straightforward method for detecting the absorption signals. However, since most of interesting materials are bulk or thin films on the substrate or interfacial hetero-structures, transmission mode cannot be applicable without fabricating some devices. Collecting total electrons emitted from the samples through the excitation by incident beams yields to the absorption processes, which is most utilized for XMCD as a conventional technique. However, the electron yield mode also has a disadvantage as a surface sensitive measurement beneath 5 nm from the surfaces. Electron yield γ is expressed as (10.1) by using absorption coefficient μ [m^{-1}] and depth L;

$$\gamma \propto 1 - e^{-\mu L} \approx \mu L \quad (1/\mu \gg L). \tag{10.1}$$

Because of the mean free path $1/\mu$ of incident x-rays of approximately 100 nm, the probing depth is estimated as $L \lesssim 5$ nm. In this condition, the electron yield is approximately proportional to absorption coefficient. On the other hand, the fluorescence mode is also applicable for XAS. Conventional fluorescent detector of silicon drift detector is available recently. Although it has a great advantage as bulk-sensitive, the self-absorption processes also occur, which cannot be distinguished from intrinsic signals and is necessary to correct the intensities.

After Schütz et al. experimentally observed the XMCD of the Fe K-edge in 1987 [3], Chen et al. succeeded in the measurements of XMCD of Ni L edges in soft X-rays [4]. Selection rules for optical absorption permit a transition in case of the difference of angular quantum numbers l as $\Delta l = \pm 1$, which corresponds to an excitation from p to d states in transition-metal (TM) compounds. For 3d TMs, the L-edge absorption energies are located at the soft-X-ray regions. Magneto-optical sum rules, proposed by Carra and Thole in 1992, enabled quantitative estimations of spin and orbital magnetic moments [5, 6] and widely utilized for the analysis of XMCD. In 1995, Chen et al. proposed conventional methods for the estimations of spin and orbital magnetic moments from sum rules using Fe and Co films in transmission set up [7]. XMCD and its spectral analysis using sum rules became one of the standard techniques to deduce element-specific magnetic properties. During the recent decade, XMCD techniques have been continuously extended and combined

with other techniques, which led to the development of XMCD microscopy [8] and time-resolved measurements [9] and external-field induced XMCD [10].

[Magneto-optical sum rules]

As XMCD analysis methods, magneto-optical sum rules for spin and orbital magnetic moments were established. Here, the principles of XMCD and their sum rules are discussed.

First, the dipole transition by circular polarized beams is considered. For the beams propagating along *z*-direction, circular polarized electric fields are defined as $E = E_x(100) \pm iE_y(010)$ for right and left hand side, respectively. Then, dipole moments are written as $er \cdot E = \mathrm{e}(\mathrm{x}E_x \pm iyE_y)$. *Second*, in hydrogen atom model as a most simple case, the wave functions are represented using quantum number sets (n, l, m) as $\Psi_{nlm} = (\frac{1}{\sqrt{2}})R_{nl}(r)Y_{lm}(\theta)e^{im\phi}$ by using polar coordinates [11]. In the case of dipole transition from ground states sets to other sets, the finite transition matrix elements are limited only in following four cases [12, 13];

$$(x+iy)^{n',l+1,m+1}_{n,l,m} = \sqrt{\frac{(l+m+2)(l+m+1)}{(2l+3)(2l+1)}}R^{n',l+1}_{n,l} \tag{10.2}$$

$$(x-iy)^{n',l+1,m-1}_{n,l,m} = -\sqrt{\frac{(l-m+2)(l-m+1)}{(2l+3)(2l+1)}}R^{n',l+1}_{n,l} \tag{10.3}$$

$$(x+iy)^{n',l-1,m+1}_{n,l,m} = -\sqrt{\frac{(l-m)(l-m-1)}{(2l+1)(2l-1)}}R^{n',l-1}_{n,l} \tag{10.4}$$

$$(x-iy)^{n',l-1,m-1}_{n,l,m} = \sqrt{\frac{(l+m)(l+m-1)}{(2l+1)(2l-1)}}R^{n',l-1}_{n,l}. \tag{10.5}$$

Here, the radial function is defined as

$$R^{n',l'}_{n,l} = \int R_{n'l'}(r)R_{nl}(r)r^3\mathrm{d}r.$$

Since the XMCD signals are produced as the difference between circular polarized transitions, the values of $D = (2)^2 - (3)^2$ and $(4)^2 - (5)^2$, corresponding to circular dichroism, are necessary for XMCD intensities because the square of transition matrix elements is proportional to transition probability. The former case increases l and when m is a positive value, the XMCD signal appear as positive intensity. On the other hand, the latter case, the transition with decreasing l occurs and the relation between m and XMCD signal is opposite. By using the total angular momentum representation j, the former and latter cases are written as $j = l \pm s$. Here, since the m is not controlled in the spin exchange splitting even in the ferromagnetic materials, the m is modified through the spin–orbit coupling which is the origin for arising the finite XMCD signals.

For 3*d* TM compounds, the transitions from spin–orbit split $2p_{3/2}$ and $2p_{1/2}$ to 3*d* states are considered. In these cases, the values of *D* are calculated using above relations for both edges, respectively,

$$D = \pm\frac{2m}{2l+1}\left(R_{n,l}^{n',l+1}\right)^2. \tag{10.6}$$

In this notation, the dipole transition depends on *m*.

Third, the 2*p*-3*d* transition through the non-polarized beam is considered. In this case, *m* should not be included in the transitions by non-polarized beam. The dipole transition matrix elements by non-polarized excitation becomes a finite value only in following conditions,

$$z_{n,l,m}^{n',l+1,m} = \sqrt{\frac{(l+1)^2 - m^2}{(2l+3)(2l+1)}}\,R_{n,l}^{n',l+1} \tag{10.7}$$

$$z_{n,l,m}^{n',l-1,m} = \sqrt{\frac{l^2 - m^2}{(2l+3)(2l+1)}}\,R_{n,l}^{n',l-1}. \tag{10.8}$$

In the case of 2*p*3*d* transition with increasing *l*, the transition probability can be described as an absorption intensity $I = \frac{((2)^2+(3)^2)}{2} + (7)^2$;

$$I = \frac{l+1}{2l+1}\left(R_{n,l}^{n',l-1}\right)^2 n_{\mathrm{h}},$$

Here, n_{h} is the hole number in 3*d* states. Using (10.6),

$$\frac{D}{I} = \frac{2m(l+1)}{n_{\mathrm{h}}}.$$

Since the average value of *m* is defined as an orbital angular momentum $\langle L_z\rangle$, the following notation is deduced,

$$\langle L_z\rangle = \frac{n_{\mathrm{h}} D}{2I(l+1)}.$$

Finally, in general case of dipole transition, the sum rule for orbital angular momentum is represented as follows,

$$\frac{\int(\mu_+ - \mu_-)\mathrm{d}\omega}{\int(\mu_+ + \mu_- + \mu_0)\mathrm{d}\omega} = \frac{l'\left(l'+1\right) - l(l+1) + 2}{2l'(l'+1)}\left(\frac{\langle L_z\rangle}{n_{\mathrm{h}}}\right). \tag{10.9}$$

Here, l' is initial occupied core level, l is unoccupied final states. Left-side term corresponds to D/I. In the special case of $l' = l + 1$, conventional orbital sum rule is deduced.

Next, the spin sum rule is discussed. The values of $D_{j\pm}$ are defined as spin–orbit split states. Due to the existence of magnetic dipole term $\langle T_z \rangle$, the spin sum rule becomes a complicated formulation not only for spin angular momentum $\langle S \rangle$ but also including $\langle T_z \rangle$. A general formula is established as follows,

$$\frac{D_{j+} - \left\{\frac{l+1}{l}\right\} D_{j-}}{2l} = \frac{l'\left(l'+1\right) - l(l+1) - 2}{3l}\left(\frac{S_z}{n_\mathrm{h}}\right) + \frac{l'\left(l'+1\right)\left\{l'\left(l'+1\right) + 2l(l+1) + 4\right\} - 3(l-1)^2(l+2)^2}{6l'l(l'+1)}\left(\frac{T_z}{n_\mathrm{h}}\right). \quad (10.10)$$

Here, $D_{j\pm}$ represent the excitation of spin–orbit coupled core levels. In the case of $2p3d$ transition, the notation is simply written as

$$\frac{D_{3/2} - 2D_{1/2}}{2} = \frac{2}{3n_\mathrm{h}}(\langle S \rangle + 7\langle T_z \rangle). \quad (10.11)$$

The $\langle T_z \rangle$ term appears corresponding to the low symmetry circumstance around TM ions. Usually, this term might be ignored but it appears at the interface and strained cases. In the cases of cubic-symmetry Heusler alloy compounds, this term might be negligible for the estimation of spin magnetic moments.

By summarizing the TM L-edge absorptions by circular polarized beams, transition probabilities are schematically shown in Fig. 10.1. Depending on circular polarization q $= \pm 1$, XMCD intensities arise at L_3 and L_2 edges.

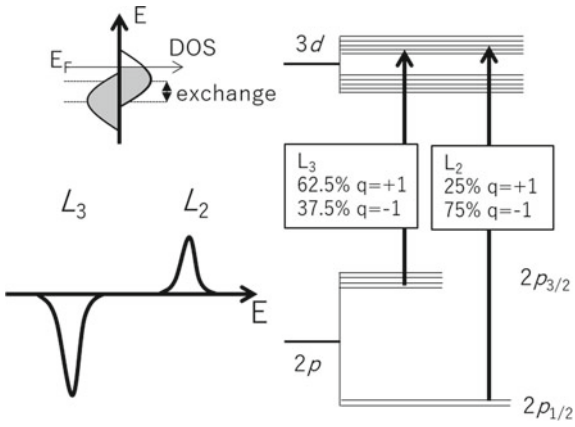

Fig. 10.1 Schematic illustration of XMCD. The spin-up and -down band structures are drawn with exchange splitting. Transition-metal L-edge excitation by different circular polarization q $= \pm 1$ from $2p$ to $3d$ states. Corresponding XMCD line shape is also displayed in L-edge [13].

10.2 Heusler Alloy Compounds

In the research fields of spintronics which are utilized in applications such as magneto-resistive random access memory (MRAM), an efficient spin current transfer without energy loss is an urgent issue in the material designs. For this motivation, there are many researches focusing on the material development of high spin polarization. As one of the final goals, 100% fully spin-polarized case is necessary. In the electronic band structure, while only up spin states contribute to the conduction electron, the other has an energy gap, which is defined as a "half metal" material. Therefore, it is required possessing the properties of half-metallicity, room temperature ferromagnetism, and good lattice matching to form abrupt interfaces with major substrates and insulating energy barrier materials, which is applicable for MRAM technologies.

Considering these demands, Heusler alloys and their related family materials are categorized in the best materials. Heusler alloys are ternary alloys originally discovered by Heusler [14]. He demonstrated the ferromagnetic property including nonmagnetic atoms in Cu_2MnSn. The original composition is defined as X_2YZ, where X and Y are transition-metal elements, and Z consists of a semiconductor or nonmagnetic atom. The unit cell of the ideal crystalline structure ($L2_1$ phase) consists of four face-centered cubic sublattices (space-group Fm-$3m$, No. 225). Stacked structures of $L2_1$ phase consist of X layer and by YZ layer in face-centered cubic structures as shown in Fig. 10.2. When the Y and Z atoms exchange their sites (Y–Z disorder) and eventually occupy their sites at random, the alloy transforms into the $B2$ phase. By increasing the disorder, the magnetic properties depart further from the half-metallicity. In order to achieve giant magnetoresistance (GMR) of higher than 100% and tunnel magnetoresistance (TMR) ratio of higher than 1000% at room temperature (RT), a great deal of effort has accordingly been devoted using a Heusler alloy [15–20].

As a typical Co-based Heusler alloy using Si as a nonmagnetic semiconductor element, Co_2MnSi and partially substituted $Co_2(Fe,Mn)Si$ are thoroughly investigated. Half metallicity of these materials are studied by the point contact Andreev

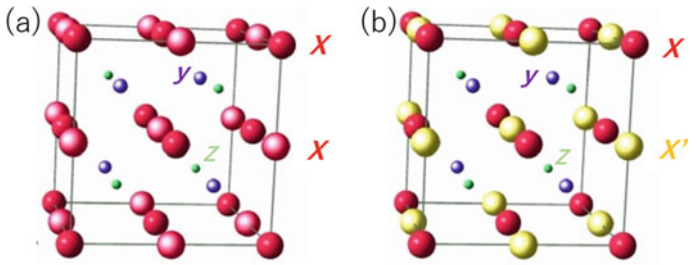

Fig. 10.2 Crystalline structures of **a** $L2_1$-type Heusler alloy X_2YZ and **b** $XX'YZ$ equatorial ordered alloy (Y-structure)

refection technique, analysis of TMR ratio using Julliere's model and guaranteed from the first-principles calculations [21, 22]. A critical subject to overcome is the large temperature dependence of spin polarization. In the case of $Co_2MnSi/MgO/Co_2MnSi$ magnetic tunnel junction, TMR is 2010% at 4.2 K, but it decreases to only 335% at 290 K [23]. It is believed as not only the interfacial atomic diffusion with MgO the insulator but also the interfacial spin fluctuation [24, 25]. Therefore, element-specific investigations near the interface regions using XMCD are strongly desired.

In order to understand the band structure of Heusler alloys, the spin-dependent densities of states (DOS) are investigated by the first-principles calculations, which is strongly related to the discussion deduced from XMCD and photoemission spectroscopy. There are many reports discussing the DOS of Co-based Heusler alloys and exhibiting half metallicity. The electronic structures of Heusler alloy are understood based on the molecular orbital picture. The hybridization between Y and Z sites split the boding and anti-bonding states. Further, hybridized states are recoupled with X layer. After filling of electron numbers, the Fermi level (E_F) is determined and mainly X sites are located in the E_F with half metal states qualitatively. This scenario is described in Fig. 10.3. In particular, the recent report of the band structure calculation by Nawa and Miura suggests the importance of intra-Coulomb interaction in Heusler alloy Co_2MnSi, especially in Mn site [26]. They drew the band diagram based on the molecular-orbital picture considering ternary elements which is developed by I. Galanakis [27]. The E_F is located in the Co 3*d* states and Coulomb interaction in the Mn site shift the level to maintain the half metallicity. Further, total valence electron number Z in X_2YZ obeys a Slater-Pauling curve with the relation of magnetization

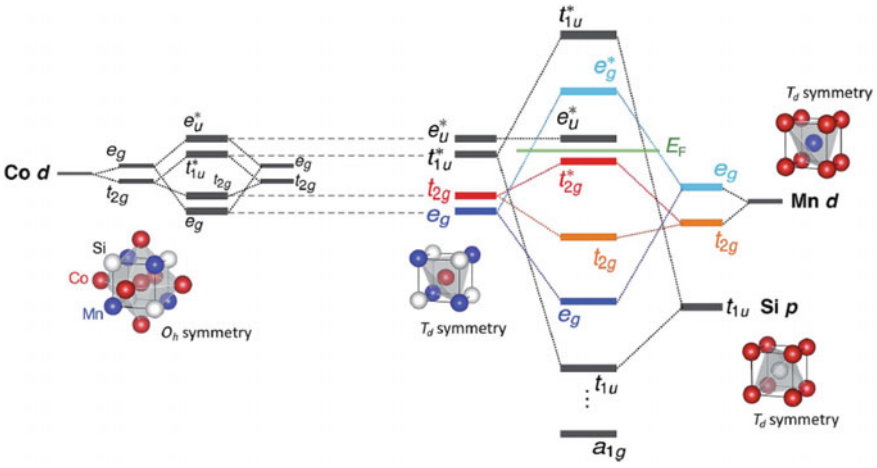

Fig. 10.3 Schematic diagram of Co_2MnSi based on molecular orbital picture. Left side is Co 3*d* states hybridized within the layer in O_h symmetry. Right side is the hybridization between Mn 3*d* and Si 3*p* valence states in T_d symmetry within the layer. Total electronic structure is also shown with the Fermi level [26]

M; $M = Z - 24$, which is established as a guideline designing the Heusler alloy compounds [27].

[Related Heusler alloy compounds]

Other Heusler alloy family is also introduced. Half-Heusler alloy compounds are defined as XYZ, where one of the X site forms a vacancy site. NiMnSb alloy was discovered in 1983 [28]. In the full-Heusler type compositions, the substitution of Y site is also effective to enhance the TMR ratio through the tuning of the DOS at E_F. Other candidate is the quaternary alloys; $XX'YZ$ with different X and X' elements (space-group F-43m, No. 216) because of tailoring of the DOS in the vicinity of E_F. The crystal structure is defined as a LiMgPdSn prototype or Y structure. It can be conceived by the combination of two ternary Heusler alloys, such as X_2YZ and X'_2YZ. In some cases, the specific band structure is modulated as spin-gapless semiconductor (SGS), where both majority and minority bands have an energy gap at E_F. The DOS of SGS is originally derived from strict condition from that of Heusler alloys. Due to their unique band structures, SGSs have been predicted to possess interesting properties, such as (i) spin-polarized current resulting from the electrons as well as holes; (ii) high spin polarization; and (iii) tunable spin polarization by voltage varying the Fermi level.

One of the advantages of SGS corresponds to the development of ferromagnetic semiconductor research field. Most famous material (Ga,Mn)As, in which Mn ions are doped into GaAs, exhibits ferromagnetism. Required items are RT ferromagnetic ordering, compatible with semiconductor technology, and carrier controlling by external fields. There were extensive efforts for clarifying the band structures of ferromagnetic semiconductors. As shown in Fig. 10.4, the hybridized states between Mn 3d and As 4p orbitals with opposite sign of exchange coupling between them correspond to the E_F which is revealed by angle-resolved photoemission spectroscopy [29, 30]. On the other hand, the SGSs are the *ultimate cases* overcoming the issues

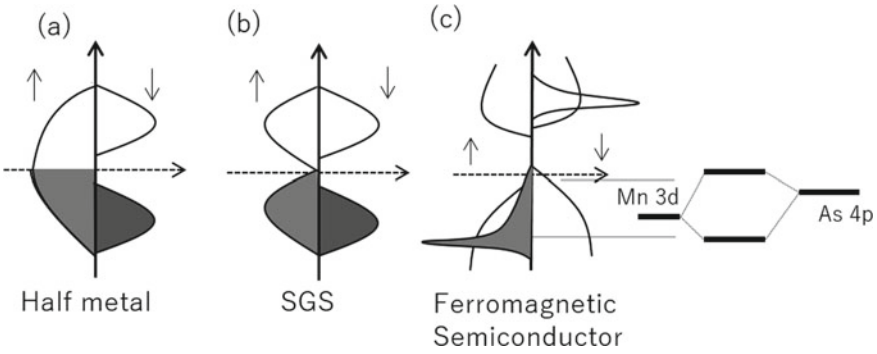

Fig. 10.4 Schematic illustrations of spin-dependent density of states of **a** half-metal, **b** spin gapless semiconductor, and **c** TM-doped ferromagnetic semiconductor (Ga,Mn)As. Schematic molecular orbital hybridization between TM 3d impurity states and host semiconductor 4p states is also illustrated

in doped ferromagnetic semiconductors because the SGSs satisfy the RT ferromagnetism and compatible with semiconductor substrate because they are composed by semiconductor Z element in the composition.

When the X and Y are Mn and Z is Ga cases, Heusler-type compounds are Mn_3Ga [31]. This material and related different composition $Mn_{3-\delta}Ga$ is well known as hard magnets which exhibit large perpendicular magnetic anisotropy (PMA). Highly ordered alloy MnGa consists of alternative Mn layer and Ga layer stacked structure, which is categorized as $L1_0$ type. With increasing Mn concentration, Ga site is substituted by Mn atoms with opposite spin direction as $D0_{22}$ type. This material is discussed in the Sect. 10.3.3 and 10.3.4.

Another aspect in topological phenomena using Heusler alloys is also interested in solid state physics as Weyl semimetals. The characteristic band structure is recognized as an appearance of Weyl points, resulting in anomalous Hall conductivity in Heusler alloy Co_2MnAl [32]. The Hall conductivity is explained as Berry curvature, which might open up new research field using Heusler alloys. Further, large thermoelectric phenomena are also demonstrated through the topological nature in Heusler alloys [33, 34].

[Aim of this study]

We investigate the element-specific magnetic and electronic structures of Heusler alloy compounds using the XMCD of 3*d* TM based Heusler alloy compounds using the *L*-edge photoexcitation from 2*p* to 3*d* states.

10.3 Results and Discussion

The element-specific magnetic and electronic structures in Heusler alloy based materials of SGS candidates are discussed for CoFeMnSi (Sect. 10.3.1), CoFeCrAl (Sect. 10.3.2). Further, in the case of both X and Y are Mn and Z is Ga, Mn_3Ga and related $Mn_{3-\delta}Ga$ are focused on the materials possessing perpendicular magnetic anisotropy (PMA) in Sect. 10.3.3. In Sect. 10.3.4, interfacial chemical reaction between $Mn_{1.5}Ga$ and TMs probed by XMCD is discussed.
[Experimental conditions for XMCD]

All experiments of XAS and XMCD system were performed using soft x-rays in the range of 50–1200 eV constructed at the BL-7A, Photon Factory, High-Energy Accelerator Research Organization (KEK) in Tsukuba, Japan [35]. For XMCD, a $\pm$ 1.2-T electromagnet has been installed at the end station. As the beam comes from the bending magnets, circularly polarized lights for XMCD are obtained using the edges from the beam center, which is adjusted by a mirror in the beam-line. The beam and magnetic-field directions are fixed to be parallel, and the sample surface normal direction is rotated for the angular-dependent XMCD. Total-electron-yield (TEY) modes are utilized for XMCD measurements.

10.3.1 Candidate for Spin-Gapless Semiconductor CoFeMnSi[1]

Dai et al. first predicted that CoFeMnSi (abbreviated as CFMS hereafter) is a half-metallic equiatomic quaternary Heusler alloys (EQHAs) from ab initio calculations and investigated the polycrystalline bulk sample [36]. The proposed Wyckoff coordinate is Co, Fe, Mn, and Si occupying the sites corresponding to *X*, *X'*, *Y*, and *Z*, respectively. Depending on the occupation of various lattice sites, three different types of *Y*-structure are possible for CFMS, i.e., types I–III [36]. The remarkable difference of CFMS is a net magnetic moment of 4 μ_B/f.u. (where f.u. represents formula unit) smaller than those for Co_2MnSi (5 μ_B/f.u.; type-I) and Co_2FeSi (6 μ_B/f.u.; type-II) and a presence of a pseudo energy band gap in the majority spin channel at the Fermi level [36, 37]. Type-III is defined as the Co site is also swapped with Fe–Mn layer. Xue et al. [38] theoretically predicted that CFMS is the spin-gapless semiconductor, although the existence of the majority spin band gap for CFMS is still under discussion from the theoretical points of view [39, 40].

Relatively high spin-polarization *P* of 64% was reported using the point contact Andreev reflection spectroscopy and nonmetallic conduction suggesting a spin-gapless semiconductor in the bulk polycrystalline CFMS samples [37], which is expected to be favorable for device applications, such as magnetic tunnel junctions. Here, the structural and magnetic properties for CFMS films grown on Cr-buffered MgO substrates are focused. This is because the use of a Cr buffer is a standard technique to obtain high-quality films with atomically flat surfaces, even though the transport properties for CFMS itself cannot be measured due to the presence of a low-resistive Cr buffer.

The sample of (001) MgO substrate/Cr(40)/CFMS(30)/Mg(0.4)/MgO(2) was prepared in the thickness of nm scales. The MgO(001) substrate was flushed thermally at 700 °C prior to the deposition process. All of the layers were deposited at RT. The Cr layer was in situ annealed at 700 °C for 1 h before the CFMS deposition in order to obtain an atomically flat Cr surface with (001) orientation. The XMCD measurements were carried out in a grazing incidence setup to the sample surface normal in order to detect the in-plane spin and orbital magnetic moments. All the measurements were performed at RT.

Figures 10.5 shows the XAS and XMCD of Mn, Fe, and Co $L_{2,3}$ edges, respectively. XAS are normalized by the photon fluxes. Clear metallic peaks are observed, which confirms that there is no mixing of oxygen atoms in the thin CFMS layer. Shoulder structures appear in the higher photon energy region of Co L_3 XAS peaks. These structures correspond to the Heusler alloys due to the Co–Co bonding states within the molecular orbital calculations [27]. The spin and orbital magnetic moments are estimated by applying the magneto-optical sum rules, and their values are estimated using the values using the sum rules, we assumed 3*d* hole numbers of 4.3, 3.4, and 2.5 for Mn, Fe, and Co, respectively, as the standard values [7]. For Mn, a

[1] This section is partly reproduced from L. Bainsla, R. Yilgin, J. Okabayashi, A. Ono, K.Z. Suzuki, and S. Mizukami, Physical Review B 96, 094,404 (2017), with the permission of APS Publishing.

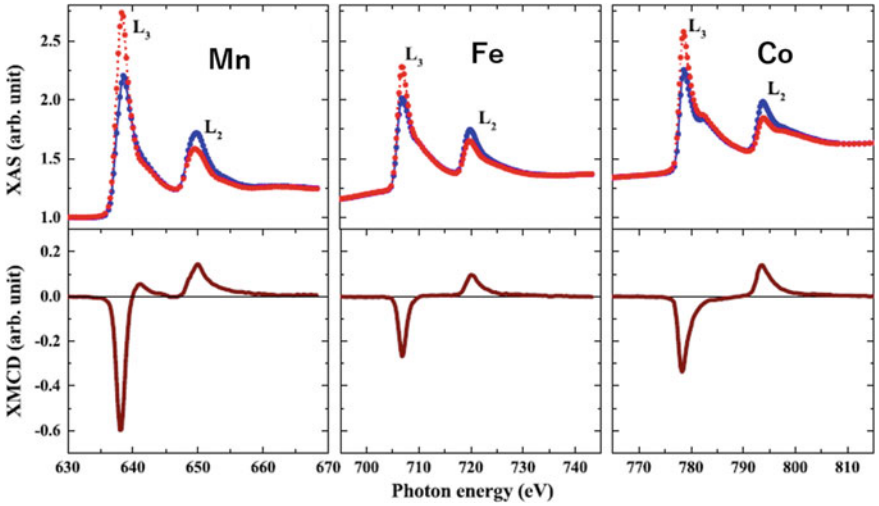

Fig. 10.5 XAS and XMCD spectra of CFMS for Mn, Fe, and Co *L*-edges. Red and blue curves correspond to photon helicities [45]

correction factor of 1.5 is applied as used previously for other Heusler alloys [41] and described in [42, 43]. The magnetic-field dependence at each transition-metal *L*3 edge was also measured, then confirmed that the magnetic fields of ± 1 T are enough to saturate the magnetization. Therefore, the spin and orbital moments are detected essentially for this alloy. The total magnetic moments evaluated by magnetization measurements are comparable with the XMCD values. The spin magnetic moments for Co, Fe, and Mn sites were 0.82, 0.77, and 2.01 μ_B, respectively, which is very close to the values reported for the bulk CFMS [41]. The obtained magnetic moment values for Fe and Co atoms in CFMS are three times smaller than those in reported bulk values. The total magnetization value obtained from XMCD is higher than the macroscopic magnetization value, which may be due to the estimation error in the Mn moment using the correction factor.

Next, we discuss the atomic disorder and its influence on the electronic structures. Dai et al. calculated the element-specific magnetic moments for the *Y* structure for CFMS as type-I ordering and for CMFS as type-II ordering [36]. In their calculations, Co had a similar magnetic moment, whereas Mn (Fe) had large magnetic moments for type-I (II) ordering, and the net values for both types were similar. Klaer et al. explained their magnetic moment value for the bulk sample by considering the Mn-Fe disorder, which was modeled by the weighted average of the magnetic moment values for type-I and type-II orderings [41]. The results obtained in this work can be explained similar to the bulk case, although we could not confirm whether our films form the *Y*-type order or not from XMCD and x-ray diffraction crystalline structure analysis. The moment value for Mn is slightly lower (∼10%), whereas the Fe moment is about 20% higher as compared to the bulk. Thus, a slightly higher Mn-Fe swapping (mixing of type-I and type-II with partially $L2_1$ and fully *B*2 orders) is expected in

the films. Considering the calculations by Klaer et al. [41], the dominant phase is type I (about $80-90\%$) with partial $L2_1$ and full $B2$ orders. According to theoretical calculations by Dai et al. [36] CFMS with type-I ordering has a pseudo gap at the Fermi level in the majority spin band and a large energy gap in the minority spin band, whereas this is not the case for type-II ordering. CFMS with type-II ordering may be the half-metallic with a smaller energy band gap in the minority spin band. This implies that the half-metallicity still remains in the presence of Mn-Fe swapping in CFMS even though Mn-Fe swapping increases the density of state at the Fermi level for the majority spin band. Feng et al. also studied the effect of various types of disorders on the electronic and magnetic properties of CFMS using the first-principles calculations, and they concluded that the half-metallicity of CFMS was broken by the appearance of Co antisites [44] and changed to type-III. In our films, the Co antisite may be negligible since the Co magnetic moment is similar to the Y structure. Therefore, the half-metallicity is expected in our films [45].

10.3.2 Candidate for Spin-Gapless Semiconductor CoFeCrAl[2]

Equiatomic quaternary Heusler alloy (EQHA) CoFeCrAl is discussed, which is a typical candidate for SGSs with a chemical formula of *XX'YZ*, where *X*, *X'*, and *Y* denote transition metal elements and *Z* represents a main group element. The crystal structure of EQHAs is a cubic LiMgPdSn or *Y*-type structure. Here, *X* is Co cite, *X'* and *Y* are positioned by Fe or Cr, and *Z* is Al cite. Basically, the Y-structure means the swap of the sites of Co and Fe within the layer and the swap between Cr and Al within the other layer. Other cases are swapping between Fe and Cr through the interlayers. Further randomness is full swapping cases. To realize SGSs, it is of vital importance to characterize the chemical orderings of EQHAs and understand their effect on both the gapless state and half-metallic gap. Xu et al. were the first to theoretically suggest that several EQHAs, including CoFeCrAl [38]. Subsequently, Ozdogan et al. theoretically studied the electronic structure of 60 EQHAs and confirmed that CoFeCrAl becomes an SGS [39]. Many experimental and theoretical studies on CoFeCrAl have since been reported [46–50]. CoFeCrAl epitaxial thin films grown on MgO substrates using a sputtering deposition technique were prepared [47, 48], which exhibit the $L2_1$ chemical order, and measured matgnetic moment of $2.0\,\mu_B$/f.u., $T\mathrm{c} = 390$ K, a semimetal-like carrier number density of 1.2×10^{18} cm^{-3}, and $P = 68\%$ [47]. Considering previous studies, the element-specific characteristics for CFCA is strongly demanded.

All samples were deposited on MgO(100) single-crystal substrates using a magnetron sputtering technique. The MTJ staking structure was

[2] This section is partly reproduced from T. Tsuchiya, T. Roy, K. Elphick, J. Okabayashi, L. Bainsla, T. Ichinose, K.Z. Suzuki, M. Tsujikawa, M. Shirai, A. Hirohata, and S. Mizukami, Physical Review Materials 3, 084,403 (2019), with the permission of APS Publishing.

substrate/Cr(40)/CoFeCrAl(30)/Mg(0.4)/MgO(2)/CoFe(5)/IrMn(10)/Ta(3)/Ru(5) (thickness is in nanometers). Before the deposition the surfaces of the substrates were cleaned by flushing at 700 °C in the chamber. All layers were deposited at RT. The Cr buffer layer was annealed in situ at 700 °C for 1 h to obtain a flat surface with (001) orientation. The CoFeCrAl layer was deposited on the substrate using an alloy target, with the film composition of $Co_{25.5}Fe_{23.1}Cr_{28.1}Al_{23.3}$ (at.%) determined using an inductively coupled plasma mass spectrometer. The samples of substrate/Cr(40)/CoFeCrAl(30)/Mg(0.4)/MgO(2) were prepared. An insight into the electronic state near the interface of MgO and CoFeCrAl via the XMCD results with the aid of ab initio calculations that take account of possible chemical disorders is obtained.

Figures 10.6 shows the XAS and XMCD spectra, respectively, of Cr, Fe, and Co $L_{2,3}$-edges with different photon helicity for the sample annealed at 700 °C. Clear metallic peaks can be observed, confirming that there is no mixing of oxygen atoms. Shoulder structures appear in the higher-photon-energy region of the Co $L_{2,3}$-edge XAS peaks. These originate from the Co–Co bonding states in Heusler alloy structures with high degree of chemical order. No finite XMCD signals can be observed at the Cr L-edges. The spin and orbital magnetic moments were estimated by applying the magneto-optical sum rules. The magnetic moments given by summing both spin and orbital components of each element are estimated to be 1.14 and 0.52 μ_B/atom for Fe and Co, respectively. The total magnetic moment m is 1.66 μ_B/atom, which

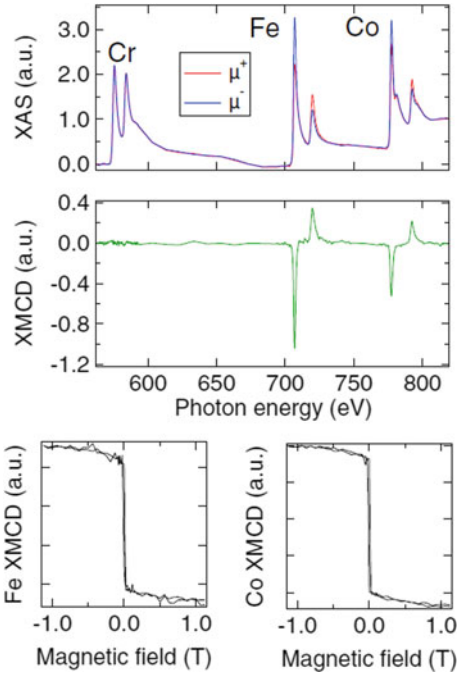

Fig. 10.6 XAS and XMCD spectra of CFCA for Cr, Fe, and Co L-edges. Red and blue curves correspond to photon helicities. Magnetic field dependence at Fe and Co L_3-edges is also shown [52]

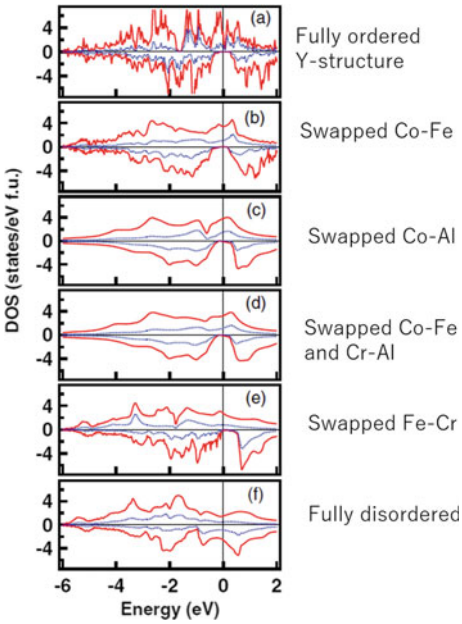

Fig. 10.7 DOS of CFCA calculated from first-principles calculation. **a** Full ordered Y structure, **b** swapped case between Co and Fe within the layer, **c** swapped case between Cr and Al within the layer, **d** swapped case Co and Fe as well as Cr and Al, **e** swapped case between Fe and Cr through interlayer, and **f** fully disordered case of Co and Cr [52]

is similar to the magnetization value of ∼1.9 μ_B/atom and the theoretical value of 2.0 μ_B/atom for *Y*-ordered CoFeCrAl. Interestingly, the XMCD results confirmed that the net magnetic moment of Co seems to be ferromagnetically coupled to that of Fe for the samples in this study. This is dissimilar to the antiferromagnetic arrangement between them that has previously been predicted for the *Y*-ordered case [49]. This finding is confirmed by the element-specific magnetic hysteresis for Fe and Co *L*-edges.

The theoretical data for the spin-resolved DOS profiles for CoFeCrAl with various chemical orderings are shown in Fig. 10.7. The lattice parameter of CoFeCrAl was fixed to 0.575 nm in these calculations. The six cases of the chemical ordering and/or disordering considered here are as follows: (i) the full ordering [*Y*-structure], (ii) the full random swapping of Co and Fe [$L2_1$ structure], (iii) the full random swapping of Cr and Al [$L2_1$], (iv) the full random swapping of Co and Fe as well as that of Cr and Al [*B*2], (v) the full random swapping of Fe and Cr [*XA*] and (vi) the full random swapping of Co and Cr [*XA*]. In cases (i)–(v), the total magnetic moment *m* is very close to 2.00 μ_B/f.u, which is consistent with the predictions given by the Slater-Pauling-like rule observed in Heusler alloys with half metallic gaps. The half-metallic gap structures in the minority spin states survive in cases (i)–(v), as seen in Fig. 10.7. However, in some cases, finite DOS appear at around the Fermi level in the gap by the disorders, meaning that the material is no longer a half-metal in a strict sense. In the case of (vi), the total magnetic moment is 3.062 μ_B/f.u., which is not consistent with the predictions given by the Slater-Pauling-like rule observed in Heusler alloys because the finite DOS appear at around the Fermi level in the gap. In

case (i) (the ordered *Y* structure), the magnetic moment associated with the Fe atom, − 0.703 μ_B/atom, is antiparallel to that of the Co and Cr atoms (1.066 μ_B/atom and 1.71 μ_B/atom, respectively). Hence, there is an overall ferrimagnetic ground state, which is in good agreement with the literature [49]. In case (ii) (Cr-Al disorder), the Fe atom, − 0.227 μ_B/atom, is antiferromagnetically coupled to both the Co and Cr atoms (0.889 μ_B/atom and 1.393 μ_B/atom, respectively). Additionally, we observe a similar kind of magnetic configuration in case (iii) (Co-Fe disorder), i.e., the Fe atom has a magnetic moment alignment opposite to that of the Cr and Co atoms, and in case (iv), both of the above disorders (Co-Fe and Cr-Al) are simultaneously present in the system. Thus, none of these cases reproduced the parallel arrangement of the magnetic moment of Fe and Co observed in XMCD. In contrast, case (v) (disorder between Fe–Cr) qualitatively reproduced the abovementioned XMCD results. The respective net moments of Fe and Co are 1.488 and 0.814 μ_B/atom, respectively, and have a parallel configuration, whereas Cr exhibits negligible net moment. The magnetic moments of Fe and Cr atoms at sites *X* (*Y*) and *Y* (*X*) are 0.268 (2.708) μ_B/atom and 1.318 (−1.682) μ_B/atom, respectively. That is, Cr has two opposite magnetic moments at different sites that tend to cancel each other out. Here, the separation between the Cr at site *X* and the Cr at site *Y* is around 0.249 nm, which is very much comparable to the separation of 0.248 nm in its bulk configuration. This may be why the antiferromagnetic coupling between two nonequivalent Cr atoms as that of its bulk configuration. In case (vi) (disorder between Co-Cr), the calculated magnetic moments also qualitatively reproduced the abovementioned XMCD results, which means Co and Fe have a parallel configuration and Cr exhibits negligible net moment. However, the magnetic moments are much larger than that for the other cases, which are quantitatively inconsistent with the magnetization measurements and XMCD results.

From the viewpoint of the formation energy, the *Y*-order state is the most stable and the Fe–Cr disorder state is unstable. Note that all these calculations result in a ground state for the bulk, whereas the experiments were conducted on films at RT. Thus, the origin of the formation of the energetically unfavorable Fe–Cr disorder can be explained as follows. Our CoFeCrAl films were deposited on the Cr buffer at RT and the in-situ annealing was done to promote the chemical ordering. This fabrication technique is one of the conventional ways to obtain the ordered alloy films with the atomically flat surface [50]. Note that this process is rather different from that in case of the well-ordered CoFeCrAl films, which was obtained at the high deposition temperature [47]. Generally, sputter deposited films at RT tend to have the disordered structure which is far from the thermal equilibrium state, similar to a rapid-cooling state. Thus, various disordered states, which are energetically higher than *Y* state, can be easily obtained. The in situ post annealing promotes the chemical ordering, so that the films have the Fe–Cr disordered state rather than Co-Cr disordered states. While, the temperature may not be enough to obtain $L2_1$ or *Y* state. Therefore, the higher temperature annealing may be one of the effective ways to obtain the ordered phase, which also requires thermally stable buffer layers to avoid significant atomic mixing. Another strategy to prevent the disorder is to partially substitute Al cation

sites by Ga. According to the bulk experiments of similar system Co_2(Cr-Fe)(Ga-Al) [51], Co_2CrFeGa system prevented to form the disorders.

10.3.3 Perpendicular Magnetic Anisotropy in $Mn_{3-\delta}Ga$[3]

Perpendicular magnetic anisotropy (PMA) is desired for the development of high-density magnetic storage technologies. Thermal stability of ultrahigh density magnetic devices is required to overcome the superparamagnetic limit [53]. Recently, research interests using PMA films have focused on not only magnetic tunnel junctions toward the realization of spin-transfer switching magneto-resistive random-access memories but also antiferromagnetic or ferrimagnetic devices [54, 55]. To design PMA materials, heavy-metal elements that possess large spin–orbit coupling are often utilized through the interplay between the spins in 3*d* transition-metals (TMs) and 4*d* or 5*d* TMs [56]. The design of PMA materials without using the heavy-metal elements is an important subject in future spintronics researches. Recent progress has focused on the interfacial PMA in Fe/MgO [57–59]. However, a high PMA of over the order of MJ/m^3 with a large coercive field is needed to maintain the magnetic directions during device operation. Therefore, the materials using high PMA constants and without using heavy-metal atoms are strongly desired.

Mn-Ga binary alloys are a candidate that could overcome these issues. $Mn_{3-\delta}Ga$ alloys satisfy the conditions of high spin polarization, low saturation magnetization, and low magnetic damping constants [60–62]. Tetragonal $Mn_{3-\delta}Ga$ alloys are widely recognized as hard magnets, basically form the Heusler alloy composition where both *X* and *Y* are Mn atoms and *Z* is Ga in X_2YZ. They exhibit high PMA, ferromagnetic, or ferrimagnetic properties depending on the Mn composition [61]. Two kinds of Mn sites, which couple antiferromagnetically, consist of $Mn_{3-\delta}Ga$ with the $D0_{22}$-type ordering. Meanwhile, the $L1_0$-type Mn_1Ga ordered alloy possesses a single Mn site. These specific crystalline structures provide the elongated *c*-axis direction, which induces the anisotropic chemical bonding, resulting in the anisotropy of electron occupancies in TM 3*d* states and charge distribution. There are many reports investigating the electronic and magnetic structures of $Mn_{3-\delta}Ga$ alloys to clarify the origin of large PMA and coercive field [63–65]. To investigate the mechanism of PMA and large coercive fields in $Mn_{3-\delta}Ga$, site-specific magnetic properties must be investigated explicitly.

The deconvolution of each Mn site using the systematic XMCD measurements for different Mn contents in $Mn_{3-\delta}Ga$ is performed. The site-specific spin (m_s) and orbital magnetic moments (m_{orb}) with magnetic dipole term (m_T) are discussed, which corresponds to electric quadrupoles to understand the PMA microscopically.

[3] This section is partly reproduced from J. Okabayashi, Y. Miura, Y. Kota, K. Z. Suzuki, A. Sakuma, and S. Mizukami, Scientific Reports 10, 9744 (2020)., in accordance with the Creative Commons Attribution (CC BY) license.

In the case of $Mn_{3-\delta}Ga$, the difficulty in the deconvolution of two kinds of Mn sites prevents site-selected detailed investigations. Within the magneto-optical spin sum rule, the m_{orb} are expressed as proportional to q/r, where q and r represent the integral of the XAS and XMCD spectra, respectively, for both L_2 and L_3 edges [7, 66]. In the cases of two existing components, the orbital moments are not obtained from the whole integrals of spectra; by using each component r_1, r_2, q_1, and q_2, the value of $(r_1/q_1) + (r_2/q_2)$ should be the average value. The value of $(r_1 + r_2)/(q_1 + q_2)$ does not make sense as an average in the case of core-level atomic excitation, leading to the wrong value in the XMCD analysis. As a typical example, for the mixed valence compound $CoFe_2O_4$, the Fe^{3+} and Fe^{2+} sites can be deconvoluted by the ligand-field theory approximation [67]. However, the deconvolution of featureless line shapes in a metallic $Mn_{3-\delta}Ga$ case is difficult by comparison with the theoretical calculations. To detect the site-specific anti-parallel-coupled two Mn sites, systematic investigations using $Mn_{3-\delta}Ga$ of $\delta = 0$, 1, and 2 provide the information of site-specific detections.

The Mn L-edge XAS and XMCD for $L1_0$-type Mn_1Ga with a single Mn site (MnI), and $D0_{22}$-type Mn_2Ga and Mn_3Ga with two kinds of Mn sites (MnI and MnII) are shown in Fig. 10.8. The XAS were normalized to be one at the post-edges. With increasing Mn concentrations (decreasing δ), the intensities of XAS increased and the difference between μ^+ and μ^- became small, resulting in the suppression of XMCD intensities because of the increase of antiparallel components. In the case of Mn_2Ga and Mn_3Ga, the XMCD line shapes in the L_3 and L_2 edges, of slightly split and

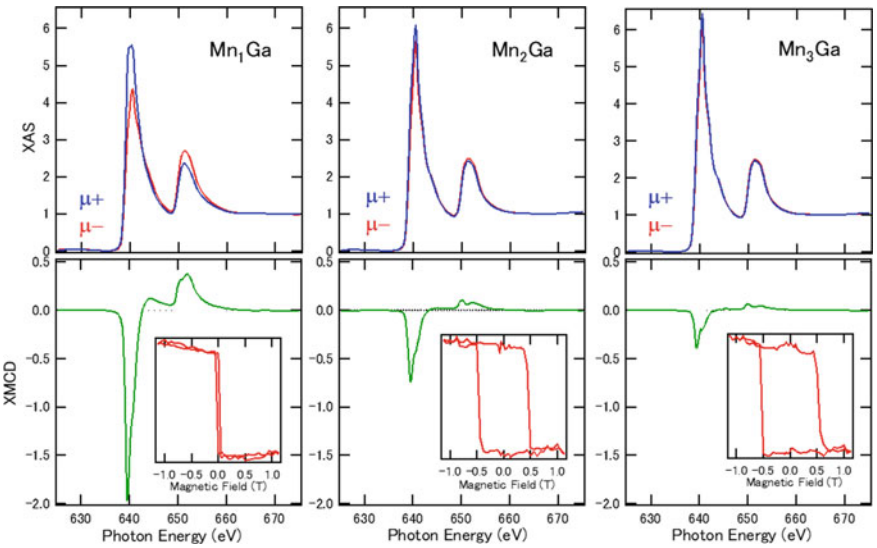

Fig. 10.8 XAS and XMCD of $Mn_{3-\delta}Ga$ for $d = 0$, 1, and 2. Spectra were measured at the normal incident setup where the incident beam and magnetic field were parallel to the sample surface normal. μ^+ and μ^- denote the absorption in different magnetic field direction. The insets show the magnetic field dependence of the hysteresis curves taken by fixed L_3-edge photon energy. All measurements were performed at RT [74].

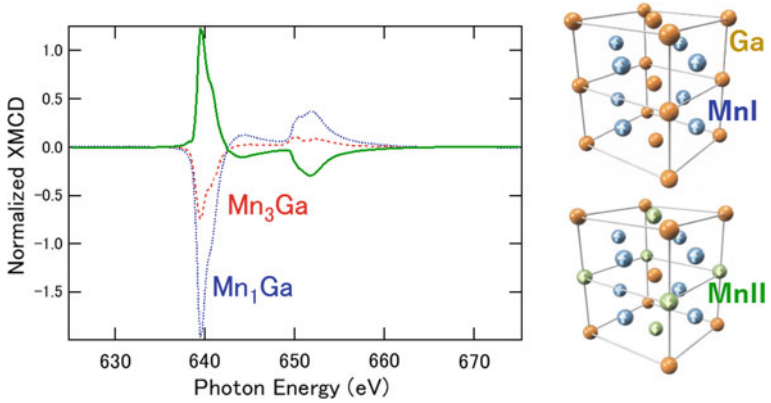

Fig. 10.9 Deconvoluted XMCD spectra of $Mn_{3-\delta}Ga$ by subtraction from Mn_1Ga. The MnI and MnII components were separated in this procedure. Illustrations of the unit-cell structures of Mn_1Ga and Mn_3Ga are also displayed [74]

doublet structures, became clear because of the increase of another MnII component with opposite sign. Furthermore, the element-specific hysteresis curves in XMCD at a fixed photon energy of Mn L_3-edge exhibit similar features with the results of the magneto-optical Kerr effects. Coercive fields (H_c) of 0.5 T were obtained for the Mn_2Ga and Mn_3Ga cases because the two kinds of Mn sites enhance the antiparallel coupling. The 3-nm-thick $Mn_{3-\delta}Ga$ samples used in the XMCD measurements were prepared by magnetron sputtering technique on MgO (001) substrates with the CoGa buffer layers. The detailed sample growth conditions are reported in [68].

To deconvolute the MnI and MnII sites in the XMCD spectra, we performed the subtraction of XMCD between Mn_1Ga and Mn_3Ga. Figure 10.9 displays the XMCD of Mn_1Ga and Mn_3Ga, and their differences after the normalization considering the Mn compositions. The XMCD signal with opposite sign was clearly detected for MnI and MnII components. As the lattice volume of $Mn_{3-\delta}Ga$ on the CoGa buffer layer remained almost unchanged with different δ, the validity of the subtraction of XMCD is warranted because the DOS for MnI is similar in all δ regions. To apply the magneto-optical sum rule for effective spin magnetic moments (m_s^{eff}) including magnetic dipole term and m_{orb}, the integrals of the XMCD line shapes are needed. Further, the integrals of XAS were also estimated for MnI and MnII, divided by the composition ratios. The electron numbers for 3*d* states of MnI and MnII were estimated from the band-structure calculations to be 5.795 and 5.833, respectively. Thus, m_s^{eff} and m_{orb} for MnI were estimated to be 2.30 and 0.163 μ_B, respectively. For MnII, 2.94 μ_B (m_s^{eff}) and 0.093 μ_B (m_{orb}) were obtained for perpendicular components with the error bars of 20% because of the ambiguities estimating spectral background. Here, we claim the validity of m_s^{eff} and m_{orb} in $Mn_{3-\delta}Ga$ deduced from XMCD. *First*, these m_{orb} values are too small to explain stabilizing the PMA because the magnetic crystalline energy $E_{MCA} \propto 1/4\alpha\xi(m_{orb}^{\perp} - m_{orb}^{\parallel})$ within the scheme of the Bruno relation [69], assuming the spin–orbit

coupling constant ξ_{Mn} of 41 meV and the band-state parameter $\alpha = 0.2$ for Mn compounds, which is estimated from the band-structure calculation. For Mn_1Ga, as the saturation magnetic field along hard axis direction was less than 1 T, the projected component ${m_{orb}}^{\parallel}$ could be deduced as $\Delta m_{orb} (= {m_{orb}}^{\perp} - {m_{orb}}^{\parallel})$ of less than 0.01 μ_B, resulting in $E_{MCA} = 1 \times 10^{-5}$ eV/atom, that is, 5.7×10^4 J/m^3 using the unit cell of MnGa. Therefore, orbital moment anisotropy cannot explain the PMA of the order of 10^6 J/m^3 in $Mn_{3-\delta}Ga$ [68]. As the electron configuration is close to the half-filled $3d^5$ case, the quenching of the orbital angular momentum occurs in principle. In $Mn_{3-\delta}Ga$, since the electron filling is not complete half-filled cases, small orbital angular momentum appears. *Second*, another origin for the large PMA is considered as the spin flipped contribution between the spin-up and -down states in the vicinity of the E_F. The magnetic dipole moment (m_T) also stabilizes the magneto-crystalline anisotropy energy (E_{MCA}) by the following equation [70, 71]:

$$E_{MCA} \sim \frac{1}{4\mu_B} \xi \Delta m_{orb} - \frac{21}{2\mu_B} \frac{\xi^2}{\Delta E_{ex}} m_T \tag{10.12}$$

where ΔE_{ex} denotes the exchange splitting of $3d$ bands. Positive values of E_{MCA} stabilize the PMA. The second term becomes dominant when proximity-driven exchange split cases, such as the $4d$ and $5d$ states, are dominant. In the case of $Mn_{3-\delta}Ga$, the Mn $3d$ states were delicate regarding the mixing of the spin-up and -down states at the E_F, which corresponds to the quadrupole formation and the band structure α values. The second term is expressed by m_T in the XMCD spin sum rule of $m_s + 7m_{Tz}$ along the out-of-plane z direction [72]. For Mn_1Ga, if m_{Tz} is negative, resulting in $Q_{zz} > 0$ in the notation of $m_{Tz} = -Q_{zz}m_s$, which exhibits the prolate shape of the spin density distribution; the second term favors PMA because of the different sign for the contribution of orbital moment anisotropy in the first term. The Q_{zz} corresponds to the quadrupole representation. Since $7m_{Tz}$ is estimated to be in the order of 0.1 μ_B from angular-dependent XMCD between surface normal and magic angle cases, Q_{zz} is less than 0.01, resulting that the orbital polarization of less than 1% contributes to stabilize PMA. In this case, the contribution of the second term in (10.12) is one order larger than the orbital term, which is essential for explaining the PMA of $Mn_{3-\delta}Ga$. *Third*, in a previous study [63], quite small Δm_{orb} and negligible m_{Tz} were reported for Mn_2Ga and Mn_3Ga. Their detailed investigation claims that Δm_{orb} of 0.02 μ_B in MnI site contributes to PMA and MnII site has the opposite sign. These are qualitatively consistent with our results. The difference might be derived from the sample growth conditions and experimental setup. Fourth, the reason why Hc in Mn_1Ga is small can be explained by the $L1_0$-type structure, due to the stacking of the Mn and Ga layers alternately, which weakened the exchange coupling between the Mn layers. *Finally*, we comment on the XMCD of the Ga L-edges shown in Fig. 10.10. Clear XMCD signals are induced with the same sign as the MnI component, suggesting that the induced moments in the Ga sites were derived from the MnI component, which was substituted by the MnII for Mn_2Ga and Mn_3Ga. In Fig. 10.10, not only L_2 and L_3-edges but also oscillation behaviors are

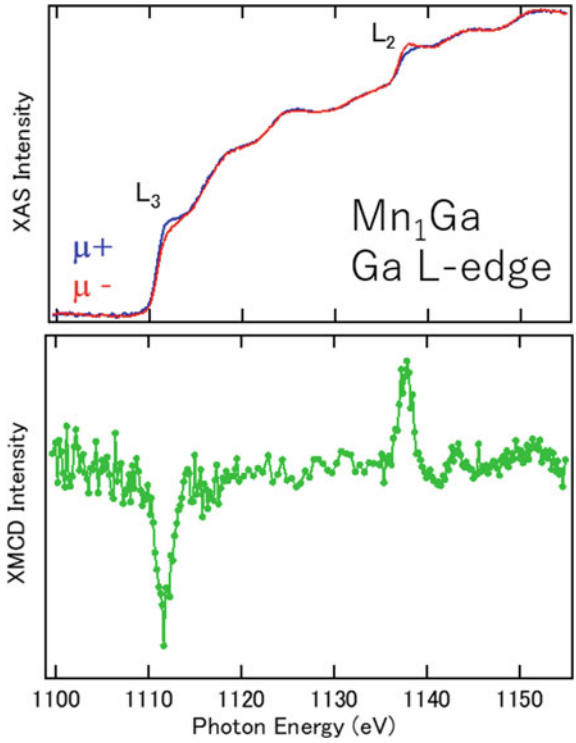

Fig. 10.10 XAS and XMCD of Mn_1Ga. Spectra were measured at the normal incident setup where the incident beam and magnetic field were parallel to the sample surface normal. μ^+ and μ^- denote the absorption in different magnetic field direction. All measurements were performed at RT

detected in XAS, which corresponds to the extended x-ray absorption fine structure and does not contribute to the magnetic signals in XMCD.

Considering the results of the XMCD, we discuss the origin of PMA in $Mn_{3-\delta}Ga$. As the orbital magnetic moments and their anisotropies are small, the contribution of the first term in (10.12) is also small, which is a unique property of Mn alloy compounds and contradicts the cases of Fe and Co compounds exhibiting PMA. Beyond Bruno's formula, the mixing of majority and minority bands in Mn 3*d* states enables the spin-flipped transition and Q_{zz}. However, comparing with the CoPd or FePt cases, where the exchange splitting was induced in the 4*d* or 5*d* states, a small ξ_{Mn} and large ΔE_{ex} in the Mn 3*d* states suppress the contribution of the second term. Large Q_{zz} values were brought by the crystalline distortion accompanied by the anisotropic spin distribution, resulting in the PMA energy of $Mn_{3-\delta}Ga$ exhibiting a similar order with those in heavy-metal induced magnetic materials. Therefore, the large PMA in $Mn_{3-\delta}Ga$ originates from the specific band structure of the Mn 3*d* states, where the orbital selection rule for the electron hopping through spin-flipped $\langle yz|L_x|z^2\rangle$ provides the cigar-type spin distribution. As the spin-flipped term for PMA energy, except the orbital contributions, can be written as:

$$E_{\text{spin-flipped}} = \sum_{u\uparrow,o\downarrow} \frac{\xi^2}{\Delta E_{\text{ex}}} \left[\langle u \uparrow | L_x^2 | o \downarrow \rangle - \langle u \uparrow | L_z^2 | o \downarrow \rangle \right]. \tag{10.13}$$

The difference between the ${L_x}^2$ and ${L_z}^2$ terms through the spin-flipped transitions between the occupied (o) to unoccupied (u) states is significant for the gain of the PMA energy. The matrix elements of $\langle yz\uparrow | L_x | z^2\downarrow \rangle$ were enhanced in the spin-flipped transition between yz and z^2, and those of $\langle yz\downarrow | L_z | z^2\downarrow \rangle$ were enhanced in the spin-conserved case between xy and $x^2 - y^2$ [73]. These transitions favor the magnetic dipole moments of prolate shapes ($\langle Q_{zz} \rangle = \langle 3{L_z}^2 - L^2 \rangle > 0$) described by the Mn $3d$ each orbital angular momenta. We emphasize that the signs of Δm_{orb} and Q_{zz} are opposite, which is essential to stabilize the PMA by the contribution of the second term in (10.12). The PMA energy of FePt exhibits around MJ/m^3 and the contribution of the second term in Pt is four times larger than the Fe orbital anisotropy energy. Therefore, MnGa has a specific band structure by crystalline anisotropy elongated to the c-axis and intra-Coulomb interaction in Mn sites to enhance the PMA without using heavy-metal atoms.

In summary, the contribution of the orbital moment anisotropy in Mn_3Ga is small and that of the mixing between the Mn $3d$ up and down states is significant for PMA, resulting in the spin-flipped process through the electron hopping between finite unforbidden orbital symmetries in the $3d$ states through the quadratic contribution. Composition dependence reveals that the orbital magnetic moments of the two antiparallel-coupled components in Mn sites were too small to explain the PMA. These results suggest that the quadrupole-like spin-flipped states through the anisotropic $L1_0$ and $D0_{22}$ crystalline symmetries are originated to the PMA in $Mn_{3-\delta}Ga$. The present study provides a promising strategy to investigate quadrupoles in antiferromagnetic or ferromagnetic materials with PMA.

10.3.4 Interfacial Exchange Coupling Between Transition Metals and $Mn_{3-\delta}Ga$[4]

As promising spintronics materials, tetragonal $L1_0$-type MnGa and $D0_{22}$-type Mn_3Ga alloys and their mixed alloy $Mn_{3-\delta}Ga$ have been extensively investigated and discussed in the Sect. 10.3.3. In order to understand the interfacial magnetic properties of multilayered structures between $Mn_{3-\delta}Ga$ and TMs, thermal and chemical diffusions at the interfaces are quite important for use in the MRAM devices using magnetic tunnel junctions. The Co substitution into $Mn_{3-\delta}Ga$ products such as Mn_2CoGa [75, 76] and the creation of magnetic tunnel junctions for TMR using Mn_3Ga/MgO/Mn_3Ga stacks of over 600% and $L1_0$-type MnGa/MgO/MnGa with an

[4] This section is partly reproduced from J. Okabayashi, K. Z. Suzuki, and S. Mizukami, Journal of Magnetism and Magnetic Materials 460, 418 (2018), in accordance with the Elsevier Science Direct.

epitaxial strain was also predicted [68, 77, 78]. Since the case of MTJs the interfaces arise inevitably between MnGa and TMs, the interfacial magnetism and the annealing effect have to be clarified explicitly to enhance the TMR characteristics.

Using the advantage that $Mn_{3-\delta}Ga$ is a hard magnetic film, the deposition of other ferromagnetic materials on $Mn_{3-\delta}Ga$ layers can be used to induce perpendicular magnetization through exchange interactions [79–83]. Ultra-thin $Fe_{1-x}Co_x$ layers deposited on $Mn_{3-\delta}Ga$ couple ferromagnetically or antiferromagnetically, depending on their compositions [82]. Antiferromagnetic coupling has been demonstrated in high-Co-concentration regions, while low-Co-concentration regions have been shown to exhibit ferromagnetic coupling. In particular, TMR ratios higher than those in as-grown samples have been found to appear after annealing at 350 °C in order to maintain the highly crystallized body-centered-cubic structures of FeCo alloys [82]. Therefore, the studies of interfacial magnetism depending on annealing temperature resolving into each element are necessary for Fe/MnGa, Co/MnGa, and Cr/MnGa cases by using XMCD for 3d TM *L*-edges and their element-specific hysteresis curves for unveiling the interfacial magnetic properties. In this sub-section, XMCD was employed to investigate the element-specific magnetic properties at TMs/$Mn_{1.5}$Ga interfaces. We discuss the interfacial coupling, which may be ferromagnetic or antiferromagnetic depending on the annealing of the samples.

The samples were prepared by magnetron sputtering. The 40-nm-thick Cr buffer layers were deposited on single-crystal MgO (001) substrates at room temperature, and in situ annealing at 700 °C was performed. Subsequently, 30-nm-thick $L1_0$-type $Mn_{1.5}Ga$ layers were grown at room temperature with in situ annealing at 500 °C. Fe and Co were sputtered at room temperature to form a layer 1 nm thick and were capped with a 2-nm-thick MgO layer. A piece of an "as-grown" sample of MgO (2 nm)/TMs (1 nm)/$Mn_{1.5}Ga$ (30 nm)/Cr (40 nm)/MgO (001) was annealed at 350 °C for 10 min to prepare the "annealed" sample. The details of the employed sample preparation method were reported in [82]. The magneto-optical polar Kerr effect (MOKE) measurement was carried out with a laser wavelength of about 400 nm and the maximum magnetic field of ± 2 T. The XAS and XMCD measurement geometries were mainly set to normal incidence because of the detection for easy-axis direction in PMA.

Figure 10.11 shows the polarization dependences of the XAS and XMCD results for the Mn and Co L_{23}-edges of the Co/$Mn_{1.5}Ga$ as-grown sample. Clear metallic spectral line shapes are observable for the Co *L*-edges. The broad line shape with the shoulder structures in the XAS results for the Mn *L*-edge is quite similar to those shown in previous reports because the two kinds of Mn components overlap as discussed in the previous section [74]. The spins of Mn and Co are coupled ferromagnetically. Because of the ferrimagnetic nature of $Mn_{1.5}Ga$, the spins of the Mn sites partially cancel, and the XMCD intensity of the Mn *L*-edge is smaller than that of Co.

After the annealing, the XMCD intensities in both Mn and Co *L*-edges become small, and the signs at the L_3 and L_2 edges in Co change. By comparing these spectral line shapes with those in the as-grown case, it is evident that the XAS intensity ratios between Mn and Co are also modulated, which suggests that the Co atoms diffuse

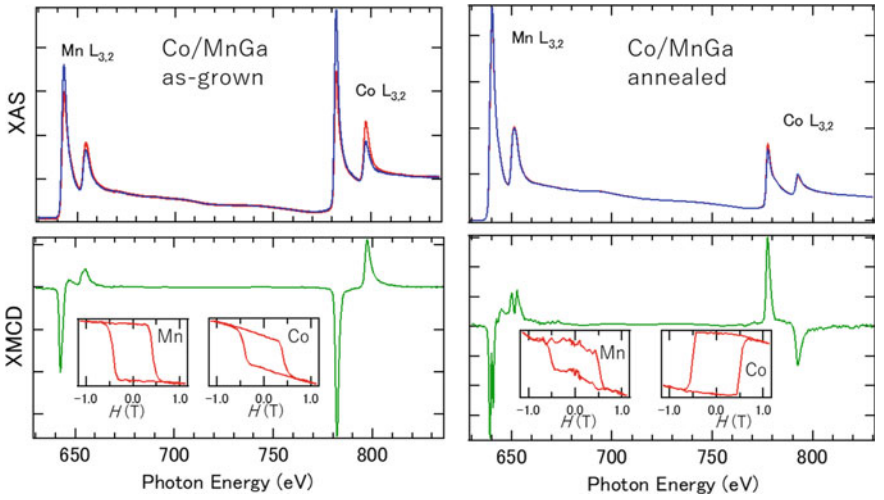

Fig. 10.11 XAS and XMCD spectra of Mn and Co *L*-edges in Co/$Mn_{1.5}$Ga. As-grown and annealed cases. Insets show the element-specific hysteresis curves taken at L_3-edges. The units of magnetic field in horizontal axis are Tesla

chemically into the MnGa layer, or vice versa, within the probing depth of beneath 5 nm from the surface with exponential detection decay. In the Mn *L*-edge XAS results, little difference between the μ^+ and μ^- XAS peaks due to the annealing process is evident, which indicates that the other antiferromagnetic Mn compounds are formed by interfacial reactions. Further, from the comparison of XAS intensities between Mn and Co, it is clear from the changes of XAS intensities by annealing. The Mn *L*-edge XMCD line shape shows two chemically shifted components, although the sign of the XMCD remains unchanged by the annealing. Generally, 1-nm-thick Co layers capped with 2-nm-thick MgO exhibit clear XMCD signals identical to those shown in the as-grown case. The fact that the differences between the μ^+ and μ^- XAS peaks of the Co *L*-edges are only slight suggests that the m_s of Co are also suppressed. Opposite XMCD signs are observed in Co, and the XMCD intensities are different from those in the as-grown case. The Co XAS line shapes exhibit small shoulder structures at the higher-energy side, which do not influence the XMCD line shapes. It might be originated from the Co-based Heusler alloy formation. Antiferromagnetic coupling between Co and $Mn_{1.5}$ Ga is consistent with the previous studies [82]. Therefore, although antiferromagnetic coupling occurs between MnGa and Co by annealing, inevitable interfacial atomic diffusion has to be also considered.

The element-specific hysteresis curves for the as-grown and annealed samples are also shown in the insets of Fig. 10.11. The photon energies at the Mn and Co L_3-edges were fixed in the normal incidence setup. In the as-grown sample, the clear hysteresis loops with a coercive field (H_c) of 0.4 T indicate PMA. In the high magnetic field regions, the intensities of Mn are saturated and become constant with almost square

while Co *L*-edge exhibits different in the high magnetic field regions with unsaturated slope. This suggests that there is no intermixing between Co and $Mn_{1.5}Ga$ at as-grown stage. In fact, the MOKE hysteresis curve also exhibits slightly increasing features in high field regions. Thus, the element-resolved hysteresis curves can clearly reveal the details of the components canted from the surface normal direction in Co.

After the annealing, interestingly, the hysteresis loops for both elements change drastically. Because of the small XMCD intensities, the statistics of the hysteresis loops are noisier than those in the as-grown cases. The characteristic features not only of the PMA, but also of the unsaturated slopes, are clearly observable for both elements and indicate the appearance of secondary phases at the interfaces with hard-axis components. The hysteresis loop of the Co *L*-edges is opposite to that of Mn, causing the XMCD signs in Co to be different. On the other hand, the slopes of the hard-axis components and the H_c values are common for both elements. For Mn, both the PMA and the in-plane components are overlapped, with the same spin direction. The PMA contributions result from the bulk $Mn_{1.5}Ga$. The slopes of Co hysteresis curves are influenced by the interfacial secondary alloy phases with anti-parallel coupling.

Next, the XAS and XMCD in the interface between Fe and $Mn_{1.5}Ga$ are shown in Fig. 10.12 in the same manner as those in Co/$Mn_{1.5}Ga$. In the case of as-grown Fe/MnGa, the line shapes of Mn XAS and XMCD is quite similar to those in Co/MnGa, which suggests that that there is no interfacial reaction at the as-grown stage. Clear XAS and XMCD in Fe *L*-edge are observed which is similar to the bulk Fe. However, hysteresis curve shown in the inset of Fig. 10.12 exhibits the

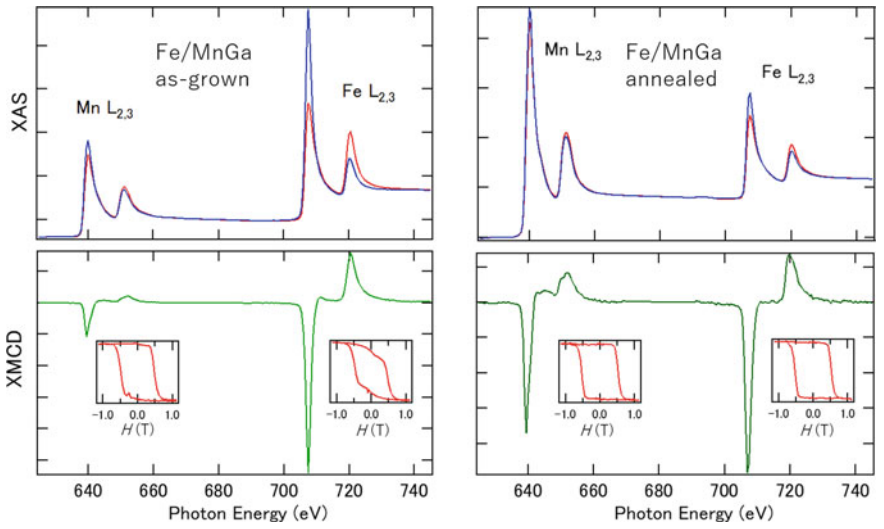

Fig. 10.12 XAS and XMCD spectra of Mn and Fe *L*-edges in Fe/$Mn_{1.5}$ Ga. As-grown and annealed cases. Insets show the element-specific hysteresis curves taken at L_3-edges. The units of magnetic field in horizontal axis are Tesla

summation of exchange coupling from MnGa and in-plane anisotropy, which is saturated at ± 0.7 T and is consistent with the MOKE results. After the annealing, the XMCD intensities of both Mn and Fe are suppressed although the line shapes remain unchanged, which is quite different from the case of Co/$Mn_{1.5}$Ga. XAS intensities also modulated. Element-specific hysteresis curves become similar, which suggests the Fe–Mn-Ga alloy formation by the annealing with the parallel coupling between Mn and Fe. Contrary to the case of Co/$Mn_{1.5}$Ga, there is no slope unsaturated at ± 1.0 T. The suppression of XMCD intensities might originate from the non-magnetic Fe–Mn-Ga alloy formation. These element-specific interfacial analyses cannot be detected by the transmission electron microscope technique because of nearly equal scattering amplitudes from Mn and Fe. Furthermore, in case of Cr/$Mn_{1.5}$Ga case, we performed similar measurements. The results shown in Fig. 10.13 clearly exhibit the no-interfacial reaction by the annealing, which argues that the interfacial reaction depends on the elements.

Considering the above results, we discuss the magnetic properties at the interfaces before and after the annealing in terms of three aspects: the exchange coupling at the interfaces, the PMA at the TMs/MgO interfaces, and the chemical reactions at the interfaces. When parallel coupling is dominant, the strong perpendicular magnetization in the TM layers is induced by exchange coupling with $Mn_{1.5}$ Ga accompanied by the large H_c values of the Fe and Co hysteresis curves. In the as-grown stages, the ratio of m_s and m_{orb} (m_{orb}/m_{spin}) was found to be 0.09 and 0.12 for Fe and Co, respectively, which is consistent with the cases of bulk Fe and Co [7]. It suggests that the interfacial reaction does not occur and PMA and large H_c is induced by

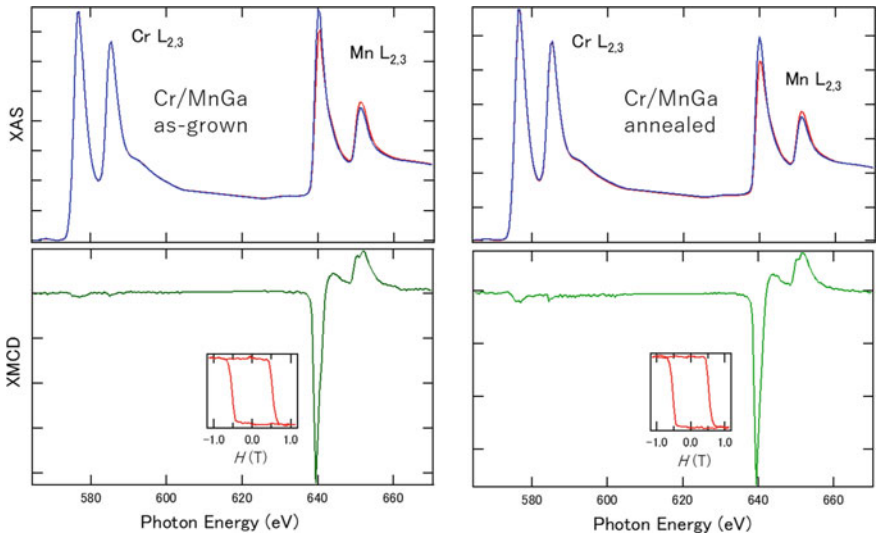

Fig. 10.13 XAS and XMCD spectra of Mn and Cr *L*-edges in Cr/$Mn_{1.5}$ Ga. As-grown and annealed cases. Insets show the element-specific hysteresis curves taken at Mn L_3-edges. The units of magnetic field in horizontal axis are Tesla

the exchange coupling from $Mn_{1.5}Ga$ layer. By annealing, anti-parallel exchange coupling becomes dominant in Co. Since the common slopes appear for both Mn and Co hysteresis curves, Co-Mn-Ga alloy formation becomes a possible candidate. Ternary-alloy phase diagram suggests the formations of Heusler-type Co_2MnGa or Mn_2CoGa [84]. In case of Co-based Heusler alloy, XAS line shapes possess the shoulder structure [27]. The line shapes of CoGa and MnCo are also different from Fig. 10.11 [68, 85]. Therefore, Mn_2CoGa-like compounds are most likely to the interfacial layer where Mn and Co are coupled antiferomagnetically. In order to confirm the alloy formation by annealing, angle dependence of XAS intensity ratios is plotted in Fig. 10.14. By tilting the angle between beam incidence and sample surface normal directions, the Co intensities are enhanced in as-grown case because the Co layer is stacked on $Mn_{1.5}Ga$. After the annealing, the ratios almost remain unchanged due to uniform alloy formation within the probing depth of XAS. On the other hand, Fe–Mn-Ga case is different. Ternary-alloy phase diagram of Fe–Mn-Ga exhibits little mixing between Fe and MnGa [86]. It suggests that the annealing promotes the interfacial coupling between Fe and MnGa, which is evident from the similar hysteresis curves after the annealing and maintaining the similar XMCD line shapes. The suppression of XMCD intensities might be derived from the non-magnetic interfacial layer formation. Furthermore, although the annealing promotes the strong chemical bonding between Fe and MgO, the exchange coupling at the Fe/$Mn_{1.5}Ga$ interface is stronger than that at the Fe/MgO. We emphasize that the interfacial secondary phases formed by annealing are not observable in a TEM image but clearly detected by the XMCD line shapes and element-specific hysteresis curves. Although the annealing process at 350 °C is necessary to obtain high quality

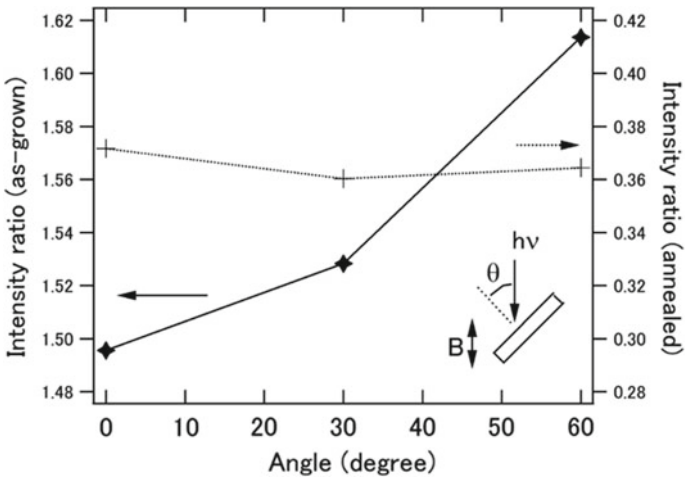

Fig. 10.14 XAS intensity ratio of Co to Mn *L*-edges depending on angle for as-grown and annealed cases in Co/$Mn_{1.5}Ga$. Inset shows the sample geometry and definition of angle. Incident beam and magnetic field directions are fixed parallel

TMs/MgO interfaces, it inevitably produces an interfacial layer at the $Mn_{1.5}Ga$/TMs boundaries, which contributes slightly to the TMR properties [77, 78].

In summary of this sub-section, by using XMCD, we found that the spins in TMs were coupled with and parallel to those in $Mn_{1.5}Ga$ under the as-grown conditions, while the post-annealing at 350 °C changed the interface magnetic coupling to antiferromagnetic in Co and ferromagnetic in Fe. The element-specific hysteresis curves at each XMCD absorption edge revealed large coercive fields in Fe and Co that obeyed the magnetic properties of $Mn_{1.5}Ga$. After the annealing, alloy formation was observed from the XAS and XMCD spectral line shapes and hysteresis curves in each absorption edge are also modulated through the interfacial alloy formation. Therefore, XMCD is a powerful tool to investigate element-specific interfacial magnetism and chemical diffusion processes [87].

10.4 Summary and Outlook in X-Ray Magnetic Spectroscopies for Heusler Alloys

Recent XMCD studies for Heusler alloys and related compounds were reviewed to clarify the element-specific electronic and magnetic states. As discussed above, the electronic structures of alloys are modulated by composition and degree of ordering, which developed novel properties such as magnetic semiconductors or SGS, PMA, antiferromagnetic or ferromagnetic ordering, topological band engineering. As the next steps of material designing using Heusler alloy based compounds, following items are necessary.

(i) The PMA properties with half-metallic properties are strongly desired without using heavy-metal elements. Recent progresses are developed by using interfacial atomic controlling with MgO for TMR device applications. The PMA at MgO/Co_2FeAl is one of the ultimate cases possessing both PMA and half-metallic properties [88, 89]. Interfacial atomic controlling has to be considered explicitly. Further, combinations with magnetic quantum dos or clusters are also expected [90]. Junction with graphene is also anticipated [91].

(ii) Since the Heusler alloys are basically formed as body- or face-centered cubic structures, a crystalline symmetry is relatively high in the bulk form. Not only ordering controlling but also active controlling of strain and designing the quantized states pave a way for creation of novel concepts. In fact, the quantized states in hetero-structures are observed in resonant TMR bias-dependent measurements [92].

(iii) Novel physics can be developed using Heusler alloys. Due to the flexible tuning of band structures, semi-metallic and Weyl-type band crossings are anticipated. These are discussed by Berry curvature [93], which affects the anomalous Hall effects.

(iv) As for the material design, the machine learning procedures for alloy compounds are also helpful techniques. With accelerating the designing of

band structures, quantum materials exhibiting topological phenomena and spin-thermal conversion effects are modified.

For probing the electronic structures, spin states, and orbital states, not only XMCD but also other techniques are also developed. The element-specific characterization is a powerful technique. X-ray magnetic linear dichroism with an element-specific characterization is also a powerful technique for the estimation of magnetic anisotropy and quadrupole moments using magneto-optical sum rules in the same manner as those in XMCD. The x-ray magnetic spectroscopy and microscopy during the bias applying are also strongly demanded. Further, to detect the spin-resolved band structures directly, high-resolution spin- and orbital-resolved photoemission spectroscopy has to be also developed with high efficiency.

Acknowledgements The authors acknowledge to the collaboration with Dr. Tomoki Tsuchiya, Dr. Lakhan Bainsla in Tohoku University for the part of Sect. 10.3.1 and 10.3.2 and with Dr. Yoshio Miura in National Institute for Materials Science (NIMS) for Sect. 10.3.3. The authors acknowledge the fruitful discussion with Dr. Seiji Mitani in NIMS. These works are partly supported by KAKENHI (16H06332) and CREST (JPMJCR17J5). Synchrotron radiation experiments were performed under the approval of the Photon Factory Program Advisory Committee, KEK (Nos. 2017G060 and 2019G028).

References

1. H.S. Bennett, E.A. Stern, Phys. Rev. **137**, 448 (1965)
2. J.L. Erskine, E.A. Stern, Phys. Rev. B **12**, 5016 (1975)
3. G. Schütz, W. Wagner, W. Wilhelm, P. Kienle, R. Zeller, R. Frahm, G. Materlik, Phys. Rev. Lett. **58**, 737 (1987)
4. C.T. Chen, F. Sette, Y. Ma, S. Modesti, Phys. Rev. B **42**, 7262 (1990)
5. B.T. Thole, P. Carra, F. Sette, G. van der Laan, Phys. Rev. Lett. **68**, 1943 (1992)
6. P. Carra, B.T. Thole, M. Altarelli, X. Wang, Phys. Rev. Lett. **70**, 694 (1993)
7. C.T. Chen, Y.U. Idzerda, H.-J. Lin, N.V. Smith, G. Meigs, E. Chaban, G.H. Ho, E. Pellegrin, F. Sette, Phys. Rev. Lett. **75**, 152 (1995)
8. T. Kinoshita, K. Arai, K. Fukumoto, T. Ohkochi, M. Kotsugi, F. Guo, T. Muro, T. Nakamura, H. Osawa, T. Matsushita, T. Okuda, J. Phys. Soc. Jpn. **82**, 021005 (2013)
9. A. Kirilyuk, A.V. Kimel, T. Rasing, Rev. Mod. Phys. **82**, 2731 (2010)
10. J. Okabayashi, Y. Miura, T. Taniyama, npj Quantum Mater. **4**, 21 (2019)
11. H.A. Bethe, E.E. Salpeter, *Quantum Mechanics of One-and Two-Electron Atoms.* (Springer, Berlin, 1957)
12. M. Weissbluth, *Atoms and Molecules* (Academic Press, New York, 1978).
13. J. Stöhr, H.C. Siegmann, Magetism (Springer, Berlin, 2006)
14. F. Heusler, Verh. Dtsch. Phys. Ges. **5**, 219 (1903)
15. A. Hirohata, H. Sukegawa, H. Yanagihara, I. Žutic, T. Seki, S. Mizukami, R. Swaminathan, IEEE Trans. Mag. **51** 0800511 (2015)
16. T. Graf, C. Felser, S.S.P. Parkin, Progress in Solid State Chem. **39**, 1 (2011)
17. Y. Sakuraba, M. Hattori, M. Oogane, Y. Ando, H. Kato, A. Sakuma, T. Miya-zaki, H. Kubota, Appl. Phys. Lett. **88**, 192508 (2006)
18. S. Tsunegi, Y. Sakuraba, M. Oogane, K. Takanashi, Y. Ando, Appl. Phys. Lett. **93**, 112506 (2008)

19. N. Tezuka, N. Ikeda, F. Mitsuhashi, S. Sugimoto, Appl. Phys. Lett. **94**, 1 (2009)
20. W. Wang, H. Sukegawa, R. Shan, S. Mitani, K. Inomata, Appl. Phys. Lett. **95**, 182502 (2009)
21. A. Rajanikanth, Y.K. Takahashi, K. Hono, J. Appl. Phys. **105**, 063916 (2009)
22. L. Bainsla, A.I. Mallick, M.M. Raja, A.K. Nigam, B.S.DCh.S. Varaprasad, Y.K. Takahashi, A. Alam, K.G. Suresh, K. Hono, Phys. Rev. B **91**, 104408 (2015)
23. B. Hu, K. Moges, Y. Honda, H.X. Liu, T. Uemura, M. Yamamoto, J.I. Inoue, M. Shirai, Phys. Rev. B **94**, 094428 (2016)
24. Y. Miura, K. Abe, M. Shirai, Phys. Rev. B **83**, 214411 (2011)
25. M. Lezaic, P. Mavropoulos, J. Enkovaara, G. Bihlmayer, S. Bl¨ugel, Phys. Rev. Lett. **97**, 026404 (2006)
26. K. Nawa, Y. Miura, RSC Adv. **9**, 30462 (2019)
27. I. Galanakis, P.H. Dederichs, and N. Papanikolaou Phys. Rev. B **66**, 174429 (2002)
28. R.A. de Groot, F.M. Mueller, P.G. van Engen, K.H.J. Buschow, Phys. Rev. Lett. **50**, 2024 (1983)
29. J. Okabayashi, A. Kimura, O. Rader, T. Mizokawa, A. Fujimori, T. Hayashi, M. Tanaka, Phys. Rev. B **64**, 125304 (2001)
30. J. Okabayashi, T. Mizokawa, D.D. Sarma, A. Fujimori, T. Slupinski, A. Oiwa, H. Munekata, Phys. Rev. B **65**, 161203(R) (2002)
31. S. Mizukami, A. Sakuma, A. Sugihara, K.Z. Suzuki, R. Ranjbar, Scripta Mater. **118**, 70 (2016)
32. J. Kübler, C. Felser, Eur. Phys. Lett. **114**, 47005 (2016)
33. K. Manna, Y. Sun, L. Muechler, J. Kübler, C. Felser, Nat. Rev. Mater. **3**, 244 (2018)
34. M. Hirschberger, S. Kushwaha, Z. Wang, Q. Gibson, S. Liang, C.A. Belvin, B.A. Bernevig, R.J. Cava, N.P. Ong, Nature Materials **15**, 1161 (2016)
35. K. Amemiya, H. Kondoh, T. Yokoyama, T. Ohta, J. Electron Spectrosc. Relat. Phenom. **124**, 151 (2002)
36. X. Dai, G. Liu, G.H. Fecher, C. Felser, Y. Li, H. Liu, J. Appl. Phys. **105**, 07E901 (2009)
37. L. Bainsla, A.I. Mallick, M. Manivel Raja, A.K. Nigam, B.S.D.C.S. Varaprasad, Y.K. Takahashi, A. Alam, K.G. Suresh, K. Hono, Phys. Rev. B **91**, 104408 (2015)
38. G.Z. Xu, E.K. Liu, Y. Du, G.J. Li, G.D. Liu, W.H. Wang, G.H. Wu, Europhys. Lett. **102**, 17007 (2013)
39. V. Alijani, S. Ouardi, G.H. Fecher, J. Winterlik, S.S. Naghavi, X. Kozina, G. Stryganyuk, C. Felser, Phy. Rev. B **84**, 224416 (2011)
40. K. Ozdogan, E. Sasioglu, I. Galanakis, J. Appl. Phys. **113**, 193903 (2013)
41. P. Klaer, B. Balke, V. Alijani, J. Winterlik, G.H. Fecher, C. Felser, H.J. Elmers, Phys. Rev. B **84**, 144413 (2011)
42. E. Goering, Philos. Mag. **85**, 2895 (2005)
43. A. Scherz, H.Wende, C. Sorg, K. Baberschke, J.Minr, D. Benea, H. Ebert, Phys. Scr., T **115**, 586 (2005)
44. Y. Feng, H. Chen, H. Yuan, Y. Zhou, X. Chen, J. Magn. Magn. Mater. **378**, 7 (2015)
45. L. Bainsla, R. Yilgin, J. Okabayashi, A. Ono, K.Z. Suzuki, S. Mizukami, Phys. Rev. B **96**, 094404 (2017)
46. L. Bainsla, A.I. Mallick, A.A. Coelho, A.K. Nigam, B.S.DCh.S. Varaprasad, Y.K. Takahashi, A. Alam, K.G. Suresh, K. Hono, J. Magn. Magn. Mater. **394**, 82 (2015)
47. Y. Jin, P. Kharel, S.R. Valloppilly, X.-Z. Li, D.R. Kim, G.J. Zhao, T.Y. Chen, R. Choudhary, A. Kashyap, R. Skomski, D.J. Sellmyer, Appl. Phys. Lett. **109**, 142410 (2016)
48. Y. Jin, R. Skomski, P. Kharel, S.R. Valloppilly, D.J. Sellmyer, AIP Adv. **7**, 055834 (2017)
49. R. Choudhary, P. Kharel, S.R. Valloppilly, Y. Jin, A. O'Connell, Y. Huh, S. Gilbert, A. Kashyap, D.J. Sellmyer, R. Skomski, AIP Adv. **6**, 056304 (2016)
50. Y. Sakuraba, J. Nakata, M. Oogane, H. Kubota, Y. Ando, A. Sakuma, T. Miyazaki, Jpn. J. Appl. Phys. **44**, 6535 (2005)
51. K. Kobayashi, R. Kainuma, K. Ishida, Mater. Trans. **47**, 20 (2006)
52. T. Tsuchiya, T. Roy, K. Elphick, J. Okabayashi, L. Bainsla, T. Ichinose, K.Z. Suzuki, M. Tsujikawa, M. Shirai, A. Hirohata, S. Mizukami, Phys. Rev. Mater. **3**, 084403 (2019)
53. B. Dieny, M. Chshiev, Rev. Mod. Phys. **89**, 025008 (2017)
54. S. Fukami, C. Zhang, S. DuttaGupta, A. Kurenkov, H. Ohno, Nat. Mater. **15**, 535 (2016)

55. X. Marti, I. Fina, C. Frontera, Jian Liu, P. Wadley, Q. He, R. J. Paull, J. D. Clarkson, J. Kudrnovsky, I. Turek, J. Kune?, D. Yi, J-H. Chu, C. T. Nelson, L. You, E. Arenholz, S. Salahuddin, J. Fontcuberta, T. Jungwirth, R. Ramesh, Nat. Mater. **13**, 367 (2014).
56. J. Okabayashi, Y. Miura, H. Munekata, Sci. Rep. **8**, 8303 (2018)
57. J.W. Koo, S. Mitani, T.T. Sasaki, H. Sukegawa, Z.C. Wen, T. Ohkubo, T. Niizeki, K. Inomata, K. Hono, Appl. Phys. Lett. **103**, 192401 (2013)
58. J. Okabayashi, J.W. Koo, H. Sukegawa, S. Mitani, Y. Takagi, T. Yokoyama, Appl. Phys. Lett. **105**, 122408 (2014)
59. J. Okabayashi, Y. Iida, Q. Xiang, H. Sukegawa, S. Mitani, Appl. Phys. Lett. **115**, 252402 (2019)
60. S. Mizukami, F. Wu, A. Sakuma, J. Walowski, D. Watanabe, T. Kubota, X. Zhang, H. Naganuma, M. Oogane, Y. Ando, T. Miyazaki, Phys. Rev. Lett. **106**, 117201 (2011)
61. S. Mizukami, T. Kubota, F. Wu, X. Zhang, T. Miyazaki, H. Naganuma, M. Oogane, A. Sakuma, Y. Ando, Phys. Rev. B **85**, 014416 (2012)
62. D. Kim, J. Hong, L. Vitos, Phys. Rev. B **90**, 144413 (2014)
63. K. Rode, N. Baadji, D. Betto, Y.-C. Lau, H. Kurt, M. Venkatesan, P. Stamenov, S. Sanvito, J.M.D. Coey, Phys. Rev. B **87**, 184429 (2013)
64. M. Glas, C. Sterwerf, J.M. Schmalhorst, D. Ebke, C. Jenkins, E. Arenholz, G. Reiss, J. Appl. Phys. **114**, 183910 (2013)
65. D. Oshima, M. Tanimoto, T. Kato, Y. Fujiwara, T. Nakamura, Y. Kotani, S. Tsunashima, S. Iwata, IEEE Trans. Magn. **52**, 1 (2016)
66. J. Okabayashi, in *Progress in Photon Science II*, ed. by K. Yamanouchi, S. Tunik, V. Makarov (Springer Nature Switzerland AG, 2019), p. 471.
67. J.A. Moyer, C.A.F. Vaz, D.A. Arena, D. Kumah, E. Negusse, V.E. Henrich, Phys. Rev. B **84**, 054447 (2011)
68. K.Z. Suzuki, R. Ranjbar, J. Okabayashi, Y. Miura, A. Sugihara, H. Tsuchiura, S. Mizukami, Sci. Rep. **6**, 30249 (2016)
69. P. Bruno, Phys. Rev. B **39**, 865(R) (1989)
70. G. van der Laan, J. Phys.: Condens. Matter **10**, 3239 (1998)
71. D. Wang, R. Wu, A.J. Freeman, Phys. Rev. B **47**, 14932 (1993)
72. J. Stöhr, H. Konig, Phys. Rev. Lett. **75**, 3748 (1995)
73. Y. Kota, A. Sakuma, J. Phys. Soc. Jpn. **83**, 034715 (2014)
74. J. Okabayashi, Y. Miura, Y. Kota, K. Z. Suzuki, A. Sakuma, S. Mizukami, Sci. Rep. **10**, 9744 (2020)
75. V. Alijani, J. Winterlik, G.H. Fecher, C. Felser, Appl. Phys. Lett. **99**, 222510 (2011)
76. S. Chadov, J. Kiss, C. Felser, Adv. Funct. Mater. **23**, 832 (2013)
77. T. Kubota, Y. Miura, D. Watanabe, S. Mizukami, F. Wu, H. Naganuma, X. Zhang, M. Oogane, M. Shirai, Y. Ando, Appl. Phys. Express **4**, 043002 (2011)
78. Q.L. Ma, T. Kubota, S. Mizukami, X.M. Zhang, H. Naganuma, M. Oogane, Y. Ando, T. Miyazaki, Phys. Rev. B **87**, 184426 (2013)
79. R. Ranjbar, K. Suzuki, A. Sugihara, Q.L. Ma, X.M. Zhang, Y. Ando, T. Miyazaki, S. Mizukami, Mater. Des. **96**, 490 (2016)
80. S. Mao, J. Lu, X. Zhao, X. Wang, D. Wei, J. Liu, J. Xia, J. Zhao, Sci. Rep. **7**, 43064 (2017)
81. S. Mizukami, T. Kubota, S. Iihama, R. Ranjbar, Q. Ma, X. Zhang, Y. Ando, T. Miyazaki, J. Appl. Phys. **115**, 17C119 (2014)
82. Q.L. Ma, S. Mizukami, T. Kubota, X.M. Zhang, Y. Ando, T. Miyazaki, Phys. Rev. Lett. **112**, 157202 (2014)
83. Q.L. Ma, X.M. Zhang, T. Miyazaki, S. Mizukami, Sci. Rep. **5**, 7863 (2015)
84. K. Minakuchi, R.Y. Umetsu, K. Kobayashi, M. Nagasako, R. Kainuma, J. Alloys Compd. **645**, 577 (2015)
85. S. Banerjee, W.L. O'Brien, B.P. Tonner, J. Magn. Magn. Mater. **198–199**, 267 (1999)
86. S. Ener, J. Kroder, K.P. Skokov, O. Gutfleisch, J. Alloys Compd. **683**, 198 (2016)
87. J. Okabayashi, K.Z. Suzuki, S. Mizukami, J. Magn. Magn. Mater. **460**, 418 (2018)
88. J. Okabayashi, H. Sukegawa, Z. Wen, K. Inomata, S. Mitani, Appl. Phys. Lett. **103**, 102402 (2013)

89. Z. Wen, J.P. Hadorn, J. Okabayashi, H. Sukegawa, T. Ohkubo, K. Inomata, S. Mitani, K. Hono, Appl. Phys. Express **10**, 013003 (2016)
90. J. Okabayashi, M. Mizuguchi, K. Ono, M. Oshima, A. Fujimori, H. Kuramochi, H. Akinaga, Phys. Rev. B **70**, 233305 (2004)
91. S. Li, K.V. Larionov, Z.I. Popov, T. Watanabe, K. Amemiya, S. Entani, P.V. Avramov, Y. Sakuraba, H. Naramoto, P.B. Sorokin, S. Sakai, Adv. Mater. **32**, 1905734 (2020)
92. Q. Xiang, H. Sukegawa, M. Belmoubarik, M. Al-Mahdawi, T. Scheike, S. Kasai, Y. Miura, S. Mitani, Advanced Science. **6**, 1901438 (2019)
93. J. Kubler, C. Felser, Phys. Rev. B **85**, 012405 (2012)

Index

K. Yamanouchi et al. (eds.), *Progress in Photon Science*, Springer Series in Chemical Physics 125, https://doi.org/10.1007/978-3-030-77646-6